

# Solar Neutrinos and Reconstruction of the SNO+ Experiment

Jie Hu

A Dissertation

Presented to the Faculty  
of University of Alberta  
in Candidacy for the Degree  
of Doctor of Philosophy

Recommended for Acceptance  
by the Department of  
Physics

January, 2020

© Copyright 2020 by Jie Hu.

All rights reserved.

# **Abstract**

## **0.1 Abstract**

A neutrino is one of the elementary particles we currently know and is included in the Standard Model (SM). However, some properties of neutrinos can not be described by the SM, which shows clues of the new physics beyond the Standard Model.

SNO+ experiment is planned to explore one of the unknown properties of neutrinos: whether the neutrinos are Majorana particles or Dirac particles.

# Acknowledgements

# Contents

|  |              |
|--|--------------|
| <b>Abstract</b>  | <b>iii</b>   |
| 0.1 Abstract . . . . .   | iii          |
| <b>Acknowledgements</b>  | <b>iv</b>    |
| <b>Contents</b>  | <b>v</b>     |
| <b>List of Figures</b>   | <b>ix</b>    |
| <b>List of Tables</b>  | <b>xviii</b> |
| <b>1 Introduction</b>  | <b>1</b>     |
| <b>2 Neutrino physics</b>  | <b>5</b>     |
| 2.1 Basic properties of Neutrinos . . . . .                              | 5            |
| 2.2 Weak Interaction . . . . .   | 6            |
| 2.3 Neutrino Flavor Transformation . . . . .                             | 7            |
| 2.3.1 Vacuum Oscillation . . . . .                                       | 8            |
| 2.3.2 Matter Effect . . . . .  | 11           |
| 2.3.3 Solar Neutrinos . . . . .  | 13           |
| 2.3.4 Status of the Neutrino Flavor Transformation Experiments . . . . . | 16           |
| 2.3.5 SNO . . . . .  | 16           |
| 2.3.6 Super-Kamiokande . . . . .   | 17           |

|          |   |           |
|----------|---|-----------|
| 2.3.7    | Borexino . . . . .  | 17        |
| 2.3.8    | Future Experiments . . . . .  | 17        |
| 2.3.9    | Rector Experiments . . . . .  | 18        |
| 2.4      | Absolute Neutrino Mass . . . . .  | 18        |
| 2.4.1    | Majorana Neutrinos . . . . .  | 18        |
| 2.4.2    | Cosmological Approach . . . . .   | 23        |
| 2.4.3    | Beta Decay . . . . .  | 23        |
| 2.4.4    | Double Beta Decay . . . . .   | 25        |
| <b>3</b> | <b>The SNO+ Experiment</b>  | <b>33</b> |
| 3.1      | Overview . . . . .  | 33        |
| 3.2      | SNO+ Physics Phases . . . . .   | 34        |
| 3.3      | Detection Media . . . . .   | 38        |
| 3.3.1    | Cherenkov Radiation . . . . .   | 38        |
| 3.3.2    | Scintillation from Organic Scintillator . . . . .                               | 39        |
| 3.3.3    | Liquid Scintillator for SNO+ . . . . .  | 42        |
| 3.3.4    | Relative Light Yield Measurements of the Te-loaded Liquid Scintillators         | 47        |
| 3.4      | Electronics . . . . .   | 56        |
| 3.5      | Calibration . . . . .   | 58        |
| 3.5.1    | Optical Calibration Sources . . . . .   | 59        |
| 3.5.2    | Radioactive Calibration Sources . . . . .                                       | 60        |
| 3.6      | Monte Carlo Simulation and RAT Software . . . . .                               | 62        |
| <b>4</b> | <b>Event Reconstruction</b>   | <b>64</b> |
| 4.1      | An Overview of the Reconstruction Algorithms in SNO+ . . . . .                  | 64        |
| 4.2      | Multi-path Reconstruction Algorithm for SNO+ . . . . .                          | 66        |
| 4.3      | Multi-path Position and Direction Reconstructions for the Water Phase . . . . . | 68        |
| 4.3.1    | Vertex Reconstruction . . . . .   | 68        |
| 4.3.2    | Direction Reconstruction . . . . .  | 70        |

|          |  |           |
|----------|--|-----------|
| 4.3.3    | Effective Group Velocity . . . . .   | 71        |
| 4.3.4    | Fitter Pull and Drive Correction . . . . .   | 74        |
| 4.3.5    | Multi-path Fitter Structure . . . . .  | 77        |
| 4.4      | Vertex and Direction Reconstruction for the Water-based Wavelength-shifter           | 80        |
| 4.5      | Vertex Reconstruction for the Partial-fill and Scintillator Phases . . . . .         | 83        |
| 4.5.1    | Complicated Situations in Partial-fill . . . . .                                     | 89        |
| 4.5.2    | Bi-Po Analysis . . . . .   | 90        |
| 4.6      | PMT Selectors for the Reconstruction . . . . .                                       | 91        |
| 4.7      | Energy Reconstruction . . . . .  | 93        |
| 4.7.1    | Figure of Merit . . . . .  | 94        |
| 4.7.2    | Energy Reconstruction in Partial-fill Phase . . . . .                                | 95        |
| 4.8      | Other Reconstruction Algorithms . . . . .  | 95        |
| 4.8.1    | Hough Transformation for Direction Reconstruction . . . . .                          | 95        |
| 4.8.2    | Reconstructions Based on the Deep Learning . . . . .                                 | 96        |
| 4.9      | Conclusion . . . . .   | 96        |
| <b>5</b> | <b>Calibration</b>   | <b>99</b> |
| 5.1      | $^{16}\text{N}$ Calibration Scans in the Water Phase . . . . .                       | 100       |
| 5.2      | High Level Cuts for the Water Phase . . . . .  | 101       |
| 5.2.1    | Effects of the High-level Cuts . . . . .   | 102       |
| 5.3      | Reconstruction Evaluations from $^{16}\text{N}$ Calibration Scans in the Water Phase | 104       |
| 5.3.1    | Position Reconstruction Evaluation . . . . .   | 104       |
| 5.3.2    | Direction Reconstruction Evaluation . . . . .  | 115       |
| 5.3.3    | $\beta_{14}$ and Its Systematic . . . . .  | 120       |
| 5.3.4    | Energy Reconstruction Evaluation . . . . .   | 123       |
| 5.4      | $^{16}\text{N}$ Calibration in Partial-fill Phase . . . . .                          | 129       |
| 5.4.1    | High Level Cuts: Sky-shine Classifier . . . . .                                      | 130       |
| 5.4.2    | $^{16}\text{N}$ Calibration in the Partial-fill Phase . . . . .                      | 135       |
| 5.4.3    | Extracting the Cherenkov Signals in Partial-fill Phase . . . . .                     | 135       |

|  |            |
|--|------------|
| <b>6 Solar Neutrino Analysis in the SNO+ Water Phase</b>                           | <b>139</b> |
| 6.1 Detector Backgrounds . . . . .   | 140        |
| 6.1.1 Physics Backgrounds . . . . .  | 140        |
| 6.2 KullbackLeibler (KL) Divergence for High Level Cuts . . . . .                  | 140        |
| 6.3 Solar $\nu_e$ Analysis and Background Separation in Water Phase . . . . .      | 142        |
| 6.3.1 Open Dataset Analysis . . . . .  | 142        |
| 6.3.2 TMVA Analysis . . . . .  | 144        |
| 6.3.3 Discussions on the TMVA Results . . . . .                                    | 150        |
| 6.3.4 Likelihood Fits for Solar Neutrino Candidate Events . . . . .                | 151        |
| <b>7 Conclusions</b>   | <b>163</b> |
| <b>A Details for the MultiPath Fitter</b>  | <b>164</b> |
| A.1 Create a Random Vertex . . . . .   | 164        |
| A.2 Levenberg-Marquardt Method for Minimization . . . . .                          | 164        |
| A.3 Detailed Light Path Calculations in the MultiPath Scint-water Fitter . . . . . | 171        |
| <b>B Information for <math>^{16}\text{N}</math> Scan Runs</b>                      | <b>173</b> |
| B.1 Information for $^{16}\text{N}$ Scan Runs . . . . .                            | 173        |
| <b>C Run Lists Used for Water Analysis</b>   | <b>179</b> |
| <b>References</b>  | <b>180</b> |

# List of Figures

|      |  |    |
|------|--|----|
| 2.1  | Feynman diagrams (at tree level) for different channels of the elastic scattering interaction. (a) and (b): charged current for s and t channels, respectively; (c): neutral current. . . . .                            | 7  |
| 2.2  | All reactions in the three PP chains: PP-I, PP-II, PP-III. The reactions producing neutrinos are labeled in the solid frames. Modified from [1]. . . . .   | 15 |
| 2.3  | All reactions in the CNO bicycle. The reactions producing neutrinos are labeled in the solid frames. Modified from [1]. . . . .  | 15 |
| 2.4  | Solar neutrino energy spectrum ( $E_\nu$ vs. flux) for the solar model BS05(OP). Figure is from [2]. . . . .   | 16 |
| 2.5  | Tree-level Feynman diagrams for the Seesaw Mechanisms, modified from [3]: type-I (left) and type-II (right). The type-III scheme shares the same diagram to the type-I, but with the $\nu_R$ replaced by $T^0$ . . . . . | 22 |
| 2.6  | $\sqrt{\langle m_{\nu_e}^2 \rangle}$ as a function of the lightest mass ( $m_1$ for NH or $m_3$ for IH). . . . .   | 25 |
| 2.7  | Feynman diagrams for $2\nu\beta\beta$ (a) and $0\nu\beta\beta$ (b). . . . .  | 26 |
| 2.8  | Effective Majorana mass as a function of the lightest mass eigenvalue. Solid lines are for NH cases and dashed lines are for IH. Different colors stand for taking different values of $(\alpha_1, \alpha_2)$ . . . . .  | 28 |
| 2.9  | Energy spectrum of the $^{130}\text{Te}$ $2\nu\beta\beta$ decay and the hypothetical $0\nu\beta\beta$ decay. The SNO+ simulation package (RAT) was used to produce the plot. . . . .                                     | 29 |
| 2.10 | Natural abundance vs. Q-values for different $2\nu\beta\beta$ isotopes[?]. . . . .   | 32 |

|      |   |    |
|------|---|----|
| 3.1  | The SNO+ detector labeled with main structures, figure modified from [4]. . . . .   | 35 |
| 3.2  | A Jablonski diagram for the organic scintillator, modified from [5, 6]. . . . .   | 40 |
| 3.3  | Structural formulae of LAB (left) and PPO (right). . . . .  | 43 |
| 3.4  | Absorption length of SNO+ optical components. ;the internal (solid blue line) and external water (dashed blue line) absorption curves are based on the measurements of the laserball scans in July 2018 during the SNO+ water phase. The horizontal lines are due to absence of the measurements and they are conservative assumptions. . . . . | 45 |
| 3.5  | Timing profiles for liquid scintillators in different SNO+ phases. . . . .  | 46 |
| 3.6  | Test sample (left) and setup (right). Left: The samples were filled into scintillation vials. The dimensions are shown in the picture. Right: two PMTs were aligned to face to the scintillation vial from each side. . . . .   | 48 |
| 3.7  | A diagram shows the light yield measurement setup. See the text for details. . . . .  | 49 |
| 3.8  | A typical waveform triggered by scintillation photons from $^{137}\text{Cs}$ $\gamma$ -rays interaction with LAB-PPO sample. . . . .  | 52 |
| 3.9  | Measured LAB-PPO energy spectrum with and without coincidence cut on the ADC channel 0. A threshold for counting is set by comparing the two spectrum. . . . .  | 52 |
| 3.10 | 2D energy spectrum of the counting measurements of LAB-PPO (a), TeSOP (b), and TeDDA (c) samples, projected the 2D plots into one channel (d). The single photo-electron (p.e.) peak is mainly caused by backgrounds while the multiple p.e. peak is from scintillation photons. . . . .  | 53 |
| 3.11 | Fit the single p.e. peak with an asymmetric Gaussian function (fasym) to obtain the adc channel for weighting. The mean value of p0 is used as the adc channel relative to a single p.e. peak. . . . .  | 55 |
| 3.12 | Two dimensional spectrum of LABPPO sample with coincidence cut. A box cut is defined for multiple PE counting. . . . .  | 55 |
| 3.13 | The SNO+ Source Manipulator System, taken from [7]. . . . .   | 59 |

|      |   |    |
|------|---|----|
| 3.14 | $^{16}\text{N}$ main decay scheme, modified from [8]. . . . .   | 61 |
| 3.15 | $^{16}\text{N}$ calibration source geometry. Left: a detailed diagram of $^{16}\text{N}$ source geometry, modified from [9, 10]; middle: source geometry implemented in RAT, modified from [11]; right: a picture of the $^{16}\text{N}$ source, taken from [12]. . . . . | 62 |
| 4.1  | Diagrams of position (left) and direction (right) reconstruction in SNO+ water phase. . . . .   | 69 |
| 4.2  | PMT response time as the timing <i>pdf</i> for vertex reconstruction. . . . .   | 70 |
| 4.3  | PMT angular distribution as the angular response <i>pdf</i> for direction reconstruction. . . . .   | 70 |
| 4.4  | Refractive index vs wavelength. These values are based on the measurements from laserball calibration scans in the SNO+ water phase[13]. . . . .  | 72 |
| 4.5  | A cartoon shows effects of tuning the effective group velocity. In this case, the effective group velocity is faster than expected, the fitted position is dragged back along the direction to increase the time of flight. . . . .                                       | 73 |
| 4.6  | $^{16}\text{N}$ central run. . . . .  | 73 |
| 4.7  | A cartoon shows fitter pull effect, modified from Fig. C.2 in [14] and Fig. 2,3,4 in [15]. . . . .  | 75 |
| 4.8  | A diagram illustrates the drive correction. . . . .   | 75 |
| 4.9  | Drive correction parameter $p_0$ , $p_1$ vs energy. . . . .   | 76 |
| 4.10 | Radial biases of simulated electron events before and after the drive correction, as a function of energy. . . . .  | 77 |
| 4.11 | Position distributions of hit PMTs (in zenith and azimuth angles) for 5 MeV electrons travelling along $+x$ direction in the pure water (left) and the water plus 0.1 ppm PPO (right). . . . .  | 80 |
| 4.12 | The energies of simulated electrons as a function of mean nhits. The values in the 0.1 ppm PPO (solid line with inverted triangle) are compared with the water (dashed line with star). . . . .   | 81 |
| 4.13 | The timing pdf for the wbWLS. . . . .   | 81 |

|   |     |
|---|-----|
| 4.14 Fit position projected on x axis. The WLS fitter reconstructed $x$ positions of the 5 MeV electron events in the wbWLS (red) are compared to the ones in the water (blue). . . . .   | 82  |
| 4.15 Light path calculation for the MP Partial Fitter. The light path intersects with the neck cylinder surface, the AV sphere as well as the water-scintillator interface. The total length of the path in the scintillator region (scintillator path, $sp$ ), $d_{sp}$ is evaluated by intersection calculations. . . . . | 84  |
| 4.16 Line-sphere intersections. (a): the light ray intersects the sphere with 2 points; (b): the light ray intersects the sphere with 1 point; (c) and (d): the light ray never passes through the sphere. . . . .  | 85  |
| 4.17 The timing pdfs used by the MP Partial Fitter. Blue: the timing pdf used by the MP Water Fitter; red: the scintillator timing pdf. . . . .   | 87  |
| 4.18 Distributions of fit position bias projected on x axis ( $x_{fit} - x_{MC}$ ). . . . .   | 88  |
| 4.19 Fit results: $\rho_{fit} = \sqrt{x_{fit}^2 + y_{fit}^2}$ vs. $z_{fit}$ . . . . .   | 88  |
| 4.20 Timing spectrum for different PPO concentrations based on the Oxford bench-top measurements. . . . .   | 90  |
| 4.21 A flow chart for Bi-Po tagging. . . . .  | 97  |
| 4.22 Group the PMTs by dividing the PMT sphere with latitudes and longitudes. . . . .   | 98  |
| 4.23 Hough transformation for catching the ring structure of Cherenkov signals and fitting the direction. . . . .   | 98  |
| <br>5.1 The deployed source positions of the $^{16}\text{N}$ scan runs used by this thesis. The black dots are internal runs while the red squares are external runs. . . . .   | 101 |
| 5.2 Position biases vs $ITR$ (top) and $\beta_{14}$ (bottom) for the $^{16}\text{N}$ central run-107055. Left is MC and right is data. For the data, the source position ( $\vec{X}_{src}$ ) was compared. . . . .  | 103 |
| 5.3 Position biases ( $ \vec{X}_{fit} - \vec{X}_{MC} $ ) vs $scaleLogL$ for the $^{16}\text{N}$ central run-107055. Left is MC and right is data. For the data, the source position ( $\vec{X}_{src}$ ) was compared. . . . .   | 105 |

|      |   |     |
|------|---|-----|
| 5.4  | Reconstructed energy vs $scaleLogL$ for the $^{16}\text{N}$ central run-107055. Left is MC and right is data. . . . .   | 106 |
| 5.5  | A cartoon shows the $^{16}\text{N}$ source. . . . .   | 107 |
| 5.6  | Spatial distributions of $^{16}\text{N}$ first $\gamma$ -rays interaction position projected on x axis, obtained from the RAT simulations. The double-peak structure is due to the wall of the stainless steel container of the $^{16}\text{N}$ source. . . . .   | 107 |
| 5.7  | Distributions of the reconstructed position projected on x axis, obtained from SNO+ $^{16}\text{N}$ central run data (red) and MC (black). The distributions are fitted with $N_R^{fit}$ (red and black lines). . . . .   | 109 |
| 5.8  | The fitted values of $\mu_P$ (top three) and $\sigma_P$ (bottom three) along x (left), y (middle) and z (right) scans. The source positions in each set of scans are projected onto x, y and z axes respectively. The MC results (red circles) are compared with the data (black boxes). . . . .  | 111 |
| 5.9  | Relative differences of $\sigma_P$ ( $\sigma_{p,\delta}$ ) as a function of the $^{16}\text{N}$ source position. For simplicity, the corner scans are not shown in this figure. The red squares represent the results from the x-scan runs; green circles represent the y-scan runs and the blue triangles represent the z-scan runs. . . . . | 112 |
| 5.10 | Vertex shifts of $\mu_P$ ( $\mu_{p,\delta}$ ) as a function of the $^{16}\text{N}$ source position. For simplicity, the corner scans are not shown in this figure. The red squares represent the results from the x-scan runs; green circles represent the y-scan runs and the blue triangles represent the z-scan runs. . . . .              | 113 |
| 5.11 | Vertex shifts along x, y, z axes and fitted with linear functions. . . . .  | 114 |
| 5.12 | Angular distributions extracted from the data (red solid line) and the MC (black dashed line); both are reconstructed by the MPW fitter. These distributions are fitted with the angular resolution functions ranging from 0.3 to 1. . . . .  | 117 |
| 5.13 | Fitted direction resolution parameters $\beta_M$ , $\beta_S$ for x, y, z-axes scans. . . . .  | 119 |

|  |     |
|--|-----|
| 5.14 Relative differences of $\beta_M$ and $\beta_S$ as a function of the $^{16}\text{N}$ source position.<br>For simplicity, the corner scans are not shown in this figure. The red squares represent the results from the x-scan runs; green circles represent the y-scan runs and the blue triangles represent the z-scan runs. . . . . | 120 |
| 5.15 Distributions of $\beta_{14}$ for the $^{16}\text{N}$ central run-107055. Dashed lines for the MC and solid lines for data; red for the MPW fitter processed results and black for the RAT results. . . . .   | 121 |
| 5.16 A comparison of the $\beta_{14}$ for the data and the MC in run-107055. . . . .   | 122 |
| 5.17 $\beta_{14}$ systematic along x, y, z scans. . . . .  | 122 |
| 5.18 $^{16}\text{N}$ central-run 107055, $U_{test}$ vs. $E_{fit}/5.1$ MeV. . . . .   | 123 |
| 5.19 $^{16}\text{N}$ central-run 107055, $G_{test}$ vs. $E_{fit}/5.1$ MeV. . . . .   | 124 |
| 5.20 $^{16}\text{N}$ central-run 107055, $Z_{factor}$ vs. $E_{fit}/5.1$ MeV. . . . .   | 124 |
| 5.21 NHit spectrum for the $^{16}\text{N}$ central run-107055. Dashed lines for the MC and solid lines for data; red for the MPW fitter results and black for the Rat results. . . . .   | 125 |
| 5.22 Reconstructed $^{16}\text{N}$ energy spectrum for run-106925 ( $\vec{X}_{source} = (-186.0, 254.0, -4999.899)$ mm). . . . .   | 125 |
| 5.23 Simulated energy spectrum for different processes, extracted from $10^5$ MC simulation events. . . . .  | 126 |
| 5.24 Electron energy vs number of Cherenkov photons. . . . .   | 126 |
| 5.25 Reconstructed energy spectrum from the $^{16}\text{N}$ central run-107055. Dashed lines for the MC and solid lines for data; red for the MPW fitter results and black for the Rat results. . . . .  | 127 |
| 5.26 Energy vs $\beta_{14}$ for the data and MC. Both the Rat and the MPW results are shown. . . . .   | 127 |
| 5.27 Fitted energy resolution function (red) with the reconstructed energy of $^{16}\text{N}$ central run-107055 MC (a) and data (b). . . . .  | 129 |
| 5.28 An illustration for the Sky-shine classifier, modified from [16]. . . . .   | 130 |
| 5.29 MC (left) and fitted positions (right) of $^{208}\text{Tl}$ simulations. . . . .  | 131 |

|  |     |
|--|-----|
| 5.30 MC positions vs. skyShine values for simulated $^{208}\text{Tl}$ events. . . . .  | 132 |
| 5.31 MC positions after Sky-shine cuts ( $\text{skyShine} < 1.7$ and $\text{skyShine} < 1.5$ ) for simulated $^{208}\text{Tl}$ events. It shows that most of the events with small $\text{skyShine}$ values are located in the neck region while very few events in the FV region can be mis-tagged. . . . .   | 132 |
| 5.32 Fit biases vs. skyShine values for simulated $^{208}\text{Tl}$ events. . . . .  | 133 |
| 5.33 Fit biases vs. skyShine values for simulated $^{208}\text{Tl}$ events. . . . .  | 134 |
| 5.34 Radial resolutions with different skyShine cuts. . . . .  | 134 |
| 5.35 Distributions of $\cos \theta_{\text{PMT}}$ after the prompt time cut for various $e^-$ energies simulations. . . . .   | 136 |
| 5.36 PMT hit patterns after the prompt time cut and NHit cut. . . . .  | 137 |
| 5.37 $^{16}\text{N}$ source calibration in external water during the partial-fill phase. . . . .   | 138 |
| 5.38 Simulated main track of 7.1 MeV $\gamma$ for one event from $^{16}\text{N}$ source in the external water during the partial-fill phase. . . . .   | 138 |
| <br>6.1 Angular distributions of the MC events in run-by-run simulation 206391, with the same event GTID =7. The black line is the MC solar $\nu_e$ distribution, while the red line is the MC $^{214}\text{Bi}$ distribution. The pdf is scaled to the number of the hits in solar $\nu_e$ event (black dashed line) and the $^{214}\text{Bi}$ event (red dotted line) respectively. . . . .  | 141 |
| 6.2 Fit results for the candidate events, projected onto PMT sinusoidal maps. Black circles stand for the hit PMTs used by the fitter; crosses stand for the hit PMTs removed by the selectors; blue full star stands for the event direction fitted by the waterFitter; red open star stands for the direction fitted by the MPW; full double diamond stands for the solar direction*-1; blue full square stands for the event position fitted by the waterFitter; open square stands for the position fitted by the MPW. . . . . | 143 |

|      |   |     |
|------|---|-----|
| 6.3  | Energy spectrum of the simulated events for $^{214}\text{Bi}$ (black), $^{208}\text{Tl}$ (blue) and solar $\nu_e$ (orange). Solid lines show the internal events and dotted lines show the AV events. . . . .                                 | 145 |
| 6.4  | TMVA outputs for signal/background separations by different methods. . . . .  | 147 |
| 6.5  | ROC curves from TMVA output, for event with $4 < E_{fit} < 15 \text{ MeV}$ . . . . .  | 148 |
| 6.6  | ROC curves from TMVA output, for event with $5 < E_{fit} < 15 \text{ MeV}$ (energy above 5 MeV). . . . .  | 148 |
| 6.7  | ROC curves from TMVA output, for event with $4 < E_{fit} < 5 \text{ MeV}$ (low energy region). . . . .  | 149 |
| 6.8  | BDT output for $\cos\theta_{sun}$ , with $4 < E_{fit} < 15 \text{ MeV}$ . The solid blue line shows the selected candidate solar $\nu_e$ events while the dotted red line shows the selected background events. . . . .                       | 151 |
| 6.9  | MLP output for $\cos\theta_{sun}$ , with $4 < E_{fit} < 15 \text{ MeV}$ . The solid blue line shows the selected candidate solar $\nu_e$ events while the dotted red line shows the selected background events. . . . .                       | 151 |
| 6.10 | BDT output for $\cos\theta_{sun}$ , with $4 < E_{fit} < 15 \text{ MeV}$ . The solid blue line shows the selected candidate solar $\nu_e$ events while the dotted red line shows the selected background events. . . . .                       | 152 |
| 6.11 | MLP output for $\cos\theta_{sun}$ , with $5 < E_{fit} < 15 \text{ MeV}$ . The solid blue line shows the selected candidate solar $\nu_e$ events while the dotted red line shows the selected background events. . . . .                       | 152 |
| 6.12 | For the $5 < E_{fit} < 15 \text{ MeV}$ , comparing the outputs of the BDT, MLP and the default cuts. The solid blue line shows the BDT results; the red slashes show the MLP results and the dotted black line shows the default cut results. | 153 |
| 6.13 | The $\cos\theta_{sun}$ distribution of solar $\nu_e$ extracted from the simulations, which was used as a pdf function. . . . .  | 154 |
| 6.14 | Real data from run-200004 to 203602 (half dataset), after the default cuts. The number of counts in $-1 < \cos\theta_{sun} < 0$ region is 19. . . . .   | 155 |

|   |     |
|---|-----|
| 6.15 An example of the randomly generated $\cos \theta_{sun}$ fitted with $(N_{sig}, N_{bkg})$ . The black dots are data points and the red line is the fitted results. For $N_{sig}^r = 73$ and $N_{bkg}^r = 44$ , the fitted results give $N_{sig} = 73.42 \pm 9.42$ and $N_{bkg} = 43.58 \pm 7.73$ , with a $\chi^2/ndf = 60.19/40 = 1.50$ .   | 155 |
| 6.16 $N_{sig}$ fit biases for 5000 fake datasets.   | 156 |
| 6.17 $N_{sig}$ fit pulls for 5000 fake datasets.  | 157 |
| 6.18 The $-2 \ln L$ of the best fitted results for 5000 fake datasets.  | 157 |
| 6.19 Fitted results for the $5 < E_{fit} < 15 \text{ MeV}$ , from BDT outputs.  | 158 |
| 6.20 Fitted results for the $5 < E_{fit} < 15 \text{ MeV}$ , from MLP outputs.  | 158 |
| 6.21 The MSW survival probability curves. The $P_{ee}$ is in solid red line and $P_{e\alpha}(= 1 - P_{ee})$ is in green dashed line.  | 160 |
| 6.22 The MC $\cos \theta_{Sun}$ distributions used as pdfs for the flux calculations. The histogram in black is the $\nu_e$ flux without oscillation. This histogram is used for fitting the elastic scattering flux. The histogram in blue is the $\nu_e$ flux combined with the $\nu_\mu$ flux, both including the oscillations. This histogram is used for fitting the total flux. The dashed red histogram is the $\nu_e$ flux only, including the oscillation. | 161 |
| A.1 Likelihood surface of an $^{16}\text{N}$ event projected on X-Y, Y-Z, X-Z planes. A clear global maxima is reached for the fitted vertex.   | 168 |
| A.2 Likelihood surface of an $^{16}\text{N}$ event projected on x, y, z, t-axis respectively.   | 169 |
| A.3 Derivatives of $\ln L$ of an $^{16}\text{N}$ event projected on x, y, z, t-axis respectively. The analytical derivatives (blue) are overlaid with numerical derivatives (red). They basically match with each other.  | 170 |
| A.4 Layouts for the scintillator light paths inside the AV sphere.  | 171 |
| A.5 Layouts of the scintillator light paths inside the neck cylinder.   | 172 |

# List of Tables

|     |   |     |
|-----|---|-----|
| 2.1 | Oscillation neutrino experiments. . . . .   | 10  |
| 2.2 | . . . . .   | 13  |
| 2.3 | . . . . .   | 14  |
| 2.4 | The limits of $T_{1/2}^{0\nu}$ and $m_{\beta\beta}$ at 90% C.L. . . . .   | 32  |
| 2.5 | The limits of $T_{1/2}^{0\nu}$ and $m_{\beta\beta}$ at 90% C.L. . . . .   | 32  |
| 3.1 | . . . . .   | 46  |
| 3.2 | Number of photons calculated by Charge weighted photon number method.   | 56  |
| 4.1 | A comparison of quantitative estimates for the angular resolution between<br>the SNO heavy water, SNO+ wbWLS and the SNO+ pure water cases. . . | 83  |
| 4.2 | Reconstructed position biases and resolutions for simulated events in partial<br>fill. . . . .  | 87  |
| 4.3 | time constants and amplitudes measured by Oxford group [17]. . . . .  | 89  |
| 4.4 | Relative light yield (RLY) measured by [17]. . . . .  | 90  |
| 4.5 | Tuned effective group velocities for different PPO concentrations. . . . .  | 91  |
| 4.6 | Fit speeds and biases for various PPO concentrations. . . . .   | 91  |
| 4.7 | Fit speeds and biases for various PPO concentrations. . . . .   | 92  |
| 5.1 | Position resolution parameters for the MPW fitter (x-axis). . . . .   | 108 |
| 5.2 | The MPW fitter position resolution systematic uncertainties in x, y and z<br>axes. Unit: mm. . . . .  | 113 |
| 5.3 | Vertex shifts for the reconstructed positions in x, y and z axes. Unit: mm. .   | 114 |

|     |   |     |
|-----|---|-----|
| 5.4 | Vertex shifts for the reconstructed positions in x, y and z axes. Unit: mm.                                       | 115 |
| 5.5 | Energy scales and resolutions.  | 129 |
| 6.1 | Candidate events in the open dataset. Compared the fitted results of the candidate events with different fitters. | 144 |
| 6.2 | Candidate events in the open dataset, searched by the MPW fitter.   | 144 |
| 6.3 | Datasets of MC simulations.   | 145 |
| 6.4 | Testing results of $4 < E_{fit} < 15 \text{ MeV}$ from different TMVA methods.                                    | 149 |
| 6.5 | Testing results of $5 < E_{fit} < 15 \text{ MeV}$ (above 5 MeV) from different TMVA methods.                      | 150 |
| 6.6 | Testing results of $4 < E_{fit} < 5 \text{ MeV}$ (low energy region) from different TMVA methods.                 | 150 |
| 6.7 | Fitted results for the whole dataset ( $5 < E < 15 \text{ MeV}$ ).  | 159 |
| 6.8 | Systematics for the solar $\nu_e$ analysis in the water phase.  | 159 |
| 6.9 | Expected number of solar $\nu_e$ , $\nu_\mu$ and the fitted number of signals in each energy bins.                | 161 |
| B.1 |   | 174 |
| B.2 |   | 175 |
| B.3 |   | 176 |
| B.4 |   | 177 |
| B.5 |   | 178 |
| C.1 |   | 179 |

# Chapter 1

## Introduction

A neutrino is a spin-1/2 fermion with a neutral electric charge and interacts only via weak interaction and gravity, which is described by the Standard Model. The Standard Model is a theory describing all of the elementary particles to our current knowledge and their interactions. In the Standard Model, neutrinos are created from weak interactions in one of three leptonic flavors: electron neutrinos ( $\nu_e$ ), muon neutrinos ( $\nu_\mu$ ) and tauon neutrinos ( $\nu_\tau$ ), accompanied by electrons ( $e$ ), muons ( $\mu$ ) and tauons ( $\tau$ ) respectively. The weak interactions are described by fermions exchanging  $W^\pm$  and  $Z^0$  bosons as weak force carriers.

The Standard Model has successfully explained and predicted phenomena in particle physics since the latter half of the 20th century, including the discovery of Higgs bosons in 2012, which is a crucial piece predicted by the Standard Model. However, there are open issues in the Standard Model, such as the requirement of input parameters which can not be determined by the theory itself. Moreover, there are a few questions and problems the Standard Model can not answer or solve. The mystery properties and behaviors of neutrinos contribute a few of those questions: What are the masses of neutrinos? How do neutrinos obtain their masses? Why their masses are so small compared to the other elementary particles? Are neutrinos their own antiparticles? And so on. To answer these questions about neutrinos will open a door to the new physics theories beyond the Standard Model.

Since neutrinos weakly interact with other particles and fields, they can penetrate

through massive matter or travel a long way through space without being interrupted. Neutrinos produced in the core of the Sun, in Supernovae, or in the galactic core of the Milky Way can carry original information of these astrophysics objects and easily reach the detectors on the Earth. This enables neutrinos as a probe to study the status of astrophysics objects.

These interesting facts put the researches of neutrinos under the spotlight. Among state-of-the-art neutrino experiments, SNO+ aims to search for an extremely rare process called neutrinoless double beta decay ( $0\nu\beta\beta$ ). This search will explore the unknown nature of neutrinos: whether they are Majorana or Dirac particles, unravel the masses of neutrinos, and test the new physics theories as well.

The SNO+ experiment will go through three major stages, which are mainly determined by the working medium inside the SNO+ detector. First, the detector was filled with water and worked as a water Cherenkov detector. This period of data collection for physics research is called the “water phase”. During this stage, certain fluxes of neutrinos from the Sun have been measured. Rare decay process modes, the invisible nucleon decay, which is predicted by the Grand Unified Theory (GUT) have also been searched. During this phase, calibration sources have been deployed for measuring the detector properties. Up until this thesis writing, the water phase stage has been completed and the water is gradually replaced by the liquid scintillator. During the scintillator filling, there were several long periods when the water level was stable at a fixed height. These stable transition stages are called the “partial-fill phase”, which are used to estimate backgrounds of the liquid scintillator for the next physics phases.

Once the detector is fully filled with the liquid scintillator, the experiment will walk into the “scintillator phase”. A 6-month data-taking is planned for counting the backgrounds of pure liquid scintillator and do measurements of solar, reactor, and geo-neutrinos as well.

After the scintillator phase, tellurium isotopes will be loaded into the liquid scintillator. Once the mixtures are stable, the experiment will start on a search of the neutrinoless double beta decay signal.

In this thesis, a framework of reconstruction algorithm, called the “multiple-path fitter” (MultiPath fitter), was developed for multiple SNO+ physics phases. This framework was first developed by the author’s supervisor, Dr. Aksel Hallin, to reconstruct and investigate the data taken at an early stage of SNO+ when the detector was partially filled with water at the end of 2014 (called “partial water fill stage”)[18]. It was further developed by the researchers from the University of Alberta: Dr. Kalpana Singh and Dr. David Auty, for investigating the wavelength shifter and water events[19, 20, 21, 22]. Dr. Jeff Tseng from the University of Oxford restructured the framework into more flexible and efficient C++ codes and implemented it into the SNO+ software[23]. I was first involved in testing and optimizing the MultiPath Fitter on the simulations and data. Then I further developed it for multiple SNO+ physics phases, i.e., to extend its usage for the partial-fill phase (MultiPath partial fitter), scintillator phase, and tellurium phase (MultiPath scint fitter for these two phases). The principles and optimizations are described in Chapter 4.

Chapter 2 introduces neutrino physics. This chapter focuses on the phenomena of neutrino flavor transformations and neutrinoless double beta decay. The relevant theories and experiments are introduced.

Chapter 3 introduces the SNO+ experiment. This chapter explains how the SNO+ detector works and reads the physics data. The chapter also shows the optical properties of liquid scintillators and the calibrations of the detector, which are crucial to the reconstruction. A bench-top light yield measurement for tellurium-loaded liquid scintillator is also discussed in this chapter. This measurement shows a light yield shift due to the humidity exposure of the tellurium-loaded scintillator as well as a change of concentrations of tellurium. Since the light yield of the scintillator is crucial to the event reconstruction, this study is helpful for the detector running in realistic situations.

Chapter 4 describes the SNO+ reconstruction. Except for the MultiPath fitter mentioned previously, the other reconstruction algorithms which were developed by the SNO+ collaboration, especially the energy reconstruction, are also introduced.

Chapter 5 focuses on the calibration during the SNO+ water phase. The MultiPath

water fitter was applied to the calibration data and simulations. Among the reconstructed quantities, the position and direction results were from the MultiPath water fitter, while the energy and classifier results were from the SNO+ official algorithms. But these results depend on the position and direction results. By comparing the simulations and data, I obtained the reconstruction resolutions and uncertainties, following the procedures suggested by the collaboration. These results were applied to the solar neutrino analysis in the next chapter. This chapter also discusses the calibration during the partial-fill phase. The MultiPath partial fitter was applied. Based on the calibration data, analysis for extracting the Cherenkov signals from the scintillation lights is discussed.

In Chapter 6, I performed an analysis of solar neutrinos during the SNO+ water phase. The MultiPath water fitter was applied to the water phase physics data and simulations. Based on the simulations, I applied a machine learning analysis to optimize the signal and background separation. Then the optimized separation parameters were applied to the data to extract the solar neutrinos from the backgrounds. I evaluated the solar neutrino rates and the background rates from the dataset. The systematics and uncertainties from Chapter 5 were evaluated and included in the results. Finally, a  ${}^8\text{B}$  solar neutrino flux was evaluated.

The last chapter summarizes the works of this thesis.

## Chapter 2

# Neutrino physics

In this chapter, I will give an overview of neutrinos and their properties. Two important properties: neutrino mass and neutrino flavor transformations are focused.

### 2.1 Basic properties of Neutrinos

The existence of neutrinos was first put forward by Wolfgang Pauli in the 1930s to solve the observed contradicts in  $\beta$ -decay process. In 1914, James Chadwick found that the electrons emitted in  $\beta$ -decay (called the “ $\beta$ -electrons”) have a continuous energy spectrum[24]. However, since nuclei have discrete energy levels, the energy spectrum of  $\beta$ -electrons should be discrete and equal to the difference between the final and initial states of nuclei. This indicates that the energy and momentum are not conserved if only nuclei and  $\beta$ -electrons present in the  $\beta$ -decay products. Pauli introduced a charge-neutral, spin-1/2, and nearly massless particle to the  $\beta$ -decay products. This particle was later called “neutrino” (the small neutral one) by Enrico Fermi. The neutrinos take away a part of energies and then cause the broad energy spectrum of  $\beta$ -electrons, thus the problem was solved.

In 1934, after Fermi developed the four-fermion vertex interaction theory to describe the weak interactions relating to neutrinos, Bethe and Peierls suggested direct neutrino detection can be made via a neutrino-induced interaction, called the inverse beta decay (IBD):  $\bar{\nu}_e + p \rightarrow e^+ + n$ . Their calculation showed that the IBD cross-section was in the

order of  $(10^{-44}) \text{ cm}^2$ , which was difficult for the detection[25]. Though the task was difficult, in 1956, Fred Reines and Clyde Cowan made the first discovery of the antineutrinos from nuclear reactors. They measured the cross-section as  $6.3 \times 10^{-44} \text{ cm}^2$ , which was consistent with Bethe's calculation[26].

## 2.2 Weak Interaction

Based on current knowledge, neutrinos only interact via the weak force and gravity. A neutrino  $\nu_\alpha$  is generated with a definite flavor from weak interaction and is related to a charged lepton with a given flavor: the electron ( $e$ ), the muon ( $\mu$ ) or the tauon ( $\tau$ ) and thus  $\alpha = e, \mu, \tau$ . Currently we know that neutrinos have three flavors. In 1962, Lederman, Schwartz, and Steinberger demonstrated that more than one type of neutrino exists by detecting the interactions of the muon neutrino ( $\nu_\mu$ ). The tau neutrino ( $\nu_\tau$ ) was proposed after the discovery of the  $\tau$  lepton and was observed in 2000 by the DONUT collaboration. The width of the  $Z^0$  boson implying three light lepton generations in the Standard Model (SM).

Helicity the measurement of neutrino helicity[27]

leptons Neutrinos mainly take part in the weak interactions. gravitational force electromagnetic force

In the SM, the Majorana fermions are not included. Based on the experimental observations such as the discovery of the parity violation in the  $\beta$ -decay[28], the measurement of neutrino helicity[27] and so on, a maximal parity violating  $V - A$  theory was built and it only allows the left-handed flavor neutrino fields  $\nu_{\alpha L}$  ( $\alpha = e, \mu, \tau$ ) (or called “active” neutrinos) and right-handed flavor antineutrino fields  $\overline{\nu}_{\alpha R}$  involving in the weak interaction. In the theory, the neutrino fields  $\nu_\alpha$  and the charged lepton fields  $\ell_\alpha$  form the left-handed weak isospin doublets (isodoublets) and the right-handed isosinglets, which belong to the SU(2) group. The isodoublet  $\Psi_L = (\nu_{\alpha L}, \ell_{\alpha L})^T$  has weak isospin  $I = \frac{1}{2}$  and its third components  $I_3 = +\frac{1}{2}$  for  $\nu_\alpha$  and  $I_3 = -\frac{1}{2}$  for  $\ell_\alpha$ ; the isosinglet  $\Psi_R = (\ell_{\alpha R})$  has  $I = 0$  and  $I_3 = 0$ [29, 30]. charged-current, the charged vector bosons  $W^+/W^-$



Figure 2.1: Feynman diagrams (at tree level) for different channels of the elastic scattering interaction. (a) and (b): charged current for  $s$  and  $t$  channels, respectively; (c): neutral current.

neutral-current, the neutral vector boson  $Z^0$

neutrino-electron elastic scattering ( $\nu - e$  ES)

$$\frac{d\sigma}{dT_e} = \frac{2G_F^2 m_e}{\pi} [g_L^2 + g_R^2 (1 - \frac{T_e}{E_\nu})^2 - g_L g_R (\frac{m_e T_e}{E_\nu^2})], \quad (2.1)$$

where  $g_L = (\sin^2 \theta_W \pm \frac{1}{2})$ ,  $g_R = \sin^2 \theta_W$ ,  $\sin^2 \theta_W = 0.23$

## 2.3 Neutrino Flavor Transformation

Neutrino flavor transformation is a quantum mechanical interference phenomenon[31]. It was first discovered in 1998, based on the analysis of atmospheric neutrino fluxes measured by the Super-Kamiokande (Super-K) experiment to solve the “atmospheric neutrino anomaly” mentioned in the last section[32]. It is the first direct evidence showing that neutrinos have finite masses and the SM is incomplete.

### 2.3.1 Vacuum Oscillation

For neutrino flavor oscillation experiments, neutrinos are detected in certain flavor eigenstates via weak interaction. A neutrino flavor state vector can be taken as a linear superposition of the mass eigenstates. For three-flavor neutrino mixing, we have[33]:

$$|\nu_f\rangle = \sum_{i=1}^3 U_{fi}^* |\nu_i\rangle, \quad (2.2)$$

where  $f = e, \mu, \tau$  and  $k = 1, 2, 3$ . The unitary PMNS matrix,  $U_{PMNS}$ , can be parameterized as<sup>1</sup> :

$$U_{PMNS} = \begin{pmatrix} 1 & 0 & 0 \\ 0 & c_{23} & s_{23} \\ 0 & -s_{23} & c_{23} \end{pmatrix} \begin{pmatrix} c_{13} & 0 & e^{-i\delta_{CP}} s_{13} \\ 0 & 1 & 0 \\ e^{-i\delta_{CP}} s_{13} & 0 & c_{13} \end{pmatrix} \begin{pmatrix} c_{12} & s_{12} & 0 \\ -s_{12} & c_{12} & 0 \\ 0 & 0 & 1 \end{pmatrix}, \quad (2.3)$$

where  $c_{ij} \equiv \cos \theta_{ij}$  and  $s_{ij} \equiv \sin \theta_{ij}$  ( $i, j = 1, 2, 3$ ) are shorthands. In the PMNS matrix, there are four parameters: the three mixing angles  $\theta_{12}$ ,  $\theta_{13}$ ,  $\theta_{23}$  and the charge-parity (CP) violation parameter of lepton sector,  $\delta_{CP}$ . The unknown value of  $\delta_{CP}$  is related to leptogenesis, the hypothetical physical process that produced an asymmetry between leptons and anti-leptons in the very early universe[34].

Now discuss the vacuum flavor oscillation: in the lab frame, assume a neutrino is generated at time  $t_0 = 0$  from a source with a certain flavor state  $|\nu_\alpha\rangle$ . It then propagates in vacuum with a speed close to the speed of light (ultra-relativistic) for a distance  $L$  and is finally detected at time  $t$  in a detector. The flavor eigenstate evolves in space-time is  $|\nu_\alpha\rangle = \sum_i U_{\alpha i}^* |\nu_i, p_i\rangle$ , where  $p_i$  is the 4-momentum of  $\nu_i$ . The momentum is assumed to be along the direction from the source to the detector and only in one dimension. Via the Schrödinger equation, the amplitude for the flavor eigenstate  $|\nu_\beta\rangle$  in the detector at  $(L, t)$  is (use the natural units:  $\hbar = c = 1$ ) [29]:

$$\mathcal{A}(\nu_\alpha \rightarrow \nu_\beta; L, E) = \sum_i U_{\alpha i}^* e^{-iE_i t + ip_i L} \langle \nu_\beta | \nu_i, p_i \rangle = \sum_i U_{\alpha i}^* U_{\beta i} e^{-iE_i t + ip_i L}, \quad (2.4)$$

---

<sup>1</sup>Here we ignore the Majorana CP violation phases, which are cancelled out when tackling with the flavor transformation probability. We will come to this part in section. 2.4.1

Then the probability of  $\nu_\alpha$  at time  $t_0 = 0$  transforms into a  $\nu_\beta$  at time  $t$  is:

$$\begin{aligned} P(\nu_\alpha \rightarrow \nu_\beta; L, E) &= |\langle \mathcal{A}(\nu_\alpha \rightarrow \nu_\beta; L, E) | \mathcal{A}(\nu_\alpha \rightarrow \nu_\beta; L, E) \rangle|^2 = \\ &(U_{\alpha 1}^* U_{\beta 1} e^{-iE_1 t + ip_1 L} + U_{\alpha 2}^* U_{\beta 2} e^{-iE_2 t + ip_2 L} + \dots)(U_{\alpha 1} U_{\beta 1}^* e^{+iE_1 t - ip_1 L} + U_{\alpha 2} U_{\beta 2}^* e^{+iE_2 t - ip_2 L} + \dots) = \\ &\sum_i |U_{\alpha i}|^2 |U_{\beta i}|^2 + \sum_{i>j} (U_{\alpha i}^* U_{\beta i} U_{\alpha j} U_{\beta j}^*) \exp\{-i(E_i - E_j)t + i(p_i - p_j)L\} + (i \leftrightarrow j), \end{aligned} \quad (2.5)$$

where  $(i \leftrightarrow j)$  stands for the second term exchanging the  $i, j$  indices.

For the second term in 2.5: in the ultra-relativistic case,  $p_i \simeq p_j \equiv p \simeq E \gg m$ , where  $E$  is the average energy. Then  $E_i = \sqrt{p_i^2 + m_i^2} \simeq p + \frac{m_i^2}{2E}$  and thus  $E_i - E_j \simeq \frac{m_i^2 - m_j^2}{2E} \equiv \frac{\Delta m_{ij}^2}{2E}$  [33, 29]. Here  $\Delta m_{ij}^2$  is a set of parameters called mass square difference, popping out in the flavor transition probability. Along with  $L \simeq ct = t$  ( $c \equiv 1$ ), we have  $\exp\{-i(E_i - E_j)t + i(p_i - p_j)L\} \simeq \exp\{-i\frac{\Delta m_{ij}^2}{2E}\}$ . In addition,  $U_{\alpha i}^* U_{\beta i} U_{\alpha j} U_{\beta j}^* = |U_{\alpha i}^* U_{\beta i} U_{\alpha j} U_{\beta j}^*| \exp\{i\phi_{\alpha\beta;ij}\}$ , where  $\phi_{\alpha\beta;ij} = \text{Arg}(U_{\alpha i}^* U_{\beta i} U_{\alpha j} U_{\beta j}^*)$  and  $\phi_{\alpha\beta;ij} = -\phi_{\alpha\beta;ji}$ . Then combine the second term and the  $(i \leftrightarrow j)$  term, 2.5 can be written as[29]:

$$P_{\nu_\alpha \rightarrow \nu_\beta}(L, E) = \sum_i |U_{\alpha i}|^2 |U_{\beta i}|^2 + 2 \sum_{i>j} |U_{\alpha i}^* U_{\beta i} U_{\alpha j} U_{\beta j}^*| \cos\left(\frac{\Delta m_{ij}^2}{2E} L - \phi_{\alpha\beta;ij}\right). \quad (2.6)$$

Further expand the second term in 2.6:

$$\begin{aligned} &|U_{\alpha i}^* U_{\beta i} U_{\alpha j} U_{\beta j}^*| \left\{ \cos\left(\frac{\Delta m_{ij}^2}{2E} L\right) \cos\left(\frac{\Delta m_{ij}^2}{2E} L\right) + \sin\left(\phi_{\alpha\beta;ij}\right) \sin\left(\frac{\Delta m_{ij}^2}{2E} L\right) \right\} = \\ &\Re(U_{\alpha i}^* U_{\beta i} U_{\alpha j} U_{\beta j}^*)(1 - 2 \sin^2 \frac{\Delta m_{ij}^2 L}{4E}) + \Im(U_{\alpha i}^* U_{\beta i} U_{\alpha j} U_{\beta j}^*) \sin \frac{\Delta m_{ij}^2 L}{2E}, \end{aligned} \quad (2.7)$$

since the matrix  $U$  is unitary and when  $t = 0$ ,

$$P_{\nu_\alpha \rightarrow \nu_\beta} = \delta_{\alpha\beta} = \sum_i |U_{\alpha i}|^2 |U_{\beta i}|^2 + 2 \sum_{i>j} \Re(U_{\alpha i}^* U_{\beta i} U_{\alpha j} U_{\beta j}^*), \quad (2.8)$$

finally it comes out the commonly used vacuum oscillation equation[33, 29]:

$$P_{\nu_\alpha \rightarrow \nu_\beta}(L, E) = \delta_{\alpha\beta} - 4 \sum_{i>j} \Re(U_{\beta i} U_{\alpha i}^* U_{\alpha j} U_{\beta j}^*) \sin^2 \frac{\Delta m_{ij}^2 L}{4E} + 2 \sum_{i>j} \Im(U_{\beta i} U_{\alpha i}^* U_{\alpha j} U_{\beta j}^*) \sin \frac{\Delta m_{ij}^2 L}{2E}. \quad (2.9)$$

Choose a set of units commonly used by experiments and with dimensional transformation, we have[33]:

$$X_{ij} \equiv \frac{\Delta m_{ij}^2 L}{4E} = \frac{1.267 \Delta m_{ij}^2 [eV^2] L [m]}{E_\nu [MeV]}. \quad (2.10)$$

Maximum oscillation occurs when  $X_{ij} \sim \pi$ , which gives an effective length  $L^{osc}(\Delta m_{ij}, E_\nu) = 4\pi E / |\Delta m_{ij}^2|$ .

Currently, the four parameters in the PMNS matrix, as well as the parameters of the  $\Delta m_{ij}$ , have been measured by neutrino oscillation experiments. These experiments can be classified by the neutrino sources they use. They are the solar, the reactor, the atmospheric, the accelerator, and the astronomical and cosmological neutrino experiments. Table 2.1 lists the energy scale of the neutrino source as well as the example experiments.

Table 2.1: Oscillation neutrino experiments.

| type         | source                      | $E_\nu$       | example |
|--------------|-----------------------------|---------------|---------|
| solar        | the Sun                     | MeV scale     | SNO     |
| reactor      | reactor                     | MeV scale     | DayaBay |
| atmospheric  | cosmic-ray                  | GeV scale     | SuperK  |
| accelerator  | $\nu$ beam from accelerator | GeV scale     | T2K     |
| astronomical | astronomical objects        | GeV-EeV scale | IceCube |

For the  $\Delta m_{21}^2$  and  $\theta_{12}$ , the combined analysis of the measurements from the reactor experiment KamLAND and SNO gave  $\Delta m_{21}^2 = 7.59_{-0.21}^{+0.21} \times 10^{-5} eV^2$  and  $\tan^2 \theta_{21} = 0.47_{-0.05}^{+0.06}$ [35].

The accelerator neutrino experiments as well as the atmospheric neutrino experiments have measured  $\Delta m_{32}^2$  and  $\theta_{23}$ . The most recent results from SuperK show that in NH,  $\sin^2 \theta_{23} = 0.588_{-0.064}^{+0.031}$  and  $\Delta m_{32}^2 = 2.5_{-0.20}^{+0.13} \times 10^{-3} eV^2$ [36].

In 2012, the reactor neutrino experiment Daya Bay reported the discovery of non-zero  $\theta_{13}$  with a significance of  $5.2\sigma$ . In 2016, Daya Bay reported that  $\sin^2 2\theta_{13} = 0.0841 \pm 0.0027(stat.) \pm 0.0019(syst.)$ . This high-precision result makes  $\sin^2 2\theta_{13}$  the best measured mixing angle[37, 38].

In addition, there are two squared-mass differences,  $\Delta m_{21}^2 = m_2^2 - m_1^2$  and  $\Delta m_{32}^2 = |m_3^2 - m_2^2|$ . The sign of  $\Delta m_{32}^2$  is unknown and it indicates a mass hierarchy problem of whether neutrino mass is normal hierarchy (NH,  $m_3 > m_2 > m_1$ ) or inverted hierarchy (IH,  $m_3 < m_1 < m_2$ )[33].

$L/L^{osc}(\Delta m_{31}, E_\nu) \sim 1$  and  $L/L^{osc}(\Delta m_{21}, E_\nu) \ll 1$

$$P_{\nu_\alpha \rightarrow \nu_\beta}(L, E) \simeq \delta_{\alpha\beta} - 4|U_{\alpha 3}|^3(\delta_{\alpha\beta} - |U_{\beta 3}|^2) \sin^2 \frac{\Delta m_{31}^2 L}{4E} = P_{\bar{\nu}_\alpha \rightarrow \bar{\nu}_\beta}(L, E) \quad (2.11)$$

In the case of antineutrino flavor oscillation, we have:  $|\bar{\nu}_\alpha\rangle = \sum_i U_{\alpha i} |\bar{\nu}_i, p_i\rangle$ , via the same calculation, a similar oscillation probability equation can be found but with the last term in 2.9 being negative[29]:

$$P_{\bar{\nu}_\alpha \rightarrow \bar{\nu}_\beta}(L, E) = \delta_{\alpha\beta} - 4 \sum_{i>j} \Re[U_{\beta i} U_{\alpha i}^* U_{\alpha j} U_{\beta j}^*] \sin^2 \frac{\Delta m_{ij}^2 L}{4E} - 2 \sum_{i>j} \Im(U_{\beta i} U_{\alpha i}^* U_{\alpha j} U_{\beta j}^*) \sin \frac{\Delta m_{ij}^2 L}{2E}. \quad (2.12)$$

This provides a measure of CP violation[29]:

$$\mathcal{A}_{CP} = P_{\nu_\alpha \rightarrow \nu_\beta}(L, E) - P_{\bar{\nu}_\alpha \rightarrow \bar{\nu}_\beta}(L, E) = 4 \sum_{i>j} \Im(U_{\beta i} U_{\alpha i}^* U_{\alpha j} U_{\beta j}^*) \sin \frac{\Delta m_{ij}^2 L}{2E}. \quad (2.13)$$

[39]

$\delta_{CP}$  is examined by the experiments which measure the difference between neutrino and antineutrino oscillation probabilities  $P(\bar{\nu}_\alpha \rightarrow \bar{\nu}_\beta)$  and  $P(\nu_\alpha \rightarrow \nu_\beta)$ [40]. In 2017, the Tokai-to-Kamioka (T2K) experiment in Japan rejected the hypothesis that neutrinos and antineutrinos oscillate with the same probability at 95% confidence ( $2\sigma$ ) level. This indicates a hint of CP symmetry broken by neutrinos[41]. In 2019, T2K claimed confidence intervals for  $\delta_{CP}$  with three standard deviations ( $3\sigma$ ): [-3.41,-0.03] for NH and [-2.54,-0.32] for IH. This result indicates that the CP violation exists in leptons[42].

### 2.3.2 Matter Effect

The matter effect is caused by neutrinos interacting with ambient electrons and nucleons in the matter such as the Sun or the Earth.  $\nu_e$  interacts with electrons via both charged weak current (exchanging  $W$  boson) and neutral weak current ( $Z$  boson) while  $\nu_\mu$  and  $\nu_\tau$  interact only by the neutral current. The  $\nu_e$  energy has an addition term,  $V_{CC} = \sqrt{2}G_F n_e$ , where  $n_e$  is the number density of the electrons in matter and  $G_F$  is the Fermi coupling constant for the weak interaction. This affects the oscillation probabilities for neutrinos propagating

in matter compared to vacuum, which is called the Mikheyev-Smirnov-Wolfenstein (MSW) mechanism[43, 44].

In vacuum two-flavor mixing, the Schrödinger equation can be written (in natural units)[40]:

$$i \frac{d}{dt} \begin{pmatrix} \nu_e \\ \nu_\mu \end{pmatrix} = H_0^f \begin{pmatrix} \nu_e \\ \nu_\mu \end{pmatrix}, \quad (2.14)$$

$$\begin{aligned} H_0^f &= \frac{1}{2E} \begin{pmatrix} m_1^2 \cos^2 \theta + m_2^2 \sin^2 \theta & (m_2^2 - m_1^2) \sin \theta \cos \theta \\ (m_2^2 - m_1^2) \sin \theta \cos \theta & m_1^2 \sin 2\theta + m_2^2 \cos^2 \theta \end{pmatrix} = \\ &\frac{\Delta m_{21}^2}{4E} \begin{pmatrix} -\cos 2\theta & \sin 2\theta \\ \sin 2\theta & \cos 2\theta \end{pmatrix} + \frac{(m_1^2 + m_2^2)}{4E} \begin{pmatrix} 1 & 0 \\ 0 & 1 \end{pmatrix}, \end{aligned} \quad (2.15)$$

and  $\Delta m_{21}^2 = (m_2^2 - m_1^2)$ .

To simplify the calculation, we can drop the second unitary term of  $H_0^f$  that is irrelevant to the neutrino flavor transformation. Including the matter effect, we obtain:

$$H_m = \begin{pmatrix} -\frac{\Delta m_{21}^2}{4E} \cos 2\theta + \sqrt{2}G_F n_e & \frac{\Delta m_{21}^2}{4E} \sin 2\theta \\ \frac{\Delta m_{21}^2}{4E} \sin 2\theta & \frac{\Delta m_{21}^2}{4E} \cos 2\theta \end{pmatrix} \quad (2.16)$$

We define a mixing angle in matter,  $\theta_m$  as:

$$\tan 2\theta_m = \frac{\Delta m^2 \sin 2\theta}{\Delta m^2 \cos 2\theta - 2\sqrt{2}EG_F n_e}, \quad (2.17)$$

and define an effective squared-mass difference in matter  $\Delta m_m^2$  as:

$$\Delta m_m^2 = \sqrt{(\Delta m^2 \cos 2\theta - 2\sqrt{2}EG_F n_e)^2 + (\Delta m^2 \sin 2\theta)^2}. \quad (2.18)$$

In analogy with mixing in vacuum, we can write the mixing equation relating the energy eigenstates in matter ( $\nu_{1m}, \nu_{2m}$ ) to the flavor eigenstates with a diagonalized Hamiltonian:

$$\begin{pmatrix} \nu_e \\ \nu_\mu \end{pmatrix} = \begin{pmatrix} \cos \theta_m & \sin \theta_m \\ -\sin \theta_m & \cos \theta_m \end{pmatrix} \begin{pmatrix} \nu_{1m} \\ \nu_{2m} \end{pmatrix}. \quad (2.19)$$

The probability of flavor transformation in matter is:

$$P_{\nu_e \rightarrow \nu_\mu} = \sin^2(2\theta_m) \sin^2 \left( \frac{\Delta m_m^2 L}{4E} \right). \quad (2.20)$$

The denominator in equation (2.17) implies a resonance condition:

$$V(n_e) = \sqrt{2}G_F n_e = \frac{\Delta m^2 \cos 2\theta}{2E}. \quad (2.21)$$

From this condition, for a given  $E$ , there is a resonance density  $n_e^{reson}$  while for a given  $n_e$ , there is a resonance energy  $E^{reson}$ . When the resonance condition is satisfied,  $\theta_m = \frac{\pi}{4}$  and two flavor neutrinos are maximally mixed, even if the vacuum mixing angle  $\theta$  is small. This is called matter enhanced neutrino oscillation[43, 45], which was observed from measuring the solar neutrinos. I will discuss it in the next two sections.

Table 2.2 summarizes the types of experiments for neutrino flavor transformation and the relating parameters[46, 47].

Table 2.2:

| Source      | Energy ( $\mathcal{O}(\text{MeV})$ ) | Distance ( $\mathcal{O}(\text{m})$ ) | $\Delta m^2$ ( $\mathcal{O}(\text{eV}^2)$ ) |
|-------------|--------------------------------------|--------------------------------------|---|
| Accelerator | $10^3 - 10^5$                        | $10 - 10^7$                          | $10^{-3} - 100$                             |
| Reactor     | 1                                    | $10^2 - 10^3$                        | $10^{-5} - 0.1$                             |
| Cosmic ray  | $10^3$                               | $10^7$                               | $10^{-4}$                                   |
| Sun         | 1                                    | $10^{11}$                            | $10^{-11}$                                  |
| Supernova   | 1-10                                 | $10^2 - 10^3$                        | $10^{-20}$                                  |

### 2.3.3 Solar Neutrinos

Since the Sun is an object provides ambient electrons and nucleons, neutrinos coming from the Sun are traditionally used to investigate the matter effects.

In the 1930s, Hans Bethe et al. explained the origin of the Sun's energy as a series of nuclear reactions[48].

Based on the available physics and experimental data, the Standard Solar Model (SSM) is a modern accepted theory for the evolution of the Sun. The energy in the Sun is mainly produced by two sets of reactions: the proton-proton (pp) chain, which contributes to  $\sim 98.6\%$  of the energy release and the Carbon-Nitrogen-Oxygen (CNO) cycle, which contributes  $\sim 1.4\%$ . Fig. 2.2 and Fig. 2.3 show all the reactions in the two sets respectively. Via these two main sets of nuclear reactions, hydrogen is eventually fused into helium, and

the net nuclear transformation is  $4p + 2e^- \rightarrow {}^4\text{He} + 2\nu_e + Q$ , where the released energy  $Q = 26.73$  MeV is mostly in the form of the kinetic energy of the photons, with a small fraction carried by neutrinos[3, 39]. The average energy of solar  $\nu_e$  is calculated by summing over the  $E_{\nu_e}$  from the  $i^{th}$  reaction chain with a flux of  $\Phi_{\nu_e}^i$  and divided by  $\Phi_{\nu_e}^{tot}$

$$\langle E_{\nu_e} \rangle = \sum_i E_i \frac{\Phi_{\nu_e}^i}{\Phi_{\nu_e}^{tot}} \approx 0.265 \text{ MeV}, \quad (2.22)$$

(the average neutrino energy  $\langle E_{2\nu_e} \rangle \sim 0.59$  MeV).

Besides, about 2 MeV of  $Q$  is from annihilation of positrons with electrons in the solar plasma[3, 39]. For every released energy, there are about 2  $\nu_e$  generated. The solar  $\nu_e$  flux at the Earth surface can be estimated via the measured solar radiation energy on the Earth surface:

$$\Phi_{\nu_e} \simeq \frac{2\mathcal{L}_\odot}{4\pi D_\odot^2} \frac{1}{Q - 2\langle E_{\nu_e} \rangle} = 6.35 \times 10^{10} \nu_e/\text{cm}^2/\text{s}, \quad (2.23)$$

where the solar constants  $G_{sc} = \mathcal{L}_\odot/(4\pi D_\odot^2) \simeq 0.136 \text{ W/cm}^2$  [49].

The electron neutrinos produced in the solar nuclear reactions are named solar neutrinos and they can be detected on the Earth. Due to the branching ratios and unterminated chains in the pp chain and CNO cycle, the solar neutrinos come from different reactions, as shown in Table 2.3. The specific solar neutrinos detected on the Earth are named after the specific fusion process[50]. They have different fluxes and energies, as shown in Fig. 2.4[2].

Table 2.3: Solar neutrinos from reactions in pp chain (a) and CNO cycle (b).

| (a) pp chain    |   | (b) CNO cycle |   |
|-----------------|---|---------------|---|
| solar $\nu_e$   | reaction  | solar $\nu_e$ | reaction  |
| pp              | $p + p \rightarrow {}^2\text{H} + e^+ + \nu_e$              | CNO           | ${}^{13}\text{N} \rightarrow {}^{13}\text{C} + e^+ + \nu_e$ |
| pep             | $p + e^- + p \rightarrow {}^2\text{H} + \nu_e$              |               | ${}^{15}\text{O} \rightarrow {}^{15}\text{N} + e^+ + \nu_e$ |
| hep             | ${}^3\text{He} + p \rightarrow {}^4\text{He} + e^+ + \nu_e$ |               | ${}^{17}\text{F} \rightarrow {}^{17}\text{O} + e^+ + \nu_e$ |
| ${}^7\text{Be}$ | ${}^7\text{Be} + e^- \rightarrow {}^7\text{Li} + \nu_e$     |               |   |
| ${}^8\text{B}$  | ${}^8\text{B} \rightarrow {}^8\text{Be}^* + e^+ + \nu_e$    |               |   |

solar neutrinos are also major backgrounds to the  $0\nu\beta\beta$  search

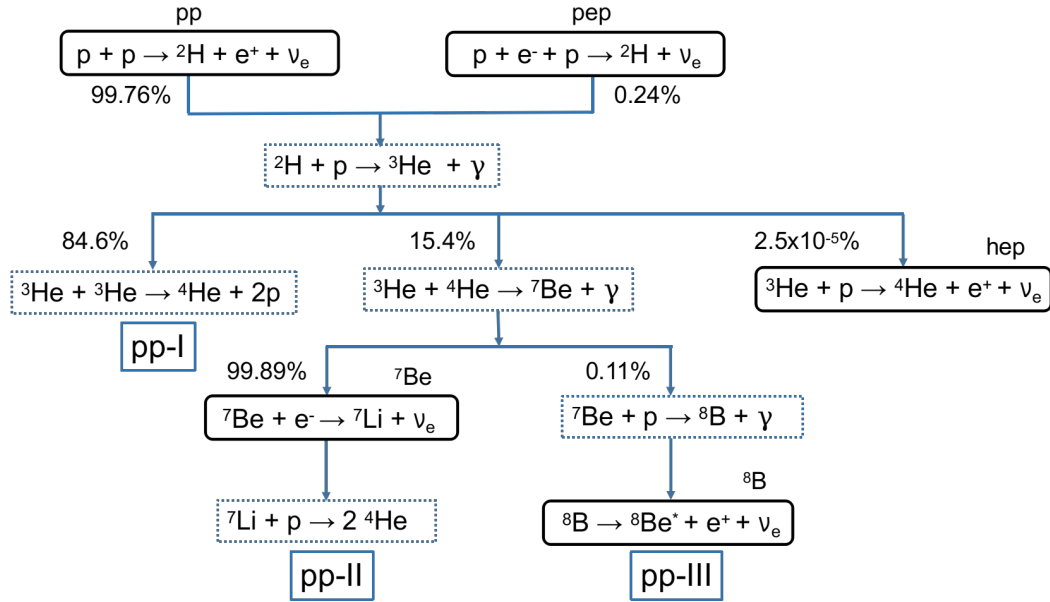


Figure 2.2: All reactions in the three PP chains: PP-I, PP-II, PP-III. The reactions producing neutrinos are labeled in the solid frames. Modified from [1].

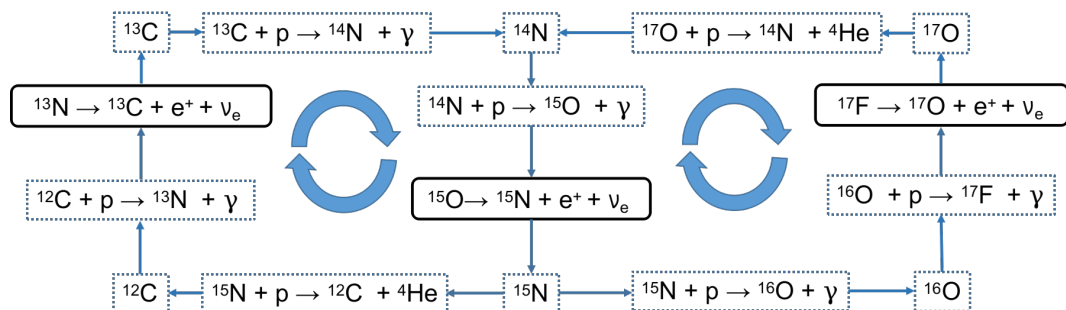


Figure 2.3: All reactions in the CNO bicycle. The reactions producing neutrinos are labeled in the solid frames. Modified from [1].

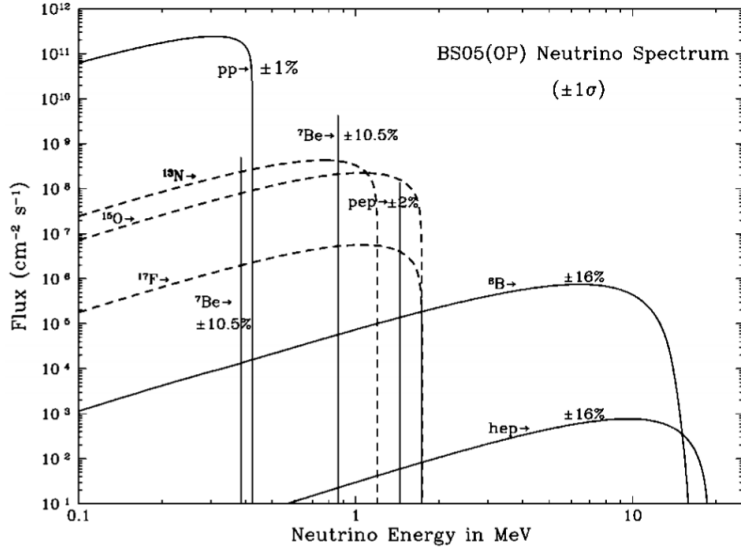


Figure 2.4: Solar neutrino energy spectrum ( $E_\nu$  vs. flux) for the solar model BS05(OP). Figure is from [2].

### 2.3.4 Status of the Neutrino Flavor Transformation Experiments

In 1964, John Bahcall and Raymond Davis proposed the first experiment to detect solar neutrinos[51, 52]. Raymond Davis designed an experiment that used a  $380 \text{ m}^3$  tank filled with Perchloroethylene ( $\text{C}_2\text{Cl}_4$ ), a dry-cleaning fluid rich in chlorine. Solar neutrinos were expected to change  $^{37}\text{Cl}$  to  $^{37}\text{Ar}$  via the endothermic reaction  $\nu_e + ^{37}\text{Cl} \rightarrow ^{37}\text{Ar} + e^-$  and the produced  $^{37}\text{Ar}$  were extracted and counted. The neutrino energy threshold ( $E_{thresh}$ ) of the experiment was 0.814 MeV, which allowed a measurement mostly of the  $^8\text{B}$  neutrino flux but also including some lower energy neutrinos[52]. Their first results, announced in 1968, showed that only about one-third of the predicted radioactive argon atoms were measured. This raised the problem of missing solar neutrinos.

### 2.3.5 SNO

Since neutrinos' extremely low interaction cross-sections, neutrinos produced in the Sun can reach the detectors on the Earth without being interrupted. This enables the solar neutrino to be a probe to stellar physics.

A combined analysis of three phases of SNO data shows that the measured total flux is  $5.25 \pm 0.16^{+0.11}_{-0.13} \text{ cm}^{-2}\text{s}^{-1}$ .

### 2.3.6 Super-Kamiokande

Super-K

$15 \nu$  events/day.

For the  $^8\text{B}$  solar neutrino flux, Super-K reported a measurement of  $(2.345 \pm 0.014 \pm 0.036) \times 10^6 \text{ cm}^{-2}\text{s}^{-1}$ .

### 2.3.7 Borexino

Borexino reported the first observation of CNO neutrino in 2020

interaction rate is  $7.2^{+3.0}_{-1.7}$  counts per day per 100 tonnes of target at 68% C.L. This result gives a flux on Earth of  $7.0^{+3.0}_{-2.0} \times 10^8 \text{ cm}^{-2}\text{s}^{-1}$ .

[53].

Borexino problems: (1) $^{11}\text{C}$  nuclei induced by the high energy cosmic muon spallation reactions cause a large background contribution (2)intrinsic  $\beta$ -decays from  $^{210}\text{Bi}$  contaminate the fiducial volume

### 2.3.8 Future Experiments

#### 2.3.8.1 Hyper-Kamiokande

Hyper-Kamiokande (Hyper-K) is the successor of Kamiokande and Super-Kamiokande.

As a water Cherenkov detector with a fiducial mass of 187 kilotonne, Hyper-K expects to observe 130  $\nu - e$  elastic scattering events per day, is aimed for a detection of *hep* solar neutrino flux, which has not been detected yet.

and precision measurements

### 2.3.8.2 JinPing

### 2.3.8.3 ASDC-THEIA

### 2.3.8.4 DARWIN

for five types of solar neutrinos: pp,  ${}^7\text{Be}$ ,  ${}^{13}\text{N}$ ,  ${}^{15}\text{O}$  and pep

via  $\nu - e^-$  elastic scattering[54].

a low energy threshold of 1 keV majority of pp neutrinos

## 2.3.9 Rector Experiments

For the same parameters,

KamLAND, Daya Bay and JUNO:

The Jiangmen Underground Neutrino Observatory (JUNO) is a reactor neutrino experiment located at Kaiping, Jiangmen in Southern China. a large liquid scintillator detector large active mass of 20 kilotonne at the energy resolution of 3% at 1 MeV. [55]

## 2.4 Absolute Neutrino Mass

### 2.4.1 Majorana Neutrinos

A free neutrino with a mass  $m$  can be described by a four-component Dirac spinor field following the Dirac equation  $(i\gamma^\mu \partial_\mu - m)\psi = 0$ , where  $\partial_\mu \equiv \partial/\partial x^\mu$ , and  $\gamma^\mu$  ( $\mu = 0, 1, 2, 3$ ) is a set of  $4 \times 4$  matrices forming a Clifford algebra which satisfies the following relations[56, 57]:

$$\{\gamma^\mu, \gamma^\nu\} = 2\eta^{\mu\nu}, \quad (2.24)$$

where  $\eta^{\mu\nu} = \text{diag}(1, -1, -1, -1)$  is the Minkowski metric. From 2.24 we can deduce  $(\gamma^0)^2 = +1$ ,  $(\gamma^i)^2 = -1$  ( $i = 1, 2, 3$ ) and  $\gamma^0 \gamma^{\mu\dagger} \gamma^0 = \gamma^\mu$ . The product of the four gamma matrices is defined as  $\gamma_5 \equiv i\gamma^0 \gamma^1 \gamma^2 \gamma^3$ , which satisfies  $\{\gamma_5, \gamma^\mu\} = 0$  and  $(\gamma_5)^2 = 1$ . From  $\gamma_5$ , we can define the left-handed and right-handed chirality projector operators:  $P_L \equiv \frac{1}{2}(1 - \gamma_5)$  and  $P_R \equiv \frac{1}{2}(1 + \gamma_5)$ .

In the SM, neutrinos are fermions without carrying electrical charges and they could be “truly neutral”, i.e., no charge-like quantum number can be used to distinguish a neutrino and an antineutrino, which is one of the reasons why neutrinos are special. As a comparison, a neutron is spin-1/2 and chargeless but it carries magnetic moments opposite to an antineutron[56].

From a viewpoint of mathematical aesthetics, Ettore Majorana found a representation which makes all the  $\gamma$  matrices be pure imaginary so that the Dirac equation gets rid of complex coefficients[58]. Then the Dirac equation can be switched to the Majorana equation:  $i\gamma^\mu \partial_\mu \psi - m\psi^c = 0$ , which also satisfies the Lorentz invariance[57]. Since  $\psi$  and  $\psi^c$  have opposite charges, this equation should describe a neutral fermion[57].

In this Dirac mass case, the masses of charged leptons and neutrinos are both proportional to the Higgs VEV. However, the experimental measurements already show the masses of neutrinos are  $\mathcal{O}(eV)$  while charged leptons are  $\mathcal{O}(MeV)$ . The smallness of neutrino masses should be obtained by the tuning of the Yukawa couplings  $y_k^\nu$ , which does not have solid physics meanings or explanations.

If neutrinos are Majorana fermions, since  $\nu_L^c = (\nu^c)_R = (\nu)_R$ , we can take the neutrino field as  $\nu = \nu_L + \nu_L^c$  without introducing the extra  $\nu_R$ . For simplicity, only considering one flavor generation (such as  $\nu_e$ ), then the Majorana mass term is:

$$\mathcal{L}_{\nu \text{ mass}}^{M,L} = -m_L \bar{\nu} \nu = -\frac{1}{2} m_L \bar{\nu}_L^c \nu_L + h.c., \quad (2.25)$$

where the 1/2 factor is to avoid double counting of  $\nu_L^c$  and  $\bar{\nu}_L$  since  $\nu_L^c = \mathcal{C} \bar{\nu}_L^T [46]$ . For this Majorana mass term, if considering the  $U(1)$  group transformations:  $\psi \rightarrow e^{i\alpha} \psi$  and  $\bar{\psi} \rightarrow \bar{\psi} e^{-i\alpha}$ , where  $\alpha$  is an arbitrary phase parameter. We find that in the Dirac case, the mass term in the form of  $\psi \bar{\psi}$  is invariant under  $U(1)$  transformations while in the Majorana case it is not. This means that the Majorana fields break the conservation of all the  $U(1)$  charges, such as the electric charge and lepton number[56]. Since the law of electric charge conservation is solid in our universe, the particle with a Majorana mass must be electrically neutral while on the other hand, the lepton number for the Majorana fermion is not conserved, which is not described in the Standard Model. This allows for the

neutrinoless double beta decay process and it will be discussed in the next section.

Also, since the terms  $\overline{\nu_L^c} \nu_L + h.c.$  are with the weak isospin  $I_3 = 1$  and then  $Y = -2$ , it requires a Higgs triplet with  $Y = 2$ , which is not included in the Standard Model[59]. Therefore, New Physics beyond the Standard Model is required for describing the Majorana mass term.

For a more general case: a hybrid mass term of Dirac and Majorana, if only considering one neutrino generation for simplicity, we can write the Dirac mass term in ?? as the same form of the Majorana mass term:  $\mathcal{L}_{\nu \text{ mass}}^D = -\frac{1}{2}m_D(\overline{\nu_L} \nu_R + \overline{\nu_R^c} \nu_L^c) + h.c..$  Likewise, introduce the  $\nu_R$  to the Majorana case and then we have a Majorana mass term with right-handed component:  $\mathcal{L}_{\nu \text{ mass}}^{M,R} = -m_R \bar{\nu} \nu = -\frac{1}{2}m_R \overline{\nu_R^c} \nu_R + h.c..$  Therefore, the hybrid mass term combining the Majorana and Dirac fields is[56, 60]:

$$-\mathcal{L}_{\nu \text{ mass}}^{D+M} = -(\mathcal{L}_{\nu \text{ mass}}^D + \mathcal{L}_{\nu \text{ mass}}^{M,L} + \mathcal{L}_{\nu \text{ mass}}^{M,R}) = \frac{1}{2}N_L^T \mathcal{C}^\dagger \mathcal{M} N_L + h.c., \quad (2.26)$$

where  $N_L \equiv (\nu_L, (\nu_R)^c)^T = (\nu_L, \mathcal{C} \overline{\nu_R}^T)$ ; with  $m_L$  ( $m_R$ ) for the mass of the left-handed (right-handed) neutrino field, the mass matrix is written as:<sup>2</sup> :

$$\mathcal{M} = \begin{pmatrix} m_L^M & m^D \\ m^D & m_R^M \end{pmatrix}. \quad (2.27)$$

Using a unitary matrix  $U$  to diagonalize the  $\mathcal{M}$  so that  $U^T \mathcal{M} U = \mathcal{M}_d = \text{diag}(m_1, m_2)$ ;  $m_{1,2} \geq 0$  are the mass eigenvalues of the eigenstates  $\nu_{1,2}$  and

$$U = \mathcal{O} \rho = \begin{pmatrix} \cos \theta & \sin \theta \\ -\sin \theta & \cos \theta \end{pmatrix} \begin{pmatrix} \rho_1 & 0 \\ 0 & \rho_2 \end{pmatrix}, \quad (2.28)$$

where  $\mathcal{O}$  is a real orthodox matrix and  $\rho$  is a phase matrix with  $(\rho_{1,2})^2 = \pm 1$  to guarantee that  $m_{1,2} \geq 0$ . From the transformation, the off-diagonal elements give a relation of  $\theta$ :  $\tan 2\theta = \frac{2m_D}{m_R^M - m_L^M}$ , which indicates a mixing of the normal active Dirac neutrino with a pair of the sterile Majorana neutrinos. For the left-handed neutrino mass eigenstates  $\nu_{1L}$  and

---

<sup>2</sup>Here only considering one neutrino generation. In the general case  $\mathcal{M}$  is a  $(n_a + n_s) \times (n_a + n_s)$  matrix, for  $n_a$  active neutrinos and  $n_s$  sterile neutrinos[56, 60].

$\nu_{2L}$ , there is[56]:

$$N_L = \begin{pmatrix} \nu_L \\ (\nu_R)^c \end{pmatrix} = U \begin{pmatrix} \nu_{1L} \\ \nu_{2L} \end{pmatrix}, \quad (2.29)$$

Define  $\nu_i = \nu_{iL} + (\nu_{iL})^c$  ( $i = 1, 2$ ), the Lagrangian 2.26 now can be written as[56, 46]:

$$-\mathcal{L} = \frac{1}{2} N_L^T \mathcal{C}^\dagger \mathcal{M} N_L + h.c. = \frac{1}{2} \nu_L^T \mathcal{C}^{-1} \mathcal{M}_{diag} \nu_L + h.c. = \frac{1}{2} (|m_1| \bar{\nu}_1 \nu_1 + |m_2| \bar{\nu}_2 \nu_2). \quad (2.30)$$

On the other hand, the mass eigenvalues are solved as:

$$m_{1,2} \equiv m_{\mp} = \frac{1}{2} [ (m_L^M + m_R^M) \mp \sqrt{(m_L^M - m_R^M)^2 + 4(m^D)^2} ], \quad (2.31)$$

From (2.31), there are 4 cases to discuss:

(1) If  $m_L^M = m_R^M = 0$  (called “Dirac limit”), then  $m_{1,2} = m^D$  and neutrinos are pure Dirac particles.

(2) If  $m^D \gg m_{L,R}^M$ , then  $\tan 2\theta = \frac{2m^D}{m_R^M - m_L^M} \gg 1$  and  $\theta \simeq \pi/4$ ,  $m_{L,R}^M/m^D \rightarrow 0$ ,  $m_{1,2} = \frac{1}{2} m^D [ \frac{(m_L^M + m_R^M)}{m^D} + \sqrt{(\frac{m_L^M - m_R^M}{m^D})^2 + 4} ] \simeq \frac{1}{2} m^D (0 + \sqrt{0+4}) = m^D$ , the pair of Majorana neutrinos behaves like one Dirac neutrino, which is called a Pseudo-(or quasi-)Dirac Neutrino.

(3) If  $m^D = 0$ ,  $m_1 = m_L^M$ ,  $m_2 = m_R^M$ , neutrinos are pure Majorana particles.

(4) If  $m_R^M \gg m^D, m_L^M$ , then  $\theta \simeq (m^D/m_R^M) \ll 1$  and  $\tan 2\theta = \frac{2m^D}{m_R^M - m_L^M} \rightarrow 0$ , we get:

$$\begin{aligned} m_1 = m_- &= \frac{1}{2} \frac{(m_L^M + m_R^M)^2 - (m_L^M - m_R^M)^2 - 4(m^D)^2}{m_L^M + m_R^M + |m_L^M - m_R^M| \sqrt{1 + (\frac{2m^D}{m_R^M - m_L^M})^2}} \simeq \frac{2m_L^M m_R^M - 2(m^D)^2}{m_L^M + m_R^M + (m_R^M - m_L^M)} \\ &= |m_L^M - (m^D)^2/m_R^M|, \end{aligned} \quad (2.32)$$

<sup>3</sup> and:

$$m_2 = m_+ = \frac{1}{2} [m_R^M + m_R^M (1 + \frac{1}{2} (2m^D/m_R^M)^2)] = m_R^M [1 + (m^D/m_R^M)^2]. \quad (2.33)$$

In the case of (4), since  $\theta \ll 1$ ,  $U \simeq \text{diag}(\rho_1, \rho_2)$ , from 2.29, the mass eigenstates  $\nu_1 \simeq \nu_L + (\nu_L)^c$ ,  $\nu_2 \simeq \nu_R + (\nu_R)^c$ . Since  $\nu_{1,2} = (\nu_{1,2})^c$ , it means that the massive neutrino eigenstates are of Majorana nature. It also shows that the mass eigenstate  $\nu_2$  relates to

---

<sup>3</sup>Here the absolute value is taken because we can find proper  $\rho_{1,2}$  values to ensure  $m_1 \geq 0$ .

the right-handed sterile neutrino  $\nu_R$  while the  $\nu_1$  relates to the left-handed active neutrino  $\nu_L$ . Considering  $m_L^M = 0$  in the Standard Model[56], if the sterile neutrino  $\nu_R$  is heavy, the mass of the active neutrino  $m_1 = (m^D)^2/m_R^M$  will be light. This is called the Seesaw Mechanism.

In the Seesaw Mechanism, new neutral force carriers or messenger particles with unknown masses  $M_x$  are added into the Standard Model. There are mainly three types of Seesaw mechanism, depending on what new particles are introduced. Generally, a dimension-5 operator  $\mathcal{O}_5 = \frac{\kappa}{M_X} \Psi_L \Psi_L \Phi \Phi$  is considered, where  $\kappa$  is an unknown dimensionless coupling constant,  $\Psi_L$  is the  $SU(2)_L$  lepton doublet and  $\Phi = (\phi^+, \phi^0)^T$  is the Higgs doublet[61]. Via symmetry breaking at the electroweak scale ( $v_0 = 246 \text{ GeV}$ ), the neutrino mass can be obtained as  $m_\nu = \kappa v_0^2/M_X$ . In case (4), adding a neutral, heavy right-handed neutrino  $\nu_R$  is called the type-I, or the conventional Seesaw Mechanism; its tree-level Feynman diagram is shown in Fig. 2.5 (left). Since we know the Dirac mass  $m^D = y_\nu v_0$  (from ??),  $m_1 = y_\nu^2 v_0^2/m_R^M$ . Since  $m^D \propto v_0 \sim \mathcal{O}(100 \text{ GeV})$ , if the active neutrinos is in the mass scale of  $m_1 \sim \mathcal{O}(0.01 \text{ eV})$ , then  $m_R^M \sim \mathcal{O}(10^{15} \text{ GeV})$ , which is a value close to the expected grand unification theory (GUT) mass scale  $m_{\text{GUT}} \mathcal{O}10^{16}$ . For the type-II, heavy  $SU(2)_L$  triplet Higgs scalars  $\Delta$  are introduced; its diagram is shown in Fig. 2.5 (right). For the type-III, heavy triplet fermions are introduced; its diagram is similar to the type-I, but with different exchanging particles.

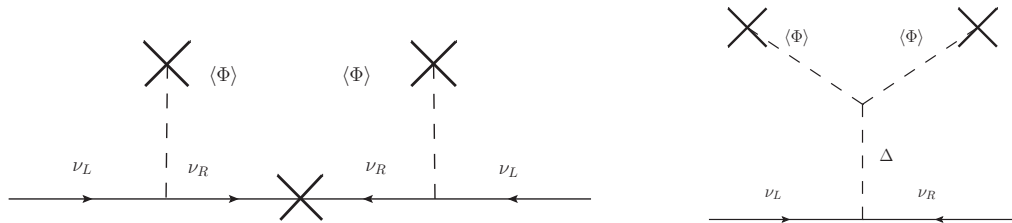


Figure 2.5: Tree-level Feynman diagrams for the Seesaw Mechanisms, modified from [3]: type-I (left) and type-II (right). The type-III scheme shares the same diagram to the type-I, but with the  $\nu_R$  replaced by  $T^0$ .

As a summary, to explain how the neutrinos acquire their masses, New Physics theories are required to extend the Standard Model. If neutrinos are Majorana particles, the induced

Seesaw Mechanism can explain the tiny mass of the active neutrinos naturally. As a bonus, the mass scale required by the Seesaw Mechanism implies the New Physics in the GUT.

The results from the neutrino flavor transformation experiments proved that neutrinos are not massless and have finite masses. However, in these experiments, the mass differences, rather than the absolute mass values are measured so we can not know the absolute scale of neutrino masses from these results. Currently, there are mainly three approaches to probe the neutrino masses: (1) cosmological measurements; (2) direct measurements for the  $\beta$ -decay spectrum; (3) a search for the  $0\nu\beta\beta$  process[3].

#### 2.4.2 Cosmological Approach

Neutrinos play an important role in the formation and evolution of the universe. The massive neutrinos can leave imprints on cosmological observables, such as the anisotropies of the Cosmic Microwave Background (CMB) temperature spectra, the matter power spectrum from the large-scale structure and the Baryon Acoustic Oscillations (BAO)[62, 63]. Combining the CMB data from the Planck space observatory (updated to 2018 results) with the BAO measurements, a tight 95% constraint on the sum of the masses of the three active types of neutrinos is obtained as:  $\sum m_\nu < 0.12 \text{ eV}$ [64]. Currently, the cosmological approaches provide the strongest upper limit of the sum of neutrino masses[62].

#### 2.4.3 Beta Decay

In a  $\beta$ -decay process:  $(Z, A) \rightarrow (Z + 1, A) + e^- + \bar{\nu}_e$ , parent nuclei with the nucleon number A and the proton number Z decay into daughter nuclei and electrons. The energy difference between the initial and final state nuclei is

the sum of the emitted electrons  $e^-$  (called the  $\beta$ -electron ) energy  $E_e$ ,  
 the antineutrino  $\bar{\nu}_e$  energy  $E_\nu$  and the nuclear recoil energy  $E_R$ :  $Q = E_e + E_\nu + E_R$ . If considering the initial and final nuclei are at rest and  $E_R$  is negligible, due to the presence of  $E_\nu$ ,  $E_e$  can range from 0 to the maximal energy  $E_0 = Q$  (called the end-point energy). For the  $\beta$ -electron with a rest mass  $m_e$ , the kinetic energy  $T_e = E_e - m_e$  (taking the natural

unit  $\hbar = c = 1$ ) and the momentum  $p_e = \sqrt{E^2 + 2Em_e}$ . Then by using the Fermi's Golden Rule, the differential  $\beta^-$ -decay spectrum of  $T_e$  is given by[65]:

$$\frac{d^2N}{dtdT_e} = \frac{G_F^2 \cos^2 \theta_C |\mathcal{M}_{nucl}|^2}{2\pi^3} \cdot F(Z+1, T_e) \cdot (T_e + m_e) \cdot p_e \cdot (E_0 - T_e) \cdot \sqrt{(E_0 - T_e)^2 - m_{\bar{\nu}_e}^2} \Theta(E_0 - T_e - m_{\bar{\nu}_e}), \quad (2.34)$$

where  $G_F$  is the Fermi constant;  $\theta_C$  is the Cabibbo angle;  $\mathcal{M}_{nucl}$  is the nuclear matrix element (NME);  $F(Z, E)$  is the Fermi function describing the electromagnetic interaction between the  $\beta$ -electron and the final-state nucleus; and the Heaviside step function  $\Theta$  ensures that a neutrino can only be emitted if enough energy is left for its mass.

In this spectrum,  $m_{\bar{\nu}_e}^2$ , the square of the  $\bar{\nu}_e$  rest mass is the measurement observable. It can be evaluated by measuring the  $\beta$ -decay event rate[65].

If considering  $m_{\nu_e} = m_{\bar{\nu}_e}$  and the CPT is conserved,  $\langle m_{\bar{\nu}_e}^2 \rangle = \langle m_{\nu_e}^2 \rangle = \sum_i |U_{ei}|^2 m_i^2 = \sum_i |U_{ei}|^2 m_i^2$ . Taking out the lightest mass eigenvalue:  $m_1$  for normal hierarchy and  $m_3$  for inverted hierarchy, the  $\langle m_{\nu_e}^2 \rangle$  can be expressed as[49]:

$$\langle m_{\nu_e}^2 \rangle = \begin{cases} m_1^2 + s_{13}^2 |\Delta m_{31}^2| + c_{13}^2 s_{12}^2 \Delta m_{21}^2 & (\text{for NH}) \\ m_3^2 + c_{13}^2 |\Delta m_{31}^2| + c_{13}^2 s_{12}^2 \Delta m_{21}^2 & (\text{for IH}), \end{cases} \quad (2.35)$$

where  $s_{13}^2, c_{13}^2, \Delta m_{31}^2$  and  $\Delta m_{21}^2$  are the flavor transformation parameters and they are determined by flavor transformation experiments. If taking the currently best global-fit values with  $3\sigma$  (the values in brackets are for IH and the others are for NH):  $\Delta m_{21}^2 = 7.37 \times 10^{-5} \text{ eV}^2$ ,  $|\Delta m_{31}^2| = 2.56$  (2.54)  $\times 10^{-3} \text{ eV}^2$ ,  $s_{12}^2 = 0.297$ ,  $s_{13}^2 = 0.0215$  (0.0216)[33], then for NH,  $\langle m_{\nu_e}^2 \rangle \simeq m_1^2 + (8.74 \text{ meV})^2$  and for IH,  $\langle m_{\nu_e}^2 \rangle \simeq m_3^2 + (50.3 \text{ meV})^2$ . Fig. 2.4.3 plots the  $\sqrt{\langle m_{\nu_e}^2 \rangle}$  as a function of the lightest mass eigenvalue. Therefore, once the  $m_{\bar{\nu}_e}^2$  is measured, the mass hierarchy as well as the mass eigenvalues  $m_i$  can be determined.

Among the  $\beta$ -decay processes, the tritium process:  ${}^3\text{H} \rightarrow {}^3\text{He}^+ + e^- + \bar{\nu}_e$  has a low end-point energy  $E_0 = 18.57 \text{ keV}$ , a favorable half-life  $T_{1/2} = 12.32 \text{ years}$  and simple atomic structure for calculation. With these experimental advantages, it has been largely investigated since 1947 and is used as a standard technology for the kinetic measurement[45]. The KArlsruhe TRItium Neutrino (KATRIN) experiment is one of the state-of-the-art tritium

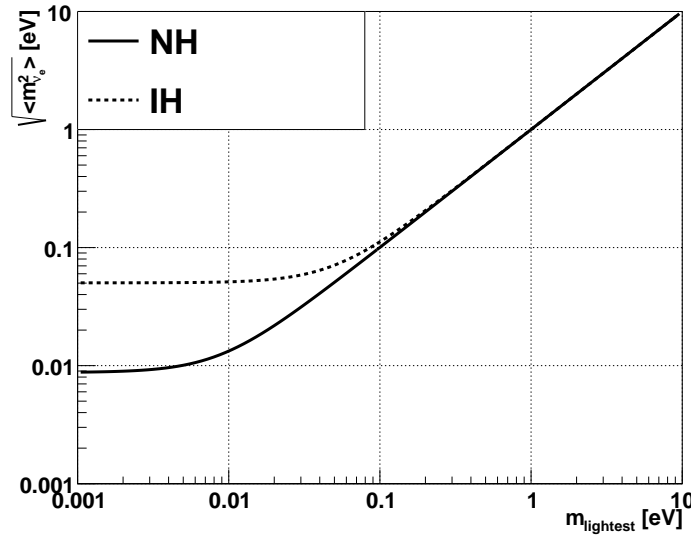


Figure 2.6:  $\sqrt{\langle m_{\nu_e}^2 \rangle}$  as a function of the lightest mass ( $m_1$  for NH or  $m_3$  for IH).

experiments which uses a large magnetic spectrometer with high energy resolution for precise measurement. In 2019, the experiment reported an upper limit of  $m_\nu < 1.1$  eV with 90% C.L.. After 5 years of measurement, the experiment is expected to reach the  $m_\nu$  sensitivity down to 0.2 eV with 90% C.L.[66].

#### 2.4.4 Double Beta Decay

For heavy radioactive isotopes ( $A > 70$ ) with nuclei of even neutron number and even proton number (called the even-even nucleus), beta decay will lead to an odd-odd nucleus which is less stable. Thus for such isotopes, the  $\beta$ -decay is energetically forbidden. In 1935, Maria Goeppert-Mayer pointed out that these isotopes can still decay through a double beta decay process:  $(Z, A) \rightarrow (Z + 2, A) + 2e^- + 2\bar{\nu}_e + Q_{\beta\beta}$ , where  $Q_{\beta\beta}$  is the released energy. This is called ordinary double beta decay or  $2\nu\beta\beta$ , which is allowed by the Standard Model and with a typical half-life  $T_{1/2} > 10^{19}$  years (yr)[67, 68].

If neutrinos are Majorana particles, a process called neutrinoless double beta decay ( $0\nu\beta\beta$ ) will also be expected:  $(Z, A) \rightarrow (Z + 2, A) + 2e^- + Q_{\beta\beta}$ . In this process, the lepton number is violated by 2, which is not allowed in the SM. As mentioned in 2.4.1, New Physics

interpretations for the process are required. The Feynman diagrams of  $2\nu\beta\beta$  and  $0\nu\beta\beta$  are illustrated in Fig. 2.7.

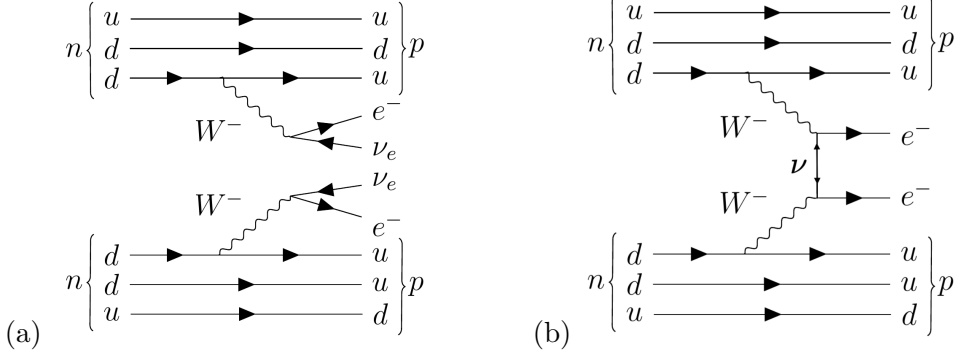


Figure 2.7: Feynman diagrams for  $2\nu\beta\beta$  (a) and  $0\nu\beta\beta$  (b).

One of the simple interpretations is the exchanging of virtual light Majorana neutrinos between the nucleus, as shown in Fig. 2.7 (b). Under the SM weak interactions, the amplitude of the lepton processes in the  $0\nu\beta\beta$  is a product of two weak charged current interactions happening at the vertices  $x$  (creating a  $\nu_{eL}$  and an  $e^-$ ) and  $y$  (absorbing a  $\nu_{eL}$  and creating an  $e^-$ ) [39]:

$$\mathcal{A} = \bar{e}(x)\gamma^\mu\nu_{eL}\nu_{eL}^T(y)\gamma_\mu^T\bar{e}^T(y), \quad (2.36)$$

Taking account of the three-neutrino mixing as well as the Majorana condition:  $\nu_i^c = \mathcal{C}\bar{\nu}_i^T = \nu_i$ , the amplitude becomes[39, 69]:

$$\mathcal{A} = -\sum_{i=1}^3 U_{ei}^2 \frac{1-\gamma_5}{2} \nu_i(x) \bar{\nu}_i(y) \frac{1-\gamma_5}{2} \mathcal{C} \quad (2.37)$$

is propagator for a mass  $m_i$  virtual fermion transiting between vertices.

For the case of small neutrino mass,  $p \gg m_i$ , then  $\mathcal{A} \propto m_{ee} \equiv \sum_{i=1}^3 U_{ei}^2 m_i$  the effective Majorana mass

$\nu_i(x)\bar{\nu}_i(y)$  with a proper time ordering:

$$\begin{aligned} \langle T(\nu_i(x)\bar{\nu}_i(y)) \rangle &= -\frac{i}{(2\pi)^4} \int dp^4 e^{-iq(x-y)} \frac{\gamma^\mu p_\mu + m_i}{p^2 - m_i^2} \\ &= -\sum_{i=1}^3 U_{ei}^2 m_i \frac{1}{p^2 - m_i^2} \frac{1-\gamma_5}{2} \mathcal{C}. \end{aligned}$$

Therefore, the massive Majorana neutrino is required for the existence of the  $0\nu\beta\beta$  process.

From [33], transition between  $\bar{\nu}_{eR}$  and  $\nu_{eL}$ .

$$|\bar{\nu}_{eR}(t = \delta t)\rangle = |\bar{\nu}_{eR}\rangle - i \sum_{i=1}^3 m_i U_{ei} |\nu_{iL}\rangle \delta t$$

$$\text{amplitude } \langle \nu_{eL} | \bar{\nu}_{eR} \rangle = -i \sum_{i=1}^3 m_i U_{ei}^2 \delta t$$

Integrating the  $\delta t$  with a weight of the nuclear matrix element, the decay width and the half-life are obtained as[49, 70]:

$$\Gamma = (T_{1/2}^{0\nu\beta\beta})^{-1} = G_{PS}(Q, Z) |M_{Nuclear}|^2 \langle m_{ee} \rangle^2, \quad (2.38)$$

where  $G_{PS}(Q, Z)$  is a phase space corresponding to the effective coupling constant, which depends on the endpoint energy  $Q$  and the atomic number  $Z$ ;  $|M_{Nuclear}|$  is the nuclear matrix element describing the nuclear transition and it can only be calculated theoretically from approximate methods based on many-body nuclear models, such as the Nuclear Shell Model (NSM),

interacting shell model (ISM) the Quasiparticle-Random Phase Approximation (QRPA), Interacting Boson Model (IBM), Energy Density Functional Method (EDF), and Projected Hartree-Fock-Bogoliubov Method (PHFB).

In this case the effective Majorana mass

$$\langle m_{ee} \rangle = \left| \sum_{i=1}^3 U_{ei}^2 m_i \right| = |c_{13}^2 c_{12}^2 m_1 + c_{13}^2 s_{12}^2 e^{i\alpha_1} m_2 + s_{13}^2 e^{i\alpha_2} m_3|, \quad (2.39)$$

where  $U_{ei}$  are the elements of the neutrino mixing matrix for the flavor state  $\nu_e$ , and  $m_i$  are the mass eigenvalues of the mass eigenstates (2.2));  $\alpha_1, \alpha_2$  are Majorana CP-violation phase factors and  $\alpha_2$  can also be taken as  $\alpha_2 - \delta_{CP}$ .

For NH,  $m_{lightest} = m_1$ ,  $m_2 = \sqrt{m_1^2 + \Delta m_{21}^2}$ ,  $m_3 = \sqrt{m_1^2 + |\Delta m_{31}^2|}$ ; for IH,  $m_{lightest} = m_3$ ,  $m_1 = \sqrt{m_3^2 + |\Delta m_{31}^2|}$ ,  $m_2 = \sqrt{m_3^2 + |\Delta m_{31}^2| + \Delta m_{21}^2}$

The phases  $\alpha$  and  $\beta$  are ranging from 0 to  $\pi$ , taking different pairs of  $(\alpha_1, \alpha_2) = (0, 0), (0, \pi), (\pi, 0)$  and  $(\pi, \pi)$  can determine the ranges of  $\langle m_{ee} \rangle$ .

Using the same best-fit values in the 2.4, a plot of  $\langle m_{ee} \rangle$  as a function of  $m_{lightest}$  is shown in Fig. 2.4.4.

the mass regions are bounded by lines taking different values of  $(\alpha_1, \alpha_2)$ .

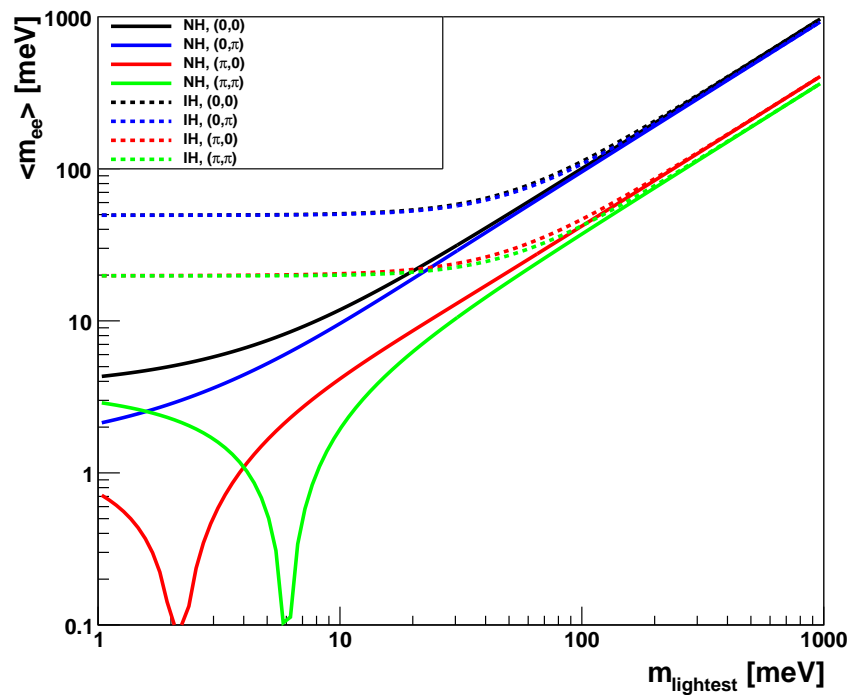


Figure 2.8: Effective Majorana mass as a function of the lightest mass eigenvalue. Solid lines are for NH cases and dashed lines are for IH. Different colors stand for taking different values of  $(\alpha_1, \alpha_2)$ .

Similar to the  $\beta$ -decay case, the  $2\nu\beta\beta$  process will cause a continuous spectrum in the detector while the  $0\nu\beta\beta$  process only has two electrons in the final state. These electrons take away the entire energy and their energy spectrum sum up to give a distinct energy peak at the Q-value. Taking the isotope  $^{130}\text{Te}$  as an example, Fig. 2.9 illustrates the shapes of the energy spectrum from the  $2\nu\beta\beta$  and the  $0\nu\beta\beta$  decay processes.

By measuring this distinct energy peak, a detector with high energy resolution can search for the  $0\nu\beta\beta$  signal from the  $0\nu\beta\beta$  decay radioactive isotopes. Diverse technologies have been developed during the past decades. The following section lists some of the mainstream experiments.

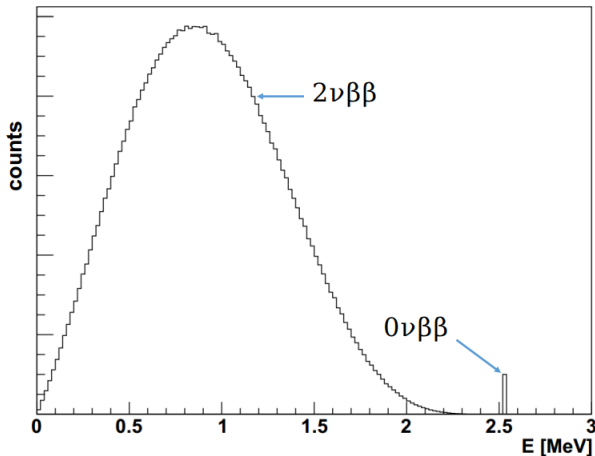


Figure 2.9: Energy spectrum of the  $^{130}\text{Te}$   $2\nu\beta\beta$  decay and the hypothetical  $0\nu\beta\beta$  decay. The SNO+ simulation package (RAT) was used to produce the plot.

#### 2.4.4.1 Status of Double Beta Decay Experiments

There are 35 isotopes that can undergo the double beta decay process, but only a few of them are suitable for the application in direct  $0\nu\beta\beta$  search experiments[46]. From the experimental view, the candidate isotopes are expected to have relatively high natural abundances, high Q-values, be deployed in a large amount with low costs, and are not toxic to the environment as well. However, in a realistic situation, no isotope fulfills all these properties, and the current experiments making trade-offs[71].

The experiments searching for direct signals of  $0\nu\beta\beta$  mainly measure the physics properties of the two emitted electrons, such as their energies, momentum, and tracks.

Inhomogeneous experiments use external  $\beta\beta$  source while homogeneous experiments use  $\beta\beta$  source as the detection medium, which are mainly referred as calorimeter experiments[72, 73].

Experiments mainly focus on the isotopes of  $^{136}\text{Xe}$ ,  $^{48}\text{Ca}$ ,  $^{76}\text{Ge}$  and  $^{130}\text{Te}$ .

The signal of  $0\nu\beta\beta$  in the range of  $10^{25} - 10^{26}$  year,

The observed number of event in expectation is:

$$N_{event} = \ln 2 \frac{N_A}{M_A} \frac{\alpha \cdot \epsilon \cdot m \cdot t}{T_{1/2}^{0\nu}},$$

where  $N_A$  is the Avogadro's number,  $\alpha$  is the abundance of the isotope in the element,  $M$  is the molar mass of the isotope and  $t$  is the measurement time of total exposure.

The GERmanium Detector Array (GERDA) experiment searches for  $0\nu\beta\beta$  of  $^{76}\text{Ge}$ . The experiment uses bare germanium crystals with enrichment of up to  $\sim 87\%$   $^{76}\text{Ge}$  operated in a radiopure cryogenic liquid argon (LAr)[74]. GERDA Phase I had an exposure of 21.6 kg·yr and Phase-II started with 35.6kg from enriched material in December 2015. With combined data of Phase I and Phase II, a total exposure of 82.4 kg·yr has been measured.

In 2017, GERDA reported a 90% confidence level (C.L.) lower limit for the half-life of  $^{76}\text{Ge}$ ,  $T_{1/2}^{0\nu}(^{76}\text{Ge}) > 8.0 \times 10^{25}$  years.

GERDA reported in 2019 a lower limit half-life of  $T_{1/2}^{0\nu}(^{76}\text{Ge}) > 0.9 \times 10^{26}$  years at 90% C.L.[75]. effective  $m_{ee}$  is [104,228] meV.

A new experiment, the Large Enriched Germanium Experiment for Neutrinoless Double-Beta Decay (LEGEND) will

Building on the successes of the MAJORANA DEMONSTRATOR and GERDA,

The Enriched Xenon Observatory (EXO) experiment uses 200-kg liquid Xenon (LXe) time projection chamber (TPC) to search for  $0\nu\beta\beta$  in  $^{136}\text{Xe}$ . In 2011 they observed the half life of double beta decay of  $^{136}\text{Xe}$  to be  $2.11 \times 10^{21}$  years and in 2014 they set a limit on  $T_{1/2}^{0\nu}(^{136}\text{Xe}) > 1.1 \times 10^{25}$  yr[76]. EXO is now upgrading to the next 5-tonne experiment

(nEXO) and is expected to reach an exclusion sensitivity of  $T_{1/2}^{0\nu}(^{136}\text{Xe})$  to about  $10^{28}$  years at 90% C.L.[77].

Also looking into  $^{136}\text{Xe}$ , the KamLAND-Zen (ZEroNeutrino) experiment exploits the existing facilities of KamLAND by setting a 3.08-m-diameter spherical inner balloon filled with 13 tons of Xe-loaded liquid scintillator at the center of the KamLAND detector.

It utilizes liquid scintillator cocktail of 82% decane and 18% pseudocumene by volume, 2.7 g/L PPO with a photocathode coverage of 34%.

Their 2016 results from a 504 kg·yr exposure obtained a lower limit for the  $0\nu\beta\beta$  decay half-life of  $T_{1/2}^{0\nu}(^{136}\text{Xe}) > 1.07 \times 10^{26}$  yr at 90% C.L. and the corresponding upper limits on the effective Majorana neutrino mass are in the range 61 – 165 meV[78].

The Particle and Astrophysical Xenon Experiment III (PandaX-III) uses a high-pressure gas-phase time projection chamber (TPC).

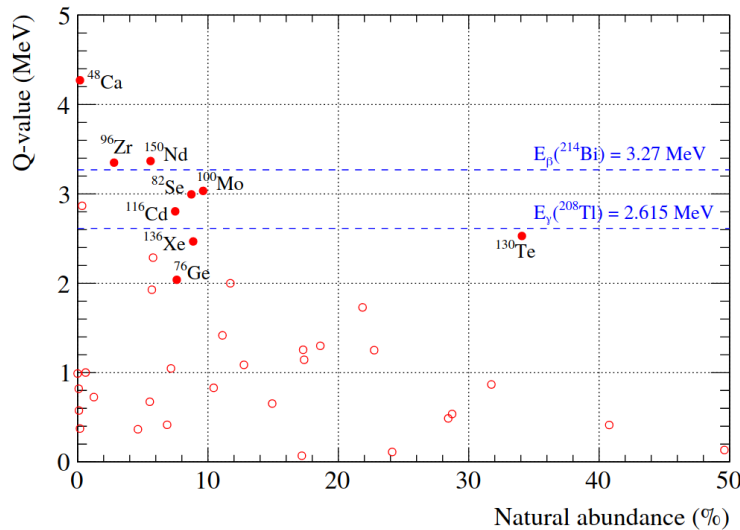
The Cryogenic Underground Observatory for Rare Events (CUORE) experiment searches for  $0\nu\beta\beta$  in  $^{130}\text{Te}$ . CUORE is a ton-scale cryogenic bolometer array that arranges 988 tellurium dioxide ( $\text{TeO}_2$ ) crystals. CUORE reported its first results in 2017 after a total  $\text{TeO}_2$  exposure of 86.3 kg·yr. An effective energy resolution of  $(7.7 \pm 0.5)$  keV FWHM and a background count of  $(0.014 \pm 0.002)$   $\text{counts}/(\text{keV} \cdot \text{kg} \cdot \text{yr})$  in the ROI were achieved in that data exposure. Combined with the early data (the data from the two precursor experiments, Cuoricino and CUORE-0), they placed a lower limit of  $T_{1/2}^{0\nu}(^{130}\text{Te}) > 1.5 \times 10^{25}$  yr at 90% C.L. and  $m_{\beta\beta} < (110 - 520)$  meV[79]. In 5 years live time, the experiment will give a projected sensitivity of  $9.5 \times 10^{25}$  yr at the 90% C.L. and set an upper limit on the effective Majorana mass in the range 50 – 130 meV[80].

A more recent evaluations of the limits of  $T_{1/2}^{0\nu}$  and  $m_{\beta\beta}$  from the above mentioned current and future experiments are summarized in

Table 2.4[81, 75] shows  $3\sigma$   $0\nu\beta\beta$  discovery sensitivities assuming 5 years of live time for planned future experiments.

Table 2.4: The limits of  $T_{1/2}^{0\nu}$  and  $m_{\beta\beta}$  at 90% C.L.

| Experiment  | Isotope           | Limit of $T_{1/2}^{0\nu}$ ( $10^{25}$ year) | Limit of $m_{\beta\beta}$ (eV) |
|-------------|-------------------|---|--------------------------------|
| GERDA       | $^{76}\text{Ge}$  | >8.0  | <0.12-0.26                     |
| KamLAND-Zen | $^{136}\text{Xe}$ | >10.7                                       | <0.05-0.16                     |
| EXO         | $^{136}\text{Xe}$ | >1.1  | <0.17-0.49                     |
| CUORE       | $^{130}\text{Te}$ | >1.5  | <0.11-0.50                     |

Figure 2.10: Natural abundance vs. Q-values for different  $2\nu\beta\beta$  isotopes[?].Table 2.5: The limits of  $T_{1/2}^{0\nu}$  and  $m_{\beta\beta}$  at 90% C.L.

| Experiment    | Isotope           | $m_{isotope}$ [kg] | $T_{1/2}^{0\nu}$ [ $\times 10^{26}$ year] | $m_{\beta\beta}$ [meV] |
|---------------|-------------------|--------------------|---|------------------------|
| LEGEND 1k     | $^{76}\text{Ge}$  |                    | 8.4                                       | 0.04-0.073             |
| KamLAND2-Zen  | $^{136}\text{Xe}$ | 8.0                | 10.7                                      | 0.05-0.16              |
| nEXO          | $^{136}\text{Xe}$ | 41.0               | 410                                       | 0.09-0.022             |
| NEXT 1.5k     | $^{136}\text{Xe}$ | 1367               | 7.9                                       | 21-49                  |
| PandaX-III 1k | $^{136}\text{Xe}$ | 901                | 9.0                                       | 20-46                  |
| CUPID         | $^{130}\text{Te}$ | 543                | 21.0                                      | 11-26                  |
| SNO+ Phase I  | $^{130}\text{Te}$ | 1367               | 1.1                                       | 46-115                 |
| SNO+ Phase II | $^{130}\text{Te}$ | 7960               | 4.8                                       | 22-54                  |

## Chapter 3

# The SNO+ Experiment

### 3.1 Overview

The SNO+ experiment is located at SNOLAB. This deep underground facility sits at Vale’s Creighton mine in Sudbury, Ontario, Canada (coordinate:  $46^{\circ}28'19.6''\text{N}$ ,  $81^{\circ}11'12.4''\text{W}$ ). It provides an environment with extremely low cosmic ray backgrounds. At sea level, an average cosmic muon ( $\mu$ ) flux rate is about  $1.44 \times 10^7 \mu/\text{m}^2/\text{day}$ [82]. Cosmic muons with high energies (mostly  $\mathcal{O}(\text{GeV})$ ) can induce spallation backgrounds, such as fast neutrons and lasting isotopes, which are harmful to the low background counting experiments[83]. The SNOLAB has a  $2092 \pm 6$  m flat overburden of rock, which is  $5890 \pm 94$  water equivalent meter (m.w.e). This rock overburden ensures that cosmic muon ( $\mu$ ) flux rate is as low as  $0.286 \pm 0.009 \mu/\text{m}^2/\text{day}$ [7], which means that every hour only about 1  $\mu$  passes through the SNO+ detector.

The SNO+ detector is a refurbishment of the SNO detector. The SNO+ collaboration makes use of the SNO infrastructure and upgraded it to be a liquid scintillator detector. As shown in Fig. 3.1, the detector is inside a barrel-like rock cavity with a diameter of 22 m at its waist and a height of 34 m. The cavity is filled with 7000 tonnes of ultrapure water (UPW) to provide buoyancy for the vessel and also to shield radiation backgrounds from the environment, such as the cosmic rays and isotope decays from the rock.

The detector consists of an acrylic vessel (AV) sphere of 12.01 m in diameter and 5.5 cm in thickness. The AV contains detection media (or called target materials) and is held in place by a rope net system including hold-up and hold-down Tensylon ropes. This spherical structure is simple in geometry and reduces the complexities of simulation and event reconstruction. Furthermore, this geometry allows for spherical fiducial volume cuts from the center of the AV to further get rid of external backgrounds, which makes the SNO+ as a graded-shield type detector[84]. On the top of the AV sphere, there is an acrylic neck cylinder with 6.8 m high and 1.46 m inner diameter. The neck connects the AV sphere to the facilities on the deck above the detector. Through the neck, pipes can fill the detection media into the AV and recirculate as well. Calibration sources for internal scans can also be lowered down into the AV through the neck.

The AV sphere is concentric within a stainless steel geodesic dome with an average radius of 8.4 m, which is called the photomultiplier support structure (PSUP). 9394 Hamamatsu 8-inch R1408 photomultipliers (PMTs) were mounted on the PSUP, looking inward to the AV. In order to increase the light collection efficiency of these PMTs and thus to obtain a large photocathode coverage of the detector, each of these PMTs was fitted into a 27 cm diameter reflective bucket (called “concentrator”), which consists reflective pedals coated with aluminum. The effective photocathode coverage of the detector reaches about 54%[85]. Besides the inward-looking PMTs, 90 PMTs look outward, serving as muon vetos. Furthermore, four Hamamatsu R5912 High Quantum Efficiency (HQE) PMTs were also installed for testing the performance of potential SNO+ phases-II[86].

### 3.2 SNO+ Physics Phases

The SNO+ experiment is designed for multi-purpose measurements of neutrino physics. The detector has been running since December 2016. There are three physics phases of the experiment and each phase has different detection media inside the AV: the water phase, the scintillator phase, and the tellurium phase[85].

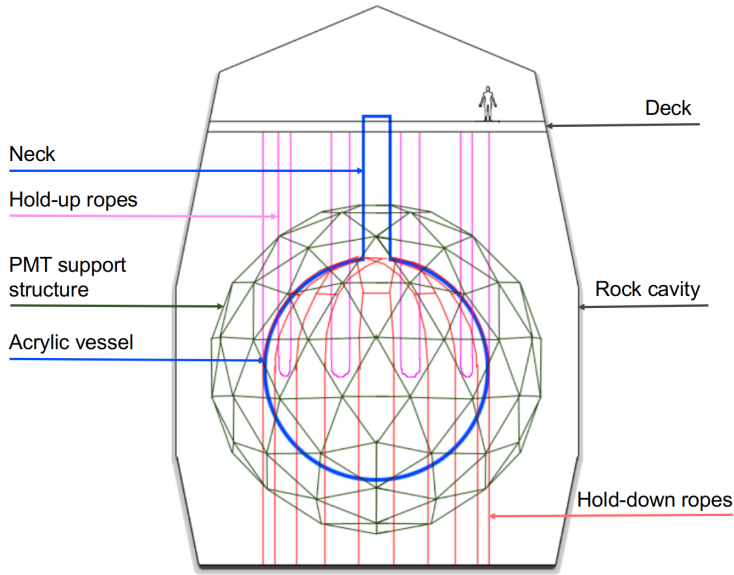


Figure 3.1: The SNO+ detector labeled with main structures, figure modified from [4].

### 3.2.0.1 Water Phase

In this initial phase, the AV was filled with about 905 tonnes of ultrapure water. The detector collected water physics data from May 2017 to July 2019.

During the data-taking, different types of calibration runs have been taken. The detector timing and energy response, systematics, and backgrounds are studied. Multiple physics analyses of invisible nucleon decay, solar neutrinos, and reactor antineutrinos are ongoing and a few results have been published[87, 88, 89]. The external backgrounds are also measured, which will be the same as the following two phases.

The main physics goal in this phase is to search for the invisible nucleon decay, which violates baryon number and is a prediction of Grand Unified Theory (GUT). In the invisible decay mode, a proton or a bound neutron decays away without releasing charged particles, compared to the “visible” decay channels of  $p \rightarrow e\pi$  and  $p \rightarrow \nu K$  which has been searched and set limits by the SuperK experiment. In the SNO+ water detector,  $^{16}\text{O}$  may decay into  $^{15}\text{O}^*$  (bound neutron invisible decay) or  $^{15}\text{N}^*$  (proton invisible decay) excited state. The  $^{15}\text{O}^*$  has 44% chance to deexcite to produce 6.18 MeV  $\gamma$  ray and 2% chance to produce

7.03 MeV  $\gamma$ ; while  $^{15}\text{N}^*$  has 41% to release 6.32 MeV  $\gamma$  and 7.01, 7.03 and 9.93 MeV  $\gamma$  with chances of 2%, 2% and 3% respectively. The experiment has searched for these  $\gamma$  signals and the first publication sets world-leading limits of  $\mathcal{O}(10^{29})$  years for both the proton and neutron invisible decay lifetime at 90% Bayesian credibility level[87].

The  $^8\text{B}$  solar neutrinos were measured with a 69.2 kilo-tonnes·day dataset. By analyzing the solar neutrino elastic scattering events based on the dataset (the method will be discussed in Chapter 5 with more details), the number of the solar neutrino events were counted in different energy regions. In the first publication[88], by fitting to the non-oscillation solar neutrino model, an observed flux was obtained from the dataset to be  $2.53_{-0.28}^{+0.31}(\text{stat.})_{-0.10}^{+0.13}(\text{syst.}) \times 10^6 \text{ cm}^{-2}\text{s}^{-1}$  for the  $^8\text{B}$  solar neutrinos with energies larger than 5 MeV. In the energy region larger than 6 MeV, the dataset has a background rate of  $0.25_{-0.07}^{+0.09}$  events/kilo-tonne·day, which is extremely pure with solar neutrinos. Currently, this background rate is the lowest one compared to the other water Cherenkov detectors[88].

Reactor antineutrinos can be captured by the SNO+ detector and get measured. 40% of these antineutrinos are from one nearby reactor complex in Canada at a 240-km baseline; 20% are from two Canadian complexes at around 350 km; the rest are from the USA and elsewhere with longer baselines[85]. Though in pure water the antineutrino event rate is much smaller than in the scintillator, during the water phase, SNO+ still has the potentials to detect reactor antineutrinos due to the low background dataset and relatively high detection efficiency. To evaluate the sensitivity for detecting reactor antineutrinos, an Americium-Beryllium (AmBe) calibration source was deployed during the water phase. This source provides neutrons along with 4.4-MeV  $\gamma$ s. Neutrons are captured by hydrogen and 2.2-MeV  $\gamma$ s are released. An analysis of delayed coincidence between 4.4-MeV and 2.2-MeV  $\gamma$ s can help to tag neutrons, which is crucial for tagging the reactor antineutrinos since they are measured by the inverse  $\beta$ -decay process which produces neutrons with similar energy scale. In the first publication for the SNO+ water phase, a neutron detection efficiency of 50% was obtained when the AmBe source was deployed at the center of the detector; the neutron-hydrogen capture time constant  $\tau$  was measured to be  $202.35_{-0.76}^{+0.87} \mu\text{s}$  and from  $\tau$ ,

a thermal capture cross-section was calculated to be  $336.3^{+1.2}_{-1.5}$  milli-barn (mb)[89].

### 3.2.0.2 Scintillator Phase

In this phase, the AV will be filled with 780 tonnes of liquid scintillator, which is a mixture of linear alkylbenzene (LAB) as a solvent and 2 g/L of 2,5-diphenyloxazole (PPO) as a fluor. This LAB-based organic liquid scintillator is referred to as the “unloaded” liquid scintillator (Section 3.3.3.2 will discuss more details).

The main physics goal of the scintillator phase is to measure low energy solar neutrinos: the CNO, pep, and low energy  ${}^8\text{B}$  neutrinos. The pep neutrinos are mono-energetic, with  $E_\nu=1.442$  MeV and their flux is well predicted by the Standard Solar Model[90]. A measurement of the pep neutrinos will give more information on the matter effects in neutrino oscillations.

The solar metallicity is the abundance of elements heavier than  ${}^4\text{He}$  (called “metal” elements in the context of astronomy). It is poorly constrained and the predictions from different solar models disagree with each other. A measurement of the CNO neutrinos can give the abundance of  ${}^{12}\text{C}$ ,  ${}^{13}\text{N}$  and  ${}^{15}\text{O}$  and can thus resolve the metallicity problem[91].

Three kinds of antineutrinos will also be measured: reactor antineutrinos as mentioned before; geoneutrinos from natural radioactivity in the Earth; and the supernova neutrinos. SNO+ is planned to join the SuperNova Early Warning System (SNEWS), which is an international network of experiments with abilities to provide an early warning of a galactic supernova[7].

### 3.2.0.3 Tellurium Phase

In this final phase, 0.5% natural Tellurium (Te) by mass (with 1.3 kilo-tonnes of  ${}^{130}\text{Te}$ ) will be loaded into the scintillator, which is referred to as the “Te-loaded” scintillator (Section 3.3.3.3 will discuss more details). Higher loading concentrations would be possible for a further loading plan[92]. The main purpose of this phase is to search for the  $0\nu\beta\beta$  signals in  ${}^{130}\text{Te}$ .

### 3.3 Detection Media

In the SNO+ detector, charged particles are expected to interact with the detection media and create Cherenkov lights and scintillation lights.

#### 3.3.1 Cherenkov Radiation

For any charged particle traveling in a transparent medium at an ultra-relativistic speed (a speed greater than the local phase speed of light in the medium), a kind of electromagnetic radiation, called Cherenkov radiation, can be emitted from the coherent response of the medium under the action of the field of the moving particle[93, 94].

Suppose a charged particle moves in a transparent, isotropic, and non-magnetic medium and creates an electromagnetic wave. The electromagnetic wave propagates with a wavenumber  $k = n \cdot \omega/c$ , where  $c$  is the speed of light in vacuum,  $n$  is the real-valued refractive index and  $\omega$  is the frequency. If the particle travels uniformly along x-axis with a velocity of  $v$ , the x-component of the wave vector is  $k_x = \omega/v$ . For a freely propagating wave,  $k > k_x$ , therefore  $v > v_p = c/n(\omega)$ , where  $v_p$  is the phase velocity in the medium. Under this condition that the speed of the charged particle is greater than the  $v_p$ , the Cherenkov radiation is emitted with a frequency of  $\omega$ [94].

The Cherenkov angle,  $\theta_c$  is the angle between the direction of the particle and the direction of Cherenkov emission and it is well-defined by  $\cos \theta_c(\omega) = \frac{c}{n(\omega)v}$ . The radiation is distributed over a surface of a cone with the half-opening angle  $\theta_c$ .

Consider the condition  $v > v_p = c/n(\omega)$ , for the case of  $e^-$  travelling in a water detector, if neglecting the dependency on  $\omega$ ,  $n_{water} \simeq 1.33$  [33], then  $\theta_c \simeq 41.25^\circ$  and  $v_p \simeq 2.254 \times 10^8 \text{ m/s}$ , which corresponds to a kinetic energy  $E_k = (\gamma - 1)mc^2 = 0.264 \text{ MeV}$  for  $e^-$ , where  $\gamma = 1/\sqrt{1 - v_p^2/c^2}$ . This is the lowest kinetic energy to create Cherenkov radiation, which is referred to the Cherenkov threshold ( $E_{thresh}$ ). In the case that the LAB-PPO liquid scintillator is the medium,  $n \simeq 1.50$ [95],  $\theta_c \simeq 48.19^\circ$  and for  $e^-$ ,  $E_{thresh} \simeq 0.175 \text{ MeV}$ .

For a particle with a charge of  $ze$ , the number of photons produced by Cherenkov

radiation per unit path length and per unit frequency of the photons is given by[96]:

$$\frac{d^2N}{d\omega dx} = \frac{\alpha^2(ze)^2}{c} \sin^2 \theta_c = \frac{z^2\alpha}{c} \left(1 - \frac{1}{\beta^2 n^2(\omega)}\right),$$

where  $\alpha$  is the fine structure constant.

Transforming the frequency into the wavelength ( $\lambda = 2\pi\omega$ ) and integrating over the wavelength, the number of photons along the particle track projected on the x-axis is[96]:

$$\frac{dN}{dx} = 2\pi(ze)^2 \alpha \sin \theta_c \int_{\lambda_1}^{\lambda_2} \frac{d\lambda}{\lambda^2},$$

For optical photons with wavelengths ranging from 350 to 550 nm (typical PMT detection sensitive range), the above formula can be calculate into[96]:

$$\frac{dN}{dx} = 476(ze)^2 \sin^2 \theta_c \text{ photons/cm.}$$

For the Cherenkov radiation caused by  $e^-$  in a water detector,  $dN/dx \simeq 207 \text{ photons/cm}$ ; while in the LAB-PPO case,  $dN/dx \simeq 264 \text{ photons/cm}$ . In a realistic measurement, the detection efficiency and the coverage of photon sensors are also required to be taken into account.

### 3.3.2 Scintillation from Organic Scintillator

Besides the Cherenkov photons described in the previous section, the majority of lights emitted from the organic scintillator are scintillation photons.

The organic liquid scintillator can convert the kinetic energy of charged particles into scintillation photons with wavelengths in the sensitive detection region of PMTs. They are aromatic hydrocarbon compounds with benzene-ring structures. When ionizing radiation happens in the scintillator, the free valence electrons of the molecules are excited and transit to occupy the  $\pi$ -molecular orbitals with the benzene rings. These highly delocalized electrons are called  $\pi$ -electrons, which can occupy a series of energy levels. A Jablonski diagram, invented by Polish physicist Aleksander Jabłoński, is generally used to describe molecular absorbance and emission of light. In Fig. 3.2, the Jablonski diagram illustrates the  $\pi$ -electronic energy levels of an organic scintillator molecule[6, 96].

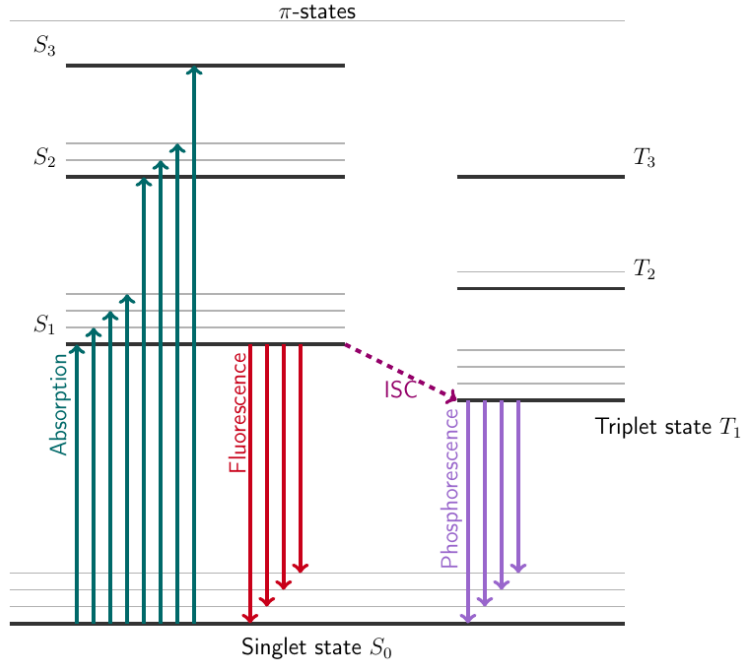


Figure 3.2: A Jablonski diagram for the organic scintillator, modified from [5, 6].

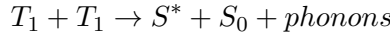
In the diagram,  $S_{0,1,2,3,\dots}$  are the energy levels of the spin-0 singlet states, where  $S_0$  is the ground state and  $S^* = S_{1,2,3,\dots}$  are the excited singlet states. Above the ground state  $S_0$ , there is also a set of spin-1 triplet states  $T_{1,2,3,\dots}$ , where  $T_1$  is the lowest triplet state. These electron energy levels are labeled with thick black lines. The energy spacings between these levels are  $\mathcal{O}(eV)$ . In each level, there are also fine structure levels that correspond to excited vibration modes of the molecule (labeled with gray lines and can be marked as  $S_{10}, S_{11}, \dots, S_{20}, S_{21}, \dots$ ). The energy spacing between these fine levels are  $\mathcal{O}(0.15\text{ eV})$ [96, 6].

The ionization radiation transfers the energy to the molecules and excites the electron levels as well as the vibrational levels, labeled as the absorption lines (in green). The decays between the excited singlet states (not to the ground state) are almost immediate ( $\leq 10\text{ ps}$ ) without the emission of light. This process is called internal degradation. The decays from the excited singlet state  $S_1$  (as well as the vibrational states  $S_{10}, S_{11}, S_{12}, \dots$ ) to the ground state (as well as the vibration states  $S_{01}, S_{02}, \dots$ ) happen promptly ( $\mathcal{O}(ns)$ ) and emit lights (labelled as red lines). This process is called fluorescence which contributes to the prompt

component of the emission of scintillation light. The probability of  $S_1$  decays into the vibrational states  $S_1 \rightarrow S_{01}, S_{02}, \dots$  among the ground state is more than  $S_1 \rightarrow S_0$ . Since the absorbed energy of  $S_0 \rightarrow S_1$  is larger than the emitted energy of  $S_1 \rightarrow S_{01}, S_{02}, \dots$ , the scintillators have very little self-absorption of the fluorescence and are transparent to their own radiation. The effect of Stokes shift, which refers to the overlap between the optical absorption and emission spectra, is small for the organic scintillator[96, 6].

The transitions between the singlet and triplet states are highly forbidden due to the electron spin-flip involved[97, 98]. There also exists a relatively rare process called inter-system crossing (ISC), which converts excited singlet states into triplet states. Besides this, 75% of triplet states can be produced by ionization-recombination[97, 99].

For the de-excitation, the similar processes of internal degradation occur among  $T_{2,3,\dots} \rightarrow T_1$ .  $T_1$  is a relatively stable state and the lifetime of the molecule in the triplet state is in  $\mathcal{O}(10^{-4} - 10 s)$ [100].  $T_1 \rightarrow S_0$  is highly forbidden. However, the  $T_1$  state can go through an indirect decay process by interacting with another excited  $T_1$  molecule and forms an excited singlet state:



The  $S^*$  will de-excite and emit delayed scintillation light. The process for emitting this delayed scintillation light is called delayed fluorescence or phosphorescence[96]. This process contributes to the delayed component of scintillation light.

For a typical scintillator detector, the time scale of detector response is  $\mathcal{O}(1-100 ns)$ . In this time region, the emission of the scintillation light contains the primary fluorescence from the de-excitation of the singlet states (prompt component) and the delayed fluorescence from the de-excitation of the indirect triplet states (delayed component)[99]. The time profile of the scintillation light emission is a mixture of prompt and delayed components.

Different charged particles can cause different ionization densities when they deposit energies to the scintillator molecules. The ionization density affects the relative population of the excited singlet and triplet states. Compared to an  $e^-$ , an  $\alpha$  particle can cause a high ionization density, which produces a higher ratio of triplet states. Therefore, the time profile

for the  $\alpha$  particle has more delayed components or longer tails than the  $e^-$ . This enables the organic scintillator to distinguish  $\alpha$  with  $e^-$  or other lighter charged particles[99, 101].

An empirical formula, called follows Birk's law[102, 5], describes the photon yield along with unit distance by the incident particle:

$$\frac{dY}{dx} = A \frac{dE/dx}{1 + k_B \cdot dE/dx},$$

where  $A$  is a normalization constant,  $k_B$  is the Birks' constant of the scintillator, which in practice is obtained by fitting the formula to the measured data.

### 3.3.3 Liquid Scintillator for SNO+

Organic scintillators can release a large number of photons with wavelengths in the sensitive regions of the PMTs and have abilities for particle identification. In addition, since organic liquids are non-polar media, it is hard for ionic impurities to dissolve in. This leads to the lower contamination levels of uranium (U), thorium (Th), and potassium (K) in the organic liquid scintillators. Among the organic scintillators, aromatic organic liquid scintillators have high electron densities and thus they can provide sufficient targets for particle interactions[103]. Due to these advantages, aromatic organic liquid scintillators have been extensively developed as detection media for large particle detectors, especially for neutrino experiments, such as KamLAND, Borexino, Day Bay, and JUNO[101].

SNO+ has developed such kind of liquid scintillators that are compatible with the detector components, especially with the acrylic materials, like the AV sphere. Two kinds of SNO+ liquid scintillators are discussed in the following sub-sections: the unloaded liquid scintillator for the scintillator phase and the Tellurium-loaded liquid scintillator (TeLS) for the tellurium phase.

#### 3.3.3.1 Water-based Wavelength Shifter (Proposal)

X. Dai et al.[104] made a proposal for adding wavelength shifters (WLS) into a water Cherenkov detector like SNO. Compared to the water Cherenkov detector, a water-based wavelength shifter (wbWLS) detector has a higher light yield (about threefold higher than

SNO[104]) and thus lowers down the energy threshold and opens opportunity to detect low energy events. At the meantime, it will still keep the directionality from Cherenkov signals compared to a loss of the directionality for the liquid scintillator detector, which can be used to suppress the backgrounds when analyzing directional signals, such as solar neutrinos. This technology is being studied by future neutrino experiments, such as the Advanced Scintillation Detector Concept (ASDC)[105], WATCHMAN experiment[106] and Jinping experiment[83].

There was a proposal of adding wavelength shifter (WLS) into the SNO+ detector in the middle of the water phase, made by the University of Alberta group. The specific wavelength shifter we considered is PPO, which is a well-studied ingredient of the liquid scintillator used in the SNO+ scintillator phase and Te-loaded phase. Although this proposal was not adopted due to the experiment schedule, it is still worthwhile for a conceptual study of a SNO+-like detector that uses water-based wavelength shifter (wbWLS) as detection medium.

In Chapter 4, a vertex reconstruction method is discussed.

### 3.3.3.2 Unloaded Liquid Scintillator

SNO+ adopts a scintillator cocktail contains two primary components: LAB as solvent and PPO as solute. LAB is doped with PPO to a concentration of 2 g/L. Fig. 3.3 shows the chemical structural formulae of LAB and PPO[101].

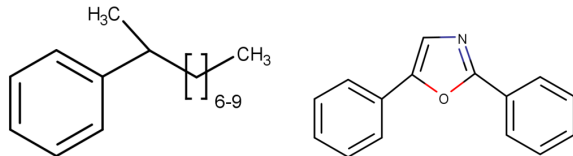


Figure 3.3: Structural formulae of LAB (left) and PPO (right).

LAB is a family of alkylated aromatic organic compounds with a phenyl group attached to a long carbon chain varying from 9 to 14 carbons[107, 101]. It has been used as a biodegradable detergent since the 1960s and it is proved to be relatively non-toxic and very

low risks for the environment or human health[107]. Due to the long carbon chain, LAB is an effective energy absorber. close to linear response to energy

Good stability and chemically compatible

High light yield and attenuation length.

attenuation length good optical transparency

flash point at 140 °C

It has very low levels of natural radioactive contaminants such as U, Th and K. The target background levels for the SNO+ LAB are expected to be  $\mathcal{O}(10^{-17})$  gram of  $^{238}\text{U}$  in per gram LAB ( $\text{g}^{238}\text{U}/\text{gLAB}$ ), which is equal to be thousands of events per year; The  $^{232}\text{Th}$  and  $^{40}\text{K}$  levels are  $\mathcal{O}(10^{-17})$  g/gLAB, which is equal to be hundreds of events per year[108].

It has fast timing response different timing spectrum for  $\alpha$  and  $\beta$  events, which enables an  $\alpha/\beta$  discrimination. High flash point and low toxicity for lab safety. appropriate density for mechanical stability Low cost.

The LAB used by SNO+ is provided by CEPSEA Química Bécancour Inc.

As a wavelength shifter, PPO is usually added and dissolved into the LAB [109]. This wavelength shifter is used as a fluor. Energies are transferred from LAB to PPO via non-radiative Förster resonant energy transfer. It can shift the wavelengths of the scintillation photons to a range of 300-550 nm, which is in the sensitive range of the PMT detection and can also reduce the probability of being the self-absorption of LAB.

A 2 g/L PPO concentration in LAB is optimized by SNO+[85]. The absolute light yield of the LAB-PPO liquid scintillator has been well-measured from large particle physics experiments [110], borexino], as well as bench-top measurements [110], novikov, tanner]. The absolute light yield of the LAB+2g/L PPO liquid scintillator determined by SNO+ is 11900 photons/MeV [cite lightyield]. And this light yield is expected to be increased by over 15% after extensive purification process[7].

Fig. 3.4 shows absorption lengths.

This transfer efficiency ( $\epsilon_{transfer}$ ) increases as the PPO concentration increasing, as shown in the Table. Above the 2 g/L concentration, the light yield reaches a plateau [101].

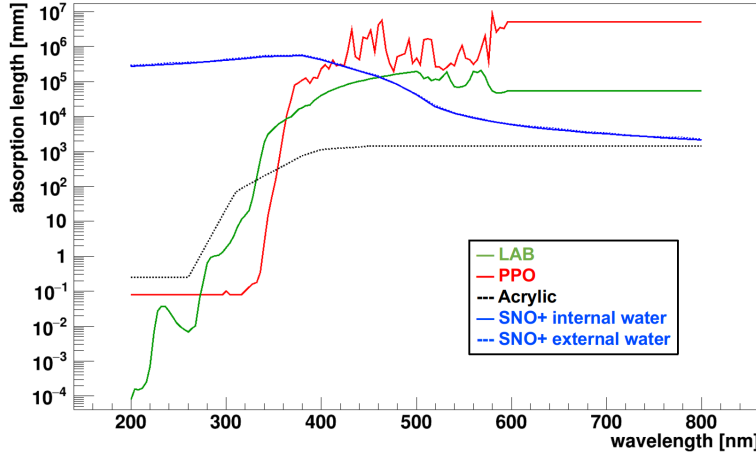


Figure 3.4: Absorption length of SNO+ optical components. ;the internal (solid blue line) and external water (dashed blue line) absorption curves are based on the measurements of the laserball scans in July 2018 during the SNO+ water phase. The horizontal lines are due to absence of the measurements and they are conservative assumptions.

The optical response of the liquid scintillator.

The time profiles of scintillator were obtained from bench-top measurement. An empirical model consists  $n$  ( $n = 3$  or  $4$ ) exponential decays with a common rise time is used to describe the time profiles[111].

Default timing fitting functions:

$$\sum_{i=1}^n A_i \cdot \frac{e^{-\frac{t}{\tau_i}} - e^{-\frac{t}{\tau_{rise}}}}{\tau_i - \tau_{rise}}$$

while the rise time,  $t_{rise} = 0.8$  ns the timing parameters  $t_i$ , amplitude  $a_i$  are determined by the bench-top measurements [112].

From Oxford timing fitting functions:

$$\left\{ \sum_{i=1}^n A_i \cdot \frac{e^{-\frac{t}{\tau_i}} - e^{-\frac{t}{\tau_{rise}}}}{\tau_i - \tau_{rise}} \otimes f_{PMT}(t - t') \right\} \otimes Gaus(t, 0)$$

3.3.3.2[101].

### 3.3.3.3 Tellurium-loaded Liquid Scintillator

To load the Te into the liquid scintillator, a compound is made by condensation reactions between telluric acid (TeA) and 1,2-butanediol (BD), with N, N-dimethyldodecylamine

| PPO concentration (g/L) | $\epsilon_{transfer}(\%)$ |
|-------------------------|---------------------------|
| 4                       | $86.0 \pm 0.8$            |
| 2                       | $78.2 \pm 1.5$            |
| 1                       | $67.7 \pm 2.3$            |
| 0.5                     | $59.3 \pm 3.2$            |
| 0.25                    | $48.7 \pm 5.0$            |

Table 3.1: scintillator  $\alpha/\beta$  timing parameters[113, 114, 112].

| scintillator<br>particles                                    | timing [ns] |       |        |       | amplitudes |       |       |        |
|--|-------------|-------|--------|-------|------------|-------|-------|--------|
|  | $t_1$       | $t_2$ | $t_3$  | $t_4$ | $a_1$      | $a_2$ | $a_3$ | $a_4$  |
| LAB + 2g/L PPO (default scintillator)                        |             |       |        |       |            |       |       |        |
| $e^-$  | 4.88        | 15.4  | 66.0   | 400   | 0.665      | 0.218 | 0.083 | 0.0346 |
| $\alpha$   | 4.79        | 18.4  | 92.0   | 900   | 0.427      | 0.313 | 0.157 | 0.1027 |
| LAB + 0.5g/L PPO (partial-fill phase)                        |             |       |        |       |            |       |       |        |
| $e^-$  | 7.19        | 24.81 | 269.87 | —     | 0.553      | 0.331 | 0.116 | —      |
| $\alpha$   | 6.56        | 23.82 | 224.19 | —     | 0.574      | 0.311 | 0.115 | —      |
| LAB + 2g/L PPO + 0.5% molar concentrations DDA               |             |       |        |       |            |       |       |        |
| $e^-$  | 5.0         | 12.1  | 33.3   | 499.0 | 0.68       | 0.21  | 0.07  | 0.04   |
| $\alpha$   | 3.8         | 11.3  | 65.3   | 758.0 | 0.48       | 0.32  | 0.14  | 0.06   |
| LAB + 2g/L PPO + 0.5% molar concentrations Te+0.5% molar DDA |             |       |        |       |            |       |       |        |
| $e^-$  | 3.7         | 10.0  | 52.0   | 500.0 | 0.72       | 0.23  | 0.02  | 0.03   |
| $\alpha$   | 3.69        | 15.5  | 79.3   | 489.0 | 0.63       | 0.23  | 0.07  | 0.07   |

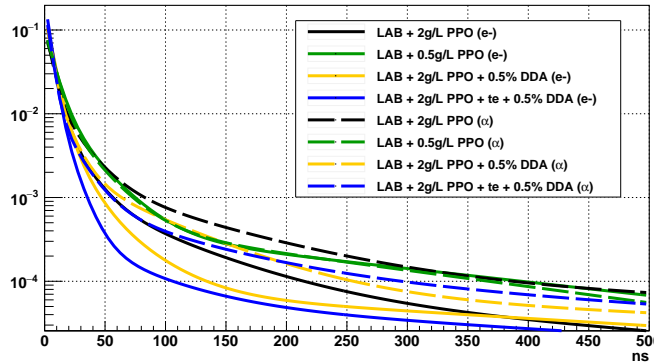


Figure 3.5: Timing profiles for liquid scintillators in different SNO+ phases.

(DDA) being used as a stabilization agent.

A tertiary amine (N, N-Dimethyldodecylamine, DDA) was added during the reaction to stabilize TeBD complexes and avoid any phase separation.

Tellurium-loaded 65% of the pure, unloaded scintillator water-based wavelength shifter timing profile, the intensity of scintillation light as a function of time the prompt fluorescence intensity at a time  $t$  excitation be  $I = I_0 e^{-\frac{t}{\tau}}$  singlet and triplet states ionization density depend  $\alpha$ -particle high ionization density quenching,

2 g/L PPO gives an absolute light yield of 11900 photons/MeV.

for the partial-fill phase, 0.5 g/L PPO gives Measurements in 0.5 g/L showed a light yield of 52% of 2 g/L, 6190 photons/MeV[113, 114].

For the  $^{130}\text{Te}$   $0\nu\beta\beta$ -decay process, the signature energy peak is at 2.5 MeV[85]. This peak is relatively small and can be immersed in the ubiquitous radioactive decays from natural sources, such as the natural Uranium and thorium decay chains existing in the materials[85]. Therefore, the  $0\nu\beta\beta$ -decay experiments require a very high energy resolution to distinguish the signal from the backgrounds. For the liquid scintillator, it is expected to create as large amount of light caused by a particle interaction as possible. A quantity of light yield, defined as the number of photons for per MeV energy deposit (photons/MeV) by a particle interaction, is used for describing the detection property of the liquid scintillator.

To meet the low background requirement of the  $0\nu\beta\beta$  analysis, the purity of the TeLS cocktail is aimed to  $\mathcal{O}(10^{-15})$  g/g level for U and Th.

### 3.3.4 Relative Light Yield Measurements of the Te-loaded Liquid Scintillators

As mentioned in the previous section, the  $0\nu\beta\beta$  analysis requires a high purity of the TeLS and proper light yield.

Here we measured the light yield of 0.5% Tellurium loaded LAB (TeLS) samples relative to the LAB-PPO scintillator (relative light yield, RLT). With tellurium loading into the LAB, the light yield of the liquid scintillator will go down since the tellurium atoms can block the photon transmissions to the photosensors. The light yield of the TeLS is crucial

for the  $0\nu\beta\beta$ -decay experiments since it determines the energy resolution. It is also crucial for the experiments that are aimed to develop high light yield Tellurium-loaded scintillators [115].

### 3.3.4.1 Measurement Setup and Data Acquisition

We first prepared LAB+2 g/L PPO by dissolving PPO into the pure LAB. The LAB-PPO mixture was distilled by heating and flowing with liquid nitrogen to remove humidity and oxygen, which can affect the light yield, for 48 hours. The distilled LAB-PPO was added into the original 16.5% weight Te-butanediol samples to dilute into the 0.5% TeLS samples. Te-butanediol samples from both of the DDA and SOP synthesis procedures were prepared. They are referred as TeDDA and TeSOP samples respectively. These samples were further transferred into scintillation vials for the measurement. These vials have PTFE caps sealed on the top of the glass cylinders. To avoid air bubbles created by squeezing the vial cap into the liquid, the liquid level for each sample was kept at 30 mm. The dimensions of the vial is shown in the left picture of Fig. 3.6.

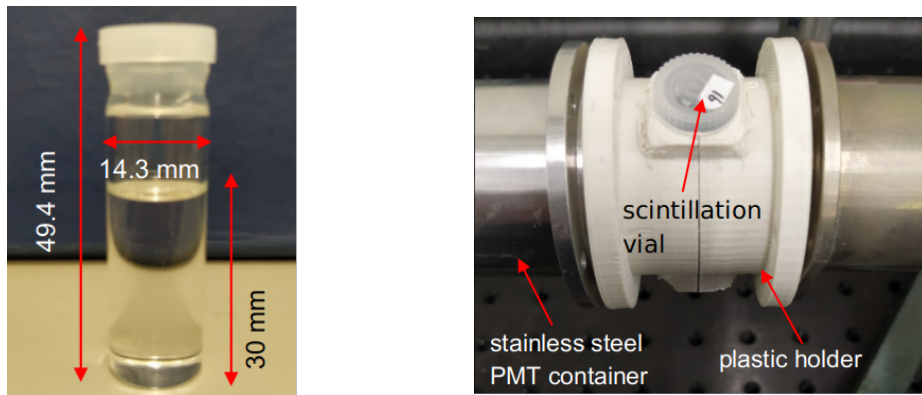


Figure 3.6: Test sample (left) and setup (right). Left: The samples were filled into scintillation vials. The dimensions are shown in the picture. Right: two PMTs were aligned to face to the scintillation vial from each side.

Two Hamamatsu R580 PMTs [cite PMT] were used for detecting the light. The diameter of the PMT round surface is 38.71 mm. These PMTs were housed in stainless steel cylinders (PMT holders), set face to face, looking at the scintillation vial from each side. The PMTs

and the vial were aligned by a plastic piece, as shown in the right picture in Fig. 12. The plastic piece is in a cylindrical shape with a hole on the top to plug in the scintillation vial and a slot at the bottom to attach a radioactive source. Inside the cylinder, there is a button-shaped groove at the bottom to fix the vial plugged in and keep the vial upright. Also, a 2-mm-diameter hole was drilled at the bottom of the piece to allow the radiation rays to go inside from the bottom. The surface inside was polished to reduce the absorption of the material to the photons. The piece is made of plant-based and biodegradable polylactide (PLA) filament and was machined by 3D-printing facility. The pictures of the pieces are shown in Fig. 3.6.

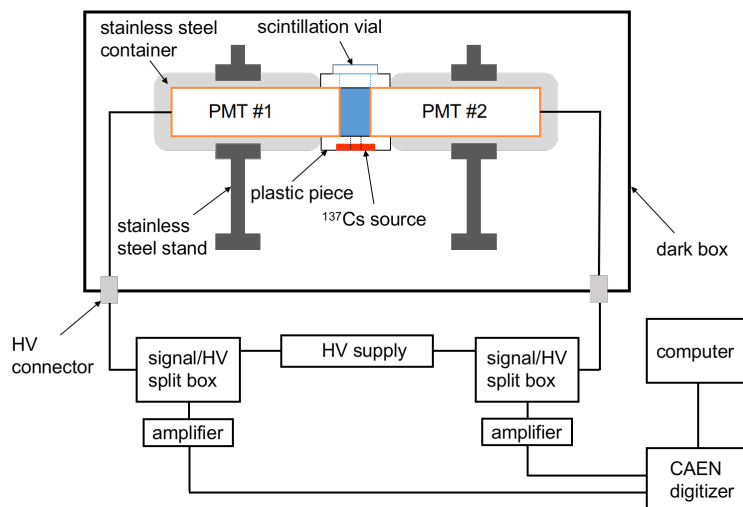


Figure 3.7: A diagram shows the light yield measurement setup. See the text for details.

Fig. 3.7 shows a diagram of the whole measurement setup. The plastic piece held the radioactive source and the scintillation vial. It also aligned two PMTs to face to the scintillation vial from each side. The piece can shield lights from outside as well. These setups were placed in a dark box to prevent the lights from lab. Two RG59/U type high voltage (HV) cables connected the PMTs to an HV supply outside the dark box. The HV cables were connected to two signal/HV split boxes to separate the HV current and electrical signals. Due to the resistor of the split box, the HV supply was set to 2200 Volts (V) for the PMT operation while the operation voltage suggested by the Hamamatsu is

1800 V.

The signal cables from the split box were connected to a two-channel Hewlett Packard (HP) amplifier. This amplifier inverted the signals and amplified them by 26 dB. The amplified signals were then input into a two-channel digitizer. The digitizer records the data and sent them to a desktop computer.

To obtain and analyze the data, we used a desktop Waveform Digitizer, the DT5751 module provided by the Costruzioni Apparecchiature Elettroniche Nucleari S.p.A (CAEN). Running at a digital pulse processing mode, the module records the digitized PMT waveforms with a data-taking rate of 1 GHz for each channel [cite CAEN].

This module was controlled by the CoMPASS software provided by CAEN. The software set up the threshold and trigger parameters. For each triggered event which passed the threshold, the software recorded event time, trigger flag and waveform histograms from the two channels. By integrating the waveforms, the energy of a triggered event was calculated [cite compass].

Each channel recorded the signals from each PMT individually. With the two-PMT setup, we applied coincidence time mode measurements. In the coincidence mode, a coincidence time window between two channels were set to 48 ns. For a certain event, the CoMPASS software compares the event time difference between two channels and only records it if the event time differences is less than 48 ns. A smaller window of 10 ns was further applied for analysis.

### **3.3.4.2 Measurement**

The liquid scintillator samples we have measured are: LAB-PPO, TeDDA, TeSOP. The unloaded LAB-PPO sample served as a standard candle.

A Cesium-137 ( $^{137}\text{Cs}$ ) radioactive source was always placed at the bottom of the scintillation vials. The source was made by Radiochemical Centre Amersham. The radioactivity measured on 1st April 1974 was 11.09 *microcurie*( $\mu\text{Ci}$ ), with an accuracy of 3.7%. The activity was expected to be

in this thesis, considering a half-life of 30.08 years for the  $^{137}\text{Cs}$ [116].

has a 85.10% chance to emit 0.661 MeV  $\gamma$ -rays[116]. These  $\gamma$ -rays can travel into the liquid scintillator samples in the vial, interact with the samples and create scintillation photon.

For each sample, measurements were taken for one-minute time duration. Waveforms from the PMT photo-current signals were digitized in a 252 ns time window. Shown in Fig. 3.8 is a typical waveform caused by  $\gamma$  rays interacted with the LAB-PPO sample. The p.e. signals triggered PMT pulses and the pulses were digitized as waveforms. For each waveform, the digitizer firmware dynamically calculated the baseline as the mean value of 256 data points inside a moving time window of 252 ns. A threshold was set as 100 units above the baseline. The data point on the 90% leading edge of the pulse was taken as the trigger time tag. From this trigger time tag, in the following 80 ns window the digitizer did not calculate another trigger to avoid introducing another pulse (trigger hold-off). Also from the trigger time tag, a pre-gate of 8 ns was set. The waveform was integrated in the time gate of [trigger time - 8, trigger time + 72] ns. This gives the integrated charge, which was calculated as a A/D converter (ADC) channel number. If the measurement system can be calibrated, the ADC channel number can be exactly converted into the energy of the particle interaction. Since here we only interested in the photon numbers, we simply used ADC channel as the energy. Once the pulse in the waveform passed the threshold and a triggered time tag can be found, the digitizer considered it as a triggered event. A time flow started when the measurement began. Time stamps were recorded as event time when the triggered event hapfpened. The waveform was recorded and the ADC channel number (energy) of this event was calculated.

In a coincidence time measurement, the event times of the events recorded by each of the two PMTs were compared. If the event time differences between two events from each PMTs were too long, these two events were considered as random noises rather than the physics events and were not recorded. We optimized a coincidence time cut as 40 ns and set that cut during the digitizer data-taking.

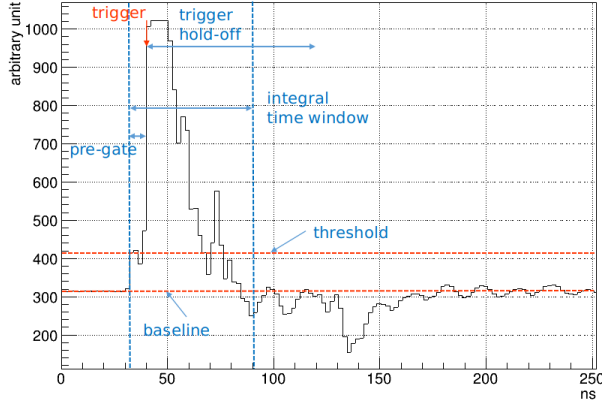


Figure 3.8: A typical waveform triggered by scintillation photons from  $^{137}\text{Cs}$   $\gamma$ -rays interaction with LAB-PPO sample.

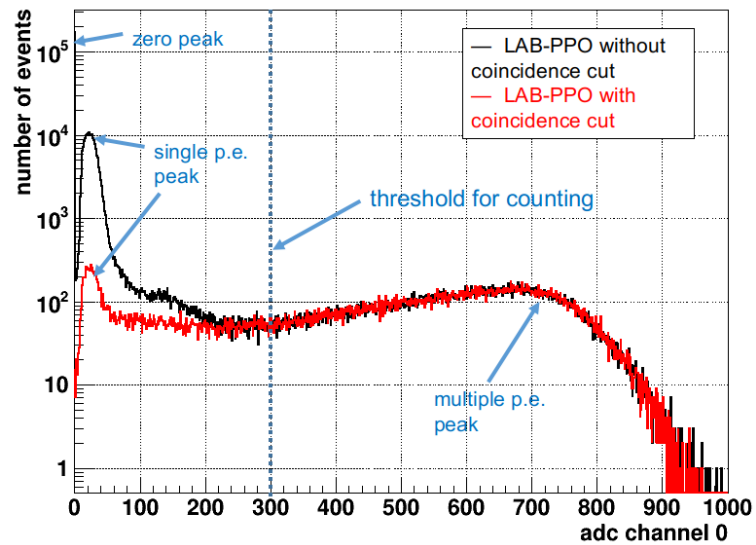


Figure 3.9: Measured LAB-PPO energy spectrum with and without coincidence cut on the ADC channel 0. A threshold for counting is set by comparing the two spectrum.

Fig. 3.9 shows the measured LAB-PPO energy spectrum with and without coincidence time cut ( $10\text{ ns}$ ) on the ADC channel 0. Without the coincidence time cut, there exists a zero peak, which is caused by the pulses from random electronic noises or fluctuations of the digitized waveforms. The peak on the left is the single p.e. peak. It is mainly caused by some light sources which are weak enough that the photons only strike out at most one single p.e. inside the PMT [cite leo]. The peak on the right is the multiple p.e. peak, in our case is mainly caused by a number of scintillation photons produced by the -ray interacting with the LAB-PPO. In the coincidence time measurement mode, it only records the photons detected by the two PMTs almost simultaneously. Therefore, the zero peak is removed while the single p.e. peak is suppressed. The multiple p.e. peak is consistent with the non-coincidence measurement. A threshold in energy can be set to count only the scintillation photons emitted from LAB-PPO.

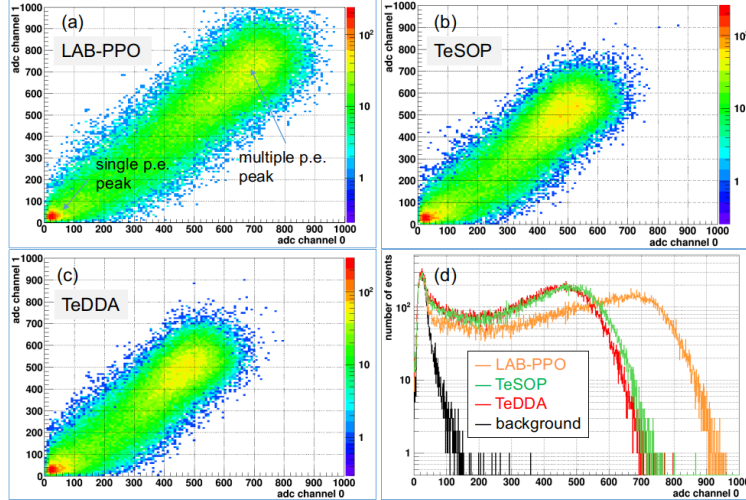


Figure 3.10: 2D energy spectrum of the counting measurements of LAB-PPO (a), TeSOP (b), and TeDDA (c) samples, projected the 2D plots into one channel (d). The single photo-electron (p.e.) peak is mainly caused by backgrounds while the multiple p.e. peak is from scintillation photons.

Fig. 3.10 shows the result of one-minute measurement for the LAB-PPO sample. The data points in the 2D plot represent the triggered event fall in certain ADC channel numbers in each channel. A  $10\text{ ns}$  coincidence window cut was applied to cut down noise, single p.e.

and background events. The events in the 0 ADC channel, which represent noises, were totally cut off after applying the coincidence. Fig. 18 shows the results of the TeSOP and TeDDA samples. Compared to the LAB-PPO sample, a shift of the multiple p.e. peak due to the different light yields between the samples can be observed clearly.

The 2D plots in Fig. 3.10 are projected onto a single channel. We used an empty vial and let  $\gamma$ -rays from  $^{137}\text{Cs}$  source pass through it for a background run (without the coincidence cut). This is to verify the single p.e. peak and noise region, shown as the black background spectrum.

From this plot, the single p.e. peaks for all the samples as well as the background match together. The multiple p.e. peaks indicate the different light yields of the scintillator samples. Here we can clearly see the multiple p.e. peak of the LAB-PPO occupies the largest ADC channel number, while the channels of TeSOP is slightly larger than the TeDDA.

To quantify the light yield differences between different samples, an analysis method of charge weighted photon number has been applied as the following:

First, from the energy spectrum, the single p.e. peak was fitted with an asymmetric Gaussian function (as  $f_{asym}$  in 3.1), as shown in Fig. 3.11. The mean value of the asymmetric Gaussian ( $p_0$ ) represents the ADC channel number corresponding to the single p.e. peak for the weighting.

$$f_{asym} = c \cdot e^{-\frac{1}{2}(\frac{x-\mu}{\sigma})^2} \cdot \text{Erfc}(\xi), \quad (3.1)$$

where  $\xi = -\frac{\alpha(x-\mu)}{\sqrt{2}\sigma}$ ,  $p_0 = \mu$ ,  $p_1 = \sigma$ ,  $p_2 = \alpha$ ,  $p_3 = c$ .

Then for the multiple p.e. region, weighting (dividing) the counts of the event in each channel with the single p.e. ADC channel number to calculate the total number of the photons.

To define the multiple p.e. region for the counting, the spectrum projected on each channel with and without coincidence cut are compared to define a threshold of the ADC channel for counting. By integrating from this threshold, the total numbers of events between two spectrum are close to each other. From two channels, we get two thresholds

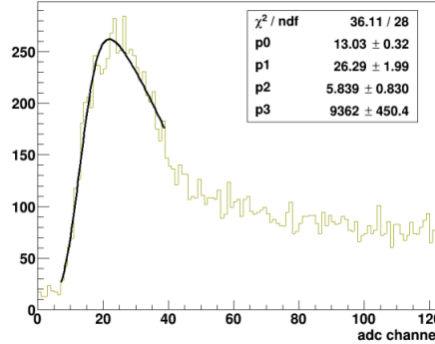


Figure 3.11: Fit the single p.e. peak with an asymmetric Gaussian function (fasym) to obtain the adc channel for weighting. The mean value of p0 is used as the adc channel relative to a single p.e. peak..

and then define a box cut in the 2D coincidence plot. We weights the events in the box to obtain the total number of photons. Fig. 16 and Fig. 19 show the case of the LAB-PPO sample.

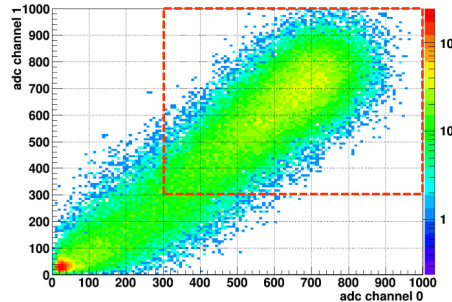


Figure 3.12: Two dimensional spectrum of LABPPO sample with coincidence cut. A box cut is defined for multiple PE counting.

Fig. 3.12 Two dimensional spectrum of LABPPO with coincidence cut. A box cut is defined for multiple PE counting.

Once the total number of the photons for a certain sample is counted, we can calculate its ratio to the LAB-PPO sample to obtain the relative light yield.

### 3.3.4.3 Results

Table. 3.2 shows the number of photons calculated by Charge weighted photon number method.

Table 3.2: Number of photons calculated by Charge weighted photon number method.

| Sample  | Number of photons ( $\times 10^6$ ) | RLY  |
|---------|-------------------------------------|------|
| LAB-PPO | 2.0811                              | 1    |
| TeDDA   | 1.2652                              | 0.61 |
| TeSOP   | 1.3976                              | 0.67 |

Here we quantify the relative light yields of our samples. The light yield of the 0.5% Te by SOP synthesis procedure (TeSOP) is 0.61 and the one of the 0.5% Te by DDA procedure is 0.67. The light yield of TeSOP is slightly larger than the TeDDA. In [115], a relative light yield of  $\sim 0.65$  was reported.

### 3.4 Electronics

In this section, the SNO+ electronics system is introduced. The system includes the trigger and readout systems. As mentioned in 3.1, the PMTs as photon sensors are the basic detection elements for the SNO+ detector. The signals from the PMTs are sent to the SNO+ electronics system, which records the PMT time and charges information and then transfers the digitized data to offsite computing systems for data analysis. These steps are detailed in the following.

The photons created from particle interactions in the detector propagate to the PMT sphere and may hit a certain PMT and strike on its photo-cathode, which is a thin cesium bialkali film coated on the inner surface of PMT glass. The photocathode then produces a photo-electron (p.e.) through a photoelectric effect. The photocathode is set at ground voltage while the anode is at a high voltage ranging from +1700 to +2100 V [117, 99]. This forms electric fields inside the PMT. The p.e. is accelerated and focused by the electric field in the PMT and goes through the volume which is under vacuum until it reaches the region of a series of secondary emission electrodes, called dynodes. When the p.e. transfers its energy to the materials in dynodes, a number of secondary electrons escape and form a measurable current which is collected by a custom-made operating circuit (called “PMT base”) at the anode[118].

The anode pulse produced from the PMT travels along 35 m-long RG59/U type coaxial cable (with a resistance of  $75 \Omega$ ) to the front-end electronics which are set up on the deck above the detector. The coaxial cable also carries the high-voltage[117].

To tackle with more than 9000 PMTs in the SNO+ detector, the coaxial cables connected to each PMTs are grouped into bundles. Each bundle is connected to a Paddle Card, which are linked to a PMT Interface Card (PMTIC). The PMTIC supplies high voltages and receives signals from the PMTs. 32 channels (for 32 PMTs) in the PMTIC are plugged into a Front End Card (FEC) that processes, digitizes, and stores PMT signals. 19 crates tackle 9728 PMT channels in total, of which 32 channels are reserved for calibration inputs and labeled as FEC Diagnose (FECD) channels. These FECD channels are mainly used to tag calibration events. The triggered PMTs can be labeled by the logical channel number (*lcn*) using the map of the PMT to the crates and cards[7, 86]:

$$lcn = 512 \times \text{crate} + 32 \times \text{FEC} + \text{channel} \quad (3.2)$$

A 10 MHz and a 50 MHz clocks are used to record the time of the triggered event. The universal time of the triggered event is calculated as the time elapsed from a predefined  $T_{zero}$ , the midnight of January 1, 2010 (GMT) to the moment when the event happens. A 10 MHz clock used for counting the absolute time started at  $T_{zero}$ . It has a 53 bit register and can run for 28.5 years. Its accuracy is maintained by a GPS system. The 50 MHz clock gives more accurate timing. It limits the best time resolution of the GT to 20 ns. This clock has a 43 bit register and rolls over every 2.04 days. The relative time between the events can be used for analyzing specific physics processes, such as radioactive decays[119, 86].

The recorded hit information of the triggered event, including the time and charge information of hit PMTs and the trigger settings, are sent to a Crate Controller Card (XL3) in each crate. These cards were installed for SNO+ to handle higher data transfer rates compared to SNO, with a max rate of 14 MB/s, which is equivalent to approximately 2 million hits per second[120]. They read out the recorded data and wrap them as ethernet packets and send them to the Data Acquisition System (DAQ) and Event Builder system[121]. The Event Builder system writes information into event records based on their GT identification

number (GTID) and saves them on storage disk[7]. These raw data are written to the disc and are further processed into ROOT format by high-performance computing clusters.

As a summary, the SNO+ electronic system can measure signals with a nanosecond-level timing resolution and a single-photon level charge resolution. It can handle an event rate of several kHz and even much higher rates for cases such as the burst events from a galactic supernova[7].

### 3.5 Calibration

Calibration sources with known physics parameters help to understand the detector response to the events and to make accurate measurements.

Two kinds of calibration sources are used by SNO+: (1) the optical sources to measure the *in-situ* optical properties of the detector media and to calibrate the PMTs; and (2) the radioactive sources to test the detector energy responses, check the performance of event reconstruction algorithms for reconstructing event position, direction and energy and then determine their systematic uncertainties. Various types of radioactive sources producing different types of particles (( $\beta$ ,  $\gamma$  particles or neutrons) with different energies can also help to test the analysis tools for particle identifications.

All the calibration sources have been designed to meet the radiopurity required by SNO+ and their materials are compatible with the detection media[7].

The deployment of calibration sources at different positions can help to understand the asymmetries in the detector responses. In geometry, the detector is not perfect symmetric due to the presence of the AV neck, ropes, gaps between the PMTs in the PSUP and differences

through a source manipulator system (SMS) umbilical vertical and side ropes

See Fig. 3.13. reduce the radio contamination in the detector

In addition, to measure the position of the calibration source deployed in the detector, six underwater cameras were mounted on the PSUP and work as a camera system to take photographs and then triangulate the source location. An accuracy of several centimeters

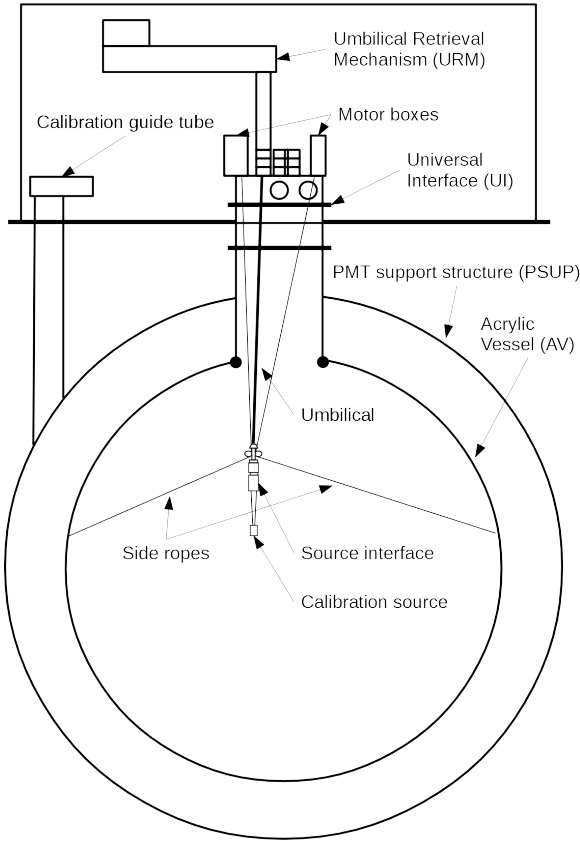


Figure 3.13: The SNO+ Source Manipulator System, taken from [7].

is achieved. This system is also used to monitor the physical state of the detector, such as the offset of the AV center with respect to the PSUP, the movement of the rope net, the height of the water-scintillator interface during the partial-fill, etc[122, 7].

### 3.5.1 Optical Calibration Sources

The optical calibration sources are used to calibrate the PMT response and to measure the optical properties of the detector media. The optical sources mainly include a light diffusing sphere (called “laserball”, LB), as well as the Embedded Light-emitting diode (LED)/Laser Light Injection Entity (ELLIE).

### 3.5.1.1 Laserball

The laserball injects lights from a nitrogen dye laser to a glass bubble.

fast pulsing LED or lasers measures optical properties, such as scattering, attenuation of the detector materials, the response of PMTs, angular and wavelength dependent wavelength dependent absorption and the optical degradation

Optical calibration *in-situ*

various dyes provide different peak wavelengths of the laser light, mainly at 365, 385, 420, 450 and 500 nm.

### 3.5.1.2 ELLIE

Due to the requirements of very low radioactive background levels for SNO+, frequent deployments of calibration sources inside the AV are needed to be avoided. To conduct weekly calibrations of the PMTs, the ELLIE system was developed by SNO+. It uses fast pulsing light injection devices which were mounted on the PSUP at fixed positions, covering all inward facing PMTs. The ELLIE system consists of three modules: (1) the timing module (TELLIE), which utilizes LED for calibrating the PMT hit-time and gains; (2) the scattering module (SMELLIE), which uses laser light to measure the Rayleigh scattering length and scattering angle of the detector media; (3) the attenuation module (AMELLIE), which is used to monitor the relative changes in attenuation lengths of detection media[4, 121, 99, 7].

## 3.5.2 Radioactive Calibration Sources

### 3.5.2.1 The $^{16}\text{N}$ Calibration Source

The  $^{16}\text{N}$  calibration source is one of the radioactive sources. This source is inherit from the SNO experiment and has been well-understood[123, 8, 124].

Since the  $^{16}\text{N}$  isotope has a short half-life of 7.13 s, it must be produced on-site during the calibration runs. A commercial deuterium-tritium (DT) generator was installed in SNOLAB to produce neutrons through:  $D + T \rightarrow n + ^4\text{He}$ ; then the produced 14-MeV

neutrons interact with the  $CO_2$  gas streaming through the small diameter capillary tubing and produce the  $^{16}N$  isotopes via the  $(n, p)$  reaction:  $n + ^{16}O \rightarrow ^{16}N + p$ . These  $^{16}N$  isotopes are transferred into the cavity or the detector by the  $CO_2$  gas tubing[8].

The  $^{16}N$  isotope mainly decays through  $\beta$ -decay process:  $^{16}N \rightarrow ^{16}O + e^- + \bar{\nu}_e$ . It has a 66.2% chance to emit an electron with  $E_{endpoint} = 4.29\text{ MeV}$  and a 22.8% chance to an electron with  $E_{endpoint} = 10.42\text{ MeV}$ ; while the resulting  $^{16}O$  deexcites and produces a cascade of  $\gamma$ 's. There are mainly  $6.13\text{ MeV}$   $\gamma$  with an intensity of 67.0% and  $7.12\text{ MeV}$   $\gamma$  with an intensity of 4.9%. The intensities of the  $\gamma$ 's with other energies are all below 1%[116]. A simplified decay scheme is shown in Fig. 3.14.

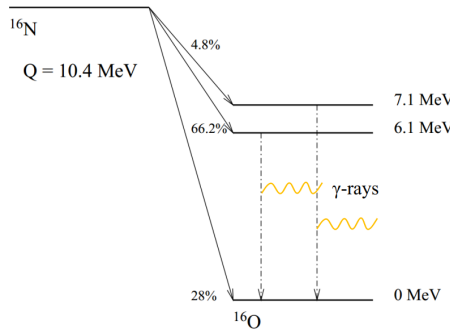


Figure 3.14:  $^{16}N$  main decay scheme, modified from [8].

Fig. 3.15 shows the geometry of the  $^{16}N$  source chamber. The chamber is a stainless steel cylinder mainly containing a small PMT and a gas decay chamber. The chamber was designed to confine the electrons from  $^{16}N$  decay within the chamber and let them be detected by the PMT inside[123].

A detailed study of using the  $^{16}N$  source for reconstruction will be shown in 5.1.

### 3.5.2.2 The Americium Beryllium (AmBe) Calibration Source

### 3.5.2.3 Other Calibration Sources

In the scintillator and tellurium phases, three additional  $\gamma$  sources:  $^{48}Sc$ ,  $^{137}Cs$  and  $^{57}Co$  are planned to be implemented.

$^{46}Sc$  source

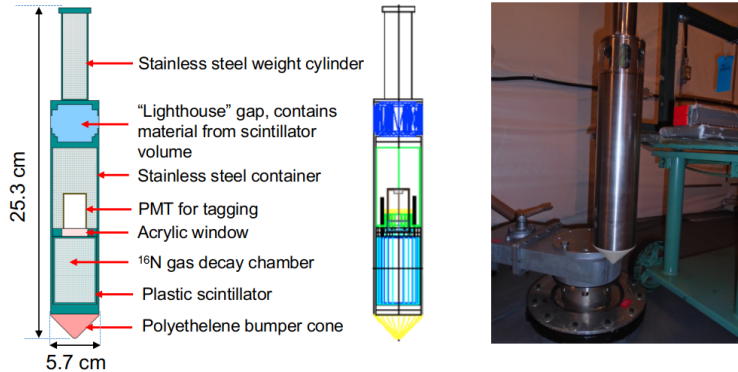


Figure 3.15:  $^{16}\text{N}$  calibration source geometry. Left: a detailed diagram of  $^{16}\text{N}$  source geometry, modified from [9, 10]; middle: source geometry implemented in RAT, modified from [11]; right: a picture of the  $^{16}\text{N}$  source, taken from [12].

### 3.6 Monte Carlo Simulation and RAT Software

The SNO+ collaboration uses a software package called the Reactor Analysis Tool (RAT) for Monte Carlo simulation as well as event-based analysis offline and online. To accomplish these two tasks, RAT integrates the **Geant4** simulation toolkit[125] and ROOT data analysis framework[126] for processing and analyzing data. This feature makes it easy to analyze Monte Carlo-generated events and real data in a same framework and data structure.

The software was originally developed by Stan Seibert from the Braidwood Collaboration to simulate a generic KamLAND-like detector[127]. A simulation package called Generic Liquid Scintillator GEANT4 simulation (**GLG4sim**) was developed and implemented in RAT[128]. It simulates the scintillation physics processes, the generations of scintillation photons and also the propagation, reflections, refraction, scattering and absorption of optical photons[99].

The SNO+ version of RAT links the existing ROOT, Geant4 and GLG4sim packages to minimize the code duplication. The SNO+ RAT is being developed by the whole collaboration and evolves with the experiment progress to precisely simulate the SNO+ detector in different physics phases as well as applying multiple analysis tasks. The relative flexible code structure of RAT allows the user to introduce their own code into the simulation or analysis process[127]. It can be tuned and optimized with the updated parameters from

detector calibration; it can be added with more precise descriptions of the physics processes in the detector; it can also be introduced with more advanced analysis tools. The users can apply different analysis tasks, such as different reconstruction algorithms on the events[127]. Therefore, different versions of `RAT` serving to different SNO+ physics phases may give different outputs. For the work in this thesis, multiple `RAT` versions were used, mainly the versions for the water phase and partial-fill phase. In this case, I will specify the `RAT` version when I discuss a specific analysis.

`RAT` is also used by other astroparticle physics experiments, such as DEAP/CLEAN[129].

# Chapter 4

## Event Reconstruction

### 4.1 An Overview of the Reconstruction Algorithms in SNO+

A particle interaction happens in the SNO+ detector can produce Cherenkov or scintillation photons. These photons propagate through the detector, and they can trigger PMTs when they reach the PSUP. As described in the last chapter, if there are enough PMTs triggered within a defined time window, an event is defined by the trigger system and for the event, the time and charge information measured by the hit PMTs are recorded.

By utilizing the recorded time and charge information, reconstruction algorithms attempt to calculate the physics quantities of an event, including its vertex (position and time), direction and energy. A few sets of reconstruction algorithms (called “fitters”) have been implemented in the SNO+ RAT software or being developed. These fitters are based on different methods and they can be coordinated and optimized for the different detector situations or physics phases.

According to the physics quantities, the SNO+ fitters can be generally classified as:

- Vertex fitter. A vertex fitter reconstructs the event position and time by utilizing the positions and timing information of the hit PMTs. Currently, vertex fitters have been used to process the data and simulations for the water and partial-fill phases. They are also ready for the scintillator and tellurium-loading phases.

On the other hand, some particular events, such as radioactive background events emitting  $\gamma$ s, can create multiple vertices which are correlated. A multi-site or multi-vertex fitter will be useful for tagging and removing these events during the  $0\nu\beta\beta$  search. This kind of fitter is being developed.

- Direction fitter. A direction fitter reconstructs the event direction by using the directional information from the Cherenkov photons, which cause ring-like patterns formed by the hit PMT positions. The direction fitter has been used in the water phase analysis. For the scintillator and tellurium-loading phases, since the Cherenkov patterns will be submerged in the scintillation photons, it requires the other efforts for the direction reconstruction, which is being developed currently.
- Energy fitter. An energy fitter translates the number of photons created from an event to the kinetic energy. The optical response of each PMT, including the PMT detection efficiency, transmission probability, attenuation, and etc. Similar to the vertex fitters, the energy fitters currently have been used in the water and partial-fill phases, and they are ready for the scintillator and tellurium-loading phases.
- Muon track fitter. This fitter is used to reconstruct the tracks of cosmic muons. It treats a muon track as a straight line and by dividing the SNO+ detector into several XY-slices along z, it reconstructs the intersection points for each slice by utilizing the positions and timing information of the hit PMTs[130]. It is currently being developed for the scintillator and tellurium-loading phases. It will help to tag and reduce the cosmogenic backgrounds, especially the  $^{11}\text{C}$  backgrounds induced by the muon spallation on the liquid scintillators[98].

For a fitter, its performance is first tested on the Monte Carlo simulations of specific physics processes. Then it is tested on both the simulations and real data of the calibration runs. Once the algorithm gives proper results which are approved by the collaboration, it is implemented into the SNO+ RAT software to process the SNO+ simulations and data files.

For a specific SNO+ physics phase, the fitters for different physics quantities of an event are integrated together. Currently, there are three integrated fitters: the **Water Fitter** for the water phase, the **Partial Fitter** for the partial-fill phase and the **Scint Fitter** for the scintillator phase and the tellurium loading phase. The fitter parameters, such as the input optical parameters, fitter iterations, are coordinated and optimized based on simulations and calibration data from that specific physics phase.

PMT selectors and classifiers are also wrapped into the integrated fitters. The PMT selectors are used to remove the outliers of the hit PMTs for a specific fitter, such as the hit PMT probably triggered by the noises. These selectors can help to make the fitter more accurate or to boost up the algorithm speed of the fitter. The classifiers mainly use the reconstructed results to calculate some specific quantities which describe the probability of an event being a specific signal or background.

In this chapter, a Multi-path (MP) reconstruction framework is discussed. It was developed by the University of Alberta group as an additional fitter to provide event vertex and direction reconstructions. In this framework, the fitters are able to be adapted for all the SNO+ physics phases by switching light path calculations as well as the input optical parameters, that is the reason why it is called "multiple paths". It was applied in the water phase to provide alternative information of the event position and direction; it also works as the vertex reconstruction algorithm for the **Partial Fitter**. After re-coordination to the scintillator phase and tellurium loading phase, I also show the potentials of the vertex fitter being applied in these two future phases.

Besides, potentials of extracting the directional information from the scintillator phase is discussed.

## 4.2 Multi-path Reconstruction Algorithm for SNO+

In the SNO+ water phase, the cavity and the AV are both filled with ultra-pure water. This is a relatively simple geometry since everything inside the PSUP can be simplified as water. Therefore, I will start with the MP water fitter (the MPW fitter) to explain the

reconstruction concepts.

The MPW fitter fits for position, time and direction of a triggered event in SNO+ water phase. First, the fitter throws a random position built up by random variables which are uniformly distributed inside a sphere with a radius of 10 *meters* (larger than the actual PSUP radius  $r_{PSUP} = 8.39\text{ m}$ ). Meanwhile, a random event time is also generated, following a uniform distribution in a range of 100 to 300 *ns*. The Class Library for High Energy Physics (CLHEP) is used for creating pseudo-random numbers (see the Appendix A.1 for details). The random position and the random time are combined to form a random event vertex, which is set as the trial event vertex.

For a triggered event, photons are created around the event position and propagate to the PMTs. In a simplified situation neglecting reflection and refraction, these photons propagate along straight line. Connecting the trial event vertex to the hit PMTs, the fitter evaluates a timing parameter, called the time residual ( $t_{res}$ ), which is defined as:

$$t_{res} = t_{PMT} - t_{transit} - t_{event}, \quad (4.1)$$

where  $t_{PMT}$  is the PMT trigger time recorded by the detector,  $t_{event}$  is the time when an event occurs (event time), and  $t_{transit}$  is the total transit time (or time of flight, *TOF*) taken by a photon traveling from the event position ( $\vec{x}_{event}$ ) to the hit PMT ( $\vec{x}_{PMT}$ ) and crossing different materials in the detector.

To calculate the  $t_{transit}$ , the fitter uses photons from prompt time window (prompt light) and assumes that photons propagate in straight lines (straight light paths). The simple straight light path calculation gives  $t_{transit} = |\vec{x}_{event} - \vec{x}_{PMT}|/v_{water}$ . Detailed calculations, such as refraction and reflection when the lights cross different detector materials, absorption and scattering from the materials, as well as the lensing effects caused by the spherical structure of the acrylic vessel, are neglected. It was found that without these details, the fitter can still produce decent results that are consistent with the ones using detailed calculations.

For a trial vertex  $(\vec{x}_0, t_0)$ , the fitter calculates a set of  $t_{res}$  values with respect to all the

hit PMTs. These values are fed into a likelihood function:

$$\ln \mathcal{L}(\vec{x}_0, t_0) = \sum_{i=1}^{\text{Nhits}} \ln P(t_{res}^i), \quad (4.2)$$

where  $t_{res}^i$  is the time residual calculated from the  $i^{th}$  hit PMT and Nhits here stands for the number of total hit PMTs by an event.

A pre-set 1-dimensional (1D) probability density function is used for fitting the model. The *pdf* was taken from the bench-top timing profile measurement as well as the measured detector response.

$P(t_{res}^i)$  is the probability returned from the *pdf* for the  $i^{th}$  hit PMT and a trial event vertex.

The Levenberg-Marquardt method, which is commonly used for fitting the nonlinear model for multiple parameters, is used as an optimizer to find the best fit event parameters (position, time and direction). Appendix A.2 describes this method; A.3 describes the implementation of the method to the MultiPath fitter framework. Also see [131, 132].

As will be shown in the following sections, one of the main tasks for the fitter is to calculate the  $t_{transit}$  by evaluating light paths. In the water phase, photons created in an event were considered as traveling along straight line paths and these paths are always in the water, i.e., the paths inside the AV or other detector components were not taken into account. In the other situations, for example, when the acrylic vessel is filled with the wavelength shifter or scintillator, the light path calculations will be modified.

Fig. 4.1 shows the reconstruction concepts for position and direction.

### 4.3 Multi-path Position and Direction Reconstructions for the Water Phase

#### 4.3.1 Vertex Reconstruction

For the position reconstruction of the MPW fitter, the likelihood function simply calculates the likelihood assuming straight line paths of prompt light from a position vertex  $\vec{X}_0$

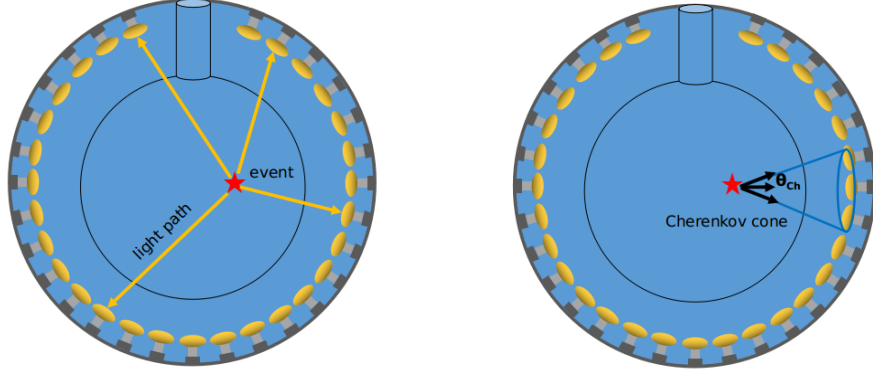


Figure 4.1: Diagrams of position (left) and direction (right) reconstruction in SNO+ water phase.

(fVertex) and a starting time offset  $t_0$  to each of the hit PMTs.

The position difference is defined as  $\vec{X}_{\text{diffCh}} = \vec{X}_0 - \vec{X}_{\text{pmt}}$ . Then the time of flight for prompt light is  $t_{\text{Ch}} = |\vec{X}_{\text{diffCh}}|/v_g$  and  $L_{\text{Ch}} = L(t_{\text{Ch}})$ .

The derivatives of the likelihood function can be calculated from explicit mathematical forms as:

$$\frac{\partial L}{\partial t_0} = \frac{dL_{\text{Ch}}}{dt_{\text{Ch}}},$$

$$\frac{\partial L}{\partial x} = \frac{\partial L_{\text{Ch}}}{\partial t_{\text{Ch}}} \frac{dt_{\text{Ch}}}{dx} = -\frac{dL_{\text{Ch}}}{dt_{\text{Ch}}} \frac{X_{\text{diffCh}}}{|\vec{X}_{\text{diffCh}}| \cdot v_g},$$

$$\frac{\partial L}{\partial y} = -\frac{dL_{\text{Ch}}}{dt_{\text{Ch}}} \frac{Y_{\text{diffCh}}}{|\vec{X}_{\text{diffCh}}| \cdot v_g},$$

$$\frac{\partial L}{\partial z} = -\frac{dL_{\text{Ch}}}{dt_{\text{Ch}}} \frac{Z_{\text{diffCh}}}{|\vec{X}_{\text{diffCh}}| \cdot v_g},$$

where  $\frac{dL_{\text{Ch}}}{dt_{\text{Ch}}}$  can be calculated numerically from the timing *pdf*.

In the WaterPosition class, it starts with a random  $(\vec{x}_0, t_0)$  as seed and calculates the likelihoods and their derivatives for various paths. These values are sent to the Multi-path Fitter, which is fitting 4 parameters:  $x, y, z, t$  and to maximize the likelihood function through the MRQ method and to find the best-fit positions.

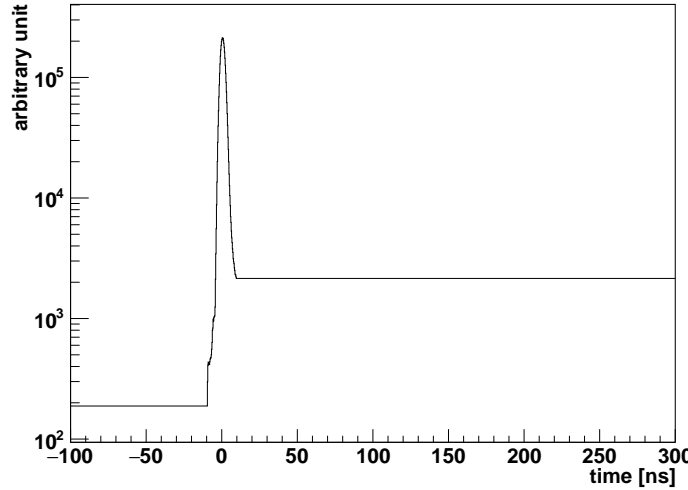


Figure 4.2: PMT response time as the timing *pdf* for vertex reconstruction.

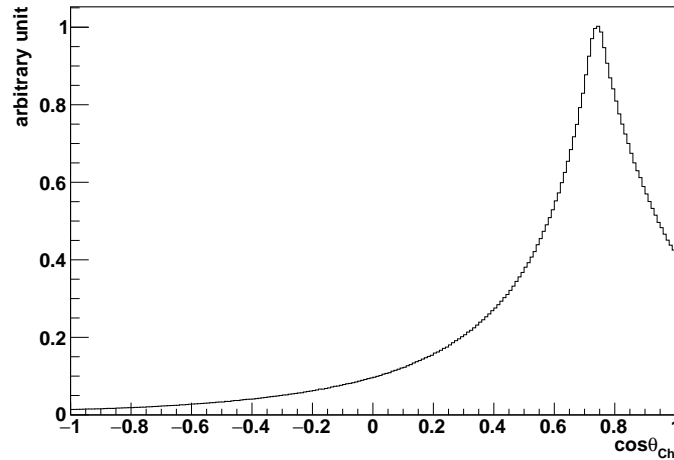


Figure 4.3: PMT angular distribution as the angular response *pdf* for direction reconstruction.

### 4.3.2 Direction Reconstruction

$\vec{u}_0 = (\cos \phi \sin \theta, \sin \phi \sin \theta, \cos \theta)$  (fDirection), where the  $\theta$  is zenith angle and  $\phi$  the azimuth.  $\cos \theta_{\text{Ch}}$  is the angle between  $\vec{u}_0$  and  $\vec{X}_{\text{diffCh}}$ , which is taken as the fitting parameter of the likelihood function for the direction reconstruction. For the  $i$ -th hit PMT,  $\cos \theta_{\text{Ch}}^i =$

$\vec{u}_0 \cdot \frac{\vec{X}_{\text{diffCh}}^i}{|\vec{X}_{\text{diffCh}}^i|}$ , then the likelihood function is:

$$L(\vec{u}_0) = \sum_{i=1}^{\text{Nhits}} L_i(\cos \theta_{\text{Ch}}^i),$$

The derivatives have explicit mathematical forms:

$$\frac{\partial L}{\partial \theta} = \frac{dL_{\text{Ch}}}{d \cos \theta_{\text{Ch}}} \frac{d \cos \theta_{\text{Ch}}}{d \theta} = \frac{dL_{\text{Ch}}}{d \cos \theta_{\text{Ch}}} \frac{d \vec{u}_0}{d \theta} \cdot \frac{\vec{X}_{\text{diffCh}}}{|\vec{X}_{\text{diffCh}}|},$$

where  $d \vec{u}_0 / d \theta = (\cos \phi \cos \theta, \sin \phi \cos \theta, -\sin \theta)$  and

$$\frac{\partial L}{\partial \phi} = \frac{dL_{\text{Ch}}}{d \cos \theta_{\text{Ch}}} \frac{d \cos \theta_{\text{Ch}}}{d \phi} = \frac{dL_{\text{Ch}}}{d \cos \theta_{\text{Ch}}} \frac{d \vec{u}_0}{d \phi} \cdot \frac{\vec{X}_{\text{diffCh}}}{|\vec{X}_{\text{diffCh}}|},$$

where  $d \vec{u}_0 / d \phi = (-\sin \phi \sin \theta, \cos \phi \sin \theta, 0)$ .  $\frac{dL_{\text{Ch}}}{d \cos \theta_{\text{Ch}}}$  can be calculated numerically from the PMT angular response pdf.

In the FitterWaterDirection class, it starts with a random  $(\theta_0, \phi_0)$  as seed and calculates the likelihoods and their derivatives for various paths. These values are sent to the Multi-path Fitter, which is now fitting 2 parameters:  $(\theta, \phi)$  and to maximize the likelihood function through the MRQ method and to find the best-fit directions.

### 4.3.3 Effective Group Velocity

When photons travel through the detector, their group velocities change with different refractive indices of different detector materials. The group velocities also depend on the wavelengths of the photons as  $v_g = c/n(\lambda)$ . Fig .4.4 shows the measured refractive indices as a function of wavelength, obtained from the measurements of laserball scans in the SNO+ water phase[13]. Furthermore, the group velocities can change when these photons are scattered, absorbed, refracted and reflected. To simplify these complicated situations for the reconstruction, an averaged value of the group velocity is used in the straight line light path calculation. This fixed group velocity is considered as an effective value.

A reasonable selection of this value is required, since the value can introduce biases in the fitted position. This kind of bias is mainly due to a “complementary” effect of the fitter. As mentioned in section 4.2, the water vertex fitter calculates the  $t_{\text{transit}}$  by evaluating

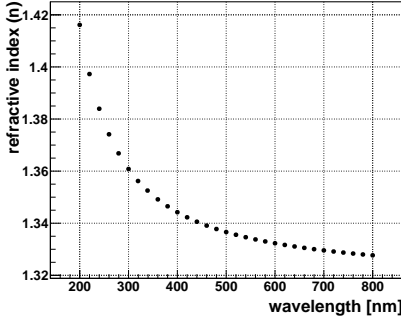


Figure 4.4: Refractive index vs wavelength. These values are based on the measurements from laserball calibration scans in the SNO+ water phase[13].

the distances from the trial vertex to the hit PMTs:  $t_{transit} = |\vec{x}_{event} - \vec{x}_{PMT}|/v_{water}$ . If the value of the group velocity  $v_{water}$  is set large (or fast speed), the value of  $t_{transit}$  will decrease, and the corresponding value of  $t_{res}$  will increase according to the definition of  $t_{res}$ (4.1). These calculated  $t_{res}$  value is compared to the time pdf for the fitting. If  $t_{res}$  is larger than the expected value, the fitter will place the trial vertex away from the hit PMTs to increase the  $t_{transit}$  and then decrease the  $t_{res}$ , as illustrated in Fig. 4.5. On the other hand, if  $v_{water}$  is set small (or slow speed),  $t_{transit}$  increases and  $t_{res}$  decreases, and the fitter will place the trial vertex closer towards the hit PMTs. Therefore, an overestimated group velocity (too fast) brings a positive radial bias to the true event position while an underestimated one (too slow) brings a negative radial bias.

In practice, the effective group velocity is tuned by an effective refractive index  $n_{eff}$  (or called *RI* value):  $v_{water} = c/n_{eff}$ . To select a reasonable effective group velocity for the water-phase vertex fitter, my first approach is to test on all the values of the refractive index provided by the SNO+ laserball measurements. The values are listed in Fig. 4.4.

I choose the one which gives the smallest radial bias based on MC simulations. For typical 5 MeV  $e^-$  events simulated uniformly inside the AV and isotropic momentum,

As shown in Fig. ??,  $n_{eff} = 1.40$  gives the smallest radial bias and is adopt for the MC case.

Later I turned to a more data-driven approach rather than just tuning from the simula-

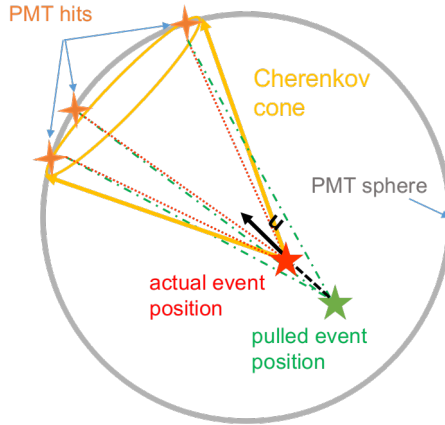


Figure 4.5: A cartoon shows effects of tuning the effective group velocity. In this case, the effective group velocity is faster than expected, the fitted position is dragged back along the direction to increase the time of flight.

tions. This approach is to extract an average group velocity by analyzing the  $^{16}\text{N}$  calibration source data.

as shown in Fig. 4.6.

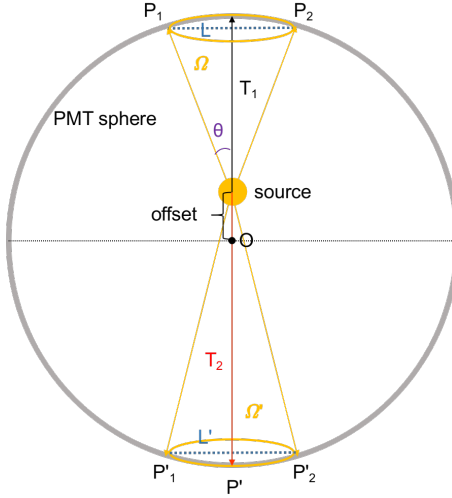


Figure 4.6:  $^{16}\text{N}$  central run.

For a more precise approach, a set of laserball calibration runs which to measure actual group velocities in the SNO+ water detector[133].

For the scintillator and partial-fill phase vertex fitters, I adopt a linear interpolation method described in [134], which will be discussed in section 4.5.

#### 4.3.4 Fitter Pull and Drive Correction

An effect of “fitter pull” in the event vertex reconstruction utilizing the Cherenkov light was observed in the SNO experiment. The distribution of  $(\vec{x}_{fit} - \vec{x}_{mc}) / |\vec{x}_{fit} - \vec{x}_{mc}| \cdot \vec{u}$  shows a large peak at +1, which indicates that the fitted position  $\vec{x}$  is prone to be pulled forward from the true position systematically along the event direction  $\vec{u}$ [15, 14, 134].

In the SNO+ water detection medium (or the SNO heavy water), Cherenkov photons created by an event trigger most of the PMT-hits with early timing and these hits are located within the Cherenkov cone; for the same event, there are also a few PMT-hits with later timing. These PMT hits can be caused by the scattered or reflected photons and they are located throughout the detector. For a random PMT hit, it is more probable to be placed outside the Cherenkov cone due to the geometry: consider an event happens at the center of the PSUP, the Cherenkov cone it produced will intersect the PSUP by an area of  $2\pi R_{PSUP}^2(1 - \cos 41^\circ)$ , which occupies about 12% of the total area of the PSUP sphere. Therefore, for a random PMT-hit on the PSUP sphere, it has more than 88% of chance to be placed outside the Cherenkov cone.

For these later timing PMT hits, a similar “complementary” effect mentioned in 4.3.3 can also happen. When the fitter fits with  $t_{res}$ , for the large  $t_{res}$  values caused by the later timing hits, it pulls the trial position away from the later timing hits to increase  $t_{transit}$  and decrease  $t_{res}$ , as illustrated in Fig. 4.7. This effect was also explained as “straighten out delayed photons” by the timing fitter in [15]. Furthermore, the major early hits can also cause small  $t_{res}$  values and thus the fitter pulls the trial position closer towards the early hits to decrease  $t_{transit}$  and increase  $t_{res}$ . Recall that the early hits are located on or around the Cherenkov cone, therefore an overall effect of this “fitter pull” is that the fitted position will be pulled along the axis of the Cherenkov cone and towards the PSUP sphere. This pull direction is coincident with the event direction.

A simple way to eliminate this “fitter pull” effect is to pull back the fitted event position against the event direction. This is called “drive correction”.

Once the MPW fitter obtains both of the fitted position and direction, the drive correc-

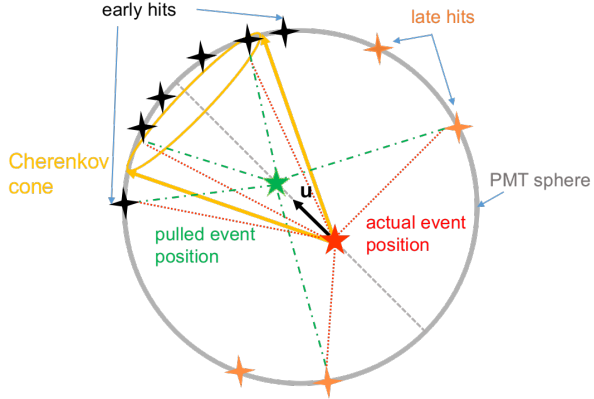


Figure 4.7: A cartoon shows fitter pull effect, modified from Fig. C.2 in [14] and Fig. 2,3,4 in [15].

tion is applied on the fitted position by  $\vec{X}_{\text{corrected}} = p_0 \vec{X}_{\text{fit}} + p_1 \vec{u}_{\text{fit}}$ , where  $p_0$  and  $p_1$  are the correction parameters, as shown in Fig. 4.8.

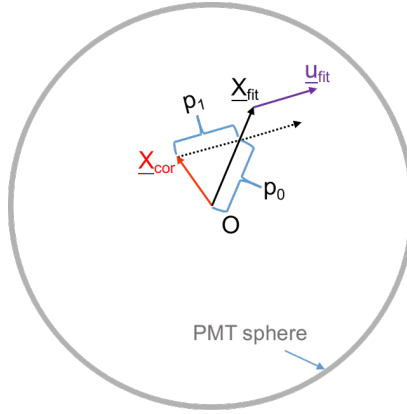


Figure 4.8: A diagram illustrates the drive correction.

To obtain the values of  $p_0$  and  $p_1$ , I generated electron events distributed isotropically inside the AV. The simulations of 2, 3, 4, ..., 10 MeV electrons are produced. Then the MPW fitter is applied on each simulations and returns the results of  $\vec{X}_{\text{fit}}$  and  $\vec{u}_{\text{fit}}$ . Take the Monte Carlo generated positions  $\vec{X}_{MC}$  as the true positions, for all the fitted events, a  $\chi^2$  function is calculated by:

$$\chi^2 = \sum_{i=1}^{N_{\text{events}}} [\vec{X}_{MC}^i - (p_0 \vec{X}_{\text{fit}}^i + p_1 \vec{u}_{\text{fit}}^i)]^2$$

The  $p_0$  and  $p_1$  are obtained by minimizing the  $\chi^2$  function. When calculating the  $\chi^2$ ,

the fitted events of  $|\vec{X}_{fit} - \vec{X}_{MC}| > 3\text{ m}$  are thrown away to improve the  $\chi^2$  minimization results.

For the 2 to 10 MeV electrons simulations, the obtained values of  $p_0$  and  $p_1$  are energy or Nhit dependent. However, it does not improve the results if using the Nhit dependent functions  $p_0(Nhit)$  and  $p_1(Nhit)$  as drive corrections. Finally we take the average values from the 5 to 10 MeV electrons simulations and the drive correction is set as  $\vec{X}_{corrected} = 0.995765\vec{X}_{fit} + -63.826\vec{u}_{fit}$ .

It is important to note that since the drive correction parameters are obtained from the reconstructions of Monte Carlo, it depends on the Monte Carlo and the results of reconstruction. Therefore, the  $n_{water}$ , mode cut and time residue cut affecting the fitted results will also affect the drive correction parameters, but not significantly.

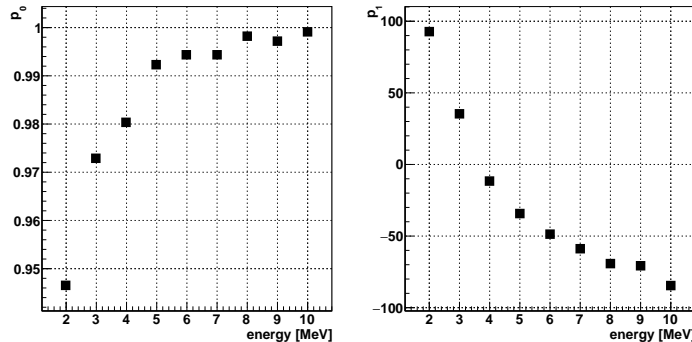


Figure 4.9: Drive correction parameter  $p_0$ ,  $p_1$  vs energy.

Electron events with various energies were generated at the detector center and their momentum were along +x direction.

By fitting the simulations of 5 MeV electrons generated at the detector center and travelling along +x direction, the drive effect of the MPW fitter causes a  $\sim 50$  mm biases from the detector center along +x axis. The drive correction reduces this drive bias down to  $\sim 0.2$  mm. For the reconstruction of  $^{16}\text{N}$  data, the drive correction can reduce the fitted position RMS by  $\sim 20$  mm.

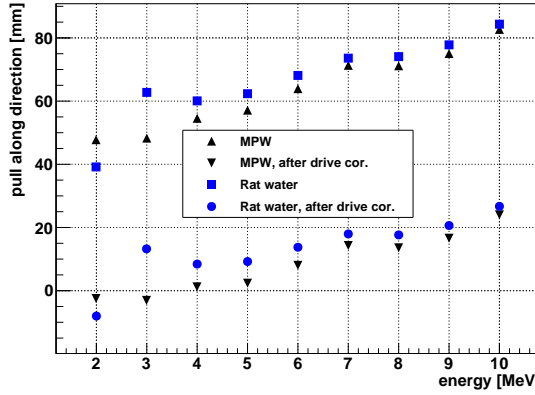


Figure 4.10: Radial biases of simulated electron events before and after the drive correction, as a function of energy.

#### 4.3.5 Multi-path Fitter Structure

The Multi-path fitter has already been implemented into the RAT software and being used in data processing and analyzing.

The MP fitter structure consists of:

- Fitter database

This database provides parameters used by the fitter, including the physics constants, detector geometry parameters, fit parameters and pdfs. The database is in a JSON format[135] and contains multiple tables tagged by indices to indicate different detection media or physics phases. In each table, there are fit parameters and pdfs optimized for the specific scintillator. For example, for the partial-fill phase with a PPO concentration of 0.5 g/L, the fitter will look for the index of “labppo\_0p5\_scintillator” and extract the pdfs and fit parameters under that index.

The fit parameters includes the fitter tolerance and the maximum iterations which determine how the fitter converges,

Reflective index (water\_RI, or  $n_{water}$ ), used for effective group velocity ( $v_g = c/n_{water}$ ) calculation. air refractive index (air\_RI), PSUP radius ( $r_{PSUP} = 8390\text{ mm}$ ). Offsets boundary settings

The MPW fitter currently uses one fixed number for  $n_{water}$ , rather than a function of wavelengths. The value of  $n_{water}$  can be tuned to give the lowest biases of the fitted positions to the Monte Carlo and to give the lowest RMS of fitted results as well. But the effect of  $n_{water}$  can also be corrected by the drive correction afterwards. Currently  $n_{water} = 1.38486$  is obtained by analyzing the time of flight from the  $^{16}\text{N}$  central run-100934 data reconstructed by the MPW fitter.

time offset, position offset, radius cut x, fitting bin-width and steps.

- PMT response time (timing) pdf for the position reconstruction, as shown in Fig. 4.2. The pdf shown in red line is modified from the measured PMT response time distribution from SNO time and the late light response is forced to be de-weighted (black). The pdf is modified in [-100,-4] ns region to match the time residual spectrum obtained from  $^{16}\text{N}$  central run-100934 (blue).

- PMT angular response pdf for the direction reconstruction, as shown in Fig. 4.3. It is taken from the Monte Carlo simulation of 5 MeV electrons traverse in the AV with one direction.

- Likelihood Calculation Classes, Constructs likelihood functions, calculates likelihoods and their derivatives. For the MPW fitter, there are two classes: `WaterPosition` for position reconstruction and `WaterDirection` for direction reconstruction. The `WaterPosition` class tackles with 4 parameters ( $x,y,z,t$ ) and the `WaterDirection` class tackles with 2 parameters ( $\theta,\phi$ ).
- Multi-path Fitter

Processes the MPW fitter and finds the best-fit of the likelihood function. It is a general processor and is shared with the fitters using the Multi-path Fitter, including the MPW fitter, air-water (AW) fitter, wavelength-shifter (WLS) fitter and scint-water fitter. It processes a certain fitter by being assigned the fitter name in macro. It processes the fitter event by event: for every triggered event, it first calls PMT selectors (ModeCut or StraightTimeResidualCut) and sends the information of the reduced

PMTs to a certain Likelihood Calculation Class for likelihood calculations. The Likelihood Calculation Class sends back the values of likelihoods and their derivatives, so the Multi-path Fitter does not care about how the likelihood functions are constructed and how the likelihoods and derivatives are calculated. Using these values, it constructs an  $n \times n$  Hessian matrix ( $n$  is the number of fitting parameters defined in Likelihood Calculation Class) and uses the Levenberg-Marquardt (MRQ) method to maximize the likelihood and finds the best-fit values. For the MPW, if the likelihood maxima is found 5 times for any position and direction then values are returned as the fitted position and direction. For the MPW case, it calls the `ModeCut` and fits for the position and time; then it calls the `StraightTimeResidualCut` and fits for the directions.

- **Dump Likelihood**

This is a function inside the Multi-path Fitter. It stores the likelihood surfaces and derivatives with respect to arrays of trial vertices of the interested events which are designated by event GTIDs in the database. From the likelihood surfaces and derivatives of an interested event, people can evaluate the fit performance of that event by checking whether the fitter finds global or local maximum.

- **SDecompQRH**

This is a fit method class modified from ROOT `TDecompQRH` class[136]. It is used by the Multi-path fitter to invert the Hessian matrix through QR decomposition method[132]. Compared to ROOT, `Solve()` for  $Ax=b$  is modified to zero the component of  $x$  for which the diagonal element in  $R$  is small. This allows a Levenberg-Marquardt optimization to continue in many cases when the matrix is singular. For the MPW case, it is used to invert a  $4 \times 4$  matrix of the WaterPosition Class while the inversion of  $2 \times 2$  matrix of the WaterDirection is calculated directly[137].

- **PMT selectors**

Detailed descriptions are shown in section 4.6.

## 4.4 Vertex and Direction Reconstruction for the Water-based Wavelength-shifter

A reconstruction algorithm was developed to investigate the proposal for the water-based wavelength-shifter, as mentioned in 3.3.3.1.

Figure 4.11 shows the position distributions of hit PMTs for MC simulated 5 MeV electrons travelling along  $+x$  direction in the AV. The left panel shows the case when the detector is filled with pure water while the right panel is for water plus 0.1 ppm PPO. For the same electrons, the number of hit PMTs ( $N_{Hit}$ ) in wbWLS is about 2.4 times greater than the pure water one. Although there is extra isotropic light emitted, the Cherenkov ring can still be seen clearly, allowing reconstruction of the directionality.

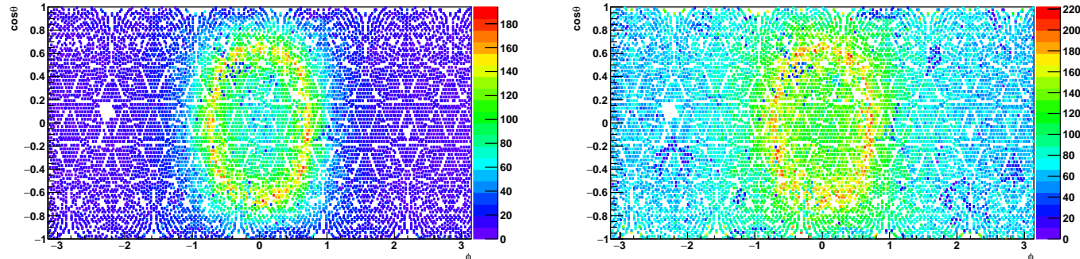


Figure 4.11: Position distributions of hit PMTs (in zenith and azimuth angles) for 5 MeV electrons travelling along  $+x$  direction in the pure water (left) and the water plus 0.1 ppm PPO (right).

Figure 4.12 shows the energies of simulated electrons as a function of the mean value of the  $N_{Hit}$  distribution (mean nhits). In pure water, a 1 MeV electron simulation does not trigger any PMTs while in wbWLS case we have a mean nhits of 20.

In the wbWLS case, since WLS absorbs and re-emits photons, the reconstruction mentioned in section 4.2 is slightly modified to build the MP WLS Fitter. According to the optical property of PPO, the prompt light emitted from an event has a probability of  $\sim 0.6$  to be absorbed by the WLS and then re-emitted at a shifted vertex along the particle direction  $\hat{n}$ . Then the fitter returns a shifted vertex,  $\vec{X}_{0,shifted} = \vec{X}_0 + \text{offset} \cdot \hat{n}$ . The offset we set in the fitter is 100 mm obtained from simulations. Figure 4.13 shows the timing pdf

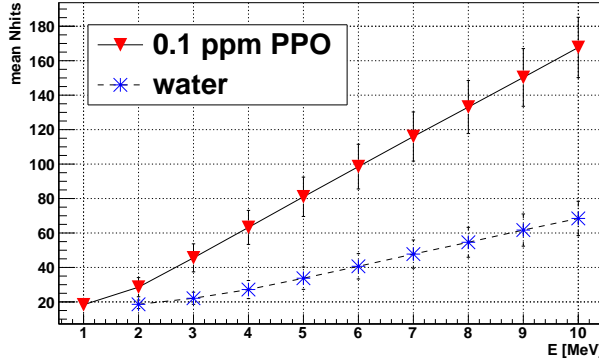


Figure 4.12: The energies of simulated electrons as a function of mean nhits. The values in the 0.1 ppm PPO (solid line with inverted triangle) are compared with the water (dashed line with star).

for the wbWLS, which is the PMT response time modified to photon propagation time in the wbWLS.

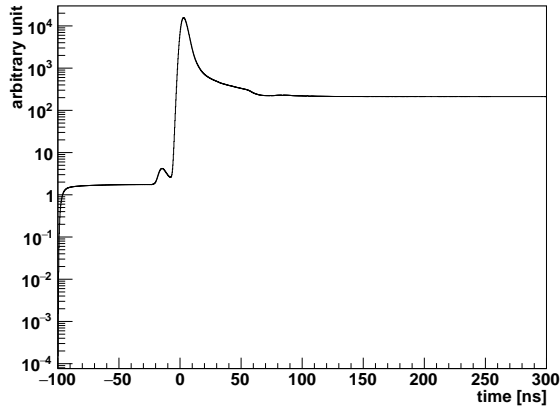


Figure 4.13: The timing pdf for the wbWLS.

To reconstruct the direction, besides the angular distribution of Cherenkov photons,  $\cos \theta_{Ch}$ , we also consider the fraction of the re-emitted and wavelength shifted photons that cause a flat angular distribution.

To test the performance of the MP WLS Fitter, 5 MeV electrons were simulated at the center of the AV filled with wbWLS and travelling along +x direction. As a comparison, the same simulation was done for the AV filled with pure water and the simulated events

were reconstructed by the water fitter.

Fig. 4.14 shows the performance of the WLS fitter reconstructed positions of the MC simulations compared to the pure water case. For the fit position distribution of 5 MeV electrons in the wbWLS, we get a root mean square (RMS) of 201 mm and a bias to the center (the mean of histogram) of 29 mm. Compared to the pure water case, the fit bias is about 19 mm better and the RMS is 188 mm better.

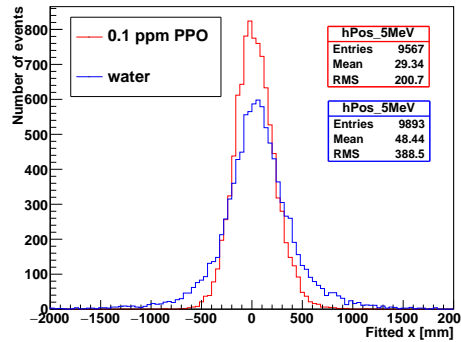


Figure 4.14: Fit position projected on x axis. The WLS fitter reconstructed  $x$  positions of the 5 MeV electron events in the wbWLS (red) are compared to the ones in the water (blue).

For a given Cherenkov event, the error in the reconstructed event direction is defined as[138]:  $\cos(\theta_e) = \vec{u}_{fit} \cdot \vec{u}_e$ , where  $\vec{u}_e$  is the simulated electron direction and  $\vec{u}_{fit}$  is the reconstructed direction. To quantify this error, we define a  $\cos \theta_a$  so that:

$$\frac{\int_{\cos \theta_a}^1 P(\cos \theta_e) d \cos \theta_e}{\int_0^1 P(\cos \theta_e) d \cos \theta_e} = a.$$

where  $P(\cos \theta_e)$  is the distribution of  $\cos \theta_e$  from MC data. The value of  $\cos \theta_a$  is found numerically to let  $\cos \theta_e$  contain  $a \cdot 100\%$  of the reconstructed data. A larger  $\cos \theta_a$  means better direction reconstruction.

Table 4.1 shows the results of  $\cos \theta_a$  for SNO heavy water data[138] and simulations for SNO+ pure water and wbWLS.

Comparing a pure water SNO+ detector and the wbWLS one, using the MP WLS Fitter for physics events gives a better position resolution without a significant loss in the performance of the direction reconstruction.

Table 4.1: A comparison of quantitative estimates for the angular resolution between the SNO heavy water, SNO+ wbWLS and the SNO+ pure water cases.

| medium          | $\cos \theta_{0.9}$ | $\cos \theta_{0.8}$ | $\cos \theta_{0.5}$ |
|-----------------|---------------------|---------------------|---------------------|
| SNO heavy water | 0.50                | 0.71                | 0.92                |
| SNO+ water      | 0.53                | 0.76                | 0.93                |
| wbWLS           | 0.37                | 0.63                | 0.90                |

This fitter was tested for in [139].

## 4.5 Vertex Reconstruction for the Partial-fill and Scintillator Phases

In the partial fill geometry, photons will travel with different speeds as they pass through two different mediums, water and scintillator. Assuming a straight light path, the MP Partial Fitter mainly calculates the total length of the light path ( $|\vec{l}_p| = |\vec{X}_{\text{PMT}} - \vec{X}_0|$ ) and separates the  $|\vec{l}_p|$  into the lengths in scintillator ( $d_{sp}$ ) and in water ( $|\vec{l}_p| - d_{sp}$ ).

In the partial-fill phase, the SNO+ detector can be considered as a geometry composed of the neck (cylinder), AV sphere and water-scintillator interface (plane). A ray connecting a position inside the PSUP to the PMT can intersect with these three geometries. As illustrated in Fig. 4.15, a detailed calculation of  $d_{sp}$  includes evaluations of (1) light path and neck (ray-cylinder) intersection; (2) light path and AV sphere (ray-sphere) intersection and (3) light path and water-scintillator interface (ray-plane) intersection.  $d_{sp}$  is further separated into the path length in the neck ( $d_{sp,neck}$ ) and in the AV ( $d_{sp,AV}$ ).

For a trial position  $\vec{X}_0 = (x_0, y_0, z_0)$  and a hit PMT position  $\vec{X}_{\text{pmt}} = (x_{\text{pmt}}, y_{\text{pmt}}, z_{\text{pmt}})$ , define a light ray (rather than a line without direction)  $\vec{l}_0 \equiv \vec{X}_0 + a \cdot \vec{u}$ , where  $a$  is the distance between vertex and intersection point and it is the parameter to be determined;  $\vec{u} = \frac{\vec{X}_{\text{pmt}} - \vec{X}_0}{|\vec{X}_{\text{pmt}} - \vec{X}_0|}$  is the direction of the light ray. It is a unit vector pointing from the  $\vec{X}_0$  to the  $\vec{X}_{\text{pmt}}$ .

In the ray-sphere intersection case (light ray passes through the AV sphere), the intersection points on the  $\vec{l}_0$  satisfy the sphere equation  $(\vec{X} - \vec{O}_{av})^2 = r_{av}^2$ , where  $\vec{O}_{av}$  is the origin

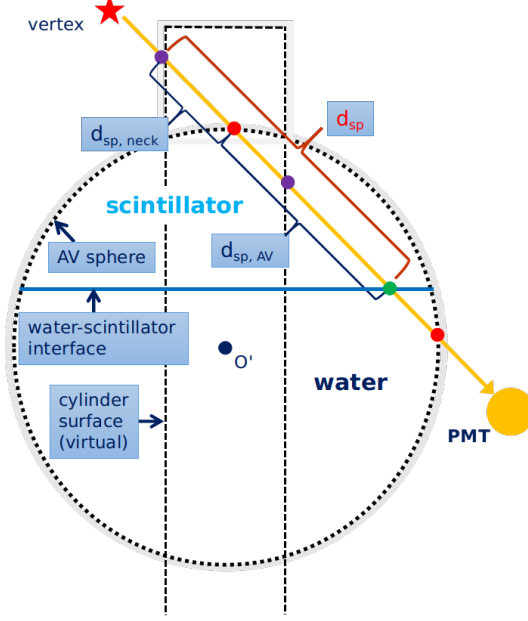


Figure 4.15: Light path calculation for the MP Partial Fitter. The light path intersects with the neck cylinder surface, the AV sphere as well as the water-scintillator interface. The total length of the path in the scintillator region (scintillator path, sp),  $d_{sp}$  is evaluated by intersection calculations.

of the AV sphere and  $\vec{O}_{av} = (0, 0, 108) \text{ mm}$  in the PSUP coordinate. Thus the intersection equation is:  $(\vec{l}_0 - \vec{O}_{av})^2 = r_{av}^2$ .

Let  $\Delta \equiv [(\vec{X}_0 - \vec{O}_{av}) \cdot \vec{u}]^2 - (\vec{X}_0 - \vec{O}_{av})^2 + r_{av}^2$ , if  $\Delta > 0$ , solve the equation and get:

$$a_{+,-} = -(\vec{X}_0 - \vec{O}_{av}) \cdot \vec{u} \pm \sqrt{\Delta}, \text{ if } \Delta > 0. \quad (4.3)$$

In this case, both  $a_+$  and  $a_-$  exist and have different values. If  $a_+ > a_- > 0$ , the length of the path inside the sphere is  $a_+ - a_-$ , as illustrated in Fig. 4.16 (a). Due to this geometry, the event position should be outside the AV, the condition  $|\vec{X}_0| \geq r_{AV}$  is automatically met. If  $a_+ > 0 > a_-$ ,  $a_-$  determines the intersection point along the opposite direction of the light ray. Thus the light ray actually does not pass that point (different to the line intersection with no direction). Thus the length of the path inside the sphere is  $a_+$ , as illustrated in Fig. 4.16 (b). Also, the condition  $|\vec{X}_0| < r_{AV}$  is automatically met.

If  $\Delta \leq 0$ , there is no intersection point or only one intersection point at the AV, the light ray never passes through the AV sphere, as illustrated in Fig. 4.16 (c) and (d).

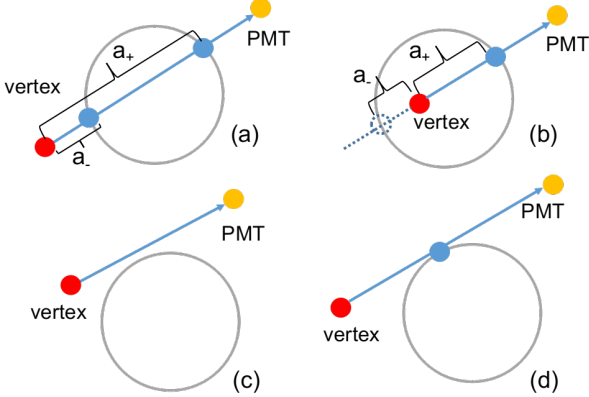


Figure 4.16: Line-sphere intersections. (a): the light ray intersects the sphere with 2 points; (b): the light ray intersects the sphere with 1 point; (c) and (d): the light ray never passes through the sphere.

For the ray-plane intersection, the z components of the intersection points on  $\vec{l}_0$  satisfy the plane equation  $z = Z_{split}$ , where  $Z_{split}$  is the water level, i.e., the z position of the water-scintillator intersection. Thus the intersection equation is:  $l_{0,z} = Z_{split}$ , where  $l_{0,z} = z_0 + a \cdot u_z$ .

If  $u_z = z_{pmt} - z_0 = 0$ , the ray is parallel to the plane and never intersects the plane.

If  $u_z \neq 0$ , solve the equation, we have:  $a = (Z_{split} - z_0)/u_z = (Z_{split} - z_0)$ . Let:

$$a_3 \equiv a = \frac{(Z_{split} - z_0)|\vec{X}_{pmt} - \vec{X}_0|}{z_{pmt} - z_0} \quad (\text{if } z_{pmt} - z_0 \neq 0).$$

Similar to the case of ray-sphere intersection, if  $a_3 < 0$ , the ray-plane intersection point is on the extended line along the opposite direction to the ray;  $a_3 \geq 0$  ensures the ray hits the interface. Note that here we consider the plane is infinitely large. Later we will combine with the calculations of the other geometries to cut it off.

For the ray-cylinder intersection, the x and y components of the intersection points on the  $\vec{l}_0$  satisfy the intersection equation:  $l_{0,x}^2 + l_{0,y}^2 = r_{neck}^2$ , where  $r_{neck}$  is the radius of the neck cylinder ( $r_{neck} = 785 \text{ mm}$ ).

To solve the equation, let:  $\Delta' \equiv [x_0 \cdot (x_{PMT} - x_0) + y_0 \cdot (y_{PMT} - y_0)]^2 - (x_0^2 + y_0^2 - r_{neck}^2) \cdot [(x_{PMT} - x_0)^2 + (y_{PMT} - y_0)^2]$ , and then we get:

$$a'_\pm = |\vec{X}_{PMT} - \vec{X}_0| \cdot \frac{-[x_0 \cdot (x_{PMT} - x_0) + y_0 \cdot (y_{PMT} - y_0)] \pm \sqrt{\Delta'}}{(x_{PMT} - x_0)^2 + (y_{PMT} - y_0)^2}, \quad \text{if } \Delta' > 0, \quad (4.4)$$

Similar to the ray-sphere case, if  $a'_+ > a'_- > 0$ , the length of the path inside the cylinder is  $a'_+ - a'_-$ . Due to this geometry, the event position should be outside the cylinder, the condition  $(x_0^2 + y_0^2 \geq r_{neck}^2)$  is automatically met. If  $a'_+ > 0 > a'_-$ , the event position should be inside the cylinder and the ray-vector intersects the cylinder with one point (while the other point is along the opposite direction). Thus the length of the path inside the cylinder is  $a'_+$ . If  $\Delta' \leq 0$ , the light ray never passes through the neck cylinder. Also note that here we consider the cylinder is infinitely long. This will also be cut off by the combined calculations of the other geometries. In addition, since only the neck region inside the PSUP is valid for the fitter, we should also ensure  $z < 8390\text{ mm}$  (in PSUP coordination).

To evaluate the length of the light ray (light path) in the scintillator region ( $d_{sp}$ ), the above three geometries needs to be combined carefully. The following two procedures go through all the possible situations. First combine the evaluations of the ray-sphere and the ray-plane intersections to calculate the light path in the AV scintillator region ( $d_{sp,AV}$ ). Then combine the evaluations of the ray-sphere and the ray-cylinder intersections to calculate the light path in the neck scintillator region ( $d_{sp,neck}$ ).

Since the valid fit requires the events inside the PSUP sphere, only the neck region inside the PSUP sphere (with  $6108 < z_{neck} < 8390\text{ mm}$ ) needs to be considered. The neck path calculation is allowed to be turned off. Detailed calculations are listed in A.3.

Once the total lengths of the light path in the scintillator region or the water region are calculated, the time of flight,  $t_{transit}$  is obtained by:

$$t_{transit} = \frac{|\vec{l}_p| - d_{sp}}{v_{gr,water}} + \frac{d_{sp}}{v_{gr,scint}}, \quad (4.5)$$

and thus the time residual,  $t_{res}$  is calculated.

If  $d_{sp} = 0$ , the light path is always in the water. In this case, the fitter is the same as the MP Water Fitter. The fitter fits with the MP Water Fitter pdf. Once the light path passes through the scintillator region, the fitter fits with a scintillator timing pdf, the PMT time response modified to photon propagation time in scintillator, as shown in Fig. 4.17.

The performance of the fitter was studied with MC simulations. In a partial fill geometry with water level at 4.435 m, 2.5 MeV electrons are simulated inside the AV in the scintillator

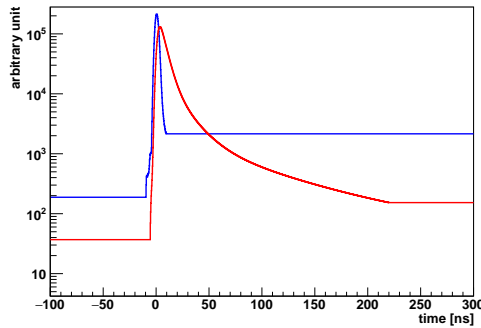


Figure 4.17: The timing pdfs used by the MP Partial Fitter. Blue: the timing pdf used by the MP Water Fitter; red: the scintillator timing pdf.

region only, the water region only and the whole AV region.

Fig. 4.18 and Fig. 4.19 show the MP Partial Fitter reconstructed results for these simulations. Fig. 4.18 shows the biases between the fit positions and MC positions, projected on the x axis. The distributions of position biases are fit with Gaussian functions. The values of Gaussian mean and sigma quantify the fit biases and resolutions. Table 4.2 lists these values.

Table 4.2: Reconstructed position biases and resolutions for simulated events in partial fill.

| regions of simulated events | bias (mm) | resolution (mm) |
|-----------------------------|-----------|-----------------|
| scintillator region         | -1.0      | 73.9            |
| water region                | -10.7     | 385.1           |
| full region                 | 6.9       | 331.72          |

For the events in water, the fit bias and resolution is comparable to the water phase results in Table 5.1. The events in the scintillator region have smaller fit bias and better resolution due to more hit PMTs in the reconstruction.

Fig. 4.19 shows the fitted  $\sqrt{x^2 + y^2}$  vs. fitted  $z$  positions. It shows that the fitter can distinguish different events in the water or scintillator region. The fitter gives reasonable results of the three different MC simulations.

pdfs for all timing 3.3.3.2.

Radial bias is defined as the difference between the fitted and true position, projected

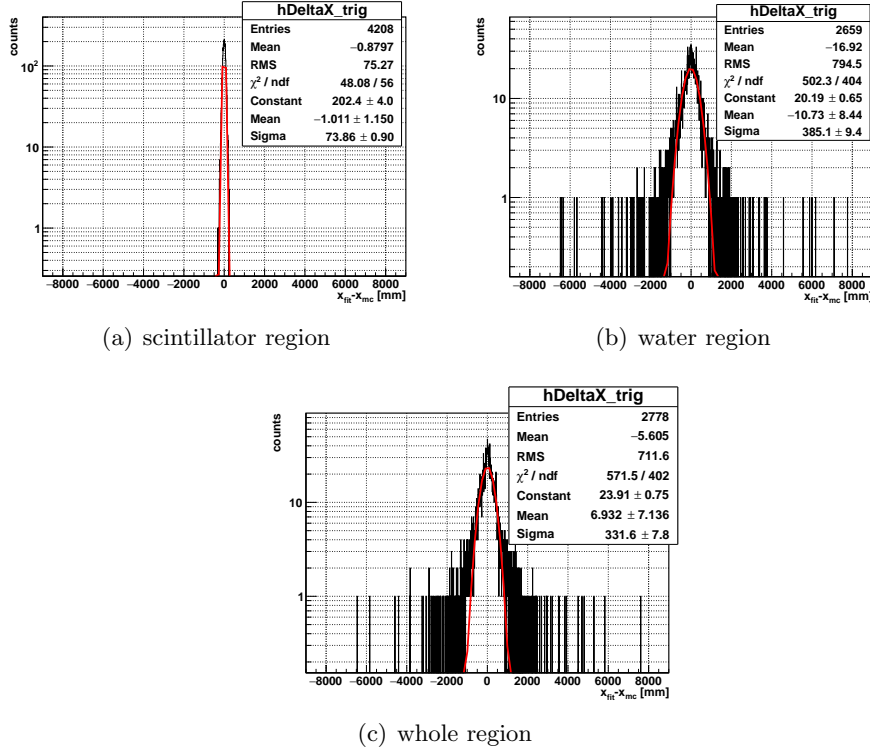


Figure 4.18: Distributions of fit position bias projected on x axis ( $x_{fit} - x_{MC}$ ).

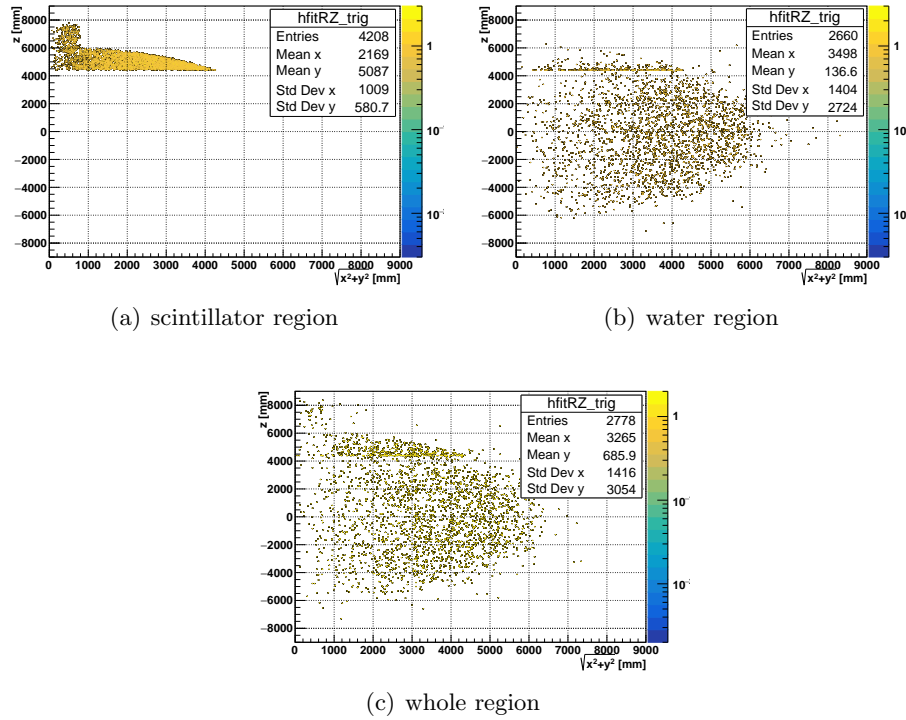


Figure 4.19: Fit results:  $\rho_{fit} = \sqrt{x_{fit}^2 + y_{fit}^2}$  vs.  $z_{fit}$ .

along the radial component (unit vector) of the true position [134].

$$(\vec{X}_{fit} - \vec{X}_{true}) \cdot \hat{X}_{true}$$

The value of the mean radial bias is taken by fitting the histogram of the distributions of radial biases with a Gaussian profile and then get the mean of the fitted Gaussian profile.

#### 4.5.1 Complicated Situations in Partial-fill

##### 4.5.1.1 Different PPO Concentrations during the Filling

During the partial-fill phase, the water level and the concentration of PPO were changing.

Oxford group in the SNO+ collaboration has done a few bench-top measurements for the time constants and relative light yields of LAB mixed with different concentrations of PPO[17].

The emission time profiles and relative light yields of PPO dissolved in LAB at the following concentrations: 0.25, 0.5, 1.0, 2.0 and 6.0 g/l.

The partial fitter is re-coordinated according to these measurements.

Table 4.3: time constants and amplitudes measured by Oxford group [17].

| PPO [g/L] | $\tau_{rise}$ [ns] | $\tau_1$ [ns] | $\tau_2$ [ns] | $\tau_3$ [ns] | $A_1$ [%] | $A_2$ [%] | $A_3$ [%] | $A'$ [%] |
|-----------|--------------------|---------------|---------------|---------------|-----------|-----------|-----------|----------|
| 0.25      | 1.25               | 8.1           | 25.0          | 68.2          | 29.2      | 53.1      | 13.9      | 3.8      |
| 0.5       | 1.12               | 7.2           | 18.7          | 49.1          | 43.5      | 40.4      | 12.6      | 3.5      |
| 1.0       | 1.18               | 5.5           | 13.3          | 40.9          | 45.6      | 37.5      | 13.3      | 3.6      |
| 2.0       | 1.06               | 4.2           | 11.7          | 48.9          | 57.9      | 27.8      | 8.9       | 5.4      |
| 6.0       | 0.94               | 2.5           | 9.3           | 46.0          | 63.7      | 17.0      | 8.6       | 10.7     |

$$\sum_{i=1}^3 \left( A_i \frac{e^{-\frac{t}{\tau_i}} - e^{-\frac{t}{\tau_{rise}}}}{\tau_i - \tau_{rise}} \right) + A' \frac{e^{-\frac{t}{\tau_{rise}}}}{\tau_{rise}}$$

based on these measured parameters, pdfs were built.

relative light yield (2g/L = 11900)

The partial fitter is invulnerable to the change of pdfs caused by different PPO concentrations.

Table 4.4: Relative light yield (RLY) measured by [17].

| PPO [g/L] | RLY  |
|-----------|------|
| 0.25      | 0.57 |
| 0.5       | 0.65 |
| 1.0       | 0.9  |
| 2.0       | 1.0  |
| 6.0       | 0.93 |

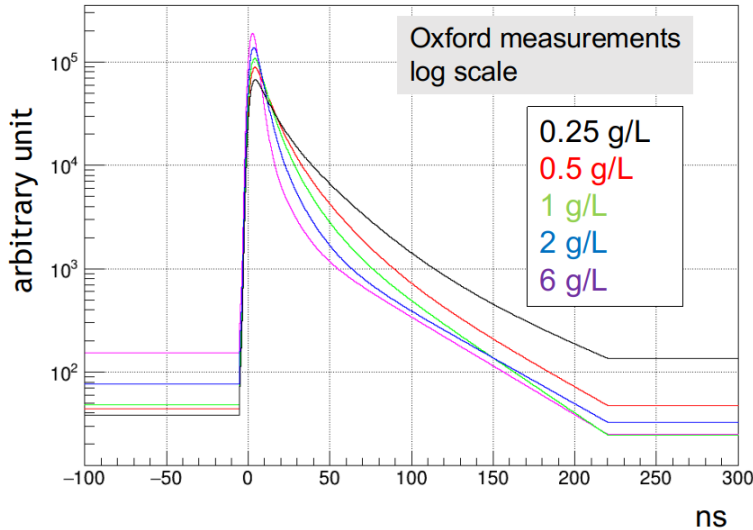


Figure 4.20: Timing spectrum for different PPO concentrations based on the Oxford bench-top measurements.

radial biases

Simulate 5000 events for 3 MeV  $e^-$ ,  $\Delta x = x_{fit} - x_{mc}$

$z_{fit}$  resolution [mm]

PPO in Fitter configuration fit with wrong PPO concentrations:

#### 4.5.2 Bi-Po Analysis

The Bi-Po analysis was performed on simulations to check the fitter efficiency. This analysis suggests a model offset of the water level to include more fitted data.

Table 4.5: Tuned effective group velocities for different PPO concentrations.

| PPO [g/L] | $V_{gr,scint}$ [mm/ns] | $n_{scint}$ | $V_{gr,water}$ [mm/ns] | $n_{water,tuned}$ |
|-----------|------------------------|-------------|------------------------|-------------------|
| 0.25      | 184.068±5.153          | 1.629       | 211.871±5.731          | 1.415             |
| 0.5       | 183.467±5.159          | 1.634       | 211.587±5.773          | 1.417             |
| 1.0       | 182.93±5.193           | 1.639       | 211.393±5.805          | 1.418             |
| 2.0       | 183.045±5.184          | 1.638       | 211.629±5.767          | 1.417             |
| 6.0       | 184.218±5.135          | 1.627       | 211.173±5.843          | 1.420             |

Table 4.6: Fit speeds and biases for various PPO concentrations.

| PPO [g/L] | fit speed [s/event] | $\Delta x$ [mm] | $\Delta y$ [mm] | $\Delta z$ [mm] | $r_{bias}$ [mm] |
|-----------|---------------------|-----------------|-----------------|-----------------|-----------------|
| 0.25      | 0.190               | 6.65            | 2.64            | -18.24          | -7.22           |
| 0.5       | 0.144               | -0.73           | -1.69           | -8.14           | 3.30            |
| 1.0       | 0.190               | 1.42            | 0.57            | -5.65           | 10.67           |
| 2.0       | 0.194               | 0.34            | 1.78            | -4.01           | 13.37           |
| 6.0       | 0.145               | -0.11           | -0.12           | -25.97          | -10.97          |

## 4.6 PMT Selectors for the Reconstruction

Several PMT selectors are used to select or remove PMTs from all the recorded PMTs triggered by an event and send the proper PMTs to the fitter for reconstruction. They are developed for optimizing the fitter or boosting up the fit speed:

- Straight Light Path Time Residual Cut Selector

This selector is used for the direction reconstruction for the SNO+ water phase. It is first developed by Singh for the MultiPath fitter. In the selector, the value of time residual ( $t_{res}$ ) is calculated for each hit PMTs from an event and the PMT with a  $t_{res}$  value in a prompt time window of  $[-10.0, 120.0]$  ns is selected for the fitter. The selector calculates  $t_{res}$  by using straight line light path, which is the same to the MultiPath water fitter. This can remove the PMTs triggered by photons with late timing, such as the photons reflected off the detector elements (late light) and keep the possible Cherenkov ring hit pattern clear for the direction fitter to fit. Also, dropping the irrelevant PMTs can potentially boost up the fit speed.

- Mode Cut Selector

Table 4.7: Fit speeds and biases for various PPO concentrations.

| PPO [g/L] | $\Delta x$ | $\Delta y$ | $\Delta z$ | $\sigma_z$ | $r_{bias}$ | $\sigma_r$ | ratio in FV (%) |
|-----------|------------|------------|------------|------------|------------|------------|-----------------|
| 0.25      | 6.80       | 2.90       | -14.61     | 121.6      | -4.82      | 120.3      | 93.70%          |
| 0.5       | 5.15       | 2.82       | -12.85     | 120.2      | 1.34       | 123.0      | 93.46%          |
| 1.0       | 2.32       | 1.95       | -13.22     | 120.3      | 0.344      | 121.9      | 93.78%          |
| 2.0       | 5.76       | 3.03       | -9.61      | 119.3      | 7.264      | 125.1      | 93.26%          |

This selector was developed by the collaboration for all fitters. It checks the hit time ( $t_{PMT}$ ) distributions of all the hit PMTs and finds a mode value of the hit time ( $t_{mode}$ ). If  $t_{mode}$  fails to be found, it calculates a median value ( $t_{median}$ ) instead[140]. Then it selects the PMT with  $t_{PMT} \in [t_{mode} + t_{low}, t_{mode} + t_{high}] \text{ ns}$ . This selector is used to remove the PMTs triggered by noise and light from reflection. The values of  $t_{low}$ ,  $t_{high}$  are optimized for different scintillators. For the MPW fitter, the optimized window is  $[t_{mode} - 50, t_{mode} + 100] \text{ ns}$  by checking with the fit biases and resolutions for the  $^{16}\text{N}$  central run data in the water phase, while for the MP scint-water fitter the optimized window is  $[t_{mode} - 100, t_{mode} + 100] \text{ ns}$  based on checking with the simulations.

- Uniform PMT Selector

I designed this selector for the partial-fill phase and the scintillator phase when a single event can trigger a large amount of PMTs. It reduces the number of the hit PMTs to a designated number ( $n_{select}$ ) in order to boost up the fit speed. When an event triggers  $N$  calibrated PMTs, the selector goes through these recorded PMTs and uniformly picks up one PMT by an interval of  $\lceil N/n_{select} \rceil$ . If  $N \leq n_{select}$ , the selector does nothing. By doing this, the selector uniformly reduces the number of the PMTs for the fitter without an obvious bias.

- Earliest Hit PMT Selector

Similar to the uniform PMT selector, this selector reduces the number of the hit PMTs to boost up the fit speed. It first groups the PMTs by their positions in the PMT support sphere. Take the centre of the sphere as coordinate origin, the sphere is

divided by the azimuth angle  $\phi$  (as longitude) and zenith angle  $\theta$  (as latitude). In the sphere, the positions of the PMTs in  $\phi$ , ranging in  $[-\pi, \pi]$ , is uniformly divided into  $n$  intervals while the positions of the PMTs in  $\cos \theta$ , ranging in  $[-1, 1]$ , is also divided into  $n$  intervals. Thus, the PMTs are grouped into  $n \times n$  panels, see Fig. 4.22.

For each panel, the selector first drops the PMTs triggered too early ( $t_{\text{PMT}} < 100 \text{ ns}$ , where  $100 \text{ ns}$  is set as a default threshold). These PMTs could be triggered by noises, such as pre-pulsing. In the rest of the PMTs, the selector picks up one PMT with the earliest  $t_{\text{PMT}}$  in each panel. Thus the number of the PMTs is reduced to  $n \times n$  for the fitter, i.e.,  $n_{\text{select}} = n \times n$ . If  $N \leq n_{\text{select}}$ , the selector does nothing.

The other timing parameters can also be used for selecting the PMT in each panel, such as the  $t_{\text{mode}}$  or the  $t_{\text{median}}$ . However, tests from the simulations for the scintillator phase show that using the earliest hit time gives less fit biases and better fit resolutions.

#### 4.6.0.1 Water Level

$$\frac{\partial L}{\partial \text{split}Z} = \frac{\partial L}{\partial \text{tof}} \cdot \frac{\partial \text{tof}}{\partial \text{split}Z} = \frac{\partial L}{\partial \text{tof}} \cdot \frac{\partial a_3}{\partial \text{split}Z}$$

$$\frac{\partial L}{\partial \text{split}Z} = 0$$

(ref: press2007numerical)

The pdf can be expanded and fit with Chebyshev polynomials to obtain an analytic approximation function[132]. This analytical function can give proper analytical derivatives

## 4.7 Energy Reconstruction

The previous sections mainly focus on vertex and direction reconstruction. For the energy reconstruction in the water phase

energy response processor, or the energy RSP fitter, is derived from SNO [138, 141].

It uses the fitted position and direction of an event as inputs and then calculates an effective

estimated  $N_\gamma$ ,

detailed detector effects are taken into account.

the asymmetric geometry of the detector, for example the neck cylinder on the top of the AV sphere; the actual number of online PMTs in a realistic physics run.

$^{16}\text{N}$  calibration scans at certain detector points.

Energy lookup table built from the simulation data set.

energy look up[142]. (energyRSP)

#### 4.7.1 Figure of Merit

Three figure of merit quantities for the energy fitter were developed by the SNO+ collaboration in order to identify the poor reconstructed results which have large biases to the true energy values, especially for the low energy regions around 2.2 MeV, which helps the analysis of neutron capture[137].

- $U$ -test ( $U_{test}$ ): A Mann-Whitney quantity uses the channel hit probabilities by EnergyRSP which are ordered and ranked. The rank of the channels with hits are summed.

$$U_{test} \equiv \frac{S - N(N + 1)/2}{N(N_{active} - N)}, \quad (4.6)$$

where  $S \equiv \sum_i^N \text{rank}_i$ .

- $G$ -test ( $G_{test}$ ): A quantity uses the hit probabilities by EnergyRSP ( $E_i$ ) which are normalized to the number of observed hits ( $N$ )

$$G_{test} \equiv \frac{1}{N} \sum_{i=1}^N \log\left(\frac{1}{E_i}\right), \quad (4.7)$$

- $Z$ -factor ( $Z_{factor}$ ): A quantity uses the medians and median absolute deviations of hit probabilities by EnergyRSP

$$Z' \equiv 1 - \frac{3(\sigma_p + \sigma_n)}{\mu_p - \mu_n}, \quad (4.8)$$

### 4.7.2 Energy Reconstruction in Partial-fill Phase

Up till this thesis writing, there is no proper energy fitter for the partial-fill phase works. I attempted two methods for the energy reconstruction in the partial-fill phase: the NHit scale method and the NHit ratio method. Both of them are based on the simulations. These two methods need more effects to be improved.

#### 4.7.2.1 NHit Scale

In the partial-fill phase , In [143], to scale  $NHits$  based on several sets of simulations.

#### 4.7.2.2 NHit Ratio

The fitter follows the idea of the charge-ratio fitter for the partial energy reconstruction[144].

$$E = p_0 + p_1 \cdot NHit + p_2 \cdot NHit^2 \quad (4.9)$$

NHit ratio table based on position.

## 4.8 Other Reconstruction Algorithms

### 4.8.1 Hough Transformation for Direction Reconstruction

Hough transformation is a pattern recognition algorithm used in image analysis and computer vision[145]. This algorithm was first invent to extract patterns in bubble chamber[146], is used by Super-K[147].

The Hough transformation algorithm was used in SNO data analysis for counting the numbers of the Cherenkov rings caused by multiple charged particles in a high energy event such as atmospheric neutrinos event[120]. It is also suggested for the reconstruction of event direction in the SNO+ scintillator phase[148].

As illustrated in Fig. 4.23,

circular Hough transformation

### 4.8.2 Reconstructions Based on the Deep Learning

The vast amount of data collected by the particle detectors make it feasible to implement machine learning algorithms for data analysis. The machine learning algorithms, such as artificial neural network (ANN), have been implemented into the data analysis as well as the event reconstruction in SNO+. In the RAT software, an ANN position reconstruction algorithm (position ANN) has been developed and will be implemented in future.

This algorithm trains the neural network from calibration data to find the position of an event.

At the time of this writing, a few machine learning or deep learning algorithms are being developed. Based on the PMT hit patterns.

Learning from the simulations as well as the calibration data, and then predicts the event position and direction. utilize the computing power of the graphics processing unit (GPU). Once a neural network is trained, inference is very fast.

Traditional approach can fail to converge parallelize the deep learning framework is being developed. and to aid data analysis 100x - 1,000x quicker on CPU (Central Processing Unit) 10,000 times quicker on GPU . [149, 150].

## 4.9 Conclusion

The Multi-path Fitter framework of event vertex reconstruction was developed for multiple SNO+ physics phases. Under this framework, the **Multi-path Water Fitter** works as an alternative fitter to provide additional reconstruction information for the water data and it gives proper position and direction resolutions for the water analysis. The **Multi-path Scint-Water Fitter** works as the prime fitter for the SNO+ partial-fill phase.

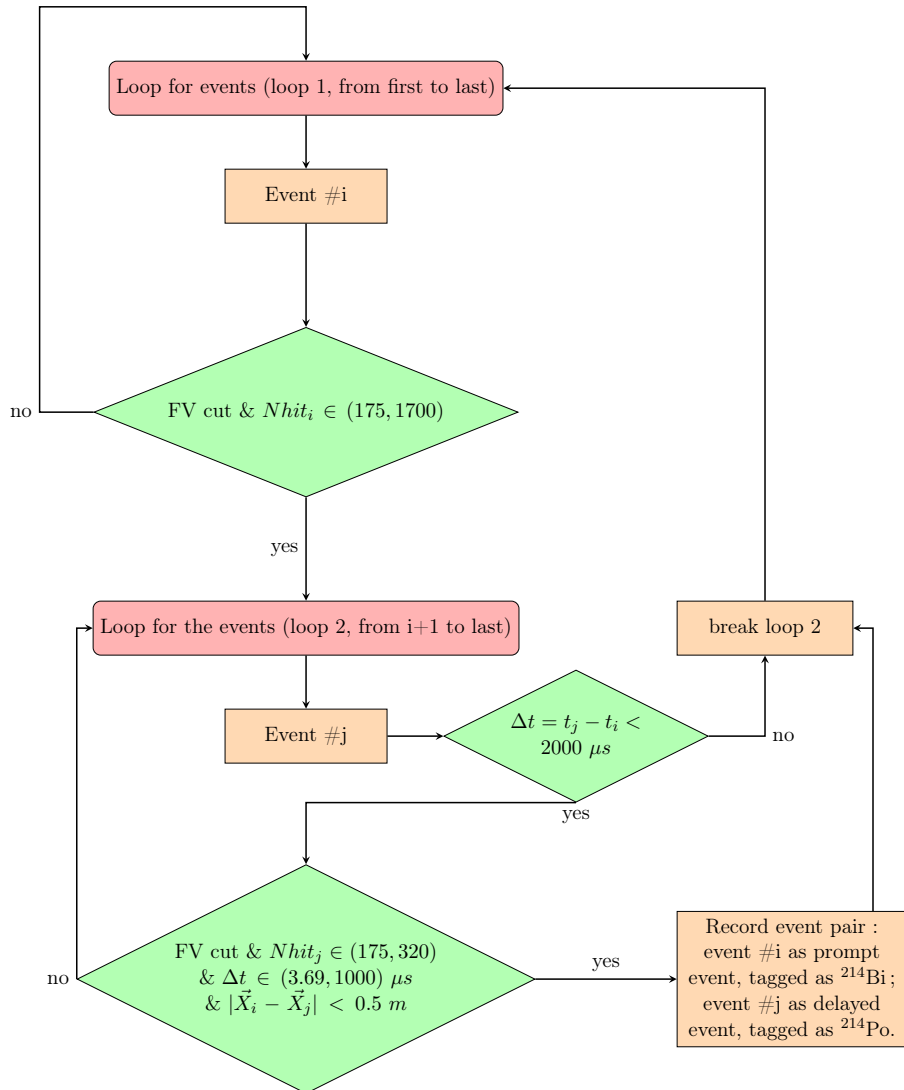


Figure 4.21: A flow chart for Bi-Po tagging.

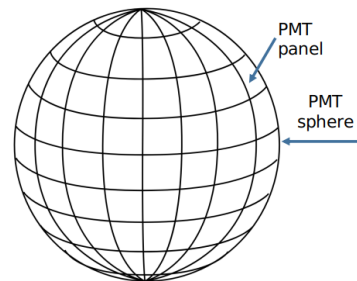


Figure 4.22: Group the PMTs by dividing the PMT sphere with latitudes and longitudes.

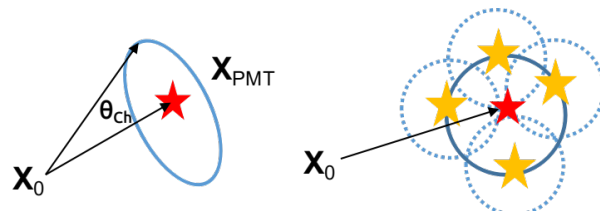


Figure 4.23: Hough transformation for catching the ring structure of Cherenkov signals and fitting the direction.

# Chapter 5

## Calibration

A detailed description of the SNO+ detector has been implemented in the RAT software package for Monte Carlo (MC) simulations, as mentioned in Chapter 3. However, when the simulations are compared to the real world, there always exist discrepancies. In order to make precise measurements, calibration sources were implemented in the SNO+ detector during the water phase and the partial-fill phase. During the water phase, the  $^{16}\text{N}$  source was used for the primary detector calibration. The  $^{16}\text{N}$  runs were mainly used for checking the performances of the reconstruction of the event position, direction and energy. The source was described in 3.5.2.1.

In this chapter, I applied the MultiPath reconstruction algorithm mentioned in Chapter 4 to the  $^{16}\text{N}$  calibration data and simulations.

First, for the  $^{16}\text{N}$  calibration runs during the water phase, the MultiPath water (MPW) fitter was applied on both data and simulations. By comparing the differences between the data and MC, systematics of the position and direction reconstruction were extracted. Setting the MPW fitted event vertex and direction as seed, the event energy was reconstructed via the energy RSP fitter. Also based on the MPW fitted vertex and direction results, the other parameters, such as the in-time-ratio (ITR) and the isotropic parameter ( $\beta_{14}$ ) were calculated. By comparing the  $^{16}\text{N}$  data and the MC simulations, the systematics were also evaluated. These systematic results were used in the solar neutrino analysis in Chapter 6.

The MultiPath water (MPW) fitter was also applied on the simulations of the AmBe source calibration runs during the water phase. The performances of the MPW fitter reconstruction on low energy events, specially the 2.2 MeV  $\gamma$  events were discussed.

The last section of this chapter is to check the performance of the MultiPath partial fitter for the  $^{16}\text{N}$  calibration runs during the partial-fill phase. An attempt of extracting the Cherenkov signals from the events in the scintillator was made. This attempt will be useful for extracting the solar neutrino events and reconstructing their directions during the scintillator phase.

## 5.1 $^{16}\text{N}$ Calibration Scans in the Water Phase

During the water phase, the  $^{16}\text{N}$  calibration source was deployed as internal calibration scans in June and November, 2017 and as external scans in March, 2018. For each calibration run, the source was placed at a fixed position and the data were taken for about 20 minutes (for central run-107055, it took 1 hour). For the internal scans, the source was inside the AV, moving along x, y and z-axes (called “X, Y, Z scans” in this thesis). It was also moved diagonally across the AV and was placed at the corners of the inner AV (“corner scans”). For the external scans, the source was placed in the external water region but outside the AV. The source was moved along z-axis with a fixed  $(x, y)$  position close to the AV at (-5861.0,-2524.0) mm. Fig. 5.1 shows the different positions of the  $^{16}\text{N}$  source deployment. In this thesis, 79 internal scan runs and 19 external runs were used. Details of the calibration runs are listed in the tables in Appendix B.

The  $^{16}\text{N}$  calibration runs provide ideal tests for the fitter performance. From a comparison of reconstructions for data and MC, we can also extract the resolution and bias of the fitter. Here I worked out the vertex and the direction reconstruction performances for both of the RAT water fitter and the MPW. The vertex shifts as well as the uncertainties were evaluated.

To tackle with the  $^{16}\text{N}$  calibration data and simulations, an FECD tag cut (*FECD == 9188*) was applied during the data processing to only save the events when the source trigger

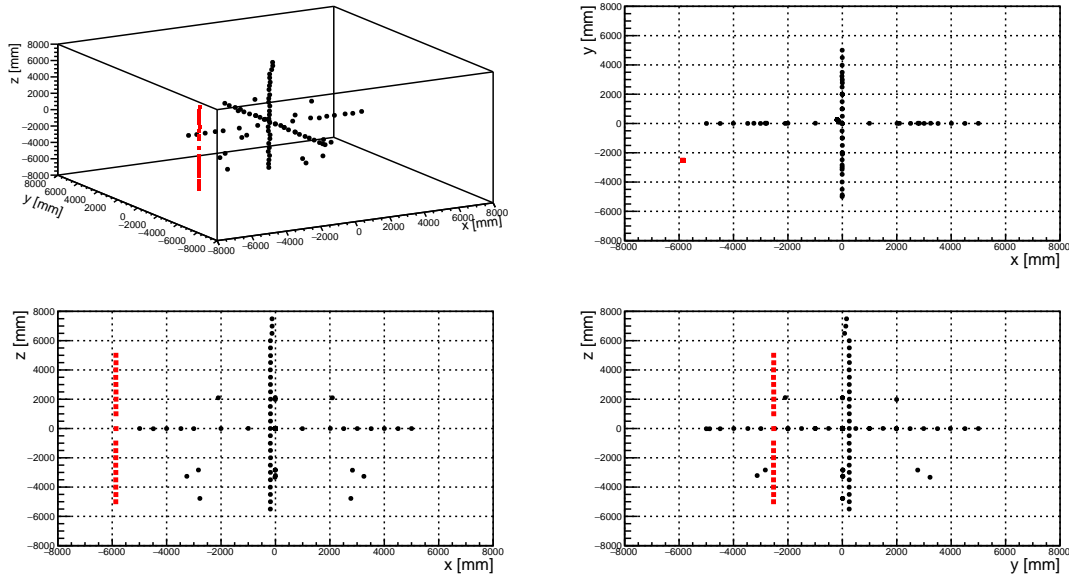


Figure 5.1: The deployed source positions of the  $^{16}\text{N}$  scan runs used by this thesis. The black dots are internal runs while the red squares are external runs.

fired. A reconstruction threshold on  $N\text{Hit}$ :  $N\text{Hit} \geq 6$  was used in both the MC and data. Besides these cuts, high level cuts based on classifiers were used.

## 5.2 High Level Cuts for the Water Phase

A set of classifiers were developed by SNO analysis and been optimized for the SNO+ water analysis[151]. These classifiers utilized the reconstructed quantities, so valid reconstructions were always required.

- In time ratio (ITR) classifier

For each event, this classifier loops the triggered PMTs (hits), calculates the  $t_{res}$  and then finds the ratio of the number of hits in an optimized prompt time window. In the water phase, the time window was [-2.5,5.0] ns. If the ITR ratio is too low for an event, it indicates that most of the triggered PMTs are not caused by the prompt lights and thus the event probably does not originate from Cherenkov lights; it can be an instrumental noise, or caused by a large amount of lights reflecting off the detector

components (called “late lights”).

- $\beta_{14}$  isotropy classifier

This classifier uses Legendre polynomials to return the first ( $\beta_1$ ) and the fourth ( $\beta_4$ ) spherical harmonics of an event, where:

$$\beta_l = \frac{2}{N(N-1)} \sum_{i=1}^{N-1} \sum_{j=i+1}^N P_l(\cos \theta_{ij})$$

and  $P_l(\cos \theta_{ij})$  are Legendre polynomials.

A combination of two  $\beta_l$  terms was chosen by the SNO collaboration to be:  $\beta_{14} = \beta_1 + 4\beta_4$ . This quantity gives a gaussian-like distribution for Cherenkov events[152]. In principle, any deviation from zero suggests some polarity or a deviation from a totally isotropic pattern.

- $\theta_{ij}$  isotropy classifier

This classifier describes the angle subtended at an event vertex by PMT #i and PMT #j, which is calculated as:

$$\cos \theta_{ij} = \frac{(\vec{X}_{PMT\#i} - \vec{X}_{event}) \cdot (\vec{X}_{PMT\#j} - \vec{X}_{event})}{|\vec{X}_{PMT\#i} - \vec{X}_{event}| |\vec{X}_{PMT\#j} - \vec{X}_{event}|}. \quad (5.1)$$

### 5.2.1 Effects of the High-level Cuts

As described above, the classifiers can help to distinguish the signals from Cherenkov events and backgrounds from non-Cherenkov events. To remove the non-Cherenkov backgrounds, cuts of  $ITR > 0.55$  and  $-0.12 < \beta_{14} < 0.95$  (called “high-level cuts”) were suggested by the collaboration[137]. These cuts are based on the analyses of data cleaning, simulated physics events as well as the SNO experience[137, 153, 152].

The  $^{16}\text{N}$  central run-107055 data and MC were used to check the effects of the high-level cuts. For the MC (data), the cut of  $ITR > 0.55$  removed 0.69% (0.79%) of the total events;  $-0.12 < \beta_{14} < 0.95$  removes 1.11% (0.93%) of the total events. Combining the ITR and  $\beta_{14}$  cuts, 1.69% (1.62%) of the total events were removed.

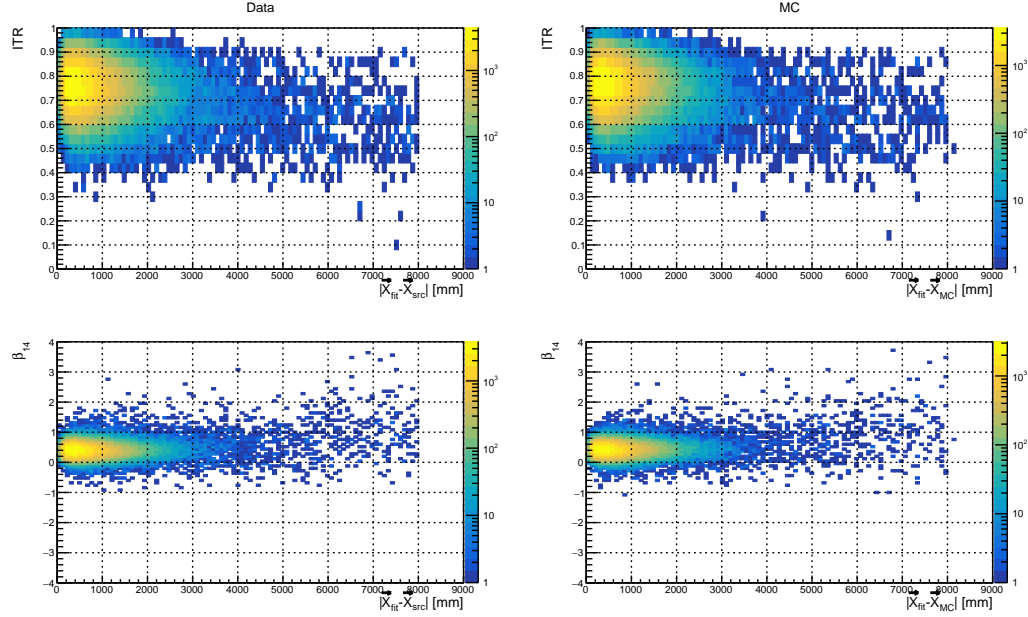


Figure 5.2: Position biases vs  $ITR$  (top) and  $\beta_{14}$  (bottom) for the  $^{16}\text{N}$  central run-107055. Left is MC and right is data. For the data, the source position ( $\vec{X}_{src}$ ) was compared.

The poorly reconstructed events with large position biases ( $> 6000\text{ mm}$ ) were counted. For the MC case, the position biases were taken as the distance between the reconstructed positions and the true positions generated by the MC:  $|\vec{X}_{fit} - \vec{X}_{MC}|$ ; while for the data case, the biases were between the reconstructed positions and the source manipulation position:  $|\vec{X}_{fit} - \vec{X}_{src}|$ . The large biases events are 0.13% of the total events in both the MC and data. The high-level cuts removed 73.12% (66.82%) of them for the MC (data).

Fig. 5.2 shows the relations between the position biases and the  $ITR$ ,  $\beta_{14}$  respectively, for the data and MC.

As a summary, the high-level cuts removes more than a half of the events with large position biases while removes about 1.6% of the total events.

## 5.3 Reconstruction Evaluations from $^{16}\text{N}$ Calibration Scans in the Water Phase

In this section, by analyzing the  $^{16}\text{N}$  data and MC in the water phase, I extracted the reconstruction resolutions of the event position, direction and energy respectively. Then by comparing the data with the MC, the reconstruction systematics were evaluated.

To do these evaluations, a few cuts were applied on both the data and MC. Firstly, the level cuts ( $ITR > 0.55$ ,  $-0.12 < \beta_{14} < 0.95$ ) were applied. For events with the position, direction and energy successfully reconstructed (i.e., the event has valid position, direction and energy reconstructions), further cuts on the reconstruction figure of merit (FoM) and source geometry (will be described in detail) were applied to ensure that the analyzed events were nicely reconstructed physics events caused by the source  $\gamma$  particles interacting with the detector water.

### 5.3.1 Position Reconstruction Evaluation

#### 5.3.1.1 Position Figure of Merit

A quantity called scaled logL ( $scaleLogL$ ) is used as the position reconstruction FoM ( $posFoM$ ):  $scaleLogL = \ln L/NHit_{selected}$ . This quantity utilizes the best log-likelihood returned by the MultiPath fitter for a successfully reconstructed event vertex, and then it is scaled by the “selected”  $NHit$ , i.e., the number of the PMTs actually used by the fitter for reconstructing the event vertex, after the PMT selections mentioned in 4.6.

Fig. 5.3 shows the  $scaleLogL$  with the position biases for the reconstructed events in  $^{16}\text{N}$  central calibration run-107055. Both of the data and the MC simulations are shown. For the MC case, the position biases are between the reconstructed positions and the true positions generated by the MC:  $|\vec{X}_{fit} - \vec{X}_{MC}|$ ; while for the data case, the biases are between the reconstructed positions and the source manipulation position:  $|\vec{X}_{fit} - \vec{X}_{src}|$ .

For the MC (data) case, about 0.035% (0.043%) of the total reconstructed events have large biases ( $|\vec{X}_{fit} - \vec{X}_{MC}| > 6000\text{ mm}$ ). A cut of  $scaleLogL > 10$  removes 96.0% (97.3%)

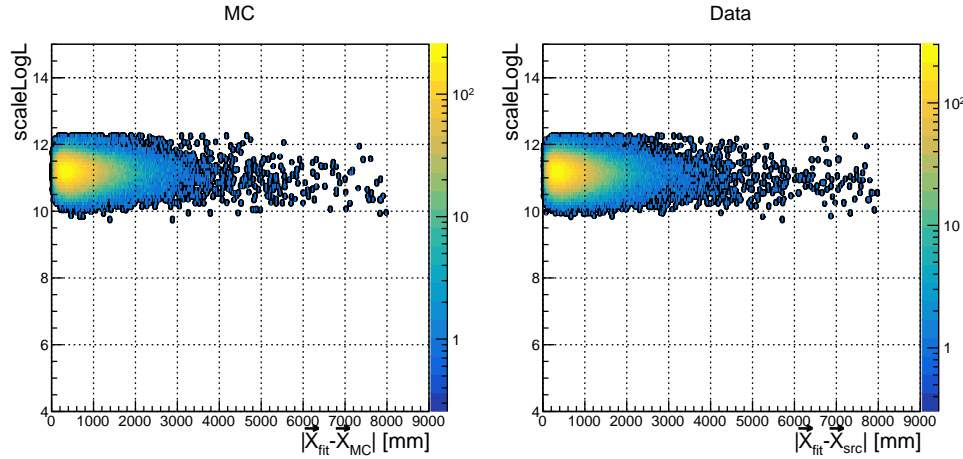


Figure 5.3: Position biases ( $|\vec{X}_{fit} - \vec{X}_{MC}|$ ) vs  $scaleLogL$  for the  $^{16}\text{N}$  central run-107055. Left is MC and right is data. For the data, the source position ( $\vec{X}_{src}$ ) was compared.

of the events which have biases over 6000 mm, with a sacrifice of removing 0.012% (0.016%) of the total events.

Fig. 5.4 shows a relation between the  $scaleLogL$  and the reconstructed energy ( $E_{fit}$ ).

For the events with reconstructed energies below the water solar neutrino analysis threshold 3.5 MeV ( $E_{fit} < 3.5 \text{ MeV}$ ), they are mostly coming from the U/Th isotopes, decays of Potassium as well as instrumental noises[137]. Their lower energies or  $NHits$  can affect the position reconstruction since there are fewer PMTs to be used and thus their  $posFoM$  can be worse. In the MC (data) case, there are about 13.04 % (12.89%) of the events with  $E_{fit} < 3.5 \text{ MeV}$ . By applying the cut of  $scaleLogL > 10$ , 0.10% (0.09%) of such events were removed.

As a summary, there are about 0.04% of the reconstructed events which were poorly reconstructed (mis-reconstructed) by the MPW fitter with position biases over 6 meters. Applying a cut in  $posFoM$  with  $scaleLogL > 10$  can remove over 96% mis-reconstructed events. This  $posFoM$  cut was used in the following direction and energy reconstruction evaluations.

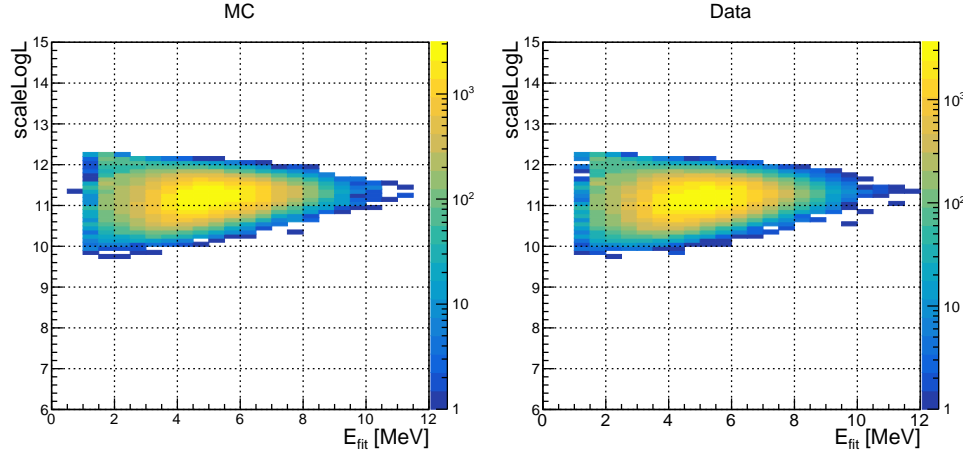


Figure 5.4: Reconstructed energy vs  $scaleLogL$  for the  $^{16}\text{N}$  central run-107055. Left is MC and right is data.

### 5.3.1.2 Position Resolution

A position resolution function is defined for the reconstructed electron position distribution[138]:

$$R(x) = \frac{1 - \alpha_e}{\sqrt{2\pi}\sigma_p} \exp\left[-\frac{1}{2}\left(\frac{x - \mu_p}{\sigma_p}\right)^2\right] + \frac{\alpha_e}{2\tau_p} \exp\left[\frac{-|x - \mu_p|}{\tau_p}\right], \quad (5.2)$$

where  $\alpha_e$  is the fractional exponential component,  $\sigma_p$  is the Gaussian width (corresponding to the position resolution),  $\mu_p$  is the Gaussian shift (corresponding to the position bias) and  $\tau_p$  is the exponential slope (corresponding to the position distributions in tails).

The  $\gamma$ -rays emitted from the  $^{16}\text{N}$  source interact with the water in the detector mainly via Compton scattering, as shown in Fig. 5.5. The position distribution of the  $\gamma$  interaction vertices is peaked around the source container, spreading to about 2 meters.

Fig. 5.6 shows the spatial distributions  $S(x)$  of the first  $\gamma$ -ray interaction positions projected on the x axis obtained from MC simulation. Therefore, the  $^{16}\text{N}$  source is considered as an electron source with a known spatial distribution[138]. For simplicity, in the following we always discuss the  $x$  component of the position vector  $\vec{X}$ .

For electrons from the  $^{16}\text{N}$  calibration source, their spatial distribution function  $N_R(x)$  can be described by the position resolution function smeared by the convolution of  $S(x)$

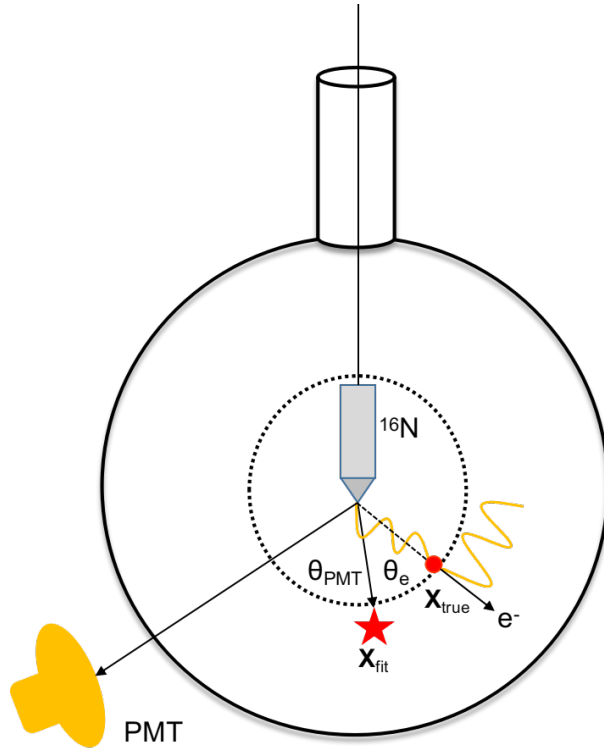


Figure 5.5: A cartoon shows the  $^{16}\text{N}$  source.

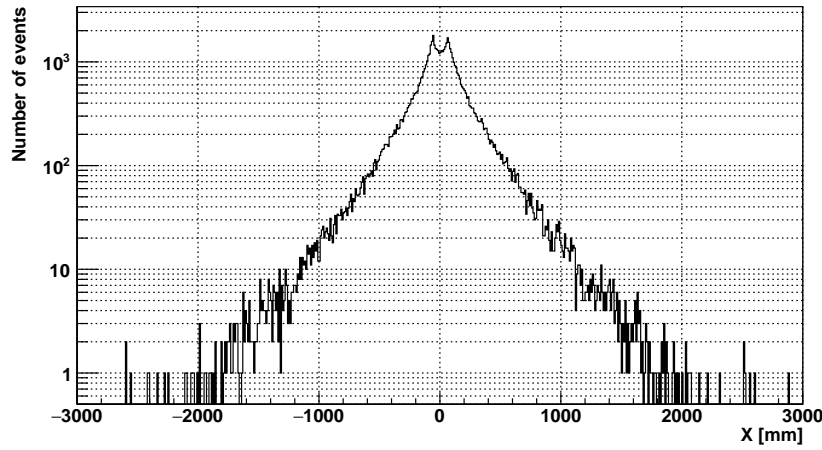


Figure 5.6: Spatial distributions of  $^{16}\text{N}$  first  $\gamma$ -rays interaction position projected on x axis, obtained from the RAT simulations. The double-peak structure is due to the wall of the stainless steel container of the  $^{16}\text{N}$  source.

as[138]:

$$N_R(x) = \int_{-\infty}^{+\infty} S(x)R(x_{fit} - x)dx.$$

The values of  $N_R(x)$  can be calculated bin by bin from the histograms of  $S(x)$  and  $R(x)$  extracted from the MC or data:

$$N_R(x_i) = \sum_{x_i=-\infty}^{+\infty} S(x_i)R(x_{fit}^i - x_i).$$

The  $\chi^2$  is calculated by:

$$\chi^2 = \sum_{i=0}^{N_{bins}} \left[ \frac{N_R(x_{fit}^i) - N_R^{fit}(x_{fit}^i)}{\sigma_i} \right]^2,$$

where  $N_R^{fit}$  is a trial fit to the  $N_R$  by tuning the  $\{\alpha_e, \mu_p, \sigma_p, \tau_p\}$  and  $\sigma_i$  is taken as the bin width of the histograms.

By minimizing the  $\chi^2$ , the parameters of the resolution function,  $\{\alpha_e, \mu_p, \sigma_p, \tau_p\}$  and a best  $N_R^{fit}$  were obtained.

Fig. 5.7 shows a comparison of the reconstructed x position of  $^{16}\text{N}$  events between data and MC. The reconstructed position distributions were fitted with  $N_R^{fit}$ .

Table 5.1 summarizes the values of position resolution parameters (for x-axis) obtained from data and MC of  $^{16}\text{N}$  calibration runs at the detector center.

Table 5.1: Position resolution parameters for the MPW fitter (x-axis).

| MPW fitter | $\alpha_e$      | $\sigma_P$ (mm) | $\tau_P$ (mm)   | $\mu_P$ (mm)    |
|------------|-----------------|-----------------|-----------------|-----------------|
| data       | $0.58 \pm 0.04$ | $175.8 \pm 3.8$ | $288.0 \pm 5.7$ | $-28.8 \pm 1.0$ |
| MC         | $0.51 \pm 0.05$ | $195.2 \pm 3.3$ | $298.4 \pm 6.1$ | $-10.9 \pm 1.0$ |

### 5.3.1.3 Position Systematics

To evaluate the position uncertainties, the MC and data runs of the  $^{16}\text{N}$  internal scans along x, y, z axes were taken to evaluate the x, y, z position uncertainties respectively (the runs are listed in Table. B.1 to B.3. Three neck runs in z-scan were not used). The high-level cuts as well as the  $E_{fit} > 3.5 \text{ MeV}$  and  $scaleLogL > 10$  cuts were applied. fit range was set as  $[-2000, +2000] \text{ mm}$ . If the lower range was smaller than -6000 mm, it was set to

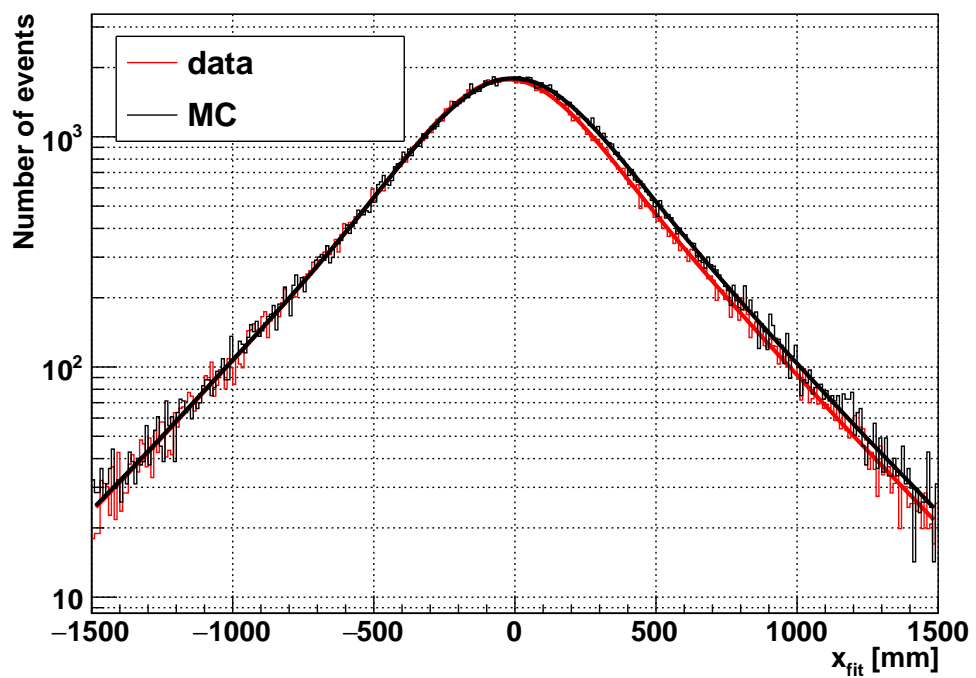


Figure 5.7: Distributions of the reconstructed position projected on x axis, obtained from SNO+  $^{16}\text{N}$  central run data (red) and MC (black). The distributions are fitted with  $N_R^{fit}$  (red and black lines).

-6000 mm; if the upper range was larger than 6000 mm, it was set to +6000 mm. This was used to remove the effects caused by the AV.

The position resolution function was first fitted with 4 free parameters:  $\alpha_e, \mu_p, \sigma_p$  and  $\tau_p$ . The average values of the  $\alpha_e$  and  $\tau_p$  were calculated from all the scan runs used here. To simplify the calculation in propagating systematics, the  $\alpha_e$  and the  $\tau_p$  were fixed to the average value:  $\alpha_e = 0.5288$  (0.5375) for the MC (data);  $\tau_p = 271.738$  (263.735) for the MC (data). With the fixed values of  $\alpha_e$  and  $\tau_p$ , both the data and the MC were refit with  $\mu_p$  and  $\sigma_p$  only. Using the fixed values of  $\alpha_e$  and the  $\tau_p$  is based on the reasons that these parameters in principle can be viewed as corrections to the  $\gamma$  distribution ( $S(x)$ ) and they can be absorbed, which would not depend on position[137].

Fig. 5.8 shows the fitted results of  $\mu_P$  and  $\sigma_P$  along the x, y, z-axes scans respective. For the sake of simplicity, for the x-scan case, only the x-axis results ( $\mu_{P,x}, \sigma_{P,x}$ ) are shown here. Similarly, only the  $\mu_{P,y}$  and  $\sigma_{P,y}$  ( $\mu_{P,z}$  and  $\sigma_{P,z}$ ) are shown for the y-scan (z-scan). The relative differences discussed later consider all the three-axes.

It shows that the position resolutions of the MC are mostly better than the data, which is expected since the non-uniformities of the detector in realistic situation can cause a broader resolution in the data[137]. Also, when the source is close to the AV or at the edges of the axes, the Gaussian shift  $\mu_P$  becomes large and the resolution goes worse. Also, the difference between the MC and data becomes large.

To quantify the discrepancies between the MC and data, a relative difference of  $\sigma_p$  between the MC and data is defined as[137]:

$$\sigma_{p,\delta} \equiv \sqrt{\sum_i |(\sigma_{P,i}^{data})^2 - (\sigma_{P,i}^{MC})^2|} \quad (i = x, y, z), \quad (5.3)$$

Fig. 5.9 shows the  $\sigma_{p,\delta}$  changing along the internal x, y and z-axes scans respectively. All the differences are below 190 mm except the run-106979 with the source at  $z = 4973.567$  mm. This worst resolution can be caused by the neck effects.

It goes worse when the source is close to the AV or at the edges of the axes. When the source is close to the AV center, the differences are below 100 mm.

The values of  $\sigma_{p,\delta}$  were taken to represent the position resolution systematics.

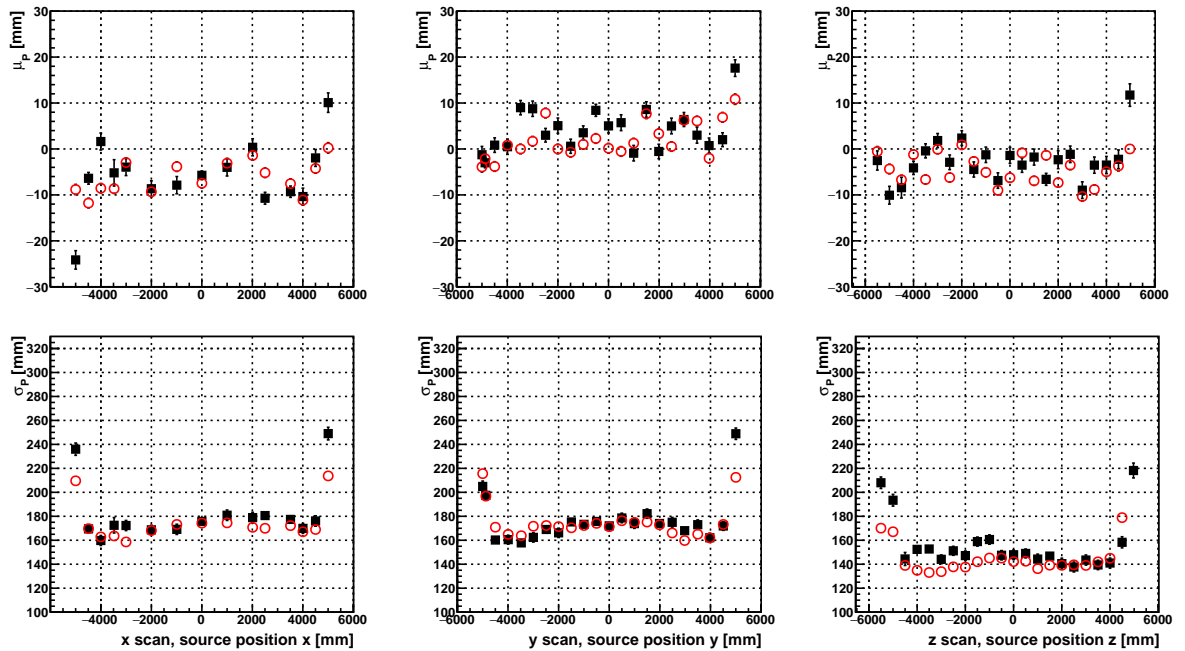


Figure 5.8: The fitted values of  $\mu_P$  (top three) and  $\sigma_P$  (bottom three) along x (left), y (middle) and z (right) scans. The source positions in each set of scans are projected onto x, y and z axes respectively. The MC results (red circles) are compared with the data (black boxes).

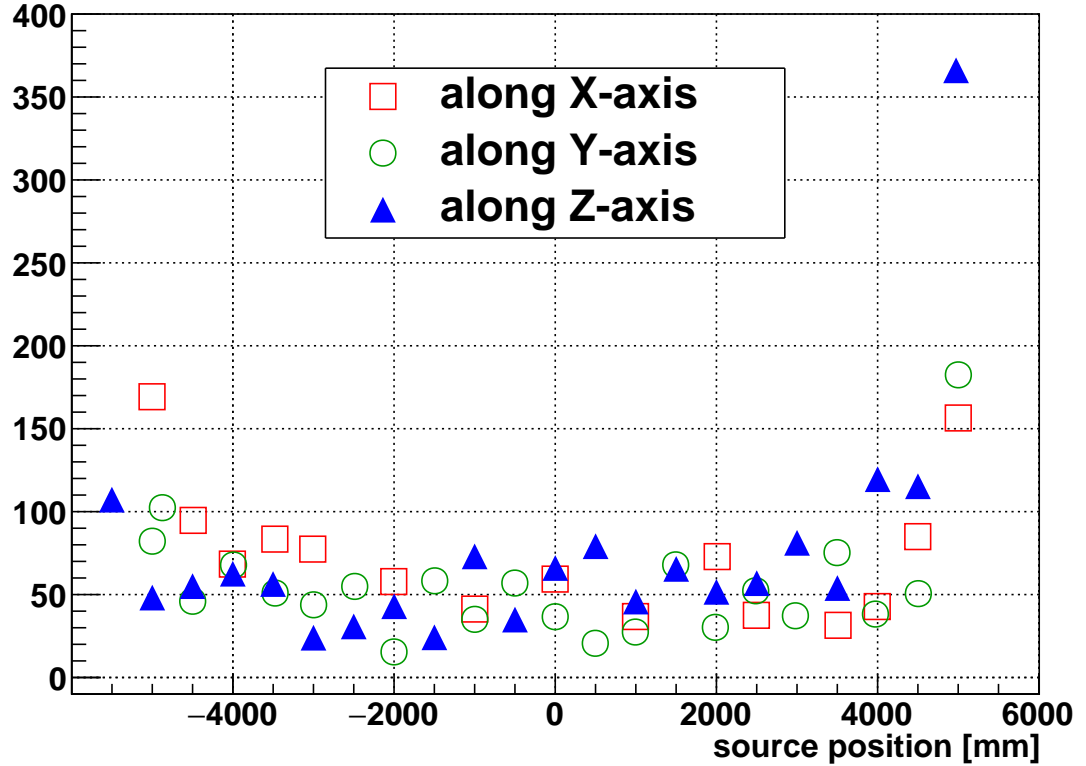


Figure 5.9: Relative differences of  $\sigma_P$  ( $\sigma_{p,\delta}$ ) as a function of the  $^{16}\text{N}$  source position. For simplicity, the corner scans are not shown in this figure. The red squares represent the results from the x-scan runs; green circles represent the y-scan runs and the blue triangles represent the z-scan runs.

As listed in Table. 5.2, the averages and the standard deviations of the  $\sigma_{p,\delta}$  were taken as the resolution systematics for x, y and z-axes respectively. To smear the position results, a Gaussian distribution  $\mathcal{N}(0, \delta)$  was convolved with positions. The upper values  $\delta$  were used to smear the positions.

To quantify the vertex shifts between the MC and data, values of vertex shifts:  $\mu_{P,\delta} \equiv \mu_P(\text{data}) - \mu_P(\text{MC})$  were calculated for the x, y and z scans respectively. Fig. 5.10 shows these results.

In Table. 5.3, the averages and the standard deviations of the  $\mu_{P,\delta}$  were taken as the vertex shifts for x, y and z-axes respectively. To smear the position results, the positions

Table 5.2: The MPW fitter position resolution systematic uncertainties in x, y and z axes.  
Unit: mm.

| axis | systematic uncertainties | systematic to be applied ( $\delta$ ) | smearing                     |
|------|--------------------------|---------------------------------------|------------------------------|
| x    | $73.89 \pm 39.71$        | 113.6                                 | $x + \mathcal{N}(0, \delta)$ |
| y    | $56.03 \pm 34.96$        | 90.99                                 | $y + \mathcal{N}(0, \delta)$ |
| z    | $75.47 \pm 70.09$        | 145.56                                | $z + \mathcal{N}(0, \delta)$ |

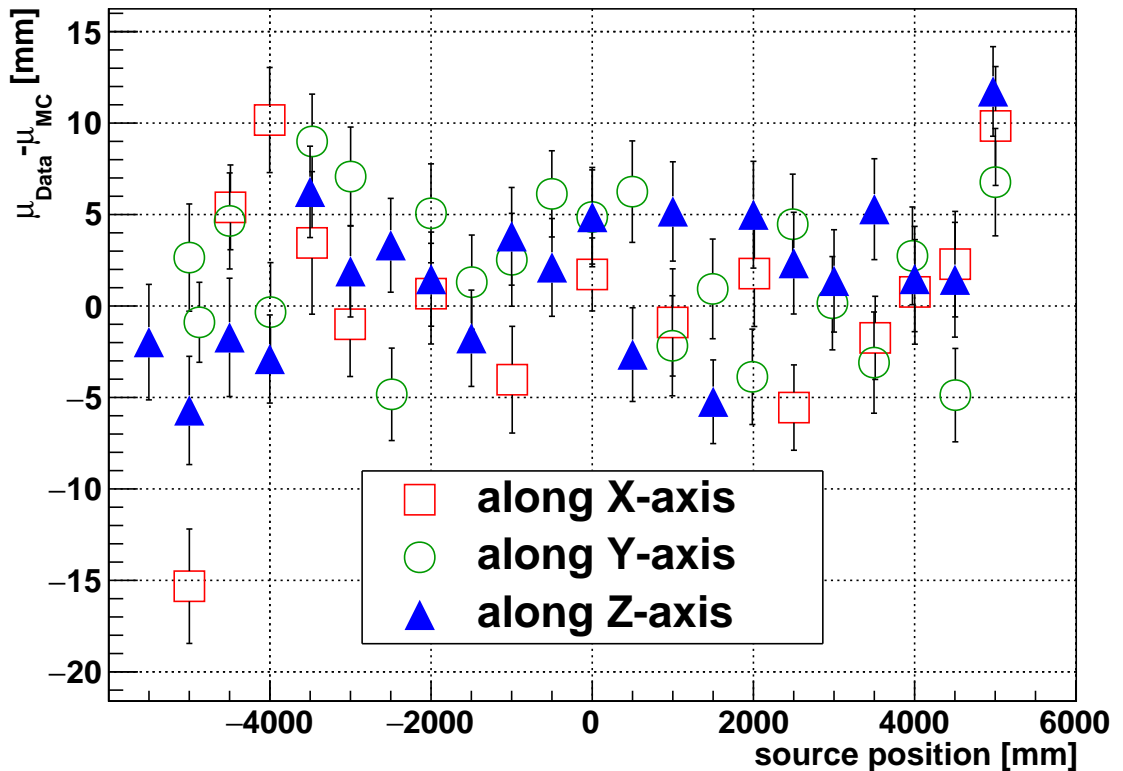


Figure 5.10: Vertex shifts of  $\mu_P$  ( $\mu_{p,\delta}$ ) as a function of the  $^{16}\text{N}$  source position. For simplicity, the corner scans are not shown in this figure. The red squares represent the results from the x-scan runs; green circles represent the y-scan runs and the blue triangles represent the z-scan runs.

were simply shifted by the upper values  $\delta$  were used to smear the positions.

Table 5.3: Vertex shifts for the reconstructed positions in x, y and z axes. Unit: mm.

| axis    | vertex shift    | systematic to be applied ( $\delta$ ) | smearing     |
|---------|-----------------|---------------------------------------|--------------|
| x shift | $0.50 \pm 5.98$ | $+6.48/-5.98$                         | $x + \delta$ |
| y shift | $2.02 \pm 4.11$ | $+6.13/-4.11$                         | $y + \delta$ |
| z shift | $1.89 \pm 4.82$ | $+6.71/-4.82$                         | $z + \delta$ |

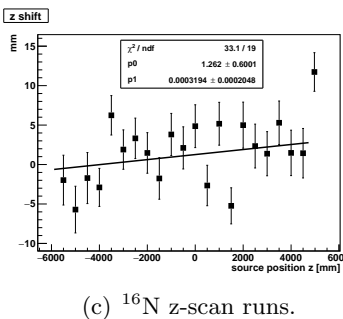
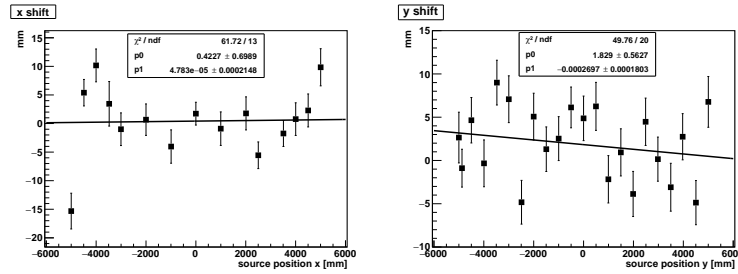


Figure 5.11: Vertex shifts along x, y, z axes and fitted with linear functions.

#### 5.3.1.4 Vertex Scale Uncertainties

In addition to the vertex shifts mentioned previously, the vertex scale is defined as a linear scale factor between the fitted positions of the data and the MC:  $x_{fit}^{data} - x_{fit}^{MC} = \mu_{P,x}^{data} - \mu_{P,x}^{MC} = \Delta + \beta \cdot x_{fit}^{MC}$ .

Since  $x_{fit}^{data} = \Delta + (1 + \beta) \cdot x_{fit}^{MC}$ , if the vertex scale factor is defined as:  $\alpha \equiv 1 + \beta$ , then  $x_{data} = \alpha x_{MC}$ .

To obtain the  $\alpha$ , the results in Fig. 5.10 were fitted with linear functions:  $shifts = p_0 + p_1 \cdot x_{src}$  (where  $x_{src}$  is the source position), as shown in 5.11.

From the linear fits, the values of vertex shifts were obtained and listed in Table. 5.4. Since the  $\chi^2/ndf$  values here were large, according to [137] and [33], inflated errors were cal-

culated as  $S \cdot \text{slope errors}$ , where the error scale factor  $S = \sqrt{\chi^2/(ndf - 1)}$ . The downward systematic was calculated as the slope minus the slop error as well as the inflated error, while the upward systematic was simply taken as the positive inflated error, as suggested by [137]. For the z scan, the position at  $(-185.037, 247.24, 4973.567)$  mm pulls the slope results to the positive due to the possible biases in simulation for the neck geometry effects and makes the slope be positive. So this point was not used in the linear fit.

Table 5.4: Vertex shifts for the reconstructed positions in x, y and z axes. Unit: mm.

| axis    | fitted slope (%)   | inflated error | systematic ( $\delta^+/\delta^-$ ) (%) |
|---------|--------------------|----------------|--|
| x scale | $0.005 \pm 0.021$  | 0.048          | +0.07/-0.06                            |
| y scale | $-0.027 \pm 0.018$ | 0.030          | +0.02/-0.07                            |
| z scale | $0.032 \pm 0.020$  | 0.027          | +0.08/-0.01                            |

The vertex scale systematics is then transformed by:  $x' = (1 + \delta_x/100)x$ , the same for  $y, z$ .

The scale systematics also depends on the radius  $r = \sqrt{x^2 + y^2 + z^2}$ [137]. By the error propagation, for an event position  $(x,y,z)$ ,  $\delta_r$  is calculated as[137]:

$$\delta_r = \sqrt{\sum_{i=1}^3 \left(\frac{\partial r}{\partial x_i}\right)^2 \delta_{x_i}^2} = \sqrt{\frac{x^2 \delta_x^2 + y^2 \delta_y^2 + z^2 \delta_z^2}{r^2}}, \quad (5.4)$$

where the  $\delta_r^+$  and  $\delta_r^-$  are calculated by  $\delta^+$  and  $\delta^-$  respectively.

Then the two-sided bounds of the radial  $r$  are calculated by:  $r^+ = (1 + \delta_r^+/100) \cdot r$  and  $r^- = (1 + \delta_r^-/100) \cdot r$ .

### 5.3.2 Direction Reconstruction Evaluation

#### 5.3.2.1 Direction Resolution

Mentioned in Chapter 4, the direction reconstruction relies on the position. Therefore, the *posFoM* cut:  $\text{scaleLogL} > 10$  was applied before evaluating the direction reconstruction.

For the reconstructed events in  $^{16}\text{N}$  calibration, the “true” direction of an event is defined as the direction pointing from the source manipulation position to the reconstructed position:  $\vec{u}_{\text{true}} = (\vec{X}_{\text{fit}} - \vec{X}_{\text{src}})/d(\vec{X}_{\text{fit}}, \vec{X}_{\text{src}})$ , where  $d(\vec{X}_{\text{fit}}, \vec{X}_{\text{src}}) = |\vec{X}_{\text{fit}} - \vec{X}_{\text{src}}|$  is the

distance between the reconstructed event position to the source manipulation position. The angle  $\theta$  is the displacement between the “true” and the reconstructed directions and  $\cos \theta = \vec{u}_{true} \cdot \vec{u}_{fit}$ .

To describe the biases between the reconstructed direction and the true particle direction of the event, an empirical function for the angular resolution was adopted by SNO[138] and it is defined as a combination of two exponential components:

$$P(\cos \theta) = \alpha_M \frac{\beta_M \exp[-\beta_M(1 - \cos \theta)]}{1 - \exp(-2\beta_M)} + (1 - \alpha_M) \frac{\beta_s \exp[-\beta_s(1 - \cos \theta)]}{1 - \exp(-2\beta_s)}, \quad (5.5)$$

where the parameters:  $\beta_M$  and  $\beta_S$  are the “decay” constants or the “slopes” of the two exponential components;  $\alpha_M$  is the fraction between two exponential components. The first component, the main peak is due to the single scattering of the electrons and is the true angular resolution of the detector, while the second component which has a broad tail is mainly due to the multiple scattering of electrons; there are also back scattering electrons on the detector components and the poorly reconstructed events in the tails[138].

Before fitting the direction resolution function to the data or simulation results, a few cuts relating to the position and energy reconstruction were applied. These cuts were suggested by the SNO+ analysis to remove the instrumental backgrounds and poor reconstructions for the events close to the source container or far away from the source. To remove the instrumental backgrounds, the cuts of  $E_{fit} > 3.5 \text{ MeV}$ ,  $ITR > 0.55$  and  $-0.12 < \beta_{14} < 0.95$  were used. To remove poorly reconstructed events which were close to the source container due to its shadow effect, and also the events far away from the source, a distance cut of  $1000 < d(\vec{X}_{fit}, \vec{X}_{src}) < 2300 \text{ mm}$  was applied. For the internal scans, a radius cut  $R' < 5850 \text{ mm}$  was also applied. This radial cut was not applied on the external and neck scans[137].

Fig. 5.12 shows the fitted results of the angular distributions in a fit range of [0.3,1] after the cuts mentioned.

To describe the  $\cos \theta_e$  distribution, the angles that contain 50%, 80% and 90% of the reconstructed events, the  $\cos \theta_{0.5}$ ,  $\cos \theta_{0.8}$  and  $\cos \theta_{0.9}$  can also be used. Their values are

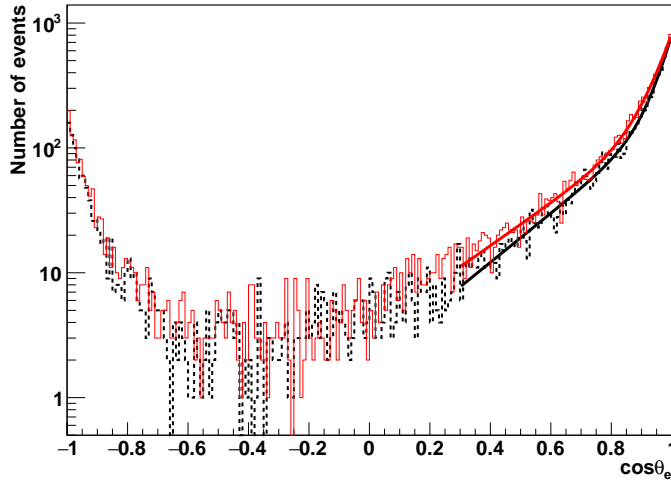


Figure 5.12: Angular distributions extracted from the data (red solid line) and the MC (black dashed line); both are reconstructed by the MPW fitter. These distributions are fitted with the angular resolution functions ranging from 0.3 to 1.

| 107055   | $\beta_M$       | $\beta_S$        | $\alpha_M$      | $\chi^2/\text{ndf}$ | $\cos \theta_{0.5}$ | $\cos \theta_{0.8}$ | $\cos \theta_{0.9}$ |
|----------|-----------------|------------------|-----------------|---------------------|---------------------|---------------------|---------------------|
| MPW data | $4.15 \pm 0.18$ | $19.08 \pm 0.94$ | $0.58 \pm 0.02$ | $77.1/66$           | 0.964               | 0.744               | 0.410               |
| MPW MC   | $4.42 \pm 0.19$ | $20.41 \pm 1.01$ | $0.56 \pm 0.02$ | $83.8/66$           | 0.974               | 0.768               | 0.454               |
| Rat data | $3.76 \pm 0.18$ | $17.90 \pm 0.82$ | $0.55 \pm 0.02$ | $70.5/66$           | 0.974               | 0.731               | 0.364               |
| Rat MC   | $4.02 \pm 0.18$ | $20.89 \pm 0.92$ | $0.54 \pm 0.03$ | $94.9/66$           | 0.979               | 0.753               | 0.409               |

solved numerically by the equation 5.6 below (take  $\cos \theta_{0.5}$  as an example):

$$\frac{\int_{\cos \theta_{0.5}}^1 P(\cos \theta_e) d \cos \theta_e}{\int_{-1}^1 P(\cos \theta_e) d \cos \theta_e} = 50\%, \quad (5.6)$$

where  $P(\cos \theta_e)$  is the direction resolution function with the best fitted parameters. If these values are large, the  $\cos \theta_e$  distribution is sharper and more peaked around +1.

From the results above, the direction resolutions of the MC are always better than the data, due to the ideal situations in the simulations. The MPW and the RAT reconstructions are similar, while the  $\beta_M$  values of the MPW are about 10% higher than the RAT in both of the data and the MC. This indicates the direction resolution of the MPW is slightly better than the RAT.

### 5.3.2.2 Direction Systematics

For all the internal  $^{16}\text{N}$  scans, the cuts mentioned in the last section were applied on both the data and simulations. Similar to the evaluation of the position uncertainties, the angular resolution function was first fitted with 3 free parameters:  $\alpha_M$ ,  $\beta_S$ ,  $\beta_M$ . To simplify the calculation in propagating systematics, an average value of the fitted  $\alpha_M$  was calculated from all the internal scans (except the three neck scans), as 0.613 for data and 0.585 for MC. With the fixed values of  $\alpha_M$ , both the data and the MC were refit with  $\beta_S$  and  $\beta_M$  only. The default fit range is [0.3,1], while for some scans close to the AV, the events can be few after the cuts. For these situations, in order to ensure more than 5000 events were fitted, the fit range was enlarged by moving a 0.1 step to the left until the left value reaches -0.5:  $[0.3 - 0.1 \cdot step, 1]$ .

Fig. 5.13 shows the results of the fitted  $\beta_M$  and  $\beta_S$  values for the internal  $^{16}\text{N}$  x, y and z-axes scans. It shows that for most of the scans, the MC results are better than the data. The three Z scans in the neck have the worst direction resolutions due to the asymmetry of the detector geometry.

The relative difference between data and MC of a fitted resolution quantity  $q \pm \delta_q$  is defined as:

$$(\Delta q)_{rel} = \frac{q_{data} - q_{MC}}{q_{MC}} \times 100\%. \quad (5.7)$$

The error of the relative difference is defined as:

$$\delta_{(\Delta q)_{rel}} = \sqrt{\left(\frac{\delta_{q_{data}}}{q_{data}}\right)^2 + \left(\frac{\delta_{q_{MC}}}{q_{MC}}\right)^2} \times 100\%. \quad (5.8)$$

Fig. 5.14 shows the relative differences for the internal x, y, z scans (not using the neck scans).

Taking the internal scans except the neck scans (77 runs in total), the means and standard deviations of the relative differences are:

$$\Delta(\beta_M)_{rel} = (-6.09 \pm 4.01)\%, \text{ and } \Delta(\beta_S)_{rel} = (-3.09 \pm 4.39)\%.$$

To be conservative, taking the largest and smallest values of the  $\Delta(\beta_M)_{rel}$  and  $\Delta(\beta_S)_{rel}$ ,

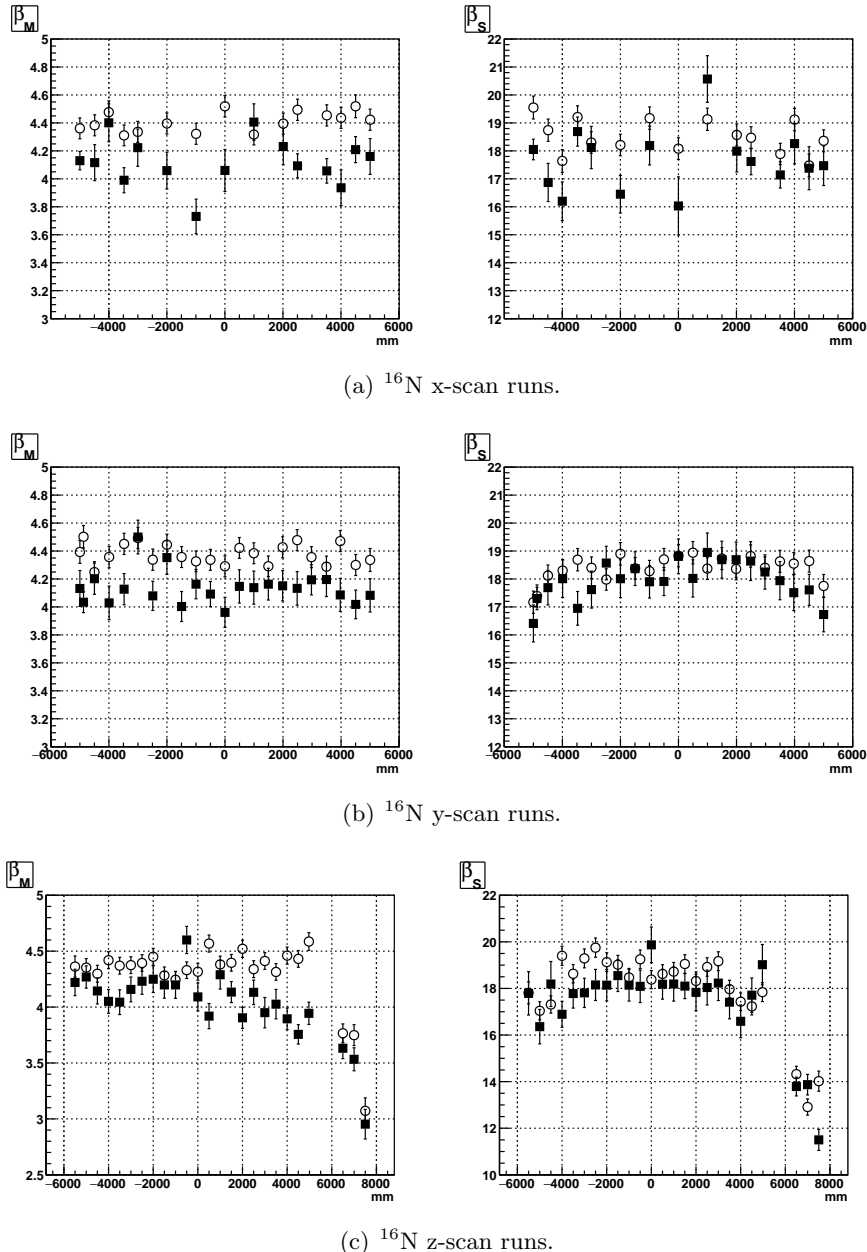


Figure 5.13: Fitted direction resolution parameters  $\beta_M$ ,  $\beta_S$  for x, y, z-axes scans.

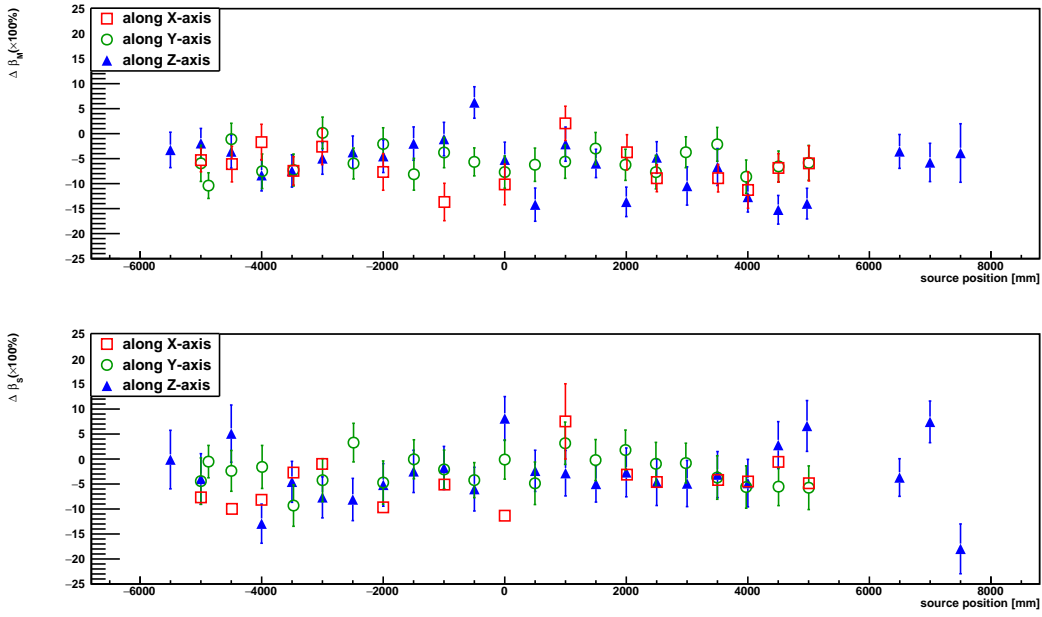


Figure 5.14: Relative differences of  $\beta_M$  and  $\beta_S$  as a function of the  $^{16}\text{N}$  source position. For simplicity, the corner scans are not shown in this figure. The red squares represent the results from the x-scan runs; green circles represent the y-scan runs and the blue triangles represent the z-scan runs.

the negative and positive values of the direction systematic ( $\delta_\theta$ ) are obtained as  $\delta_\theta = -0.101 / +0.013$ .

To propagate the uncertainties of  $\beta$  to the direction resolution, a first-order approximation function was derived by the SNO collaboration[154]:

$$\cos \theta' = 1 + (\cos \theta - 1)(1 + \delta_\theta). \quad (5.9)$$

This angular remapping function is used to smear the angular distributions for systematic studies. In the next chapter, it will be applied on the angular distribution of solar neutrino data.

### 5.3.3 $\beta_{14}$ and Its Systematic

Since  $\beta_{14}$  itself is used as the high-level cut, here only the cuts of  $ITR > 0.55$  and  $NHits > 5$  were applied on the data and MC to extract the  $\beta_{14}$  distributions. Fig. ?? shows the  $\beta_{14}$

distributions of the central run-107055 data and MC, reconstructed by the MPW fitter and the official RAT fitter. The  $\beta_{14}$  is calculated based on the reconstructed position, time and direction of an event while the  $\beta_{14}$  distributions from the MPW and the RAT fitter results are consistent. However, both of the two fitters show a discrepancy between the data and the MC. This discrepancy can be caused by an inaccurate modeling of the Cherenkov process in the Geant4 simulation[152, 155]. Fig. 5.15 shows a comparison of the  $\beta_{14}$  for the data and the MC in run-107055. Both of the distributions are the MPW processed results and are fitted with Gaussian distributions in a region of  $[-0.5, 1.5]$ . The data shows a smaller Gaussian mean value,  $\mu_{data} = 0.4157$ , compared to the  $\mu_{MC} = 0.4388$ .

Fig. 5.17 shows effects when the source moving along x, y and z axes.

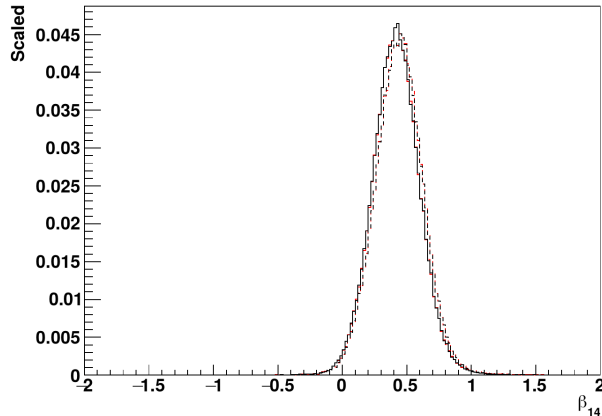


Figure 5.15: Distributions of  $\beta_{14}$  for the  $^{16}\text{N}$  central run-107055. Dashed lines for the MC and solid lines for data; red for the MPW fitter processed results and black for the RAT results.

For all the 80 internal runs mentioned before, I calculated the  $\Delta\beta_{14} \equiv \mu_{data} - \mu_{MC}$ . The mean and standard deviation were taken as the shift in  $\beta_{14}$ :  $-0.026 \pm 0.010$ . Following the suggestion in [137], an asymmetric uncertain was taken: the upward shift was taken as  $+0.010$  while the downward was taken as  $-0.026 - 0.01 = -0.036$ . Thus the shifts:  $+0.010 / -0.036$  was taken as the  $\beta_{14}$  systematics. It will be applied on the solar neutrino analysis in the next chapter.

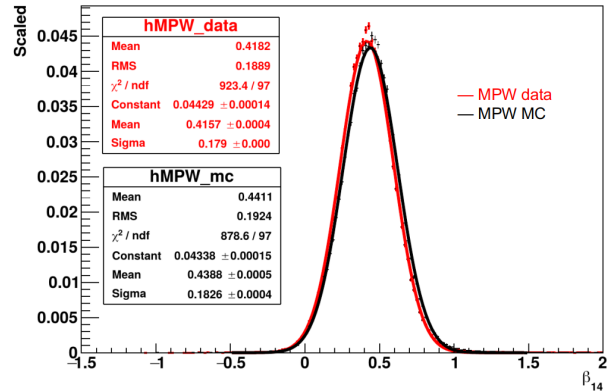


Figure 5.16: A comparison of the  $\beta_{14}$  for the data and the MC in run-107055.

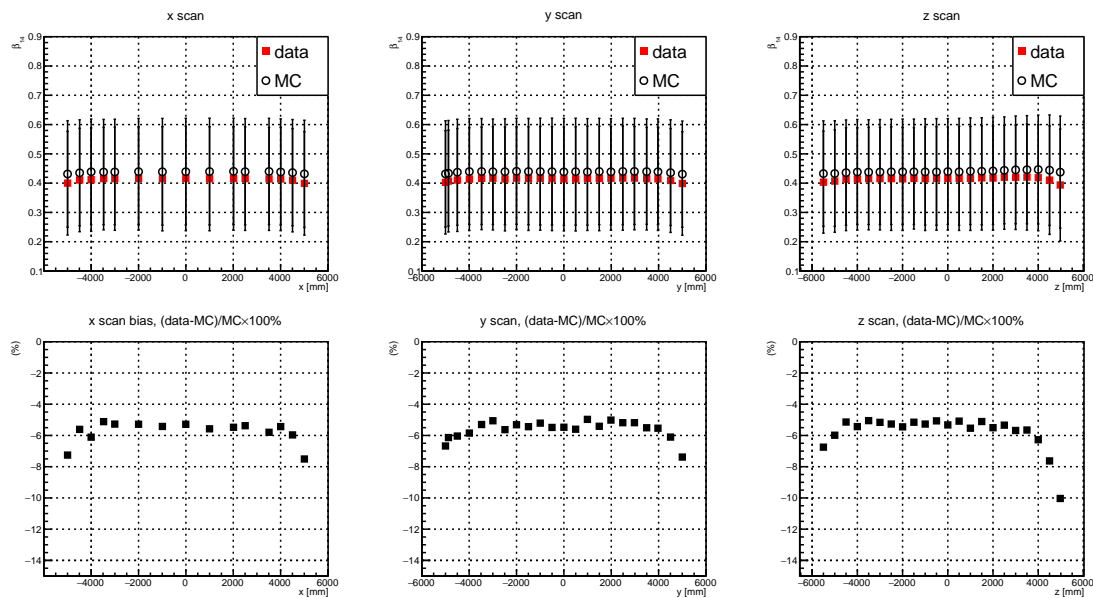


Figure 5.17:  $\beta_{14}$  systematic along x, y, z scans.

### 5.3.4 Energy Reconstruction Evaluation

#### 5.3.4.1 Energy Figure of Merits

Three energy FoM quantities:  $G_{test}$ ,  $U_{test}$  and  $Z_{factor}$  were introduced in 4.7.1. Here I used the MC simulations as well as the data of the  $^{16}\text{N}$  central run-107055 to check the effects of the cuts on FOM quantities to reduce the energy biases. The sacrifices of the events were calculated.

- $U_{test}$ : Fig. 5.18 shows  $U_{test}$  vs. energy biases. A cut of  $0.61 < U_{test} < 0.95$  was suggested by the collaboration, to remove the events were mostly caused by the source encapsulation. This cut removes 0.38% of MC events and 0.34% of data events.

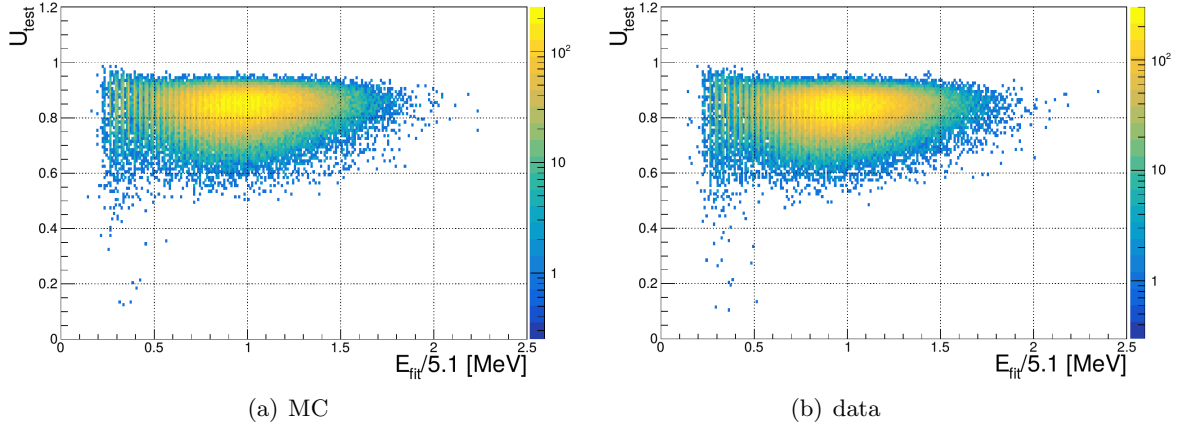


Figure 5.18:  $^{16}\text{N}$  central-run 107055,  $U_{test}$  vs.  $E_{fit}/5.1$  MeV.

- $G_{test}$ : Fig. 5.19 shows  $G_{test}$  vs. energy biases. A cut of  $0 < G_{test} < 1.9$  was suggested by the collaboration, which removes 0.01% events for both MC and data.
- $Z_{factor}$ : Fig. 5.20 shows  $Z_{factor}$  vs. energy biases. A cut of  $-11 < Z_{factor} < 1$  was suggested by the collaboration, which removes 0.13% events for both MC and data.

All the cuts on the three energy FoM quantities removes 0.40% events from MC and 0.37% events from data. These cuts were also used in the water phase analysis which will be described in the next chapter.

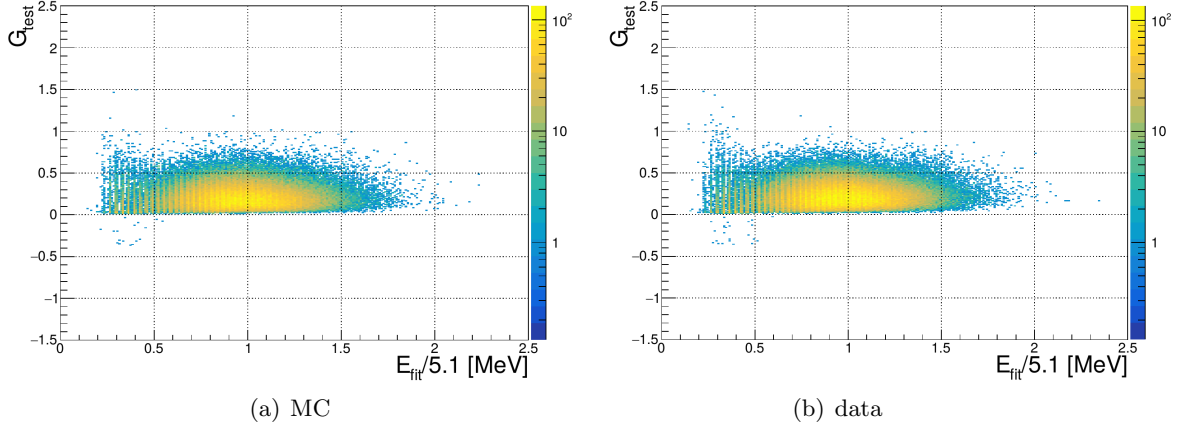


Figure 5.19:  $^{16}\text{N}$  central-run 107055,  $G_{test}$  vs.  $E_{fit}/5.1$  MeV.

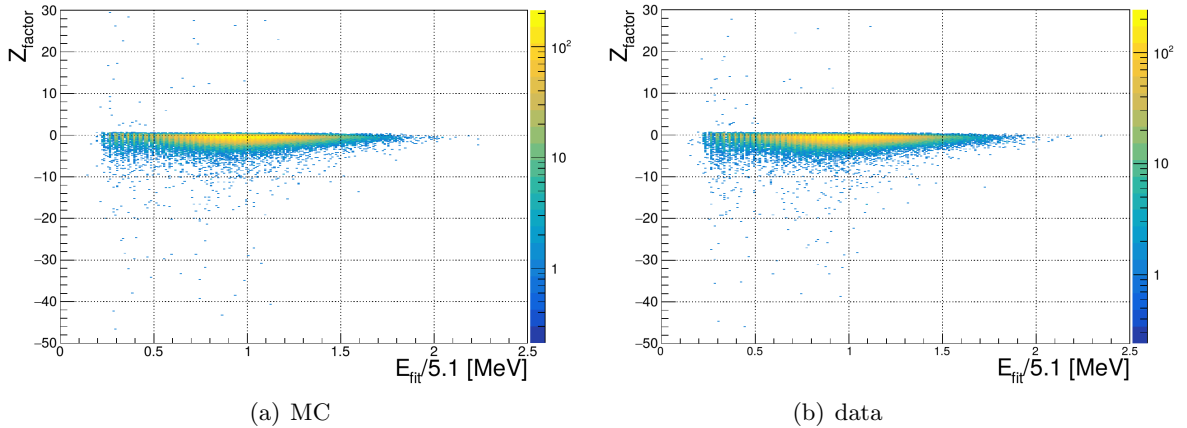


Figure 5.20:  $^{16}\text{N}$  central-run 107055,  $Z_{factor}$  vs.  $E_{fit}/5.1$  MeV.

### 5.3.4.2 Energy Resolution and Systematics

The RSP energy reconstruction algorithm mentioned in Chapter 4 was applied on  $^{16}\text{N}$  MC simulations and data. The reconstructed energy of the  $^{16}\text{N}$  events are shown in Fig. 5.25. The results from the MC and the data are compared.

The energy spectrum of the photons is converted into an apparent electron energy spectrum[137].

By simulating mono-energetic electrons events with different energies,

A 2D map describes the relationship between the number of Cherenkov photons and electron energy is shown in Fig. 5.24.

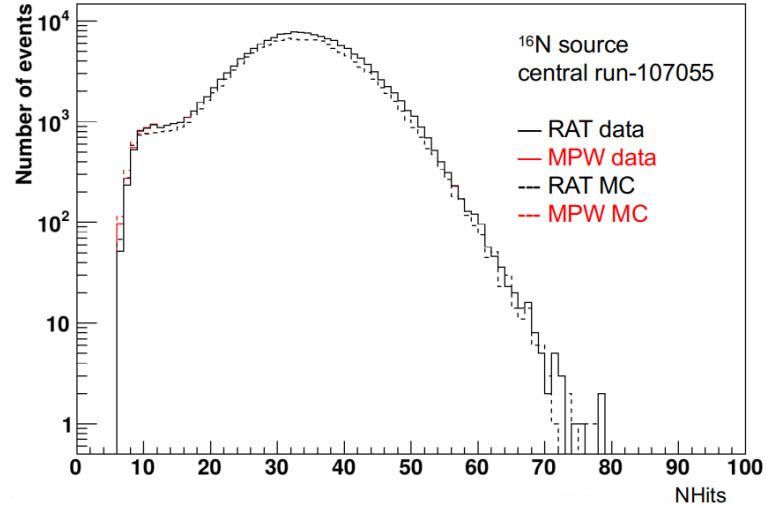


Figure 5.21: NHit spectrum for the  $^{16}\text{N}$  central run-107055. Dashed lines for the MC and solid lines for data; red for the MPW fitter results and black for the Rat results.

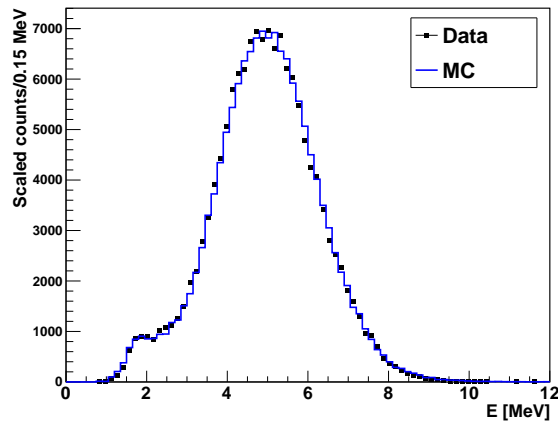


Figure 5.22: Reconstructed  $^{16}\text{N}$  energy spectrum for run-106925 ( $\vec{X}_{source} = (-186.0, 254.0, -4999.899)$  mm).

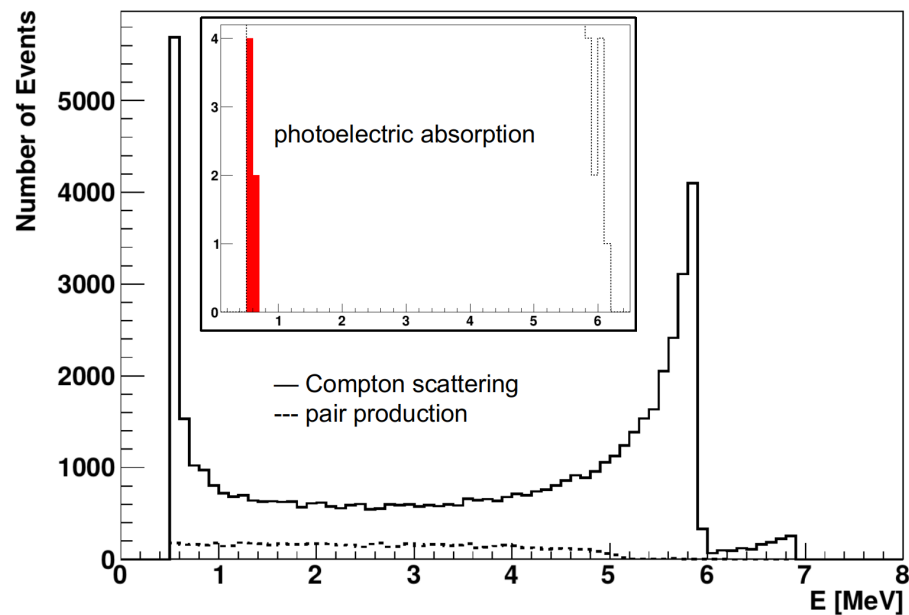


Figure 5.23: Simulated energy spectrum for different processes, extracted from  $10^5$  MC simulation events.

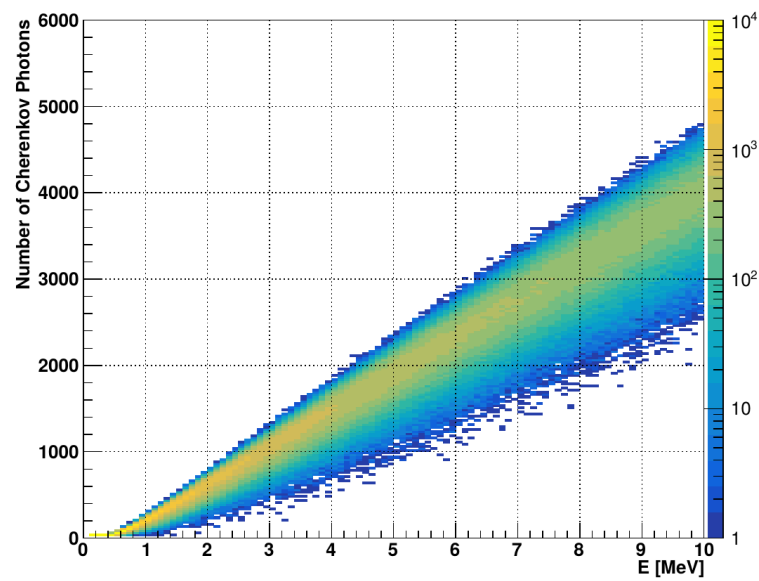


Figure 5.24: Electron energy vs number of Cherenkov photons.

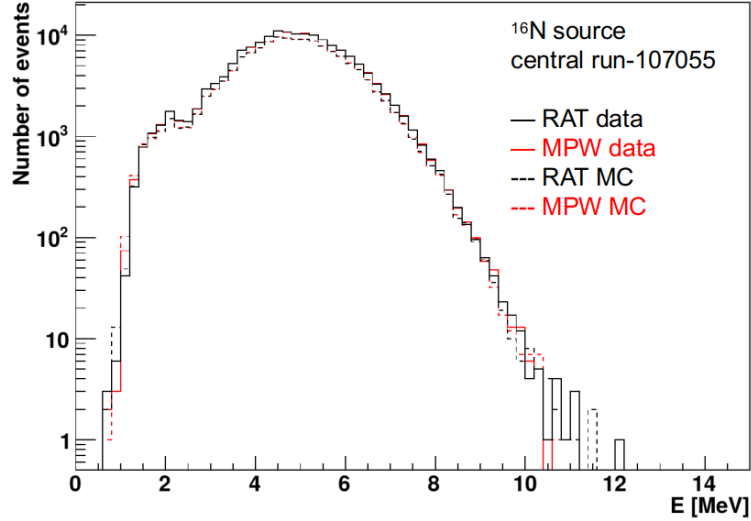


Figure 5.25: Reconstructed energy spectrum from the  $^{16}\text{N}$  central run-107055. Dashed lines for the MC and solid lines for data; red for the MPW fitter results and black for the Rat results.

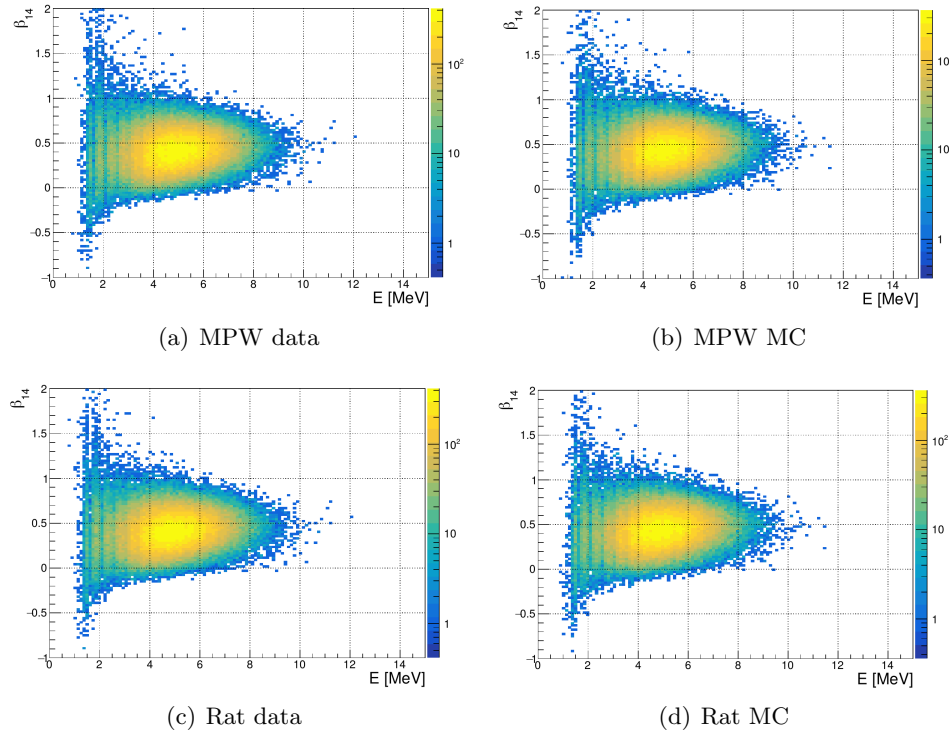


Figure 5.26: Energy vs  $\beta_{14}$  for the data and MC. Both the Rat and the MPW results are shown.

### 5.3.4.3 Energy Resolutions

To obtain the energy reconstruction resolutions, the reconstructed energy spectrum  $P(T_{eff})$  is fitted with the energy resolution function defined as[137]:

$$P(T_{eff}) = N \int P_{source}(T_e) \frac{1}{\sqrt{2\pi}\sigma} \exp\left\{-\frac{[(1 + \delta_E)T_{eff} - T_e]^2}{2\sigma^2}\right\}, \quad (5.10)$$

where the predicted apparent energy spectrum,  $P_{source}(T_e)$ , is convolved with a Gaussian resolution function. The  $P_{source}(T_e)$  spectrum includes

In the Gaussian function,  $\sigma$  is the detector resolution and  $\sigma = b\sqrt{T_{eff}}$ .

Before fitting the reconstructed energy spectrum with the energy resolution function, a few cuts were applied on both the data and MC: the position FoM cut  $scaleLogL > 10$  and the energy FoM cuts:  $0 < G_{test} < 1.9$ ,  $U_{test} < 0.95$  and  $-11 < Z_{factor} < 1$  mentioned in the previous sections were used; the cuts of  $NHit > 5$ ,  $ITR > 0.55$  and  $-0.12 < \beta_{14} < 0.95$  were used to remove instrumental backgrounds; a distance cut:  $d(\vec{X}_{fit}, \vec{X}_{src}) > 700$  mm was suggested by [156, 137] to remove the shadow effects when the events are close to the source container; for the event reconstructed within the 700 mm distance, if its direction  $\vec{u}_{fit}$  is within  $45^\circ$  of the vector from the source to its vertex, i.e., if  $\sqrt{2}/2 < \vec{u}_{true} \cdot \vec{u}_{fit} < 1$ , its energy will also be kept.

A default fit range of [3.5, 8.8] MeV was suggested by [137] to remove poorly reconstructed events due to the trigger inefficiency.

Fig. 5.27 shows the reconstructed energy spectrum fitted with the energy resolution functions, for both the MC and data.

### 5.3.4.4 Energy Uncertainties

The uncertainty of energy scale  $\delta_E$  and resolution are calculated as[137]:

$$\Delta_{\delta_E}^2 = (\delta_{E,data} - \delta_{E,MC})^2 + Error_{\delta,data}^2 + Error_{\delta,MC}^2, \quad (5.11)$$

$$\Delta_b^2 = (b_{data} - b_{MC})^2 + Error_{b,data}^2 + Error_{b,MC}^2, \quad (5.12)$$

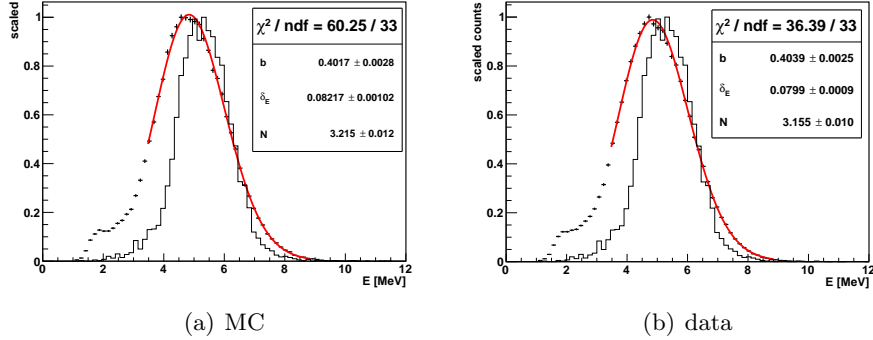


Figure 5.27: Fitted energy resolution function (red) with the reconstructed energy of  $^{16}\text{N}$  central run-107055 MC (a) and data (b).

For a fiducial volume  $r < 5.5 \text{ m}$ , I took the results from the  $^{16}\text{N}$  scans in this FV region and simply took the average of the results. This gives  $\overline{\Delta_{\delta_E}^2} = 0.036 \text{ MeV}$  and  $\overline{\Delta_b^2} = 0.011 \sqrt{\text{MeV}}$ .

Table 5.5: Energy scales and resolutions.

|                  | Data     | MC                             |
|------------------|----------|--------------------------------|
| b (MPW)          | 0.006%   | $(1 + 0.006/100) \cdot x_{MC}$ |
| $\delta_E$ (MPW) | -0.026 % | $(1 - 0.026/100) \cdot y_{MC}$ |

## 5.4 $^{16}\text{N}$ Calibration in Partial-fill Phase

During the August to October 2019, the PPO is added into the LAB when the water level was at 5100 mm (in PSUP coordinate). This is one of the stages of the partial-fill phase.

As mentioned in Chapter 3, the main purpose of the partial-fill phase is to identify the background level of the liquid scintillator.  $^{16}\text{N}$  and  $AmBe$  calibration sources were also deployed in the external water to test the response of the detector.

During the filling, the LAB was first filled into the AV to replace the water. PPO was later mixed with LAB and added into the AV. At some stage, the PPO concentration was kept at 0.53 g/L, which was lower than the nominal 2 g/L. At the lower PPO concentration, the liquid scintillator has a slower timing profile. This also brings an opportunity to extract

the Cherenkov signals from the liquid scintillator with low PPO concentration.

#### 5.4.1 High Level Cuts: Sky-shine Classifier

During the partial-fill phase, a Sky-shine classifier was suggested by Mark Chen and developed by Jeff Tseng to discriminate the noise events coming from the top of the detector, the so-called “sky shine” events, from other backgrounds events in the AV detection region[16]. These sky shine events are mostly the backgrounds from radioactive decays happening in the neck region.

For an event happens in the neck region, it can trigger more PMTs in the bottom (or the lower hemisphere) of the PSUP sphere than in the higher hemisphere, as illustrated in Fig. 5.28. The classifier counts the number of the triggered PMTs with  $z_{PMT} < -1000 \text{ mm}$  (in PSUP coordinate) as  $n_{Signal}$  and the number of the ones with  $-1000 < z_{PMT} < 8000 \text{ mm}$  as  $n_{Side}$ . The ratio  $skyShine = n_{Side}/n_{Signal}$  is the output value of the classifier. Meanwhile, the classifier also saves the counts of the triggered neck PMTs ( $n_{Neck}$ ) as well as the triggered outward looking (OWL) PMTs in high z positions with  $z_{OWL} > 8000 \text{ mm}$  ( $n_{OWL}$ ).

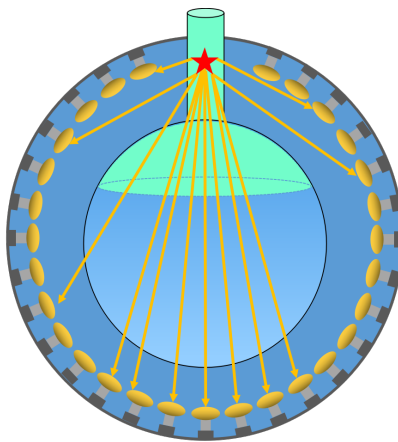


Figure 5.28: An illustration for the Sky-shine classifier, modified from [16].

In the following, I studied the performance of the Sky-shine classifier and attempted to obtain an optimized cut on the value of  $skyShine$  based on the MC simulations.

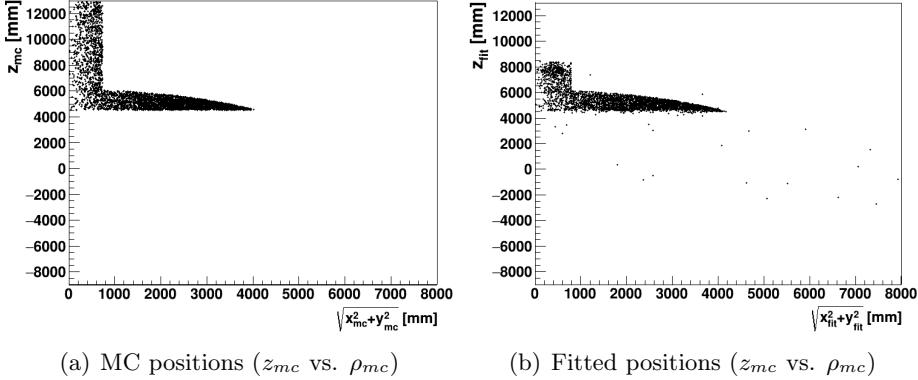


Figure 5.29: MC (left) and fitted positions (right) of  $^{208}\text{Tl}$  simulations.

#### 5.4.1.1 Performance of the Sky-shine Classifier

The MC simulations of the  $^{208}\text{Tl}$  decay events were produced in a partial-fill geometry with the water level set at 4435 mm (in AV coordination) and 2 g/L PPO concentration. The  $^{208}\text{Tl}$  decay events were distributed uniformly in the scintillator region. 4067 events of  $^{208}\text{Tl}$  decays were simulated (about 16 times the expected number of events per year based on the SNO+ background evaluations[108]) and 3784 events were triggered. RAT version 6.16.9 was used.

Fig. 5.29 shows the positions of the simulated events and the fitted events. In the MC simulations, events are distributed in the AV as well as the whole region of the neck. Recall that the neck of the detector is 8-m tall, the MC simulated neck events from  $z_{neck,bottom} = 6108\text{ mm}$  up to about  $z_{neck,top} = 13000\text{ mm}$  in the PSUP coordinate. The valid reconstruction region is inside the PSUP sphere, thus only a small fraction of the neck events in the volume of the neck cylinder inside the PSUP sphere can be fitted or even be triggered.

The plots shows events with small values of Sky-shine calculations can be tagged as neck events.

By checking the MC events positions (“true” event positions), for all the triggered events, 16.8% of them are outside the AV. Apply skyShine<sub>>1.7</sub> can remove 98.6% of the events outside the AV (mostly in the neck) with a sacrifice of 0.2% of the events inside the

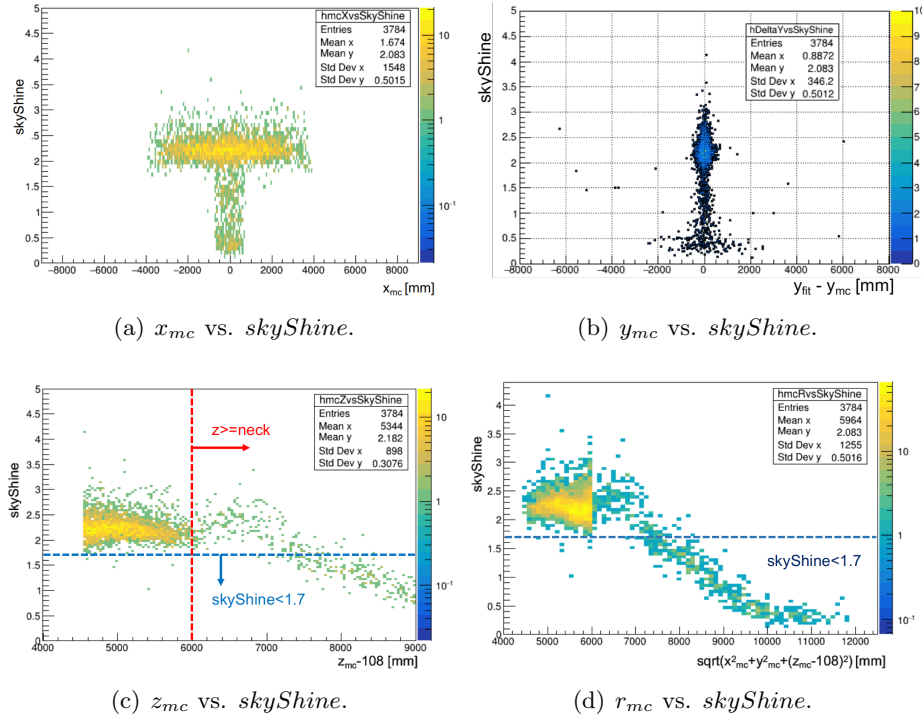


Figure 5.30: MC positions vs. skyShine values for simulated  $^{208}\text{Tl}$  events.

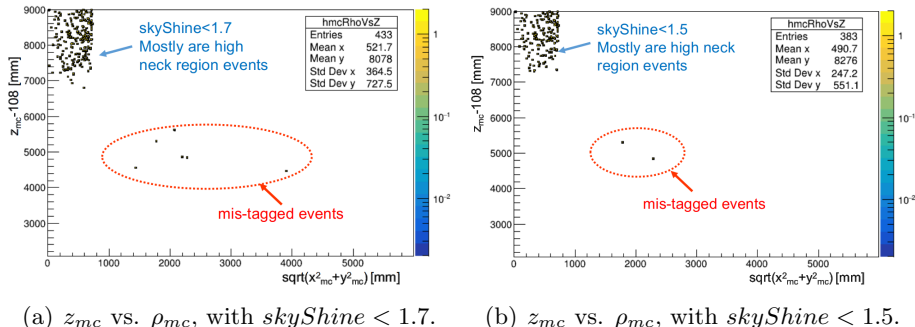


Figure 5.31: MC positions after Sky-shine cuts ( $skyShine < 1.7$  and  $skyShine < 1.5$ ) for simulated  $^{208}\text{Tl}$  events. It shows that most of the events with small  $skyShine$  values are located in the neck region while very few events in the FV region can be mis-tagged.

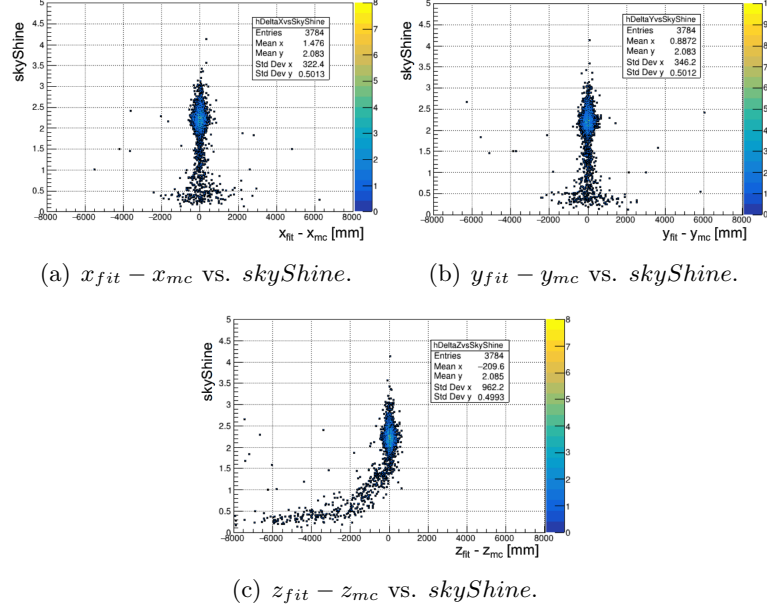


Figure 5.32: Fit biases vs. skyShine values for simulated  $^{208}\text{Tl}$  events.

AV.

#### 5.4.1.2 Optimize the Sky-shine Cuts

Since the Sky-shine classifier removes neck events (most of them are outside the PSUP) which are not properly fitted, a skyShine cut can reduce the fit biases and improve the fit resolution.

skyShine vs. fit biases ( $^{208}\text{Tl}$ )

An improvement of  $\sim 18$  mm in z resolution.

Apply different cuts of  $skyShine$ :  $skyShine > 1, 1.01, 2.0$ , begins from 1.0 with a 0.01 step until 2.0. Plot the x bias  $x_{fit} - x_{mc}$  versus the  $skyShine$  cut values.

Fit a gaussian to  $x_{fit} - x_{mc}$  and get  $\sigma_x$ , Do the same thing to the  $y_{fit} - y_{mc}$ ,  $z_{fit} - z_{mc}$  and obtain  $\sigma_x, \sigma_y, \sigma_z$  Fill a 1D histogram of Sky-shine cut and  $\Delta R = \sqrt{\sigma_x^2 + \sigma_y^2 + \sigma_z^2}$

Compare to the number of MC events inside the scintillator  $\sqrt{(x^2 + y^2 + (z - 108)^2)} < 6005$  mm &  $z - 108 < 6000$  mm, number of MC events/number fitted events after cut:  $skyShine > 1.6$ : 3149/3376  $skyShine > 1.7$ : 3149/3351 Can check with more produc-

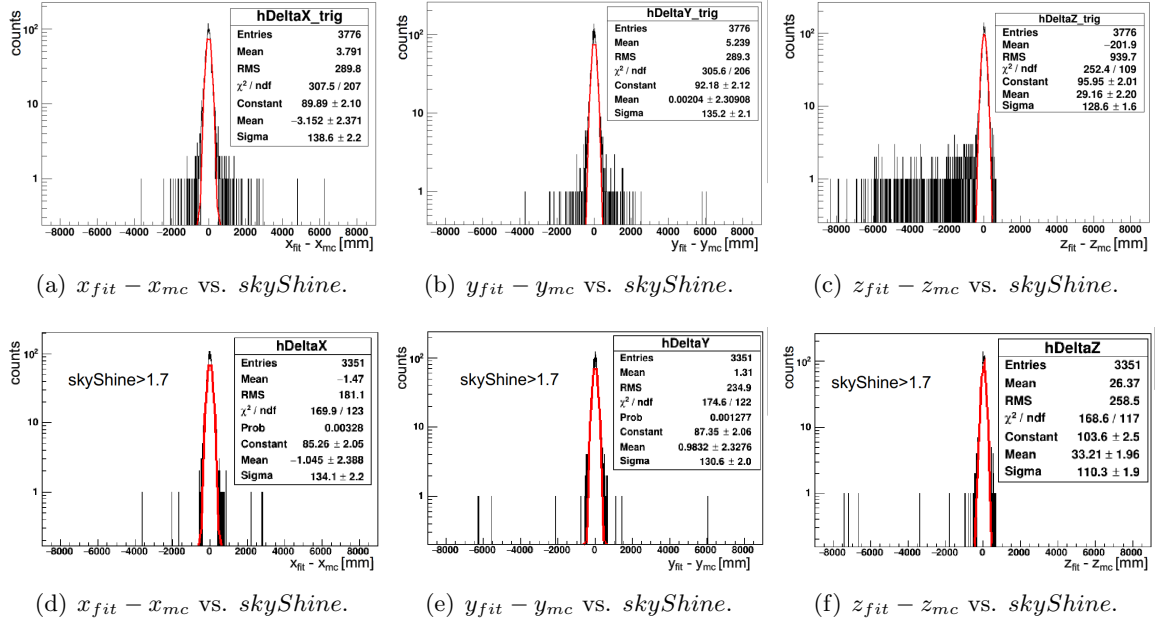
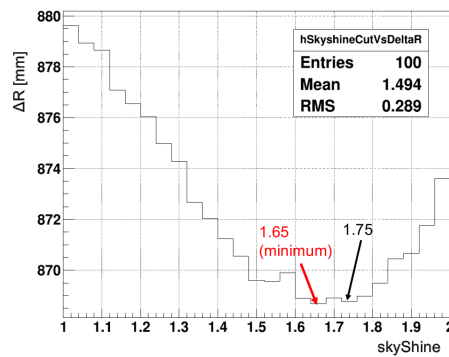
Figure 5.33: Fit biases vs. skyShine values for simulated  $^{208}\text{Tl}$  events.

Figure 5.34: Radial resolutions with different skyShine cuts.

tions/higher statistics.

### 5.4.2 $^{16}\text{N}$ Calibration in the Partial-fill Phase

water level was at 5100 mm from the center of the AV (in AV coordination). LAB with a PPO concentration of 0.53 g/L

Effect of the water level.

The  $^{16}\text{N}$  source was deployed in the external water region during the partial-fill phase. run 251748 2019/09/19 and

Source position was at  $(-1120.8, 1041.4, 6172.5)$  mm for a 30-minute duration and at  $(-1120.8, 1041.4, 6108.0)$  mm for a 7-hour duration (separated into 7 runs).

### 5.4.3 Extracting the Cherenkov Signals in Partial-fill Phase

For an event happens in liquid scintillator, the number of Cherenkov photons it created is only  $\sim 5\%$  of the total photon numbers, which is a very small fraction compared to the number of scintillation photons. This causes the directional Cherenkov signals are submerged in the isotropic lights.

Since the  $^{16}\text{N}$  source provides high energy events around 6 MeV,

a time cut window on the time residual was optimized for the searching based on MC. simulations in pure scintillator phase.

In the case that  $e^-$  are generated uniformly and isotropically in the detector, to enhance the Cherenkov ring pattern, a transformation is applied as following:

$$\phi = \arccos(\hat{\vec{u}}_e \cdot \hat{\vec{u}}_{assume})$$

$$\vec{n} = \hat{\vec{u}}_e \times \hat{\vec{u}}_{assume}$$

$$R = \begin{bmatrix} n_x^2(1 - \cos \phi) + \cos \phi & n_x n_y(1 - \cos \phi) - n_z \sin \phi & n_x n_z(1 - \cos \phi) + n_y \sin \phi \\ n_x n_y(1 - \cos \phi) + n_z \sin \phi & n_y^2(1 - \cos \phi) + \cos \phi & n_y n_z(1 - \cos \phi) - n_x \sin \phi \\ n_x n_z(1 - \cos \phi) - n_y \sin \phi & n_y n_z(1 - \cos \phi) + n_x \sin \phi & n_z^2(1 - \cos \phi) + \cos \phi \end{bmatrix}$$

$$\vec{u}'_e = R \vec{u}_e$$

$$\vec{X}'_{evt} = R \vec{X}_{evt}$$

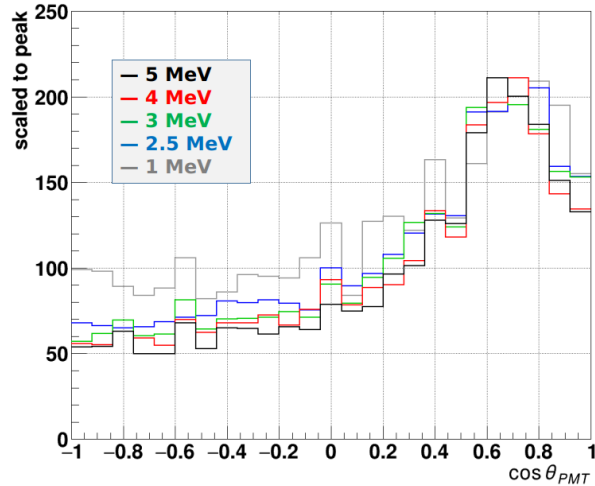


Figure 5.35: Distributions of  $\cos \theta_{PMT}$  after the prompt time cut for various  $e^-$  energies simulations.

Move  $\vec{X}'_{evt}$  to the origin,

$$\vec{X}'_{pmt} = R\vec{X}_{pmt} - \vec{X}'_{evt}$$

Turning off the Cherenkov process in the Monte Carlo simulations.

Breit-Wigner function

$$p(x) = \frac{c_0}{\pi} \frac{\frac{1}{2}\Gamma}{(x - m)^2 + (\frac{1}{2}\Gamma)^2} + c_1$$

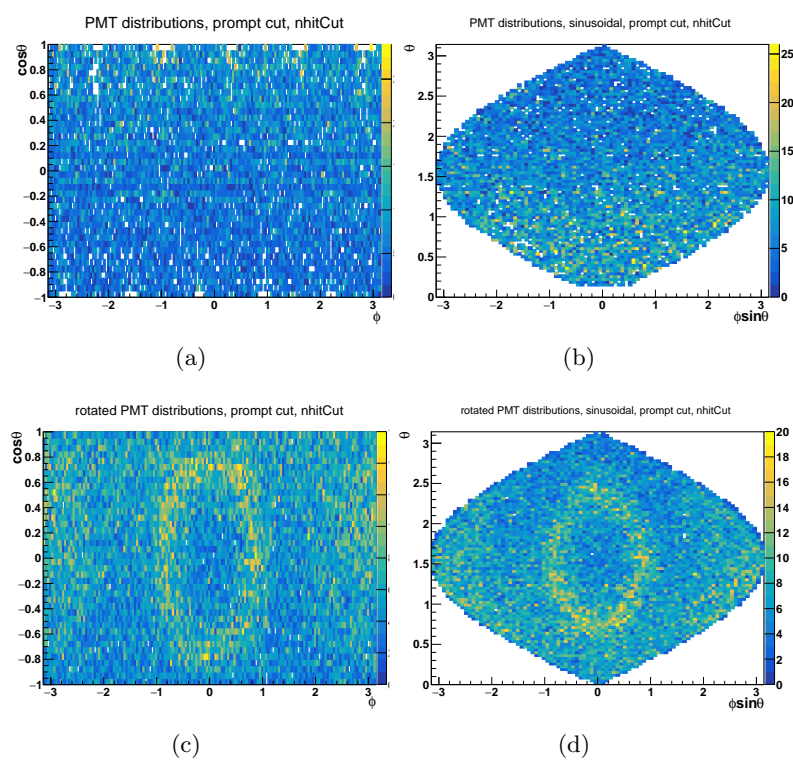


Figure 5.36: PMT hit patterns after the prompt time cut and NHit cut.

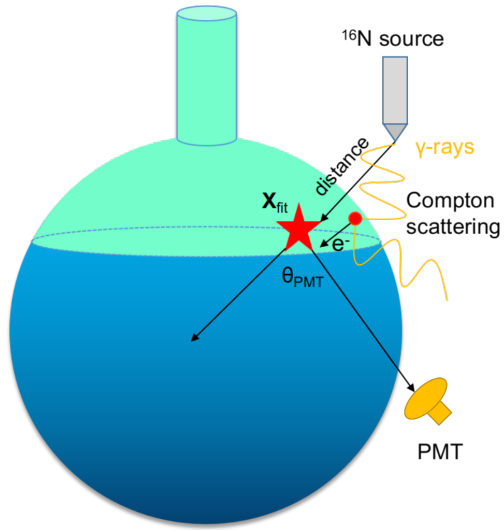


Figure 5.37:  $^{16}\text{N}$  source calibration in external water during the partial-fill phase.

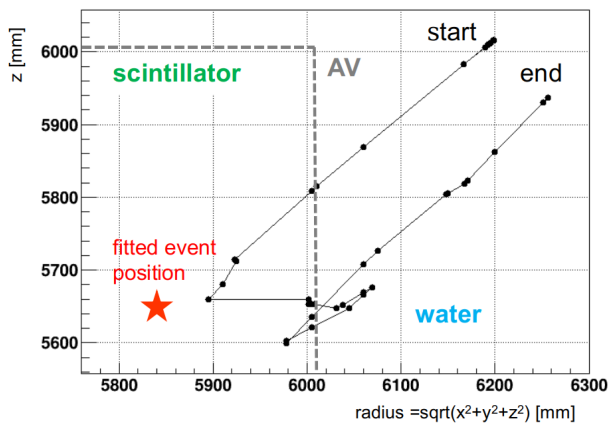


Figure 5.38: Simulated main track of 7.1 MeV  $\gamma$  for one event from  $^{16}\text{N}$  source in the external water during the partial-fill phase.

## Chapter 6

# Solar Neutrino Analysis in the SNO+ Water Phase

The SNO+ water phase data were taken from May 2017 to September 2018. The period from May 2017 to October 2018 is the first stage of the water phase. During this stage, several calibration runs were taken, including the  $^{16}\text{N}$  calibration scans and the laserball scans. During the period from October 2018 to July 2019, over 20 tonnes of LAB (without PPO) was filled into the detector and the LAB mostly occupied the neck volume, slightly below the neck bottom. With the nitrogen cover gas on the top of the AV, the dataset taken during this period is called “low background dataset”. In this study, 4838 runs of data were used, which summed up a total live time of 190.31 days after the data cleaning process.

In this chapter, I applied the MPW reconstruction algorithm described in Chapter 4 as a position and direction fitter to the raw dataset as well as the run-by-run MC simulations. The fitted event vertex was used by the energy fitter developed by the SNO+ collaboration.

First, the open dataset taken in 2017 was used to test the MPW results, compared to the official RAT results. A quantity called “KullbackLeibler Divergence” was developed to evaluate the Cherenkov signals. After that, I mainly analyzed the low background dataset. I used sub datasets of the run-by-run MC simulations to evaluate the ability of separating

the solar  $\nu_e$  signals from the backgrounds. The Toolkit for Multivariate Data Analysis with ROOT (TMVA) package [157, 158] was used to train and test on the MC simulations to obtain optimized discriminants. These optimized discriminants were applied on the whole dataset to remove the backgrounds.

The outputs from the data were fitted to obtain the number of signal events and the background events. Ensemble tests were performed on fake datasets to check the fit pull and bias. The systematics obtained from the  $^{16}\text{N}$  calibration in Chapter 5 were applied on the results. Finally, the solar  $\nu_e$  interaction rates and the  $^8\text{B}$  solar neutrino flux were evaluated.

## 6.1 Detector Backgrounds

### 6.1.1 Physics Backgrounds

As mentioned in Chapter 2, 3.1, since the depth of the SNO+, the cosmogenic backgrounds induced by the cosmic muons are very few. Most backgrounds come from radioactive isotopes inside or around the detector, mostly from the  $\beta$ -decays of  $^{214}\text{Bi}$  and  $^{208}\text{Tl}$ . Table. is a summary of the  $\beta$ -decays from these two isotopes.

Data taken from [116].

To investigate the background contamination, ex-situ and in-situ ... Radon assays. MC simulations were produced.

the instrumental backgrounds can be removed by the data-cleaning approaches.

## 6.2 KullbackLeibler (KL) Divergence for High Level Cuts

The KullbackLeibler (KL) divergence (also called “relative entropy”) is used to measure the dissimilarity of two probability distributions[159]. I used this quantity to compare the reconstructed angular distribution of an event,  $\vec{u}_{fit} \cdot (\vec{X}_{PMT} - \vec{X}_{fit}) / |\vec{X}_{PMT} - \vec{X}_{fit}|$ , with the angular distribution of solar  $\nu_e$  events extracted from the MC (expected as a Cherenkov distribution) to check the dissimilarity of the event compared with the solar  $\nu_e$  event. The

quantity  $D_{KL}(p||q)$  is calculated as:

$$klDiv(p||q) \equiv \sum_i^N p(x_i) \log \frac{p(x_i)}{q(x_i)}, \quad (6.1)$$

where  $p(x_i)$  is the angular distribution after a time residual window cut:  $-5 < t_{Res} < 1 \text{ ns}$ , to extract prompt Cherenkov lights. Both of the event and the MC distributions were filled into a histogram with 40 bins ranging from [-1,1] and the  $klDiv$  values were calculated bin by bin except the empty bins (zero count). A small  $klDiv$  value indicates a small dissimilarity.

These values were used for distinguishing the signal from backgrounds, which will be discussed in the section ???. Fig. 6.1 shows an example of the  $klDiv$  calculation. Two events are compared here. One is a randomly selected event from the solar  $\nu_e$  run-by-run MC ( $E = 4.78 \text{ MeV}$ ), the other is from the  $^{214}\text{Bi}$  MC ( $E = 2.18 \text{ MeV}$ ), with the same event GTID. It can be seen that the background event with lower energy is more dispersive while the signal event has a peak around the Cherenkov angle ( $\sim 0.75$ ) and thus its shape is more close to the pdf. The calculation of 6.1 gives  $klDiv(\text{solar } \nu_e) = 11.78$  and  $klDiv(^{214}\text{Bi}) = 22.69$ , which verifies the observation.

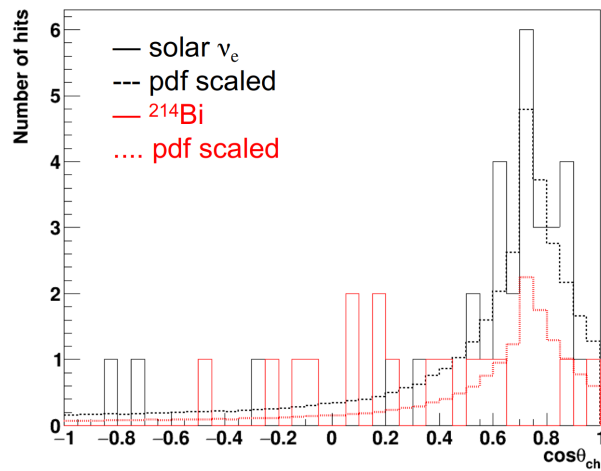


Figure 6.1: Angular distributions of the MC events in run-by-run simulation 206391, with the same event GTID = 7. The black line is the MC solar  $\nu_e$  distribution, while the red line is the MC  $^{214}\text{Bi}$  distribution. The pdf is scaled to the number of the hits in solar  $\nu_e$  event (black dashed line) and the  $^{214}\text{Bi}$  event (red dotted line) respectively.

A symmetrical form of  $klDiv$  can be taken as:

$$klDiv(p, q) \equiv \frac{1}{2} \sum_i^N (p \log \frac{p}{q} + q \log \frac{q}{p}), \quad (6.2)$$

Since  $klDiv(p, q) = klDiv(q, p)$ , it has a meaning of distance. The quantity is not used in the thesis, but can be considered in future.

## 6.3 Solar $\nu_e$ Analysis and Background Separation in Water Phase

### 6.3.1 Open Dataset Analysis

This open dataset was used to compare the MPW and the RAT fitted results.

In SNO+ water phase, solar  $\nu_e$ s are basically measured via elastic scattering  $\nu_e + e^- \rightarrow \nu_e + e^-$ . The maximum kinetic energy of the recoil electron is  $T_{max} = \frac{2E_\nu^2}{2E_\nu + m_ec^2}$  the cross section is  $\sigma(\nu_e + e^- \rightarrow \nu_e + e^-) = 9.52 \times 10^{-44}(E_\nu/10 \text{ MeV}) \text{ cm}^2$  the expected solar neutrino rate is  $R = A \int_{T_{thresh}}^{T_{max}} \frac{d\sigma}{dE} \frac{dN}{dE_\nu} dE_\nu$ .

The direction of the scattered electron is correlated with the direction of the incident neutrino. A “solar angle”,  $\theta_{sun}$  is the direction of the event relative to the Sun’s location,  $\nu - e^-$  elastic scattering:

$$\cos \theta_{sun} = \sqrt{\frac{T_e(m_e + E_\nu)^2}{2m_e E_\nu^2 + T_e E_\nu^2}} \quad (6.3)$$

For the data, the solar angle is defined as:

$$\cos \theta_{sun} \equiv \vec{u}_{event} \cdot \frac{\vec{X}_{event} - \vec{X}_{sun}}{|\vec{X}_{event} - \vec{X}_{sun}|}, \quad (6.4)$$

where  $\vec{X}_{sun}$  is taken as the Sun’s location relative to the SNOLAB location since the whole lab can be treated as a point regarding the long distance to the Sun.

High level cuts mentioned in 5.2 were applied.

solar neutrino candidate events in the open dataset.

Compare the  $klDiv$  quantities for the MPW and RAT results.

A plot of refitting the RAT candidate solar events with the MPW on old dataset.

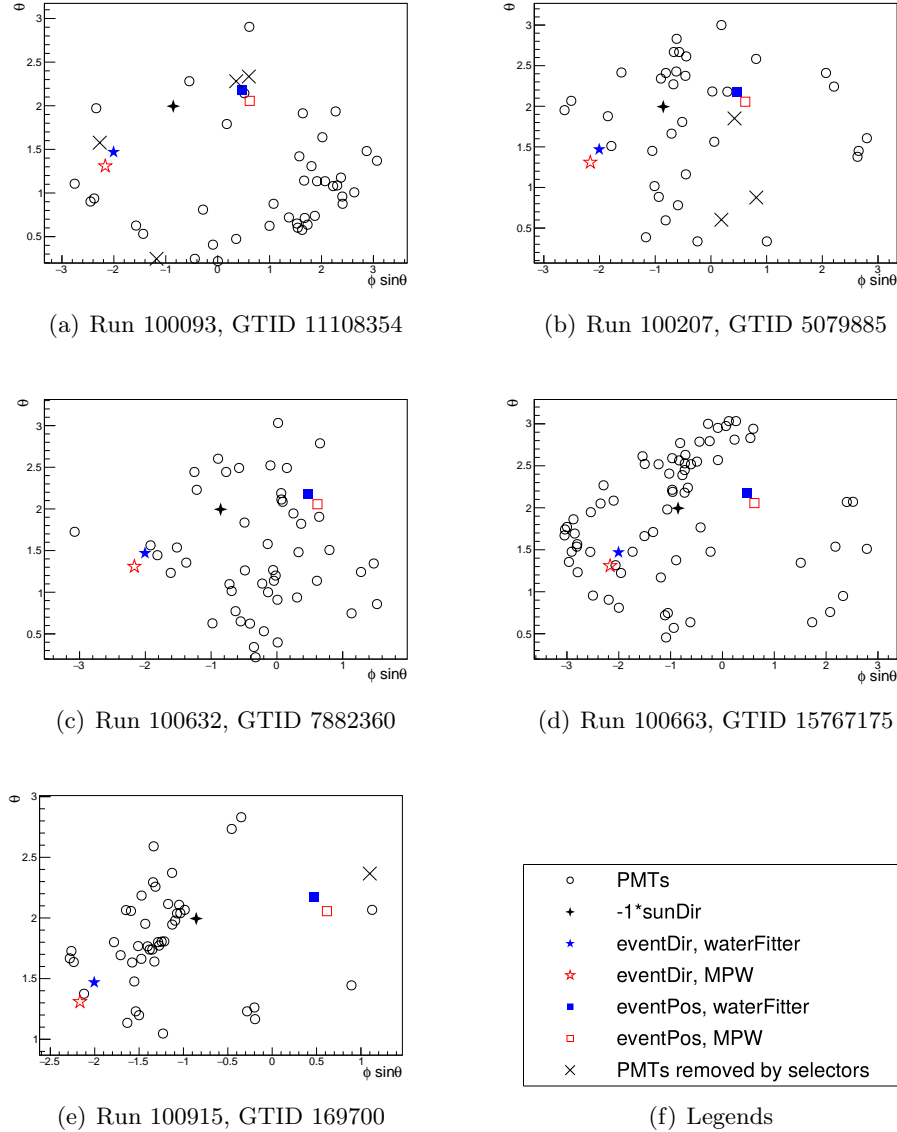


Figure 6.2: Fit results for the candidate events, projected onto PMT sinusoidal maps. Black circles stand for the hit PMTs used by the fitter; crosses stand for the hit PMTs removed by the selectors; blue full star stands for the event direction fitted by the waterFitter; red open star stands for the direction fitted by the MPW; full double diamond stands for the solar direction\*-1; blue full square stands for the event position fitted by the waterFitter; open square stands for the position fitted by the MPW.

Table 6.1: Candidate events in the open dataset. Compared the fitted results of the candidate events with different fitters.

| Fitter | Run    | GTID     | $z - 0.108(\text{m})$ | $R(\text{m})$ | $(R/R_{av})^3$ | $\cos \theta_{\text{sun}}$ | SNO+ Day |
|--------|--------|----------|-----------------------|---------------|----------------|----------------------------|----------|
| Rat    | 100093 | 11108354 | 3.49                  | 3.57          | 0.21           | -0.954                     | 2683.92  |
| MPW    | –      | –        | 3.43                  | 3.52          | 0.20           | -0.906                     | –        |
| Rat    | 100207 | 5079885  | -2.61                 | 4.60          | 0.45           | 0.816                      | 2687.04  |
| MPW    | –      | –        | -3.63                 | <b>7.61</b>   | 2.03           | <b>0.656</b>               | –        |
| Rat    | 100632 | 7882360  | 1.77                  | 3.19          | 0.15           | 0.937                      | 2696.93  |
| MPW    | –      | –        | 1.67                  | 3.11          | 0.14           | 0.911                      | –        |
| Rat    | 100663 | 15767175 | -4.33                 | 4.96          | 0.56           | 0.978                      | 2698.18  |
| MPW    | –      | –        | -4.45                 | 5.07          | 0.60           | 0.980                      | –        |
| Rat    | 100915 | 169700   | -1.00                 | 5.10          | 0.61           | 0.341                      | 2701.23  |
| MPW    | –      | –        | -1.08                 | 5.08          | 0.61           | 0.337                      | –        |

Table 6.2: Candidate events in the open dataset, searched by the MPW fitter.

| Run    | GTID     | energy | $z - 0.108$ | $R$  | $(R/R_{av})^3$ | $\cos \theta_{\text{sun}}$ |
|--------|----------|--------|-------------|------|----------------|----------------------------|
| 100093 | 11108354 | 5.827  | 3.43        | 3.52 | 0.20           | -0.907005                  |
| 100632 | 7882360  | 6.183  | 1.67        | 3.11 | 0.14           | 0.9146124                  |
| 100663 | 15767175 | 6.182  | -4.45       | 5.07 | 0.60           | 0.9807349                  |
| 100915 | 169700   | 5.684  | -1.07       | 5.08 | 0.61           | 0.3385341                  |
| 100984 | 8621621  | 5.701  | 0.76        | 4.75 | 0.502          | -0.647735                  |
| 101075 | 11673714 | 5.667  | 4.43        | 5.18 | 0.64           | 0.5873025                  |

### 6.3.2 TMVA Analysis

?? The MC simulations of the runs 200004 to 203602 were used. These run-by-run simulations simulated the full detector conditions for every run. This is a sub-dataset to the whole “low background dataset”, with a live time of 92.54 days for testing and training the TMVA methods.

Two types of background isotopes,  $^{208}\text{Tl}$  and  $^{214}\text{Bi}$  were simulated in different detector regions. In this study, the background events simulated in the inner AV (internal backgrounds) , in the AV and in the external water region were checked. The solar  $\nu_e$  events simulated in the inner AV were used as signals. Table. 6.3 summarizes the types of simulations used in this study.

Different types of the simulations were merged into a mixed dataset. The simulated solar  $\nu_e$  events are tagged as signals and mixed with  $^{214}\text{Bi}$  and  $^{208}\text{Tl}$  background events.

Table 6.3: Datasets of MC simulations.

| Simulations       | Simulated positions in the detector          |
|-------------------|--|
| $^{208}\text{Tl}$ | inner AV (internal $^{208}\text{Tl}$ )       |
| –                 | AV   |
| –                 | external water (external $^{208}\text{Tl}$ ) |
| $^{214}\text{Bi}$ | inner AV (internal $^{214}\text{Bi}$ )       |
| –                 | AV   |
| –                 | external water (external $^{214}\text{Bi}$ ) |
| Solar $\nu_e$     | inner AV (internal $\nu_e$ )                 |
| –                 | AV   |
| –                 | external water (external $\nu_e$ )           |

The total dataset was divided into training and testing sets.

Fig. 6.3 shows the energy spectrum of simulated internal events with their fitted positions inside the 5.5-m fiducial volume, i.e., with a radial cut of  $R'_{fit} < 5.5 \text{ m}$ , where the  $R'_{fit}$  is the magnitude of the reconstructed event position  $\vec{X}_{fit}$  after the AV coordinate correction:  $R'_{fit} \equiv \sqrt{x_{fit}^2 + y_{fit}^2 + (z_{fit} - 108)^2}$ . The 108 mm offset in  $z$  was discussed in Chapter 3 and Chapter 4.

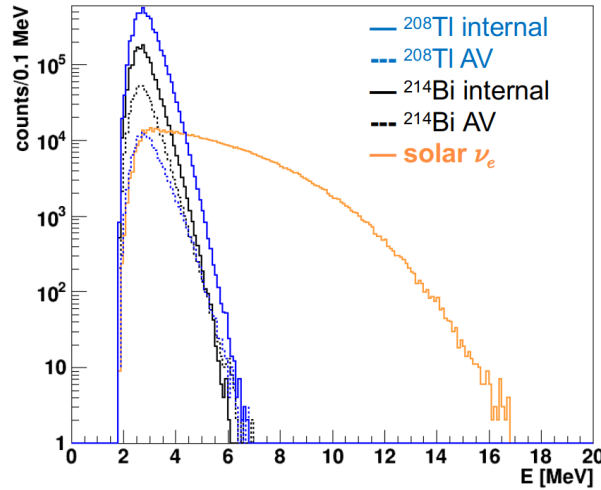


Figure 6.3: Energy spectrum of the simulated events for  $^{214}\text{Bi}$  (black),  $^{208}\text{Tl}$  (blue) and solar  $\nu_e$  (orange). Solid lines show the internal events and dotted lines show the AV events.

In this sub-dataset, runs from 201700 to 202516 were taken as the training set (69.5% of the total sub-dataset), and the rest 30.5% were taken as testing set. Once the weights of

the variables were tuned, they were put into the actual data.

Before the analysis, a few “beforehand cuts” were applied:  $N_{Hits} > 20$ ,  $R'_{fit} < 5500\text{ mm}$ ,  $ITR > 0.55$ ,  $-0.12 < \beta_{14} < 0.95$ . Here  $N_{Hits} > 20$  was applied as a reconstruction threshold. Only the events with  $N_{Hits} > 20$  were reconstructed by the MPW fitter for the solar neutrino analysis; a default fiducial volume of  $5.5\text{ m}$  was set; the  $ITR$  and  $\beta_{14}$  cuts were suggested by the collaboration, which were mostly based on the experiences for removing the instrumental backgrounds[137].

Distributions of input variables: signal vs combined backgrounds

After applying these beforehand cuts, for  $4 < E_{fit} < 15\text{ MeV}$ , the training dataset had 416780 events and the testing dataset had 184330 events.

Two other ranges of  $E_{fit}$  were also tested:  $4 < E_{fit} < 5$  (low energy region) and  $5 < E_{fit} < 15$  ( $E > 5$  region).

After the training and testing datasets were ready, three classification methods implemented in the TMVA package were used: the Fisher discriminants/linear discriminant analysis (Fisher/LD), the Boosted Decision Tree (BDT), and the Artificial Neural Networks Multilayer Perceptron (ANN-MLP, or MLP in short)[158].

The Fisher discriminant  $y_{F_i}(i)$  for classifying event  $i$  is defined by [157]:

$$y_{F_i}(i) = F_0 + \sum_{k=1}^{n_{params}} F_k x_k(i), \quad (6.5)$$

where  $n_{params}$  is the number of input variables; the Fisher coefficients,  $F_k$  is given by:

$$F_k = \frac{\sqrt{N_S N_B}}{N_S + N_B} \sum_{l=1}^{n_{params}} 1/W_{kl}(\bar{x}_{S,l} - \bar{x}_{B,l}), \quad (6.6)$$

where  $N_{S(B)}$  are the number of signal (background) events in the training sample;  $x_{S(B),l}$  are the means of input variables for signal (background);  $W_{kl}$  is the covariance matrix[157].

For the BDT method, the adaptive boosting (AdaBoost) algorithm was used; 400 trees were trained with a maximum depth of 3; gini index was used for the decision tree.

For the MLP method, sigmoid function was set as the activate function; 4 hidden layers, 200 training cycles were used.

I used 9 variables as inputs:  $ITR$ ,  $\beta_{14}$ ,  $E_{fit}$ ,  $G_{test}$ ,  $U_{test}$ ,  $scaleLogL$ ,  $Z_{factor}$ ,  $\vec{u} \cdot \vec{R}$  and  $kldiv$ . Among them, the input values of  $ITR$  and  $\beta_{14}$  were after the beforehand cuts mentioned above. The  $NHits$  and  $\theta_{ij}$  were not used, since the  $NHits$  is correlated to the energy while the  $\theta_{ij}$  is anticorrelated to the  $\beta_{14}$ .

The MLP method gave the best results, while it was the most CPU-consuming method. The output signal/background distributions on the test sub dataset are shown in Fig. 6.4.

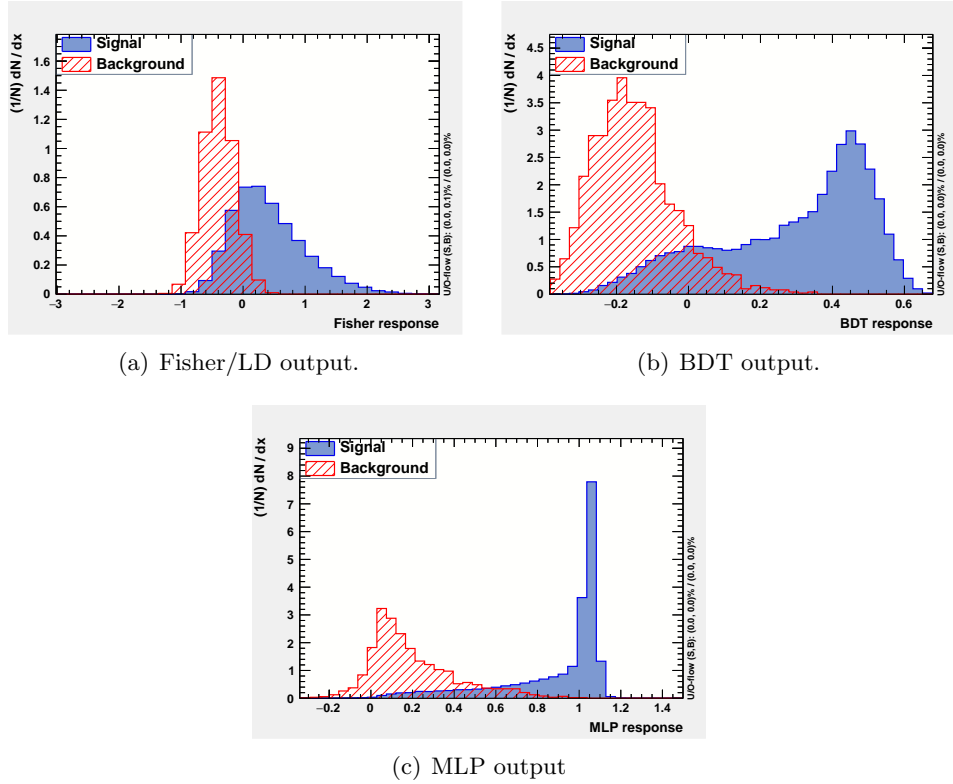


Figure 6.4: TMVA outputs for signal/background separations by different methods.

As one of the essential TMVA output, the background rejection versus signal efficiency curve is also called a receiver operating characteristic (ROC) curve, which is usually used to test the performance of machine learning classifier. A quantity taking the integrals of the ROC curve: called the “area under the curve” (AUC) is often used to summarize the quality of a ROC curve[159]. Fig. 6.5 shows the ROC curves for different methods: where

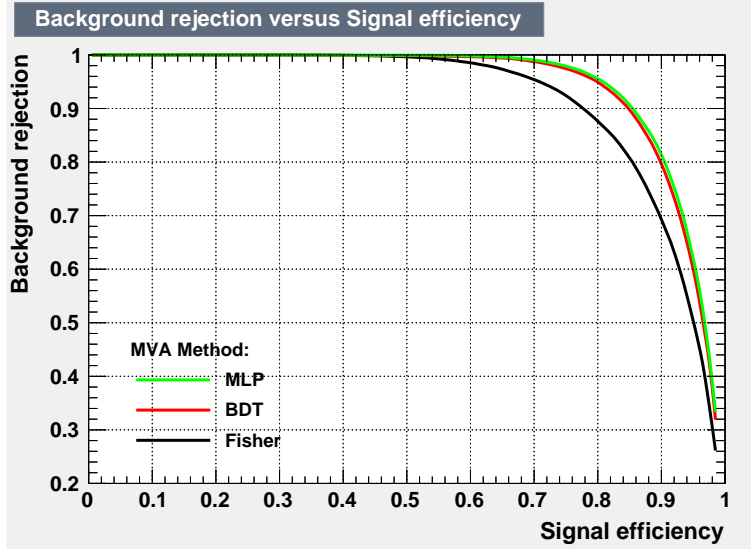


Figure 6.5: ROC curves from TMVA output, for event with  $4 < E_{fit} < 15 \text{ MeV}$ .

the Fisher/LD is the worst case; the BDT and MLP outputs are close to each other while the MLP gives the largest AUC values.

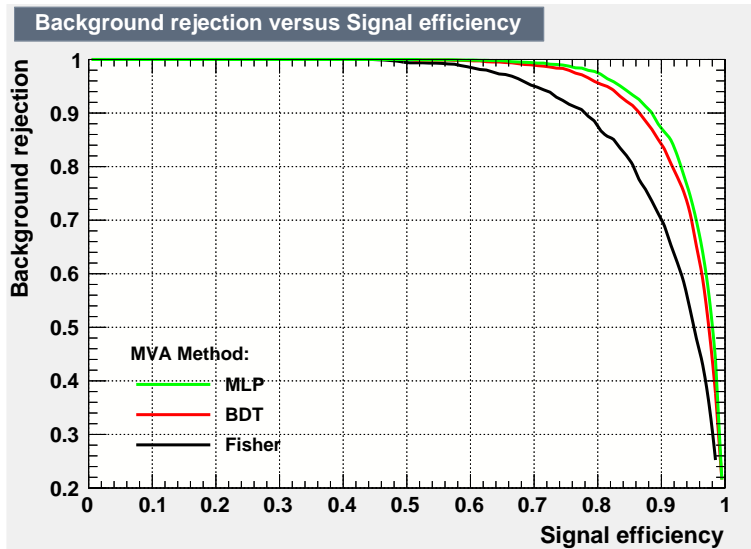


Figure 6.6: ROC curves from TMVA output, for event with  $5 < E_{fit} < 15 \text{ MeV}$  (energy above 5 MeV).

A typical CPU time for a certain method to train the dataset is listed in Table. 6.4, 6.5 and 6.6.

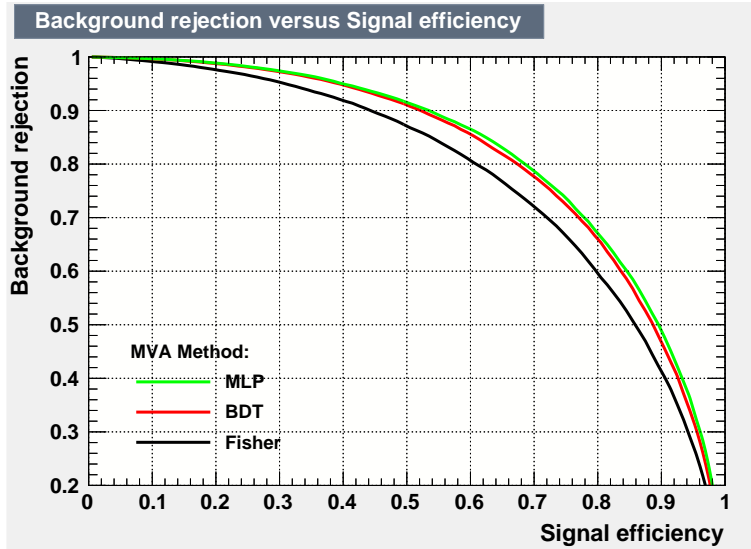


Figure 6.7: ROC curves from TMVA output, for event with  $4 < E_{fit} < 5 \text{ MeV}$  (low energy region).

Table 6.4: Testing results of  $4 < E_{fit} < 15 \text{ MeV}$  from different TMVA methods.

| Method    | AUC   | CPU time (second/ $10^6$ events) |
|-----------|-------|----------------------------------|
| Fisher/LD | 0.915 | 0.81                             |
| BDT       | 0.940 | 249.53                           |
| MLP       | 0.944 | 1370.02                          |

It shows that, when the energy goes lower, it is more difficult to separate the signals from the backgrounds.

The distributions of the “solar angle”,  $\cos \theta_{sun}$  were used to show the performance of the solar  $\nu_e$  event selection and background event discrimination. It is also used to extract the number of signal and background events, which will be discussed in the following sections. Here I applied the BDT and the MPL method on the test sub dataset. For the real dataset from run-200004 to 207718, the trained weights and variables from the BDT and the MLP methods were applied event by event and the discriminator responses,  $D_{BDT}$  and  $D_{MLP}$  were calculated respectively. Cuts of  $D_{BDT} > 0.0$  and  $D_{MLP} > 0.5$  were applied to extract the solar  $\nu_e$  signals from backgrounds.

Table 6.5: Testing results of  $5 < E_{fit} < 15 \text{ MeV}$  (above 5 MeV) from different TMVA methods.

| Method    | AUC   | CPU time (second/ $10^6$ events) |
|-----------|-------|----------------------------------|
| Fisher/LD | 0.915 | 0.93                             |
| BDT       | 0.950 | 269.71                           |
| MLP       | 0.958 | 1450.90                          |

Table 6.6: Testing results of  $4 < E_{fit} < 5 \text{ MeV}$  (low energy region) from different TMVA methods.

| Method    | AUC   | CPU time (second/ $10^6$ events) |
|-----------|-------|----------------------------------|
| Fisher/LD | 0.782 | 0.84                             |
| BDT       | 0.816 | 280.1                            |
| MLP       | 0.823 | 1337.9                           |

### 6.3.2.1 TMVA Outputs for Data

Fig. 6.8 and Fig. 6.10 show the BDT selection outputs from the 190.33-day dataset. Fig. 6.9 and Fig. 6.11 show the MLP outputs. Table. ?? shows the number of the output events for different energy regions and from different methods.

Cuts on the position and energy FOMs suggested by the collaboration[160] are <sup>1</sup> :  $-11 < Z_{factor} < 1$ ,  $scaleLogL > 10.85$ ,  $0 < G_{test} < 1.9$ ,  $U_{test} < 0.95$ ,  $ITR > 0.55$ ,  $-0.12 < \beta_{14} < 0.95$ . Combined with the “beforehand cuts”, the whole set of cuts is considered as “default cuts” here and is compared with the TMVA outputs.

The main analysis is focused on the [5,15] MeV energy region. A comparison of the outputs of  $5 < E_{fit} < 15 \text{ MeV}$  from the BDT, MLP and the default cuts is shown in Fig. 6.12.

### 6.3.3 Discussions on the TMVA Results

A more stringent radial cut (or tighter FV) can be applied on lower energy region  $4 < E_{fit} < 5 \text{ MeV}$  to further remove the backgrounds which are dominant in lower energy region. However, this tighter cut can also reduce the number of signals.

<sup>1</sup>There is also a suggested cut on the quantity of *position<sub>error</sub>* (*position<sub>error</sub>* < 525 mm). However, since this quantity was not calculated by the MPW fitter, it was not included here.

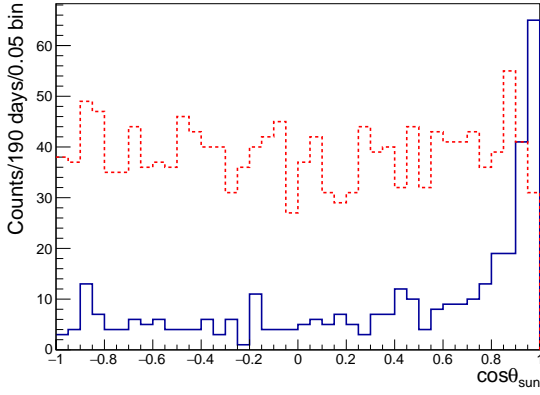


Figure 6.8: BDT output for  $\cos \theta_{\text{sun}}$ , with  $4 < E_{\text{fit}} < 15 \text{ MeV}$ . The solid blue line shows the selected candidate solar  $\nu_e$  events while the dotted red line shows the selected background events.

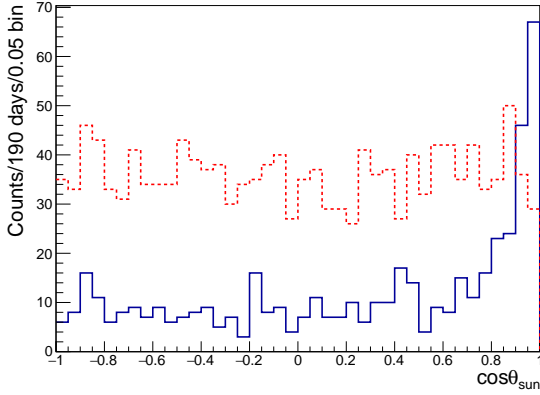


Figure 6.9: MLP output for  $\cos \theta_{\text{sun}}$ , with  $4 < E_{\text{fit}} < 15 \text{ MeV}$ . The solid blue line shows the selected candidate solar  $\nu_e$  events while the dotted red line shows the selected background events.

Other packages developed for high energy particle physics, such as StatPatternRecognition (SPR)[161], can also be considered as an alternative tool or as a reference for results comparisons.

### 6.3.4 Likelihood Fits for Solar Neutrino Candidate Events

In the previous section, the optimized cuts obtained from the TMVA analysis were applied on the dataset.

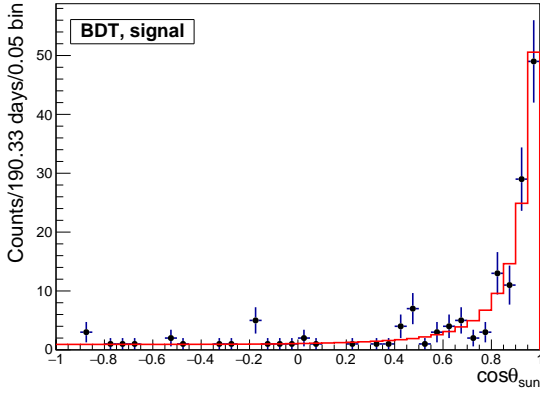


Figure 6.10: BDT output for  $\cos \theta_{\text{sun}}$ , with  $4 < E_{\text{fit}} < 15 \text{ MeV}$ . The solid blue line shows the selected candidate solar  $\nu_e$  events while the dotted red line shows the selected background events.

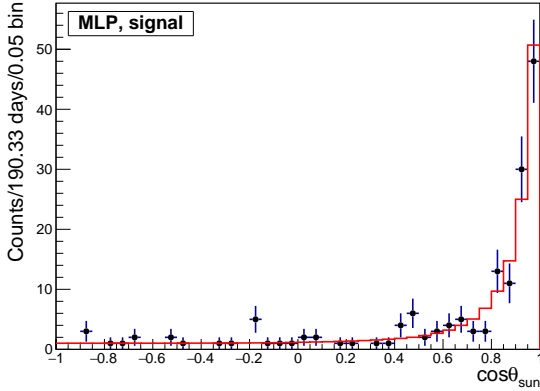


Figure 6.11: MLP output for  $\cos \theta_{\text{sun}}$ , with  $5 < E_{\text{fit}} < 15 \text{ MeV}$ . The solid blue line shows the selected candidate solar  $\nu_e$  events while the dotted red line shows the selected background events.

After the event selections, a distribution of  $\cos \theta_{\text{sun}}$  extracted from the solar  $\nu_e$  candidate events was obtained.

#### 6.3.4.1 Maximum Likelihood Fit

A maximum likelihood method was applied on the distribution to extract the number of the solar  $\nu_e$  interaction events ( $N_{\text{sig}}$ ) as well as the number of the background events ( $N_{\text{bkg}}$ ).

The values of  $\cos \theta_{\text{sun}}$  from the selected events were filled into a histogram divided

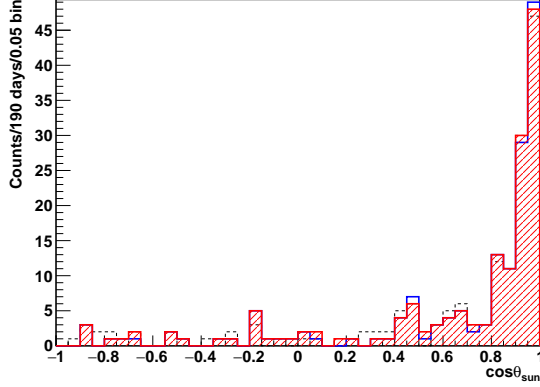


Figure 6.12: For the  $5 < E_{\text{fit}} < 15 \text{ MeV}$ , comparing the outputs of the BDT, MLP and the default cuts. The solid blue line shows the BDT results; the red slashes show the MLP results and the dotted black line shows the default cut results.

into bins. For each bin, the observed event number ( $n_{\text{obs}}$ ) was considered as a sum of solar  $\nu_e$  and background events. The  $n_{\text{obs}}$  in each bin was assumed to follow a Poisson distribution:  $\text{Poisson}(n_{\text{obs}}, N_{\text{bkg}} \cdot P_{\text{bkg}} + N_{\text{sig}} \cdot P_{\text{ES}}(E))$ , where  $P_{\text{bkg}}$  and  $P_{\text{ES}}(E)$  are the assumed distribution of backgrounds and solar  $\nu_e$  events respectively.

For the background events, a uniform distribution of  $\cos\theta_{\text{sun}}$  was assumed. On the other hand, the  $\cos\theta_{\text{sun}}$  distributions of solar  $\nu_e$  were extracted from the realistic run simulations after applying the optimized cuts, as shown in Fig. 6.13.

Adding up each bin  $i$  and taking  $N_{\text{bkg}}$  and  $N_{\text{sig}}$  as the free parameters for fitting, the maximum likelihood function was built as[33]:

$$-2 \ln \lambda(N_{\text{sig}}, N_{\text{bkg}}) = 2 \sum_{i=0}^{N_{\text{bins}}} [\mu_i(N_{\text{sig}}, N_{\text{bkg}}) - n_i + n_i \ln \frac{n_i}{\mu_i(N_{\text{sig}}, N_{\text{bkg}})}], \quad (6.7)$$

where  $\mu_i(N_{\text{sig}}, N_{\text{bkg}})$  is the expected number of events in each bin:  $\mu_i(N_{\text{sig}}, N_{\text{bkg}}) = N_{\text{sig}} \cdot P_{\text{ES}}^i(E^i) + N_{\text{bkg}} \cdot 1/N_{\text{bins}}$ ;  $N_{\text{bins}}$  is the total number of the bins, usually taken as 40 (per 0.05 bins). This quantity also includes the cases when the bin contains zero ( $n_i = 0$ ).

Fitting the data with  $(N_{\text{bkg}}, N_{\text{sig}})$  by maximizing the quantity 6.7,  $N_{\text{bkg}}$  and  $N_{\text{sig}}$  were obtained. In the next section, an ensemble test based on fake datasets was used for testing the fit results.

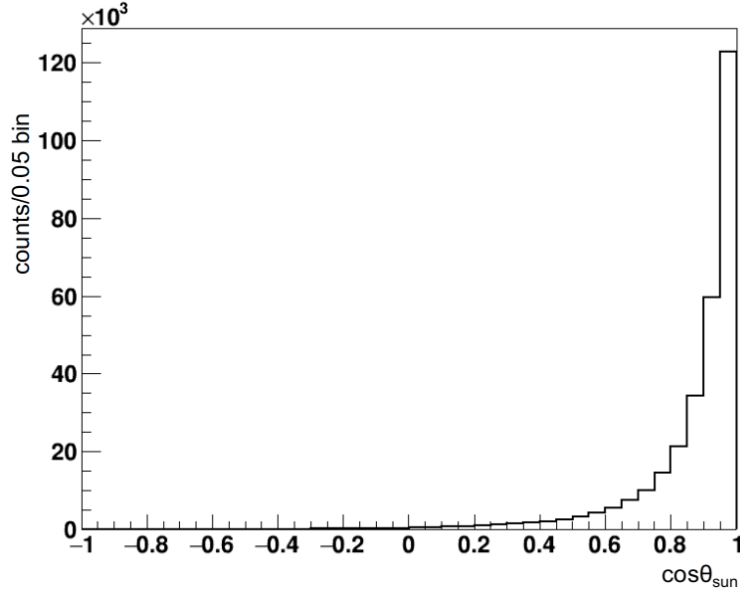


Figure 6.13: The  $\cos\theta_{\text{sun}}$  distribution of solar  $\nu_e$  extracted from the simulations, which was used as a pdf function.

#### 6.3.4.2 Ensemble Test

To check the uncertainty of the Poisson fit, 5000 fake datasets were generated. Here I used the method similar to the [156]. The fake data were taken from the MC simulation dataset of run-200004 to 203602 after the default cuts (the same to the one used by the TMVA).

The number of backgrounds in a fake dataset,  $N_{bkg}^f$ , was assumed to be two times of the event number in the  $-1 < \cos\theta_{\text{sun}} < 0$  region while the number of signals  $N_{sig}^f = N_{total}^f - N_{bkg}^f$ . Reading from the sub dataset of run-200004 to 203602 (see Fig. 6.14), it found  $N_{bkg}^f = 38$  and then  $N_{sig}^f = 109 - N_{bkg}^f = 71$ . To do the ensemble test, for each fake dataset, two random numbers:  $N_{sig}^r$  and  $N_{bkg}^r$  were generated by the ROOT TRandom3 random number generator class. Each of the two random numbers followed the random Poisson distribution:  $e^{-\mu}\mu^{N^r}/N^r!$ , where  $\mu = 71$  or  $38$ , and thus they fluctuated around  $N_{sig}^f$  or  $N_{bkg}^f$ .

To create the fake datasets,  $N_{sig}^r$  ( $N_{bkg}^r$ ) events after the cuts were randomly and uniformly selected from the solar  $\nu_e$  (merged backgrounds) MC simulations. For each randomly selected event, the values of  $E_{fit}$  and  $\cos\theta_{\text{sun}}$  were recorded. Each dataset was fitted with

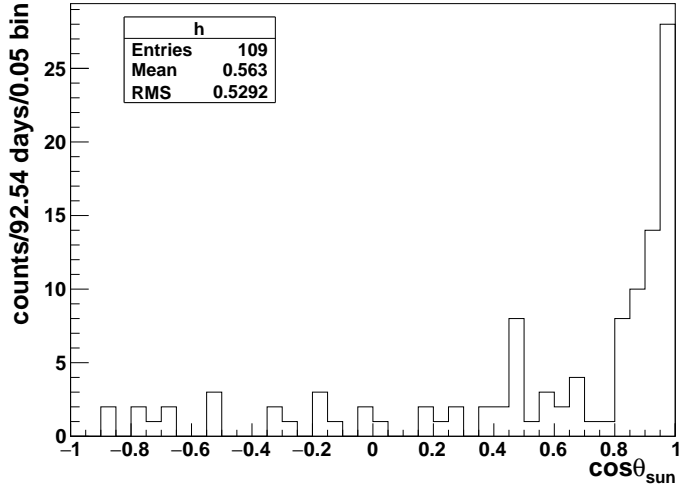


Figure 6.14: Real data from run-200004 to 203602 (half dataset), after the default cuts. The number of counts in  $-1 < \cos \theta_{\text{sun}} < 0$  region is 19.

the maximum likelihood function described in 6.3.4.1. Fig. 6.15 shows an example of the fitted results.

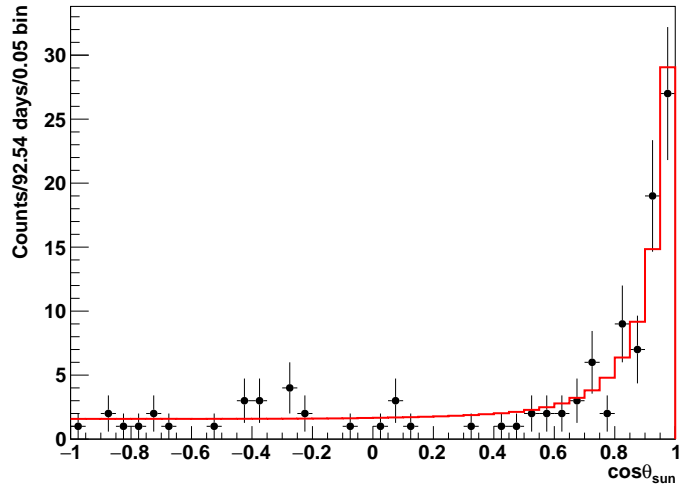


Figure 6.15: An example of the randomly generated  $\cos \theta_{\text{sun}}$  fitted with  $(N_{\text{sig}}, N_{\text{bkg}})$ . The black dots are data points and the red line is the fitted results. For  $N_{\text{sig}}^r = 73$  and  $N_{\text{bkg}}^r = 44$ , the fitted results give  $N_{\text{sig}} = 73.42 \pm 9.42$  and  $N_{\text{bkg}} = 43.58 \pm 7.73$ , with a  $\chi^2/\text{ndf} = 60.19/40 = 1.50$ .

The fit pull and the fit bias were defined by [156]:

$$bias = \frac{N_{sig} - N_{sig}^r}{\sigma_{sig}}, \quad (6.8)$$

$$pull = \frac{N_{sig} - N_{sig}^r}{\sigma_{sig}}, \quad (6.9)$$

where  $N_{sig}$  is the fitted number of signal events,  $\sigma_{sig}$  is the statistical uncertainty of  $N_{sig}$ ;  $N_{sig}^r$  is used as the true number of signal events in the fake dataset.

Fig. 6.17 and Fig. 6.16 show the fit pull and biases respectively. The histograms were fitted with Gaussians. For the fitted number of signal events, the Gaussian mean of the fit biases is  $-0.0044 \pm 0.0008$  for 5000 fake datasets while the Gaussian mean of the fit pulls is  $-0.026 \pm 0.006$ . These pulls and biases will be applied on the data. Fig. 6.18 shows the distributions of the  $-2 \ln L$  returned by the best fitted results ( $-2 \ln L_{best}$ ). The distribution,  $f(-2 \ln L_{best})$ , follows the asymptotic  $\chi^2$  pdf with a degree of 40 and is used to compute the p-values[33]. For a best-fit set  $(N_{sig}^i, N_{bkg}^i)$  with a value of  $-2 \ln L_{best}^i$ , the p-value is calculated as  $p = \int_{-2 \ln L_{best}^i}^{-2 \ln L_{best}^{max}} f(-2 \ln L_{best}) d(-2 \ln L_{best})$ .

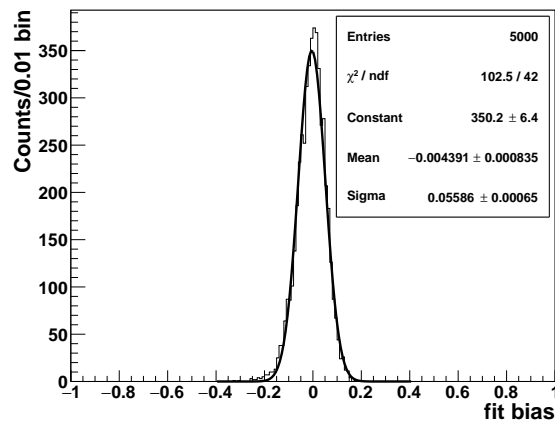


Figure 6.16:  $N_{sig}$  fit biases for 5000 fake datasets.

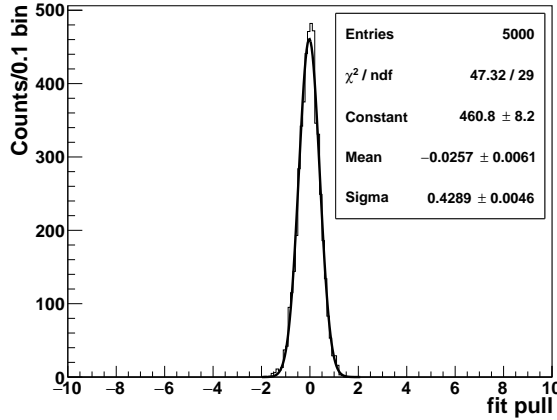


Figure 6.17:  $N_{sig}$  fit pulls for 5000 fake datasets.

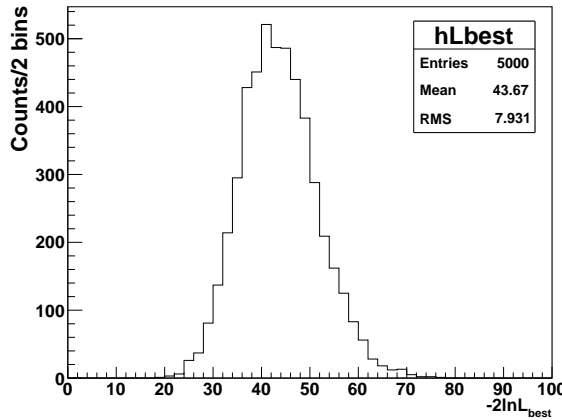


Figure 6.18: The  $-2 \ln L$  of the best fitted results for 5000 fake datasets.

#### 6.3.4.3 Fitting on the Whole Dataset (run-200004 to 207718)

The whole dataset started from run-200004 (on 24 Oct, 2018) to run-207718 (on 10 July, 2019). This dataset has a live time of 190.33 days. The BDT and MLP were applied on this dataset.

In the region of  $5 < E_{fit} < 15 \text{ MeV}$ , the outputs from the BDT and MLP were fitted to obtain the  $N_{sig}$  and  $N_{bkg}$ . Fig. 6.19 and Fig. 6.20 show their results respectively.

These results are also summarized in Table. 6.7.

It can be concluded here that in the  $[5, 15] \text{ MeV}$  energy region, the BDT results are

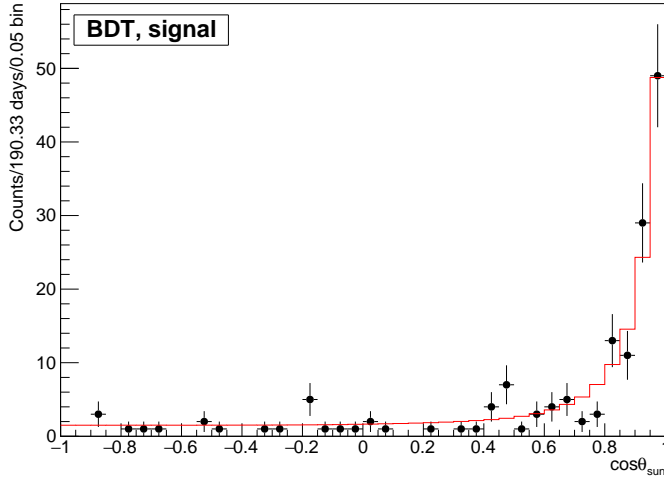


Figure 6.19: Fitted results for the  $5 < E_{fit} < 15 \text{ MeV}$ , from BDT outputs.

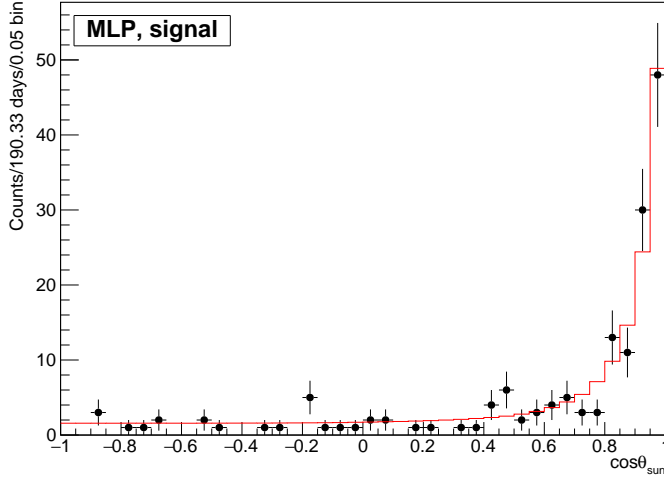


Figure 6.20: Fitted results for the  $5 < E_{fit} < 15 \text{ MeV}$ , from MLP outputs.

consistent with the MLP results. The estimated background rate is lower than the signal rate, which indicates that an extremely low background is achieved for the data.

#### 6.3.4.4 Systematics Evaluation

The systematics of position, direction and energy reconstruction were obtained from the Chapter 5. The quantities of position scale ( $XYZ_{\text{scale}}$ ), position resolution ( $XYZ_{\text{resol}}$ ),

Table 6.7: Fitted results for the whole dataset ( $5 < E < 15 \text{ MeV}$ ).

| Methods | $N_{sig}$          | $N_{bkg}$        | $R_{sig}$       | $R_{bkg}$       | p-value |
|---------|--------------------|------------------|-----------------|-----------------|---------|
| BDT     | $119.40 \pm 11.84$ | $36.55 \pm 7.57$ | $0.90 \pm 0.09$ | $0.28 \pm 0.06$ | 0.07    |
| MLP     | $119.49 \pm 11.89$ | $40.51 \pm 7.91$ | $0.90 \pm 0.09$ | $0.31 \pm 0.06$ | 0.20    |

direction resolution ( $Dir_{resol}$ ), energy scale ( $E_{scale}$ ) and energy resolution ( $E_{resol}$ ) were used. Table. 6.8 summarizes these quantities used for this analysis.

Table 6.8: Systematics for the solar  $\nu_e$  analysis in the water phase.

| Systematics         | values (positive/negative) |
|---------------------|----------------------------|
| x shift             | +6.48/-5.98 mm             |
| y shift             | +6.13/-4.11 mm             |
| z shift             | +6.71/-4.82 mm             |
| x scale             | +0.07%/-0.06%              |
| y scale             | +0.02%/-0.07%              |
| z scale             | +0.08%/-0.01%              |
| $\delta_\theta$     | +0.013/-0.101              |
| $E_{scale}$         | 2.0%                       |
| $E_{resol}$         | 0.011                      |
| $\beta_{14}$ shifts | +0.010/-0.036              |

For the energy scale, the reconstructed MC energies were scaled up and down the expected number of signal events, the uncertainty on the expected number of events was obtained to be  $^{+0.05}_{-0.06}$ .

A remapping of  $\cos \theta_{sun}$  by using the equation 5.9 was applied on the spectrum for evaluating the systematics. a minus symbol should be applied, and it is found as:

$$-\cos \theta'_{sun} = 1 + (-\cos \theta_{sun} - 1)(1 + \delta_\theta), \quad (6.10)$$

So the transformation then becomes:  $\cos \theta'_{sun} = -1 + (\cos \theta_{sun} + 1)(1 + \delta_\theta)$ .

Its impact is  $^{+0.3}_{-0.2}$  events.

### 6.3.4.5 Extracting the Solar Neutrino Flux

live time scale:  $t_{frac} = \frac{t_{data \ live \ time}}{t_{MC \ run \ time}} = 0.96$ .

A software called **PSelmaa** (Physics interpretation Sun-Earth Large Mixing Angle Adiabatic Approximation) was implemented in **RAT**[162]. BS05(OP) model, normal mass hierarchy, the MSW effects from the Earth (regeneration of coherence in the Earth) are neglected. Fig. 6.21 shows the survival probability curve as a function of energies (in 0.1 MeV intervals).

Since SNO+ can not discriminate  $\nu_\mu$  and  $\nu_\tau$ ,  $P_{e\alpha}$  includes only the  $\nu_\mu$  MC.

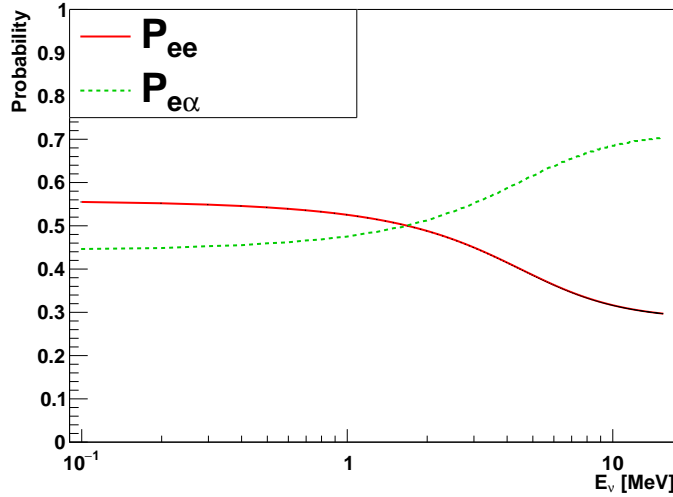


Figure 6.21: The MSW survival probability curves. The  $P_{ee}$  is in solid red line and  $P_{e\alpha}(= 1 - P_{ee})$  is in green dashed line.

To evaluate the  $^8B$  solar neutrino flux, the fitted number of  $\nu - e^-$  elastic scattering (ES) is divided by the expected number of ES and is then multiplied by the flux in the MC:

$$\Phi_{^8B} = \Phi_{^8B, MC} \frac{N_{fit}}{N_{expected}}, \quad (6.11)$$

In the RAT MC simulations, to gain more statistics, the solar  $\nu_e$  events is generated by 1700 times the nominal (*flux scale* =  $\frac{1}{1700}$ ); while the solar  $\nu_\mu$  events is generated by 9600 times the nominal (*flux scale* =  $\frac{1}{9600}$ ). Since it is impossible for the SNO+ detector to discriminate between  $\nu_\mu$  and  $\nu_\tau$  via detecting the elastic scattering events,  $\nu_\tau$  is not generated separately. Therefore, the generated solar  $\nu_\mu$  events are considered as a combination of  $\nu_\mu$  and  $\nu_\tau$  ( $\nu_\mu \approx \nu_{\mu,\tau}$ ) in the solar neutrino flux.

Therefore, the MC generated  $\nu_e$  and  $\nu_{mc}$  are scaled by the  $t_{frac}$  and *flux scale*, and

then weighted by the oscillation probability  $P_{ee}$  and  $P_{e\alpha} = 1 - P_{ee}$ . Combined together.

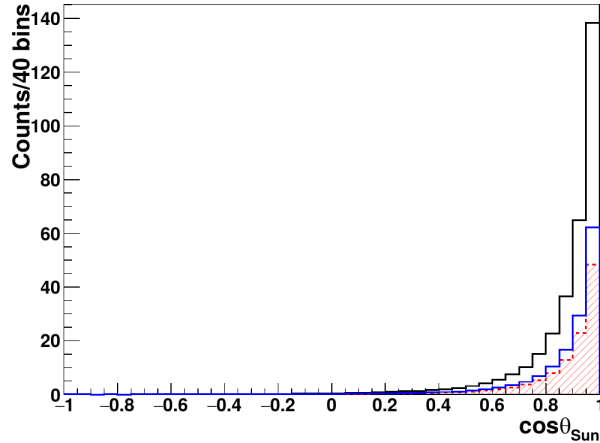


Figure 6.22: The MC  $\cos \theta_{Sun}$  distributions used as pdfs for the flux calculations. The histogram in black is the  $\nu_e$  flux without oscillation. This histogram is used for fitting the elastic scattering flux. The histogram in blue is the  $\nu_e$  flux combined with the  $\nu_\mu$  flux, both including the oscillations. This histogram is used for fitting the total flux. The dashed red histogram is the  $\nu_e$  flux only, including the oscillation.

Table. 6.9 shows the numbers of the MC generated  $\nu_e$  and  $\nu_\mu$  after scaling by 1700 or 9600 as well as the BDT selections.

Table 6.9: Expected number of solar  $\nu_e$ ,  $\nu_\mu$  and the fitted number of signals in each energy bins.

| E (MeV)  | $N_{\nu_e}^{expect}$ | $N_{\nu_e}^{osci.}$ | $N_{fit,sig}$      |
|----------|----------------------|---------------------|--------------------|
| [5, 6]   | 68                   | 26                  | $26.07 \pm 5.72$   |
| [6, 7]   | 91                   | 32                  | $36.52 \pm 6.70$   |
| [7, 8]   | 68                   | 23                  | $20.87 \pm 4.95$   |
| [8, 9]   | 47                   | 15                  | $16.24 \pm 4.30$   |
| [9, 10]  | 30                   | 10                  | $11.50 \pm 3.56$   |
| [10, 15] | 32                   | 10                  | $9.09 \pm 3.06$    |
| [5, 15]  | 336                  | 116                 | $119.40 \pm 11.84$ |

To fit for the flux,

For a nominal  ${}^8B$  solar neutrino flux  $\Phi_{MC} = 5.46 \times 10^6 \text{ cm}^{-2}\text{s}^{-1}$ , the flux is estimated to be  $\Phi_{ES} = \Phi_{MC} \cdot N_{fit,sig} = 1.96 \pm 0.20 \times 10^6 \text{ cm}^{-2}\text{s}^{-1}$ , compared to the Super-K measurement:  $\Phi_{ES} = (2.345 \pm 0.039) \times 10^6 \text{ cm}^{-2}\text{s}^{-1}$  and the SNO+ 2018 published results:  $\Phi_{ES} = 2.53^{+0.31}_{-0.28}(stat.)^{+0.13}_{-0.10}(syst.) \times 10^6 \text{ cm}^{-2}\text{s}^{-1}$ .

Fig. ?? shows the flux as a function of energies. A  $P_{ee}$  curve obtained from the RAT was overlay with the spectrum.

The fitted elastic scattering flux is  $\Phi_{ES}(2.09 \pm 0.20) \times 10^6$ .

Taking the systematics into accounts,

$$\Phi_{sB,sys} = \Phi_{sB,MC} \frac{N_{fit}}{N_{expected}} \sqrt{\left(\frac{N_{expected,sys}}{N_{expected}}\right)^2 + \left(\frac{N_{fit,sys}}{N_{fit}}\right)^2}, \quad (6.12)$$

#### 6.3.4.6 Limits of this Study

Here I used the background types described in the Table. 6.3. However, there are a few other backgrounds, such as the backgrounds from the AV ropes, the PMTs and the cosmogenic ones mainly caused by the cosmic muons. A more comprehensive study requires to include all possible backgrounds.

For the background events, I assumed a flat distribution of  $\cos \theta_{sun}$ . A more realistic shape of the distribution can be investigated to describe the backgrounds more properly.

# Chapter 7

## Conclusions

In this thesis, a reconstruction algorithm framework was developed for multiple SNO+ physics phases.

This framework was used in the SNO+ water phase as an event vertex-direction fitter Especially for the water phase, to analyze solar neutrino fluxes.

By looking at the low background dataset (run-200001 to 207718) for 190.33 live days, a  $^8B$  solar neutrino rate of  $119.40 \pm 11.84 \text{ events/}kt$  with a background rate of  $36.55 \pm 7.57 \text{ events/}kt$  in the energy region [5,15] MeV were obtained. This result gives an estimated  $^8B$  solar neutrino flux  $\Phi_{^8B} = (4.48 \pm 0.44(\text{stats.})) \times 10^6 \text{ cm}^{-2}s^{-1} \times (\text{syst.})$ . The elastic scattering in this energy region is  $\Phi_{ES} = (2.09 \pm 0.20(\text{stats.}) \times (\text{stats.})) \times 10^6 \text{ cm}^{-2}s^{-1}$ .

## Appendix A

# Details for the MultiPath Fitter

### A.1 Create a Random Vertex

Four random seeds are generated from the uniform distribution function: `RandFlat` in Class Library for High Energy Physics (CLHEP) library.

One random seed is used for generating the time of the vertex:  $t$  is a random variable following a uniform distribution in a range of [100, 300] ns, say,  $t \sim U(100, 300)$ .

Three random seeds are used for generating the position of the trial vertex:  $\text{ran0} \sim U(0, 1)$ ,  $\text{ran1} \sim U(-1, 1)$  and  $\text{ran2Pi} \sim U(0, 2\pi)$ .

Let  $r = \sqrt[3]{\text{ran0}} * 10000$  mm,  $\phi = \text{ran2Pi}$ ,  $\cos \theta = \text{ran1}$  and  $\sin \theta = \sqrt{1 - \cos^2 \theta}$ , then the trial position can be built in Cartesian coordinate system:  $\vec{x}_{trial} = (r \sin \theta \cos \phi, r \sin \theta \sin \phi, r \cos \theta)$ . This procedure ensures that a proper random position is generated inside a sphere with a radius of 10 m.

### A.2 Levenberg-Marquardt Method for Minimization

1

Levenberg-Marquardt (MRQ) method is a common routine for non-linear fitting. Let  $\mathbf{a} = [a_0, a_1, \dots, a_{M-1}]^T$  be an  $M$ -dimensional vector with  $M$  unknown parameters to be fit,

---

<sup>1</sup>This section refers to [132].

for example,  $\mathbf{a}$  is an event vertex with 4 parameters:  $\mathbf{a} = [x, y, z, t]^T$ .

A  $\chi^2$  merit function with the unknown parameter vector  $\mathbf{a}$  can be built and by minimizing the function, the best-fit  $\mathbf{a}$  can be found.

The  $\chi^2(\mathbf{a})$  can be approximately expanded into a quadratic form of Taylor-series:

$$\chi^2(\mathbf{a}) \simeq \gamma - \mathbf{d} \cdot \mathbf{a} + \frac{1}{2} \mathbf{a} \cdot \mathbf{D} \cdot \mathbf{a}, \quad (\text{A.1})$$

where  $\gamma$  is a  $M$ -dimension constant vector around  $\mathbf{a}$ ,  $\mathbf{d}$  is a  $M$ -dimension vector and  $\mathbf{D}$  is a  $M \times M$  Hessian matrix.

To find a  $\mathbf{a}_{min}$  so that a  $\min \chi^2(\mathbf{a}_{min})$  is reached, in computing science we usually use iteration steps:

$$\mathbf{a}_{min} = \mathbf{a}_{cur} + D^{-1}[-\nabla \chi^2(\mathbf{a}_{cur})], \quad (\text{A.2})$$

where  $\mathbf{a}_{cur}$  is the current trial value of  $\mathbf{a}$  and we assume matrix  $\mathbf{D}$  is invertible. The  $\mathbf{a}_{cur}$  thus jumps onto  $\mathbf{a}_{min}$ .

According to the definition of a  $\chi^2$  merit function, it can be written out explicitly as:

$$\chi^2(\mathbf{a}) = \sum_{i=0}^{N-1} \left[ \frac{y_i - y(x_i|\mathbf{a})}{\sigma_i} \right]^2, \quad (\text{A.3})$$

and with the same Taylor expansion, the quadratic form is written as:

$$\chi^2(\mathbf{a}) \approx \chi^2(\mathbf{a}_{cur}) + \sum_k \frac{\partial \chi^2(\mathbf{a}_{cur})}{\partial \alpha_k} \delta \alpha_k + \frac{1}{2} \sum_{kl} \frac{\partial^2 \chi^2(\mathbf{a}_{cur})}{\partial \alpha_k \partial \alpha_l} \delta \alpha_k \delta \alpha_l, \quad (\text{A.4})$$

where the first derivatives are:

$$\frac{\partial \chi^2}{\partial a_k} = -2 \sum_{i=0}^{N-1} \left[ \frac{y_i - y(x_i|\mathbf{a})}{\sigma_i} \right] \frac{\partial y(x_i|\mathbf{a})}{\partial a_k}, \quad k = 0, 1, \dots, M-1, \quad (\text{A.5})$$

and the second derivatives are:

$$\frac{\partial^2 \chi^2}{\partial a_k \partial a_l} = 2 \sum_{i=0}^{N-1} \left\{ \frac{\partial y(x_i|\mathbf{a})}{\partial a_k} \frac{\partial y(x_i|\mathbf{a})}{\partial a_l} - [y_i - y(x_i|\mathbf{a})] \frac{\partial^2 y(x_i|\mathbf{a})}{\partial a_k \partial a_l} \right\}, \quad k = 0, 1, \dots, M-1. \quad (\text{A.6})$$

Let  $\beta_k \equiv -\frac{1}{2} \frac{\partial \chi^2}{\partial a_k}$ ,  $\alpha_{kl} \equiv \frac{1}{2} \frac{\partial^2 \chi^2}{\partial a_k \partial a_l}$ , then the factor of 2 is removed. The  $\alpha_{kl}$  is defined as the curvature matrix and  $\alpha = \frac{1}{2} \mathbf{D}$ , which implies that it is the half of the Hessian matrix.

From A.2, we have:  $D(\mathbf{a}_{min} - \mathbf{a}_{cur}) = [-\nabla\chi^2(\mathbf{a}_{cur})] \implies 2\alpha\delta\mathbf{a} = 2\beta$ . The A.2 is now transformed into a systems of linear equations:

$$\sum_{l=0}^{M-1} \alpha_{kl}\delta a_l = \beta_k, \quad (\text{A.7})$$

where  $\delta a_l$  is a varying amount added to the current value of parameter for the next iteration.

The main task now is to calculate  $\alpha_{kl}$  and  $\beta_k$  and then solve for  $\delta a_l$  in A.7. Once  $\delta a_l$  is solved, we can vary the current trial or approximate values of  $\mathbf{a}_{cur}$  and let it go close to or reach the  $\mathbf{a}_{min}$ .

If we consider the method of steepest descent:  $\mathbf{a}_{next} = \mathbf{a}_{cur} - \text{const} \cdot \nabla\chi^2(\mathbf{a}_{cur})$ , where const is a constant, then the  $\delta a_l$  is solved by

$$\delta a_l = \text{const} \cdot \beta_l, \quad (\text{A.8})$$

where no Hessian matrix is needed.

In the Levenberg-Marquardt method, in order to solve for  $\delta a_l$ , the detailed calculation of  $\mathbf{D}^{-1}$  in A.2 and the simplified calculation of steepest descent in A.8 are combined and a smooth transition between A.2 and A.8 is considered.

In A.8, the const describes the distance or magnitude of how far the parameter should go along the gradient  $\beta_l$ . From dimensional analysis, since  $\beta_k \equiv -\frac{1}{2} \frac{\partial \chi^2}{\partial a_k}$  and  $\chi^2$  is a non-dimensional number,  $[\beta_l] = [1/a_l]$ . Then from A.8,  $[\text{const}] = [a_l^2]$ . The const has the same dimension to the term  $1/\alpha_{ll} = 1/(\frac{1}{2} \frac{\partial^2 \chi^2}{\partial a_l \partial a_l})$ , i.e., the diagonal elements in the curvature matrix. A bridge between A.2 and A.8 is thus built. The diagonal elements in the curvature matrix can control the magnitude of the const, tells how far the parameter should go along the gradient.

Then A.8 can be written as:

$$\delta a_l = \frac{1}{\lambda \alpha_{ll}} \beta_l \text{ or } \lambda \alpha_{ll} \delta a_l = \beta_l, \quad (\text{A.9})$$

where  $\alpha_{ll}$  is written in a form of  $\alpha_{ll} = \sum_{i=0}^{N-1} \frac{1}{\sigma_i^2} [\frac{\partial y(x_i|\mathbf{a})}{\partial a_l} \frac{\partial y(x_i|\mathbf{a})}{\partial a_l}]$  to ensure that  $\alpha_{ll}$  is always positive; a fudge factor  $\lambda$  can be set to  $\lambda \gg 1$  to avoid the case when the value of const is taken too large.

Compare A.7 and A.9, if define a new curvature matrix  $\alpha'$  as  $\alpha'_{jj} \equiv (1 + \lambda)\alpha_{jj}$  (for diagonal elements) and  $\alpha'_{jk} \equiv \alpha_{jk}$  ( $j \neq k$ ) (for non-diagonal elements), these two equations can be combined into one:

$$\sum_{l=0}^{M-1} \alpha'_{kl} \delta a_l = \beta_k \quad (\text{A.10})$$

From the definition of  $\alpha'$ , if  $\lambda$  takes a large value,  $\alpha'$  is dominated by diagonal elements, then A.10 is close to A.9; while if  $\lambda \rightarrow 0$ , A.10 is close to A.7.

The algorithm of Levenberg-Marquardt method requires a reasonable start value (first guess) of the fitting parameter  $\mathbf{a}$  and a reasonable preset value of  $\lambda$  (usually take  $\lambda = 0.001$ ). The iteration loop of the algorithm is: calculate the value of  $\chi^2(\mathbf{a})$ , solve for  $\delta \mathbf{a}$  from A.10 and then calculate  $\chi^2(\mathbf{a} + \delta \mathbf{a})$ . During this loop, the algorithm checks whether  $\chi^2(\mathbf{a} + \delta \mathbf{a}) \geq \chi^2(\mathbf{a})$ , if it is,  $\lambda$  is increased by  $\lambda = 10 \cdot \lambda$ ; if not,  $\lambda$  is decreased by  $\lambda = 0.1 \cdot \lambda$ .

The iteration loop is terminated when the change amount of the  $\chi^2$  is negligible: if the loop calculates several  $\chi^2$  values which are close to each other within a fit tolerance (**fTolerance**):  $|\chi^2_{current} - \chi^2_{previous}| < \text{fTolerance}$ , the algorithm will consider the  $\chi^2$  is minimized with a set of best-fit parameters. Here the termination condition of iterating the  $\chi^2$  value to convergence to the machine accuracy or to the roundoff limit is not used, since  $\chi^2$  is a statistical quantity rather than a solution of an equation. It is not statistical meaningful to vary the value of  $\mathbf{a}$  to vary  $\chi^2$  by a small amount  $\ll 1$ .

Once the minimum is reached,  $\lambda$  is set to 0 and then the estimated covariance matrix of the standard errors in the fitted  $\mathbf{a}$  can be calculated as:  $C \equiv \alpha^{-1}$ .

The MRQ method is the core algorithm in the MultiPath Fitter Framework for fitting the results. A few parameters can be optimized in practice. The main parameters are:

The trade-off between precision of the results and the CPU time is considered. **fTolerance**=0.001; the number of maximum iteration  $iter_{max}$  500, 100 the number of maximum good fits  $nGood_{max}$  6, 4

- fit tolerance: **fTolerance**, which is set for  $|\chi^2_{current} - \chi^2_{previous}| < \text{fTolerance}$ .
- the number of good fits: **nGood**.

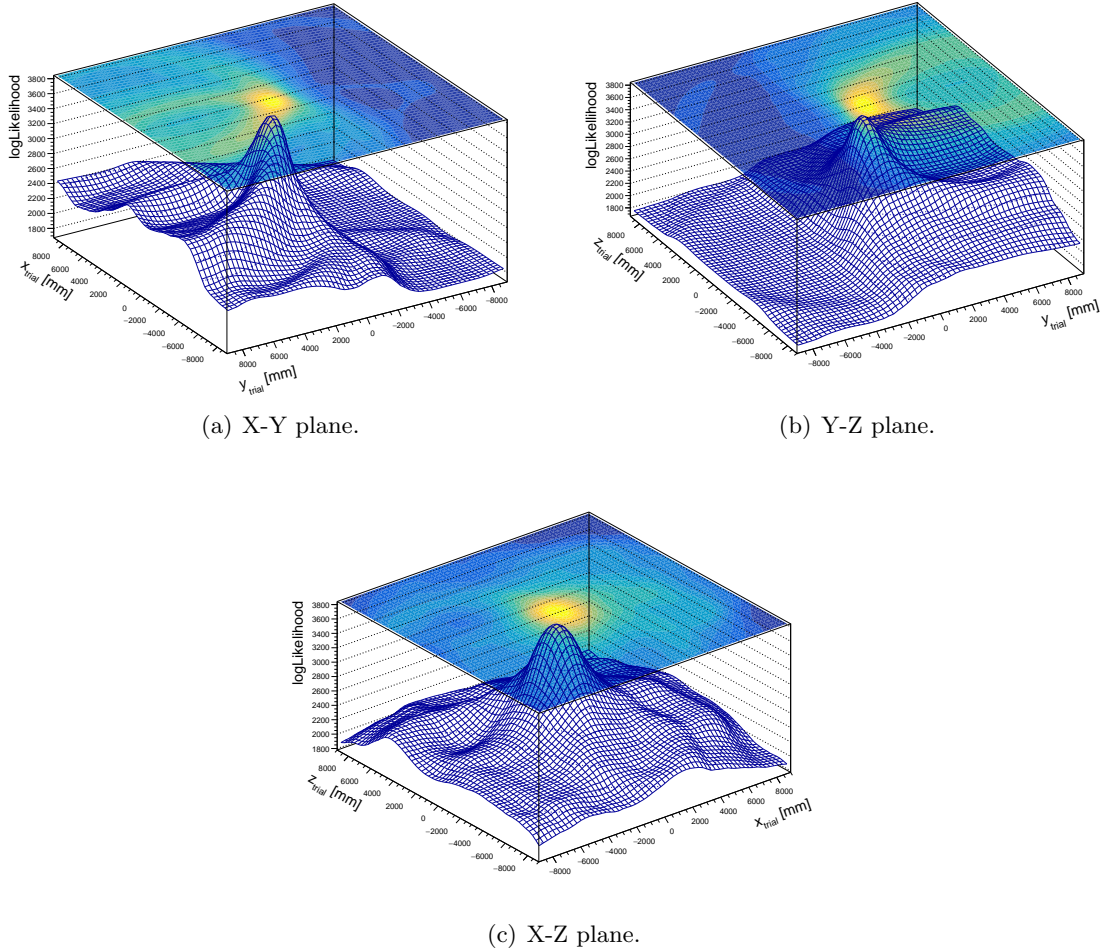


Figure A.1: Likelihood surface of an  $^{16}\text{N}$  event projected on X-Y, Y-Z, X-Z planes. A clear global maxima is reached for the fitted vertex.

- the maximum iteration number

the parameters used by the MultiPath Fitter for different phases are summarized in Table. ??.

Fig. A.1 shows vertex likelihood surfaces produced by the MRQ method in the MultiPath Water Fitter, for an typical  $^{16}\text{N}$  event (central run-100934, event GTID = 61836), projected on X-Y, X-Z and Y-Z planes. A clear global maxima gives the reconstructed vertex:  $\vec{X}_{fit} = (-211.958, 503.399, 275.990)$  mm and  $t_{fit} = 217.039$  ns.

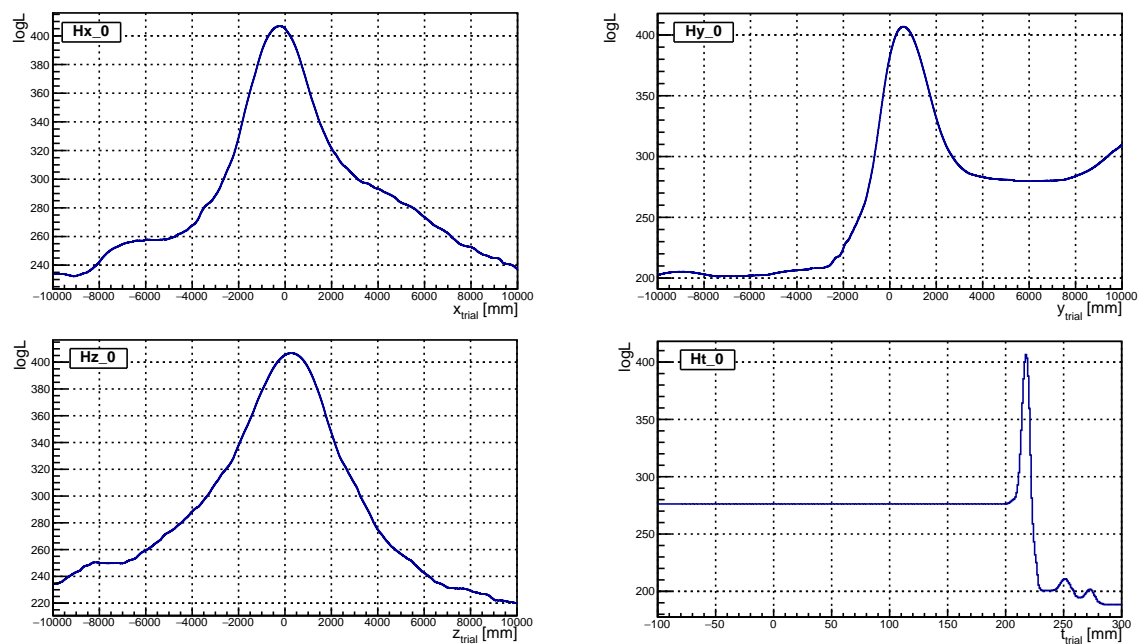


Figure A.2: Likelihood surface of an  $^{16}\text{N}$  event projected on x, y, z, t-axis respectively.

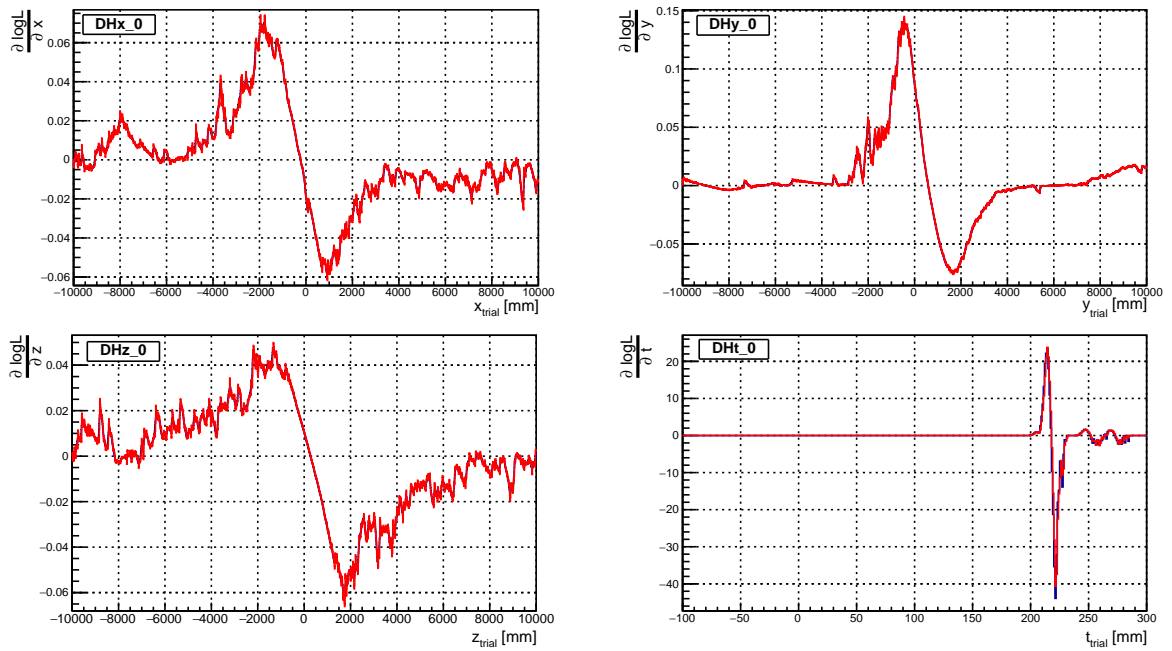


Figure A.3: Derivatives of  $\ln L$  of an  $^{16}\text{N}$  event projected on x, y, z, t-axis respectively. The analytical derivatives (blue) are overlaid with numerical derivatives (red). They basically match with each other.

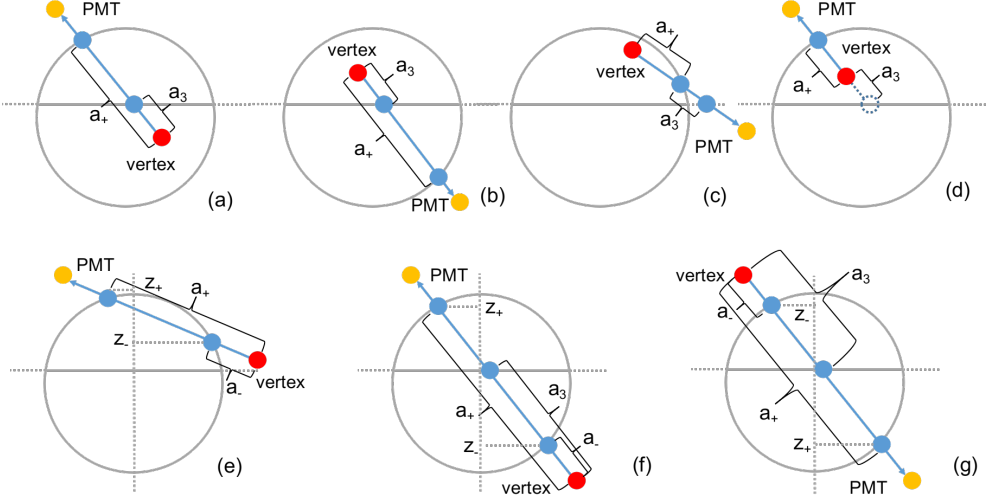


Figure A.4: Layouts for the scintillator light paths inside the AV sphere.

### A.3 Detailed Light Path Calculations in the MultiPath Scintwater Fitter

The following algorithm shows the detailed calculations for evaluating the light path in the scintillator regions. Each check steps are marked by number and if-conditions are marked by latin letters (a, b or c).

---

First check the ray-sphere intersection (equation. 4.4):

If  $\Delta > 0$ ,

(step. 1a) if  $|\vec{x}_0| < r_{AV}$  (and  $a_+ > 0 > a_-$ ), check the ray-plane intersection:

(2a-a) if  $a_3 > 0$ , the ray-vector hits the interface plane:

(3a-a-a) if  $z_0 < Z_{split}$  and  $a_3 < a_+$ :  $d_{sp,AV} = a_+ - a_3$ , see Fig. A.4 (a).

(3a-a-b) if  $z_0 \geq Z_{split}$ :

(4a-a-b-a) if  $a_3 < a_+$ :  $d_{sp,AV} = a_3$ , see Fig. A.4 (b).

(4a-a-b-b) if  $a_3 \geq a_+$ :  $d_{sp,AV} = a_+$ , see Fig. A.4 (c).

(2a-b) if  $a_3 \leq 0$ :

(3a-b) if  $z_0 > Z_{split}$ :  $d_{sp,AV} = a_+$ , see Fig. A.4 (d).

(step. 1b) if  $|\vec{x}_0| \geq r_{AV}$  (and  $a_+ > a_- > 0$ ), calculate the z position of the intersection point:  $z_{\pm} = z_0 + a_{\pm} \cdot (z_{PMT} - z_0) / |\vec{X}_{PMT} - \vec{X}_0|$ :

(1-b-a) if  $z_- \geq Z_{split}$  and  $z_+ \geq Z_{split}$ :  $d_{sp,AV} = a_+ - a_-$ , see Fig. A.4 (e).

(1-b-b) if  $z_- < Z_{split}$  and  $z_+ > Z_{split}$  and  $a_3 > 0$ :  $d_{sp,AV} = a_+ - a_3$ , see Fig. A.4 (f).

(1-b-c) if  $z_- > Z_{split}$  and  $z_+ < Z_{split}$  and  $a_3 > 0$ :  $d_{sp,AV} = a_3 - a_-$ , see Fig. A.4 (g).

---

First check the ray-cylinder intersection (equation. 4.4):

If  $\Delta_{neck} > 0$ ,

(step. 1a) if  $a'_+ a'_- < 0$  (event position is inside the cylinder), check the z position of the intersection point on neck,  $z_+ = z_0 + a'_+ u_z$ :

(2a-a) if  $6108 < z_+ < 8390 \text{ mm}$  (in the valid neck region), then check the AV sphere:

(3a-a-a) if  $|\vec{X}_0| \geq r_{AV}$ :  $d_{sp,neck} = a'_+$ , see Fig. A.5 (a).

(3a-a-b) if  $|\vec{X}_0| < r_{AV}$  and  $a_+ a_- < 0$ :  $d_{sp,neck} = a'_+ - a_+$ , the light ray first hits the sphere inside the cylinder and then hits the cylinder, see Fig. A.5 (b).

(2a-b) if  $z_+ < 6108 \text{ mm}$ :

(3a-b) if  $|\vec{X}_0| \geq r_{AV}$  and  $6108 < z_0 < 8390 \text{ mm}$ :

(4a-b) if  $a_+ > a_- > 0$ :  $d_{sp,neck} = a_-$ , see Fig. A.5 (c).

(step. 1b) if  $a'_+ > a'_- > 0$  (event position is outside the cylinder), check the z position of the intersection point on neck,  $z'_\pm = z_0 + a'_\pm \cdot u_z$ :

(2b-a) if  $6108 < z'_\pm < 8390 \text{ mm}$ , check the AV intersection:

(3b-a-a) if  $a_\pm$  do not exit (never passes through AV),  $d_{sp,neck} = a'_+ - a'_-$ , see Fig. A.5 (d).

(3b-a-b) if  $a_+ > a_- > 0$ , evaluate the z positions of the ray-sphere intersection points  $z_\pm = z_0 + a_\pm \cdot u_z$ :

(4b-a-a) if  $z_\pm \geq 6108 \text{ mm}$ :  $d_{sp,neck} = a'_+ - a'_- - (a_+ - a_-)$ , see Fig. A.5 (e). The path inside the sphere is subtracted to avoid duplicated calculation.

(4b-a-b) if  $z_+ < 6108$  and  $6108 < z_- < 8390 \text{ mm}$ :

(5b-a-b-a) if  $a_+ > a_- > 0$ :  $d_{sp,neck} = a_- - a'_-$ , see Fig. A.5 (f).

(5b-a-b-b) if  $z_- < 6108$  and  $6108 < z_+ < 8390 \text{ mm}$ :

in this case, either the event position is inside the sphere ( $a_+ a_- < 0$ ), shown in Fig. A.5 (g), or outside the sphere ( $a_+ a_- < 0$ ), shown in Fig. A.5 (h)), the path in neck is same:  $d_{sp,neck} = a'_+ - a_+$ .

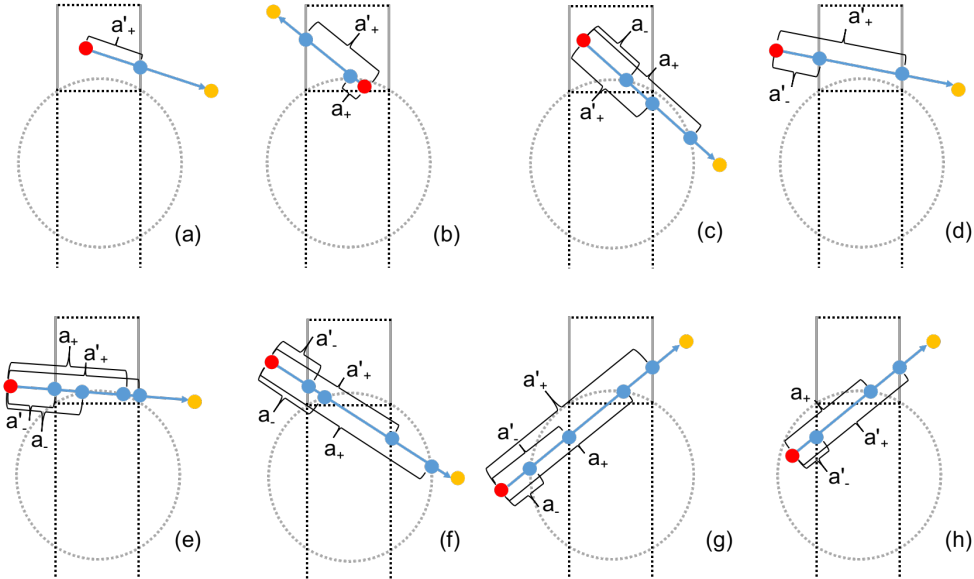


Figure A.5: Layouts of the scintillator light paths inside the neck cylinder.

## **Appendix B**

# **Information for $^{16}\text{N}$ Scan Runs**

### **B.1 Information for $^{16}\text{N}$ Scan Runs**

The tables below show the  $^{16}\text{N}$  runs used in this thesis. Table. B.1 to B.3 are the internal scans inside the AV along the detector z-axis, y-axis and x-axis respectively. Table. B.4 shows the runs when the source was at the detector corner. Table. B.5 shows the external scans.

Table B.1:  $^{16}\text{N}$  internal z-axis scan runs. The last 3 scans were inside the AV neck (neck runs).

| run number | nominal source position [mm] |         |           |
|------------|------------------------------|---------|-----------|
|            | x                            | y       | z         |
| 100934     | -186.0                       | 256.0   | 1.0       |
| 106923     | -186.0                       | 254.0   | -5501.2   |
| 106925     | -186.0                       | 254.0   | -4999.899 |
| 106930     | -186.0                       | 254.0   | -4500.2   |
| 106942     | -186.0                       | 254.0   | -4001.0   |
| 106944     | -186.0                       | 254.0   | -3501.399 |
| 106946     | -186.0                       | 254.0   | -2999.7   |
| 106948     | -186.0                       | 254.0   | -2500.399 |
| 106950     | -186.0                       | 254.0   | -1998.499 |
| 106952     | -186.0                       | 254.0   | -1499.5   |
| 106954     | -186.0                       | 254.0   | -1000.099 |
| 106956     | -186.0                       | 254.0   | -499.6    |
| 106958     | -186.0                       | 254.0   | 0.401     |
| 106960     | -186.0                       | 254.0   | 500.8     |
| 106962     | -186.0                       | 254.0   | 1000.3    |
| 106964     | -186.0                       | 254.0   | 1500.9    |
| 106967     | -186.0                       | 254.0   | 2000.001  |
| 106969     | -186.0                       | 254.0   | 2500.3    |
| 106971     | -186.0                       | 254.0   | 3000.3    |
| 106973     | -186.0                       | 254.0   | 3500.9    |
| 106975     | -186.0                       | 254.0   | 4000.5    |
| 106977     | -186.0                       | 254.0   | 4500.4    |
| 106979     | -185.037                     | 247.24  | 4973.567  |
| 107049     | -121.599                     | 81.021  | 6496.04   |
| 107051     | -123.099                     | 126.177 | 6997.52   |
| 107053     | -124.4                       | 153.386 | 7499.79   |

Table B.2:  $^{16}\text{N}$  internal y-axis scan runs.

| run number | nominal source position [mm] |           |         |
|------------|------------------------------|-----------|---------|
|            | x                            | y         | z       |
| 106992     | -5.995                       | -0.201    | -1.107  |
| 106994     | -7.761                       | -998.068  | 0.159   |
| 106996     | -7.084                       | -2000.578 | -0.716  |
| 106998     | -5.491                       | -2998.017 | -4.196  |
| 107000     | -3.774                       | -3992.167 | -7.374  |
| 107002     | -1.624                       | -4999.882 | -12.012 |
| 107004     | -1.745                       | 5002.057  | -9.897  |
| 107006     | -3.967                       | 3973.021  | -7.359  |
| 107008     | -5.984                       | 2980.035  | -3.441  |
| 107010     | -7.952                       | 1986.669  | -1.714  |
| 107012     | -9.242                       | 994.183   | 0.553   |
| 107014     | -9.867                       | 496.858   | 0.269   |
| 107016     | -8.414                       | 1494.71   | 0.634   |
| 107018     | -6.835                       | 2487.539  | -1.126  |
| 107026     | -4.949                       | 3496.338  | -5.971  |
| 107028     | -2.539                       | 4505.371  | -7.453  |
| 107030     | -7.711                       | -501.268  | 0.126   |
| 107033     | -7.534                       | -1494.927 | -0.096  |
| 107035     | -6.349                       | -2487.912 | -1.434  |
| 107043     | -4.366                       | -3475.769 | -6.019  |
| 107045     | -2.799                       | -4498.62  | -10.213 |
| 107047     | -1.898                       | -4874.53  | -11.077 |

Table B.3:  $^{16}\text{N}$  internal x-axis scan runs.

| run number | nominal source position [mm] |        |         |
|------------|------------------------------|--------|---------|
|            | x                            | y      | z       |
| 107055     | -5.283                       | -0.209 | -1.057  |
| 107075     | -4999.043                    | 2.46   | -9.899  |
| 107077     | -4002.525                    | 5.269  | -7.364  |
| 107079     | -3004.229                    | 8.101  | -2.54   |
| 107081     | -2000.155                    | 10.637 | -0.361  |
| 107083     | -992.994                     | 11.641 | 0.024   |
| 107085     | 998.133                      | 10.897 | -0.044  |
| 107087     | 2011.103                     | 9.874  | 0.057   |
| 107091     | 4003.323                     | 4.378  | -5.974  |
| 107093     | 5004.868                     | 2.262  | -7.547  |
| 107095     | 4503.445                     | 3.278  | -7.0    |
| 107110     | -4489.301                    | 3.918  | -10.545 |
| 107116     | 3511.147                     | 5.742  | -2.578  |
| 107118     | 2502.805                     | 8.681  | -2.803  |
| 107120     | -3476.709                    | 6.643  | -4.886  |

Table B.4:  $^{16}\text{N}$  corner scan runs.

| run number | nominal source position [mm] |           |          |
|------------|------------------------------|-----------|----------|
|            | x                            | y         | z        |
| 106981     | -186.0                       | 254.0     | 5500.9   |
| 106985     | -186.0                       | 254.0     | 5999.8   |
| 107058     | -8.765                       | 996.891   | 0.172    |
| 107060     | -7.518                       | 1990.663  | -0.445   |
| 107062     | -7.794                       | -997.865  | 0.155    |
| 107064     | -7.083                       | -1990.651 | -0.744   |
| 107089     | 3003.718                     | 7.258     | -0.69    |
| 107098     | 2091.016                     | 6.312     | 2099.444 |
| 107020     | -5.399                       | 1991.04   | 1988.97  |
| 107022     | -9.92                        | 2776.47   | -2839.41 |
| 107024     | -10.44                       | 3227.32   | -3324.9  |
| 107037     | -8.377                       | -2832.33  | -2839.69 |
| 107039     | -9.284                       | -3137.21  | -3212.18 |
| 107041     | -4.719                       | -2099.25  | 2110.71  |
| 107100     | 2824.56                      | 13.507    | -2840.13 |
| 107102     | 3245.74                      | 13.681    | -3264.76 |
| 107104     | -3250.29                     | 13.438    | -3264.7  |
| 107106     | -2834.05                     | 13.893    | -2839.43 |
| 107108     | -2109.28                     | 6.613     | 2098.57  |
| 107112     | -2771.9                      | 16.196    | -4773.96 |
| 107114     | 2771.1                       | 15.596    | -4773.27 |

**Table B.5:**  $^{16}\text{N}$  external scan runs.

| run number | nominal source position [mm] |         |           |
|------------|------------------------------|---------|-----------|
|            | x                            | y       | z         |
| 111211     | -5861.0                      | -2524.0 | -1.62     |
| 111213     | -5861.0                      | -2524.0 | -5000.525 |
| 111215     | -5861.0                      | -2524.0 | -4000.021 |
| 111217     | -5861.0                      | -2524.0 | -3000.151 |
| 111219     | -5861.0                      | -2524.0 | -1999.248 |
| 111221     | -5861.0                      | -2524.0 | -998.923  |
| 111223     | -5861.0                      | -2524.0 | 1000.798  |
| 111225     | -5861.0                      | -2524.0 | 2000.597  |
| 111228     | -5861.0                      | -2524.0 | 3000.734  |
| 111230     | -5861.0                      | -2524.0 | 4000.977  |
| 111232     | -5861.0                      | -2524.0 | 5000.86   |
| 111234     | -5861.0                      | -2524.0 | 4498.167  |
| 111236     | -5861.0                      | -2524.0 | 3498.838  |
| 111238     | -5861.0                      | -2524.0 | 2498.641  |
| 111240     | -5861.0                      | -2524.0 | 1498.713  |
| 111242     | -5861.0                      | -2524.0 | -1501.717 |
| 111244     | -5861.0                      | -2524.0 | -2500.89  |
| 111246     | -5861.0                      | -2524.0 | -3500.764 |
| 111248     | -5861.0                      | -2524.0 | -4500.812 |

## Appendix C

# Run Lists Used for Water Analysis

The following table shows the run lists used by this thesis during the SNO+ water phase.

Table C.1: Run numbers used in the solar neutrino analysis.

|        |        |        |        |        |        |        |        |        |        |
|--------|--------|--------|--------|--------|--------|--------|--------|--------|--------|
| 200004 | 200005 | 200006 | 200007 | 200008 | 200009 | 200010 | 200011 | 200014 | 200015 |
| 200016 | 200017 | 200018 | 200019 | 200020 | 200021 | 200022 | 200026 | 200031 | 200032 |

# References

- [1] L. Oberauer, A. Ianni, and A. Serenelli, *Solar Neutrino Physics: The Interplay Between Particle Physics and Astronomy*. John Wiley & Sons, 2020.
- [2] J. N. Bahcall, A. M. Serenelli, and S. Basu, “New solar opacities, abundances, helioseismology, and neutrino fluxes,” *The Astrophysical Journal Letters*, vol. 621, no. 1, p. L85, 2005.
- [3] J. W. F. Valle and J. Romao, *Neutrinos in high energy and astroparticle physics*. John Wiley & Sons, 2015.
- [4] P. G. Jones, *Background rejection for the neutrinoless double beta decay experiment SNO+*. PhD thesis, University of Oxford, 2011.
- [5] J. Birks and F. Firk, “The theory and practice of scintillation counting,” *Physics Today*, vol. 18, p. 60, 1965.
- [6] G. F. Knoll, *Radiation Detection and Measurement*. John Wiley & Sons, 2010.
- [7] the SNO+ collaboration, “The SNO+ experiment,” *arXiv preprint arXiv:2104.11687*.
- [8] M. Dragowsky, A. Hamer, Y. Chan, R. Deal, E. Earle, W. Frati, E. Gaudette, A. Hallin, C. Hearns, J. Hewett, *et al.*, “The  $^{16}\text{N}$  calibration source for the sudbury neutrino observatory,” *Nuclear Instruments and Methods in Physics Research Section A: Accelerators, Spectrometers, Detectors and Associated Equipment*, vol. 481, no. 1-3, pp. 284–296, 2002.

- [9] R. F. MacLellan, *The energy calibration for the solar neutrino analysis of all three phases of the Sudbury Neutrino Observatory*. PhD thesis, Queen's University, 2009.
- [10] M. Mottram, "N16 source update," *SNO+ Internal Document, docDB-1769-v1*.
- [11] Z. Barnard, "Update to N16 geometry," *SNO+ Internal Document, docDB-4414-v1*.
- [12] R. Bayes, "Analysis of N16 scan," *SNO+ Internal Document, docDB-4482-v2*.
- [13] E. Turner, "A water scattering scaling factor for rat," *SNO+ Internal Document, docDB-5864-v2*.
- [14] S. J. Brice, *Monte Carlo and Analysis Techniques for the Sudbury Neutrino Observatory*. PhD thesis, University of Oxford, 1996.
- [15] P. Skensved and B. Robertson, "Miscellaneous effects," *SNO Technical Report, SNO-STR-90-28*.
- [16] J. Tseng, "Skyshine classifier," *SNO+ Internal Document, docDB-5341-v1*.
- [17] E. Leming, "Oxford LAB + PPO timing and light yield measurements," *SNO+ Internal Document, docDB-6179-v1*.
- [18] A. Hallin, "Fitting partial fill data from december 2014," *SNO+ Internal Document, docDB-2888-v3*.
- [19] D. Auty and A. Hallin, "Partial water fitter," *SNO+ Internal Document, docDB-2965-v2*.
- [20] K. Singh, "Wavelength shifter: Carbostyryl 124," *SNO+ Internal Document, docDB-3351-v2*.
- [21] K. Singh, "Wavelength shifter in water phase of SNO+," *SNO+ Internal Document, docDB-3869-v2*.
- [22] K. Singh, "Multipath fitter processor," *SNO+ Internal Document, docDB-3849-v1*.

- [23] J. Hu and J. Tseng, “Updates on the multipath water fitter 2018,” *SNO+ Internal Document, docDB-4936-v2*.
- [24] J. Leite-Lopes, “Weak interaction physics: from its origin to the electroweak model,” tech. rep., SCAN-9607019, 1996.
- [25] H. Bethe and R. Peierls, “The “neutrino”,” *Nature*, vol. 133, no. 3362, pp. 532–532, 1934.
- [26] F. Reines, C. Cowan Jr, F. Harrison, A. McGuire, and H. Kruse, “Detection of the free antineutrino,” *Physical Review*, vol. 117, no. 1, p. 159, 1960.
- [27] M. Goldhaber, L. Grodzins, and A. Sunyar, “Helicity of neutrinos,” *Physical Review*, vol. 109, no. 3, p. 1015, 1958.
- [28] C.-S. Wu, E. Ambler, R. Hayward, D. Hoppes, and R. P. Hudson, “Experimental test of parity conservation in beta decay,” *Physical review*, vol. 105, no. 4, p. 1413, 1957.
- [29] I. J. Aitchison and A. J. Hey, *Gauge theories in particle physics: A practical introduction, Volume 2: Non-Abelian Gauge theories: QCD and the electroweak theory*, vol. 2. CRC Press, 2012.
- [30] W. Greiner and B. Müller, *Theoretical Physics Text and Exercise Books: Volume 5: Gauge Theory of Weak Interactions*. Springer Science & Business Media, 2012.
- [31] E. Akhmedov, “Quantum mechanics aspects and subtleties of neutrino oscillations,” *arXiv preprint arXiv:1901.05232*, 2019.
- [32] Y. Fukuda, T. Hayakawa, E. Ichihara, K. Inoue, K. Ishihara, H. Ishino, Y. Itow, T. Kajita, J. Kameda, S. Kasuga, *et al.*, “Evidence for oscillation of atmospheric neutrinos,” *Physical Review Letters*, vol. 81, no. 8, p. 1562, 1998.
- [33] P. D. Group, P. Zyla, R. Barnett, J. Beringer, O. Dahl, D. Dwyer, D. Groom, C.-J. Lin, K. Lugovsky, E. Pianori, *et al.*, “Review of particle physics,” *Progress of Theoretical and Experimental Physics*, vol. 2020, no. 8, p. 083C01, 2020.

- [34] Wikipedia, *CP violation*, 2020 (accessed Mar 15, 2020). <https://en.wikipedia.org/wiki/CPViolation>.
- [35] S. Abe, T. Ebihara, S. Enomoto, K. Furuno, Y. Gando, K. Ichimura, H. Ikeda, K. Inoue, Y. Kibe, Y. Kishimoto, *et al.*, “Precision measurement of neutrino oscillation parameters with kamland,” *Physical Review Letters*, vol. 100, no. 22, p. 221803, 2008.
- [36] K. Abe, C. Bronner, Y. Haga, Y. Hayato, M. Ikeda, K. Iyogi, J. Kameda, Y. Kato, Y. Kishimoto, L. Marti, *et al.*, “Atmospheric neutrino oscillation analysis with external constraints in super-kamiokande i-iv,” *Physical Review D*, vol. 97, no. 7, p. 072001, 2018.
- [37] F. P. An, A. Balantekin, H. Band, M. Bishai, S. Blyth, D. Cao, G. Cao, J. Cao, W. Cen, Y. Chan, *et al.*, “Measurement of electron antineutrino oscillation based on 1230 days of operation of the daya bay experiment,” *Physical Review D*, vol. 95, no. 7, p. 072006, 2017.
- [38] X. Qian and J.-C. Peng, “Physics with reactor neutrinos,” *Reports on Progress in Physics*, vol. 82, no. 3, p. 036201, 2019.
- [39] E. Antonio, *State Of The Art Of Neutrino Physics, The: A Tutorial For Graduate Students And Young Researchers*, vol. 28. World Scientific, 2018.
- [40] Z. Xing and S. Zhou, *Neutrinos in particle physics, astronomy and cosmology*. Springer Science & Business Media, 2011.
- [41] K. Abe, J. Amey, C. Andreopoulos, M. Antonova, S. Aoki, A. Ariga, Y. Ashida, S. Ban, M. Barbi, G. Barker, *et al.*, “Measurement of neutrino and antineutrino oscillations by the t2k experiment including a new additional sample of  $\nu e$  interactions at the far detector,” *Physical Review D*, vol. 96, no. 9, p. 092006, 2017.
- [42] K. Abe, R. Akutsu, A. Ali, C. Alt, C. Andreopoulos, L. Anthony, M. Antonova, S. Aoki, A. Ariga, Y. Asada, *et al.*, “Constraint on the matter-antimatter symmetry-violating phase in neutrinooscillations,” *arXiv preprint arXiv:1910.03887*, 2019.

- [43] A. Y. Smirnov, “Solar neutrinos: Oscillations or no-oscillations?,” *arXiv preprint arXiv:1609.02386*, 2016.
- [44] A. Y. Smirnov, “The msw effect and matter effects in neutrino oscillations,” *Physica Scripta*, vol. 2005, no. T121, p. 57, 2005.
- [45] M. Fukugita and T. Yanagida, *Physics of Neutrinos: and Application to Astrophysics*. Springer Science & Business Media, 2013.
- [46] C. Giunti and C. W. Kim, *Fundamentals of neutrino physics and astrophysics*. Oxford university press, 2007.
- [47] Y. Nagashima, *Beyond the standard model of elementary particle physics*. John Wiley & Sons, 2014.
- [48] H. A. Bethe, “Energy production in stars,” *Physical Review*, vol. 55, no. 5, p. 434, 1939.
- [49] F. Suekane, *Neutrino oscillations: a practical guide to basics and applications*, vol. 898. Springer, 2015.
- [50] W. C. Haxton, R. Hamish Robertson, and A. M. Serenelli, “Solar neutrinos: status and prospects,” *Annual Review of Astronomy and Astrophysics*, vol. 51, pp. 21–61, 2013.
- [51] J. N. Bahcall, “Solar neutrinos. i. theoretical,” *Physical Review Letters*, vol. 12, no. 11, p. 300, 1964.
- [52] R. Davis Jr, “Solar neutrinos. ii. experimental,” *Physical Review Letters*, vol. 12, no. 11, p. 303, 1964.
- [53] B. Collaboration *et al.*, “Experimental evidence of neutrinos produced in the cno fusion cycle in the sun,” *Nature*, vol. 587, no. 7835, pp. 577–582, 2020.

- [54] J. Aalbers, F. Agostini, S. A. Maouloud, M. Alfonsi, L. Althueser, F. Amaro, J. Angevaare, V. Antochi, B. Antunovic, E. Aprile, *et al.*, “Solar neutrino detection sensitivity in darwin via electron scattering,” *The European Physical Journal C*, vol. 80, no. 12, pp. 1–10, 2020.
- [55] A. Giaz, “Status and perspectives of the JUNO experiment,” *arXiv preprint arXiv:1804.03575*, 2018.
- [56] E. Akhmedov, “Majorana neutrinos and other majorana particles: Theory and experiment,” *arXiv preprint arXiv:1412.3320*, 2014.
- [57] A. Zee, *Quantum field theory in a nutshell*, 2nd edn., vol. 7. Princeton university press, 2011.
- [58] E. Majorana and L. Maiani, *A symmetric theory of electrons and positrons*. Springer, 2006.
- [59] R. Z. Funchal, B. Schmauch, and G. Giesen, “The physics of neutrinos,” *arXiv preprint arXiv:1308.1029*, 2013.
- [60] K. Zuber, “On the physics of massive neutrinos,” *Physics Reports*, vol. 305, no. 6, pp. 295–364, 1998.
- [61] V. Barger, D. Marfatia, and K. Whisnant, *The physics of neutrinos*. Princeton University Press, 2012.
- [62] C. Dvorkin, M. Gerbino, D. Alonso, N. Battaglia, S. Bird, A. D. Rivero, A. Font-Ribera, G. Fuller, M. Lattanzi, M. Loverde, *et al.*, “Neutrino mass from cosmology: Probing physics beyond the standard model,” *arXiv preprint arXiv:1903.03689*, 2019.
- [63] M. Gerbino and M. Lattanzi, “Status of neutrino properties and future prospectscosmological and astrophysical constraints,” *Frontiers in Physics*, vol. 5, p. 70, 2018.

- [64] N. Aghanim, Y. Akrami, M. Ashdown, J. Aumont, C. Baccigalupi, M. Ballardini, A. Banday, R. Barreiro, N. Bartolo, S. Basak, *et al.*, “Planck 2018 results-vi. cosmological parameters,” *Astronomy & Astrophysics*, vol. 641, p. A6, 2020.
- [65] C. Rötteler, “Tritium suppression factor of the katrin transport section,” 2019.
- [66] M. Aker, K. Altenmüller, M. Arenz, M. Babutzka, J. Barrett, S. Bauer, M. Beck, A. Beglarian, J. Behrens, T. Bergmann, *et al.*, “Improved upper limit on the neutrino mass from a direct kinematic method by katrin,” *Physical review letters*, vol. 123, no. 22, p. 221802, 2019.
- [67] B. Povh, K. Rith, and F. Zetsche, *Particles and nuclei*, vol. 1. Springer, 2008.
- [68] B. R. Martin and G. Shaw, *Nuclear and particle physics: an introduction*. John Wiley & Sons, 2019.
- [69] S. Bilenky, *Introduction to the physics of massive and mixed neutrinos*, vol. 947. Springer, 2018.
- [70] K. Zuber, *Neutrino physics*. CRC press, 2020.
- [71] M. J. Dolinski, A. W. Poon, and W. Rodejohann, “Neutrinoless double-beta decay: status and prospects,” *Annual Review of Nuclear and Particle Science*, vol. 69, pp. 219–251, 2019.
- [72] O. Cremonesi and M. Pavan, “Challenges in double beta decay,” *Advances in High Energy Physics*, vol. 2014, 2014.
- [73] I. Shimizu and M. Chen, “Double beta decay experiments with loaded liquid scintillator,” *Frontiers in Physics*, vol. 7, p. 33, 2019.
- [74] M. Agostini, M. Allardt, A. Bakalyarov, M. Balata, I. Barabanyov, L. Baudis, C. Bauer, N. Becerici-Schmidt, E. Bellotti, S. Belogurov, *et al.*, “Search of neutrinoless double beta decay with the gerda experiment,” *Nuclear and particle physics proceedings*, vol. 273, pp. 1876–1882, 2016.

- [75] M. Agostini, A. Bakalyarov, M. Balata, I. Barabanov, L. Baudis, C. Bauer, E. Bellotti, S. Belogurov, A. Bettini, L. Bezrukov, *et al.*, “Probing majorana neutrinos with double- $\beta$  decay,” *Science*, vol. 365, no. 6460, pp. 1445–1448, 2019.
- [76] J. Albert, D. Auty, P. Barbeau, E. Beauchamp, D. Beck, V. Belov, C. Benitez-Medina, J. Bonatt, M. Breidenbach, T. Brunner, *et al.*, “Search for majorana neutrinos with the first two years of exo-200 data,” *Nature*, vol. 510, no. 7504, pp. 229–234, 2014.
- [77] J. Albert, G. Anton, I. Arnquist, I. Badhrees, P. Barbeau, D. Beck, V. Belov, F. Bourque, J. Brodsky, E. Brown, *et al.*, “Sensitivity and discovery potential of the proposed nexo experiment to neutrinoless double- $\beta$  decay,” *Physical Review C*, vol. 97, no. 6, p. 065503, 2018.
- [78] A. Gando, Y. Gando, T. Hachiya, A. Hayashi, S. Hayashida, H. Ikeda, K. Inoue, K. Ishidoshiro, Y. Karino, M. Koga, *et al.*, “Search for majorana neutrinos near the inverted mass hierarchy region with kamland-zen,” *Physical Review Letters*, vol. 117, no. 8, p. 082503, 2016.
- [79] C. Alduino, F. Alessandria, K. Alfonso, E. Andreotti, C. Arnaboldi, F. Avignone III, O. Azzolini, M. Balata, I. Bandac, T. Banks, *et al.*, “First results from cuore: A search for lepton number violation via  $0\nu\beta\beta$  decay of te-130,” *Physical review letters*, vol. 120, no. 13, p. 132501, 2018.
- [80] G. Piperno, “Dark matter search with the cuore-0 experiment,” 2015.
- [81] M. Agostini, G. Benato, and J. A. Detwiler, “Discovery probability of next-generation neutrinoless double- $\beta$  decay experiments,” *Physical Review D*, vol. 96, no. 5, p. 053001, 2017.
- [82] “Muons,” 2001 (accessed 19-July-2019). [https://cosmic.lbl.gov/SKliewer/Cosmic\\_Rays/Muons.htm](https://cosmic.lbl.gov/SKliewer/Cosmic_Rays/Muons.htm).

- [83] J. F. Beacom, S. Chen, J. Cheng, S. N. Dousttimotlagh, Y. Gao, G. Gong, H. Gong, L. Guo, R. Han, H.-J. He, *et al.*, “Physics prospects of the jinping neutrino experiment,” *Chinese physics C*, vol. 41, no. 2, p. 023002, 2017.
- [84] J. Waterfield, *Optical calibration system for SNO+ and sensitivity to neutrinoless double-beta decay*. PhD thesis, University of Sussex, 2017.
- [85] S. Andringa, E. Arushanova, S. Asahi, M. Askins, D. Auty, A. Back, Z. Barnard, N. Barros, E. Beier, A. Bialek, *et al.*, “Current status and future prospects of the SNO+,” *Advances in High Energy Physics*, vol. 2016, 2016.
- [86] M. Stringer, *Sensitivity of SNO+ to supernova neutrinos*. PhD thesis, University of Sussex, 2019.
- [87] M. Anderson, S. Andringa, E. Arushanova, S. Asahi, M. Askins, D. Auty, A. Back, Z. Barnard, N. Barros, D. Bartlett, *et al.*, “Search for invisible modes of nucleon decay in water with the SNO+ detector,” *Physical Review D*, vol. 99, no. 3, p. 032008, 2019.
- [88] M. Anderson, S. Andringa, S. Asahi, M. Askins, D. Auty, N. Barros, D. Bartlett, F. Barão, R. Bayes, E. Beier, *et al.*, “Measurement of the  ${}^8\text{B}$  solar neutrino flux in SNO+ with very low backgrounds,” *Physical Review D*, vol. 99, no. 1, p. 012012, 2019.
- [89] M. Anderson, S. Andringa, M. Askins, D. Auty, N. Barros, F. Barão, R. Bayes, E. Beier, A. Bialek, S. Biller, *et al.*, “Measurement of neutron-proton capture in the SNO+ water phase,” *Physical Review C*, vol. 102, no. 1, p. 014002, 2020.
- [90] S. Davini, M. Agostini, S. Appel, G. Bellini, J. Benziger, D. Bick, G. Bonfini, D. Bravo, B. Caccianiga, F. Calaprice, *et al.*, “CNO and pep solar neutrino measurements and perspectives in borexino,” vol. 675, no. 1, p. 012040, 2016.
- [91] D. G. Cerdeno, J. H. Davis, M. Fairbairn, and A. C. Vincent, “Cno neutrino grand prix: The race to solve the solar metallicity problem,” *Journal of Cosmology and Astroparticle Physics*, vol. 2018, no. 04, p. 037, 2018.

- [92] J. Paton, “Neutrinoless Double Beta Decay in the SNO+ Experiment,” 2019.
- [93] J. D. Jackson, *Classical Electrodynamics*. John Wiley & Sons, 2007.
- [94] L. D. Landau, J. Bell, M. Kearsley, L. Pitaevskii, E. Lifshitz, and J. Sykes, *Electrodynamics of Continuous Media*, vol. 8. elsevier, 2013.
- [95] H. W. C. Tseung and N. Tolich, “Ellipsometric measurements of the refractive indices of linear alkylbenzene and ej-301 scintillators from 210 to 1000 nm,” *Physica Scripta*, vol. 84, no. 3, p. 035701, 2011.
- [96] W. R. Leo, *Techniques for Nuclear and Particle Physics Experiments: a How-to Approach*. Springer Science & Business Media, 2012.
- [97] B. Von Krosigk, *Measurement of Proton and  $\alpha$  Particle Quenching in LAB Based Scintillators and Determination of Spectral Sensitivities to Supernova Neutrinos in the SNO+ Detector*. PhD thesis, Technische Universitaet Dresden, 2015.
- [98] A. Sørensen, “Temperature quenching in lab based liquid scintillator and muon-induced backgrounds in the sno+ experiment,” 2016.
- [99] J. Dunger, *Topological and time based event classification for neutrinoless double beta decay in liquid scintillator*. PhD thesis, University of Oxford, 2018.
- [100] D. A. McQuarrie and J. D. Simon, *Physical chemistry: a molecular approach*, vol. 1. University science books Sausalito, CA, 1997.
- [101] S. Collaboration, M. Anderson, S. Andringa, L. Anselmo, E. Arushanova, S. Asahi, M. Askins, D. Auty, A. Back, Z. Barnard, *et al.*, “Development, characterisation, and deployment of the SNO+ liquid scintillator,” *arXiv preprint arXiv:2011.12924*, 2020.
- [102] J. B. Birks, “Scintillations from organic crystals: specific fluorescence and relative response to different radiations,” *Proceedings of the Physical Society. Section A*, vol. 64, no. 10, p. 874, 1951.

- [103] PerkinElmer, “Liquid scintillation cocktails,” 1998-2021 (accessed 20-Dec-2019). <https://www.perkinelmer.com/en-ca/lab-products-and-services/application-support-knowledgebase/radiometric/liquid-scintillation-cocktails.html>.
- [104] X. Dai, E. Rollin, A. Bellerive, C. Hargrove, D. Sinclair, C. Mifflin, and F. Zhang, “Wavelength shifters for water cherenkov detectors,” *Nuclear Instruments and Methods in Physics Research Section A: Accelerators, Spectrometers, Detectors and Associated Equipment*, vol. 589, no. 2, pp. 290–295, 2008.
- [105] J. Alonso, N. Barros, M. Bergevin, A. Bernstein, L. Bignell, E. Blucher, F. Calaprice, J. Conrad, F. Descamps, M. Diwan, *et al.*, “Advanced scintillator detector concept (asdc): a concept paper on the physics potential of water-based liquid scintillator,” *arXiv preprint arXiv:1409.5864*, 2014.
- [106] M. Askins, M. Bergevin, A. Bernstein, S. Dazeley, S. Dye, T. Handler, A. Hatzikoutelis, D. Hellfeld, P. Jaffke, Y. Kamyshkov, *et al.*, “The physics and nuclear non-proliferation goals of watchman: A water cherenkov monitor for antineutrinos,” *arXiv preprint arXiv:1502.01132*, 2015.
- [107] Wikipedia, “Linear alkylbenzene,” 2020 (accessed 1-Jan-2020). [https://en.wikipedia.org/wiki/Linear\\_alkylbenzene](https://en.wikipedia.org/wiki/Linear_alkylbenzene).
- [108] M. C. Helen O’Keeffe, Valentina Lozza, “Lab backgrounds expected numbers,” *SNO+ Internal Document, docDB-507-v42*.
- [109] S. W. Wunderly and J. M. Kauffman, “New quench-resistant fluors for liquid scintillation counting,” *International Journal of Radiation Applications and Instrumentation. Part A. Applied Radiation and Isotopes*, vol. 41, no. 9, pp. 809–815, 1990.
- [110] Y. Xing-Chen, Y. Bo-Xiang, Z. Xiang, Z. Li, D. Ya-Yun, L. Meng-Chao, D. Xue-Feng, Z. Xuan, J. Quan-Lin, Z. Li, *et al.*, “Preliminary study of light yield dependence on lab liquid scintillator composition,” *Chinese Physics C*, vol. 39, no. 9, p. 096003, 2015.

- [111] S. D. Biller, E. J. Leming, and J. L. Paton, “Slow fluors for highly effective separation of cherenkov light in liquid scintillators,” *arXiv preprint arXiv:2001.10825*, 2020.
- [112] A. LaTorre, “New measurements for the timing spectrum of electrons and alphas in lab+ppo,” *SNO+ Internal Document, docDB-4081-v1*.
- [113] T. Kaptanoglu, “Measurements of light yield and timing of 0.5 g/l lab+ppo,” *SNO+ Internal Document, docDB-5997-v1*.
- [114] J.-S. Wang, “Bipo analysis using partial fill data,” *SNO+ Internal Document, docDB-5950-v3*.
- [115] S. Biller, S. Manecki, S. collaboration, *et al.*, “A new technique to load 130te in liquid scintillator for neutrinoless double beta decay experiments,” in *Journal of Physics: Conference Series*, vol. 888, p. 012084, IOP Publishing, 2017.
- [116] *National Nuclear Data Center*, 2019 (accessed Oct 30, 2019). <https://www.nndc.bnl.gov/>.
- [117] J. Boger, R. Hahn, J. Rowley, A. Carter, B. Hollebone, D. Kessler, I. Blevis, F. Dalnoki-Veress, A. DeKok, J. Farine, *et al.*, “The sudbury neutrino observatory,” *Nuclear Instruments and Methods in Physics Research Section A: Accelerators, Spectrometers, Detectors and Associated Equipment*, vol. 449, no. 1-2, pp. 172–207, 2000.
- [118] K. Hamamatsu Photonics, “Photomultiplier tubes: Basics and applications, 2007,” 2018.
- [119] G. O. Gann, “Dealing with time in rat,” *SNO+ Internal Document, docDB-481-v2*.
- [120] R. Bonventre, *Neutron multiplicity in atmospheric neutrino events at the Sudbury Neutrino Observatory*. PhD thesis, University of Pennsylvania, 2014.
- [121] J. M. Walker, *Study of Invisible Mode Nucleon Decay in the SNO+ Detector*. PhD thesis, University of Liverpool, 2016.

- [122] K. Singh, P. Gorel, A. Hallin, C. Krauss, and Z. Petriw, “Underwater photometry system of the SNO+ experiment,” in *Journal of Physics: Conference Series*, vol. 1342, p. 012130, IOP Publishing, 2020.
- [123] M. R. Dragowsky, *Sudbury Neutrino Observatory energy calibration using gamma-ray sources*. PhD thesis, Oregon State University, 1999.
- [124] A. S. Hamer, *Energy calibration of SNO for measurement of the charged-current neutrino reaction*. PhD thesis, Queen’s University, 2001.
- [125] S. Agostinelli, J. Allison, K. a. Amako, J. Apostolakis, H. Araujo, P. Arce, M. Asai, D. Axen, S. Banerjee, G. . Barrand, *et al.*, “Geant4a simulation toolkit,” *Nuclear instruments and methods in physics research section A: Accelerators, Spectrometers, Detectors and Associated Equipment*, vol. 506, no. 3, pp. 250–303, 2003.
- [126] R. Brun, F. Rademakers, P. Canal, *et al.*, “Root: An object oriented data analysis framework, 2007,” *See Also <http://root.cern.ch>.*
- [127] *RAT Overview*, 2020 (accessed Mar 15, 2020). <https://rat.readthedocs.io/en/latest/overview.html>.
- [128] G. Horton-Smith *et al.*, “Introduction to glg4sim,” 2006.
- [129] T. Caldwell, “Simulation of noble liquid detectors using rat,” in *AARM Meeting at Fermilab*, 2014.
- [130] J. Dittmer and M. Meyer, “Topological track reconstruction with the sno+ experiment,” *SNO+ Internal Document, docDB-5749-v1*.
- [131] P. Gregory, *Bayesian Logical Data Analysis for the Physical Sciences: A Comparative Approach with Mathematica® Support*. Cambridge University Press, 2005.
- [132] W. H. Press, S. A. Teukolsky, W. T. Vetterling, and B. P. Flannery, *Numerical recipes 3rd edition: The art of scientific computing*. Cambridge university press, 2007.

- [133] F. Barao and J. Maneira, “Group velocity measurement, plot for approval,” *SNO+ Internal Document, docDB-5071-v1*.
- [134] I. T. Coulter, *Modelling and Reconstruction of Events in SNO+ related to Future Searches for Lepton and Baryon Number Violation*. PhD thesis, University of Oxford, 2013.
- [135] Wikipedia, *JSON*, 2020 (accessed Mar 15, 2020). <https://en.wikipedia.org/wiki/JSON>.
- [136] ROOT, *TDecompQRH Class Reference*, 2020 (accessed Mar 15, 2020). <https://root.cern.ch/doc/master/classTDecompQRH.html>.
- [137] W. P. Group, “Water physics unidoc,” *SNO+ Internal Document*.
- [138] M. G. Boulay, *Direct Evidence for Weak Flavour Mixing with the Sudbury Neutrino Observatory*. PhD thesis, Queens University, 2004.
- [139] P. Mekarski, *Electron Antineutrinos in the Water Phase of the SNO+ Experiment*. PhD thesis, University of Alberta, 2018.
- [140] L. Lebanowski, “Improved mode cut,” *SNO+ Internal Document, docDB-5488-v1*.
- [141] B. A. Moffat, *The optical calibration of the Sudbury Neutrino Observatory*. PhD thesis, Queens University, 2001.
- [142] M. Mottram, “Note on RSP fitter,” *SNO+ Internal Document, docDB-3939-v1*.
- [143] M. Mottram, “Energy reconstruction in partial scintillator fill,” *SNO+ Internal Document, docDB-3133-v1*.
- [144] Y. Zhang, “Performance of qenergy based on q,” *SNO+ Internal Document, docDB-6065-v1*.
- [145] E. Davies, “Machine vision: Theory, algorithms, practicalities. academic press., 2-nd edition,” 1997.

- [146] Wikipedia, *Hough Transform*, 2019 (accessed Nov 3, 2019). [https://en.wikipedia.org/wiki/Hough\\_transform](https://en.wikipedia.org/wiki/Hough_transform).
- [147] M. Shiozawa, “Reconstruction algorithms in the super-kamiokande large water cherenkov detector,” *Nuclear Instruments and Methods in Physics Research Section A: Accelerators, Spectrometers, Detectors and Associated Equipment*, vol. 433, no. 1-2, pp. 240–246, 1999.
- [148] G. Beier, “Study of direction reconstruction in scintillator,” *SNO+ Internal Document, docDB-3503-v4*.
- [149] M. Anderson, “Status and updates on neural network fitter,” *SNO+ Internal Document, docDB-6298-v1*.
- [150] M. Anderson, “Deep learning to reconstruct particle interaction properties for the SNO+ neutrino physics experiment,” *Canadian AI Conference 2020 - Talk*.
- [151] J. Klein, “Leta high level cuts (including qpdt and itr),” *SNO+ Internal Document, docDB-2512-v1*.
- [152] J. A. Dunmore, *The separation of CC and NC events in the Sudbury Neutrino Observatory*. PhD thesis, University of Oxford, 2004.
- [153] E. Marzec, “Measurement of 8b solar neutrinos in the sno+ water phase and a model of vacuum-enhanced neutrino mixing,” 2019.
- [154] P.-L. Drouin, *Three-phase extraction of the electron neutrino survival probability at the Sudbury Neutrino Observatory*. PhD thesis, Carleton University, 2012.
- [155] B. K. Ryan Bayes, “Beta 14 discrepancy in sno+,” *SNO+ Internal Document, docDB-6613-v2*.
- [156] L. W. Group, “Low energy threshold analysis (leta) unidoc v. 0.1,” *SNO+ Internal Document, docDB-4322-v1*.

- [157] *TMVA*, 2020 (accessed Mar 30, 2020). <https://root.cern.ch/tmva>.
- [158] K. Albertsson, S. Gleyzer, A. Hoecker, L. Moneta, P. Speckmayer, J. Stelzer, J. Therhaag, E. von Toerne, H. Voss, and S. Wunsch, “Tmva 4,” *arXiv preprint physics/0703039*, 2007.
- [159] K. P. Murphy, *Machine learning: a probabilistic perspective*. MIT press, 2012.
- [160] M. Askins, “Water phase figures of merit selection,” *SNO+ Internal Document, docDB-6560-v1*.
- [161] *StatPatternRecognition and Machine Learning in HEP*, 2020 (accessed Mar 30, 2020). <http://www.hep.caltech.edu/~narsky/spr.html>.
- [162] F. Shaker, “PSelmaa a solar neutrino tool,” *SNO+ Internal Document, docDB-6013-v1*.
- [163] J. Bramante, B. Broerman, J. Kumar, R. F. Lang, M. Pospelov, and N. Raj, “Foraging for dark matter in large volume liquid scintillator neutrino detectors with multiscatter events,” *Physical Review D*, vol. 99, no. 8, p. 083010, 2019.
- [164] R. Becker-Szendy, C. Bratton, D. Casper, S. Dye, W. Gajewski, M. Goldhaber, T. Haines, P. Halverson, D. Kielczewska, W. Kropp, *et al.*, “Electron-and muon-neutrino content of the atmospheric flux,” *Physical Review D*, vol. 46, no. 9, p. 3720, 1992.
- [165] W. Allison, G. Alner, D. Ayres, W. Barrett, C. Bode, P. Border, C. Brooks, J. Cobb, D. Cockerill, R. Cotton, *et al.*, “Measurement of the atmospheric neutrino flavour composition in soudan 2,” *Physics Letters B*, vol. 391, no. 3-4, pp. 491–500, 1997.
- [166] T. Kajita, “Atmospheric neutrinos,” *Advances in High Energy Physics*, vol. 2012, 2012.
- [167] H. H. Chen, “Direct approach to resolve the solar-neutrino problem,” *Physical Review Letters*, vol. 55, no. 14, p. 1534, 1985.

- [168] Q. R. Ahmad, R. Allen, T. Andersen, J. Anglin, J. Barton, E. Beier, M. Bercovitch, J. Bigu, S. Biller, R. Black, *et al.*, “Direct evidence for neutrino flavor transformation from neutral-current interactions in the sudbury neutrino observatory,” *Physical review letters*, vol. 89, no. 1, p. 011301, 2002.
- [169] B. Aharmim, S. Ahmed, A. Anthony, N. Barros, E. Beier, A. Bellerive, B. Beltran, M. Bergevin, S. Biller, K. Boudjemline, *et al.*, “Combined analysis of all three phases of solar neutrino data from the sudbury neutrino observatory,” *Physical Review C*, vol. 88, no. 2, p. 025501, 2013.
- [170] K. Abe, Y. Haga, Y. Hayato, M. Ikeda, K. Iyogi, J. Kameda, Y. Kishimoto, L. Marti, M. Miura, S. Moriyama, *et al.*, “Solar neutrino measurements in super-kamiokande-iv,” *Physical Review D*, vol. 94, no. 5, p. 052010, 2016.
- [171] H. W. Zaglauer and K. H. Schwarzer, “The mixing angles in matter for three generations of neutrinos and the msw mechanism,” *Zeitschrift für Physik C Particles and Fields*, vol. 40, no. 2, pp. 273–282, 1988.
- [172] K. Kimura, A. Takamura, and H. Yokomakura, “Exact formula of probability and cp violation for neutrino oscillations in matter,” *Physics Letters B*, vol. 537, no. 1-2, pp. 86–94, 2002.
- [173] P. B. Denton, S. J. Parke, and X. Zhang, “Eigenvalues: The rosetta stone for neutrino oscillations in matter,” *arXiv preprint arXiv:1907.02534*, 2019.
- [174] J. Schechter and J. W. Valle, “Neutrinoless double- $\beta$  decay in  $\text{su}(2) \times \text{u}(1)$  theories,” *Physical Review D*, vol. 25, no. 11, p. 2951, 1982.
- [175] M. Duerr, M. Lindner, and A. Merle, “On the quantitative impact of the schechter-valle theorem,” *Journal of High Energy Physics*, vol. 2011, no. 6, p. 91, 2011.
- [176] E. Takasugi, “Can the neutrinoless double beta decay take place in the case of dirac neutrinos?,” *Physics Letters B*, vol. 149, no. 4-5, pp. 372–376, 1984.

- [177] M. Agostini, M. Allardt, A. Bakalyarov, M. Balata, I. Barabanov, L. Baudis, C. Bauer, E. Bellotti, S. Belogurov, S. Belyaev, *et al.*, “Background-free search for neutrinoless double- $\beta$  decay of  $^{76}\text{Ge}$  with gerda,” *Nature*, vol. 544, no. 7648, pp. 47–52, 2017.
- [178] M. Spurio, Spurio, and Bellantone, *Probes of Multimessenger Astrophysics*. Springer, 2018.
- [179] D. H. Perkins, *Particle astrophysics*. No. 10, Oxford University Press, 2009.
- [180] G. Kane, *Modern elementary particle physics: explaining and extending the standard model*. Cambridge University Press, 2017.
- [181] J. Lesgourgues, G. Mangano, G. Miele, and S. Pastor, *Neutrino cosmology*. Cambridge University Press, 2013.
- [182] N. Vinyoles, A. M. Serenelli, F. L. Villante, S. Basu, J. Bergström, M. Gonzalez-Garcia, M. Maltoni, C. Peña-Garay, and N. Song, “A new generation of standard solar models,” *The Astrophysical Journal*, vol. 835, no. 2, p. 202, 2017.
- [183] I. Esteban, M. Gonzalez-Garcia, A. Hernandez-Cabezudo, M. Maltoni, and T. Schwetz, “Global analysis of three-flavour neutrino oscillations: synergies and tensions in the determination of  $\theta_{23}$ ,  $\delta_{CP}$ , and the mass ordering,” *Journal of High Energy Physics*, vol. 2019, no. 1, p. 106, 2019.
- [184] C. Weinheimer, “Neutrino mass from triton decay,” *Progress in Particle and Nuclear Physics*, vol. 57, no. 1, pp. 22–37, 2006.
- [185] A. Bialek, M. Chen, B. Cleveland, P. Gorel, A. Hallin, P. Harvey, J. Heise, C. Kraus, C. Krauss, I. Lawson, *et al.*, “A rope-net support system for the liquid scintillator detector for the SNO+ experiment,” *Nuclear Instruments and Methods in Physics Research Section A: Accelerators, Spectrometers, Detectors and Associated Equipment*, vol. 827, pp. 152–160, 2016.

- [186] A. M. Richie Bonventre, “Everything a detector operator ever wanted to know about electronics and much more you didnt want to know.”
- [187] “SNO+ detector operator manual,” *SNO+ Internal Document*.
- [188] “Triggering options for SNO+ water fill,” *SNO+ Internal Document, docDB-4323-v1*.
- [189] T. Kaptanoglu, “Characterization of the hamamatsu 8 r5912-mod photomultiplier tube,” *Nuclear Instruments and Methods in Physics Research Section A: Accelerators, Spectrometers, Detectors and Associated Equipment*, vol. 889, pp. 69–77, 2018.
- [190] M. Anderson, “Neural network fitter updates,” *SNO+ Internal Document, docDB-6298-v1*.
- [191] M. Dunford, *Measurement of the  $^8B$  solar neutrino energy spectrum at the Sudbury Neutrino Observatory*. PhD thesis, University of Pennsylvania, 2006.
- [192] B. Krar, “Lowbg water solar analysis,” *SNO+ Internal Document, docDB-6698-v3*.